Laser precision metrology for probing variation of fundamental constants

VRIJE UNIVERSITEIT

Laser precision metrology for probing variation of fundamental constants

ACADEMISCH PROEFSCHRIFT

ter verkrijging van de graad Doctor aan
de Vrije Universiteit Amsterdam,
op gezag van de rector magnificus
prof.dr. L.M. Bouter,
in het openbaar te verdedigen
ten overstaan van de promotiecommissie
van de faculteit der Exacte Wetenschappen
op dinsdag 26 mei 2009 om 15.45 uur
in de aula van de universiteit,
De Boelelaan 1105

door

Edcel John Salumbides

geboren te Cebu, Filippijnen

promotor:	prof.dr. W.M.G. Ubachs
copromotor:	dr. K.S.E. Eikema

for Marian

The game of science is, in principle, without end. He who decides one day
that scientific statements do not call for any further test, and that
they can be regarded as finally verified, retires from the game.

Karl Popper

This thesis was reviewed by the members of the reviewing committee:

Prof. Dr. K. Jungmann (KVI, University of Groningen)
Dr. H. Knöckel (Leibniz University Hannover, Germany)
Prof. Dr. F. Merkt (ETH Zurich, Switzerland)
Prof. Dr. H. Rudolph (Utrecht University)
Prof. Dr. M.J.J. Vrakking (AMOLF, Amsterdam)

FOM The work described in this thesis was performed as part of the research program of the "Stichting voor Fundamenteel Onderzoek der Materie" (FOM) and was carried out at the Laser Centre of the Vrije Universiteit Amsterdam.

The painting on the cover is entitled **The Measurers** and is attributed to the 16th-century Flemish school, with the copyright belonging to the Museum of the History of Science, University of Oxford, England. The author is grateful to Dr. Jim Bennett, Director of the Museum, for his kind permission for the use of the painting as cover art.

Printed by PrintPartners Ipskamp BV, Enschede
isbn 978-90-8659316-3

Contents

Chapter 1

Introduction

The interaction of light and matter is a very familiar phenomenon, yet it is also a very subtle and fundamental interaction. The dispersion of the colors of white light as it passes through a prism, and the beautiful colors of the rainbow come to mind as vibrant examples. Light-matter interaction is conveniently exploited in spectroscopy, where studying the spectrum of the light absorbed or emitted by a material is used to investigate the properties of the material itself. Since (almost) all matter interacts with light, spectroscopy has widespread applications ranging from the study of protein dynamics to the determination of the composition of astronomical objects.

The absorption or emission spectra of atoms are relatively simple, and consist of sharp features or spectral lines. Molecular spectra are more complex, and become even more so, due to inter-atomic interactions as the number of constituent atoms increases. Further complications arise from interactions between atoms or molecules within a sample or with the environment. These can modify and reduce the level of detail in the recorded spectra. This is apparent when one compares the spectra of a solid that typically consist of a broad and featureless spectral band, while that of a dilute gas consist of sharp lines. In our high-resolution spectroscopic investigations, several techniques are employed to obtain high-precision atomic and molecular spectra.

The work presented in this thesis comprises of a collection of precision spectroscopic studies on several atoms and molecules. The high accuracy achieved in the experiments creates opportunities for the results to be useful in studies that detect very subtle physical effects. Some of these studies attempt to probe the possible variation of fundamental physical constants on a cosmological timescale. This is done by a comparison of present-day laboratory spectroscopic data with absorption spectra collected from very distant astronomical objects. Another theme is to compare the accurate experimental results to calculation results using the most accurate quantum theoretical model of the hydrogen molecule.

In this chapter, we present motivations explaining the great interest in the subject of fundamental constants and their possible variation. We present an overview of the different experimental and observational strategies used to probe the variations of fundamental constants. We discuss in some detail the particular strategy most relevant to laboratory precision spectroscopy described in this thesis. Finally, we present a summary of the following chapters.

1.1 Fundamental constants of nature

The collective human enterprise that is *Science* has proven its effectiveness in producing the most accurate models that represent reality. Over the centuries, scientists have striven for, and have successfully uncovered, the forms of universal physical laws that constitute the best description of nature. At present, the formulations of these physicals laws have been satisfactorily established, that is, these laws provide a correct description within the present experimental accuracies. Yet, there are quantities referred to as the *constants of nature* that are not derivable from the physical theories themselves. The constants serve as free parameters of the theories, and the values of these constants can only be determined empirically. In general, the constants can be considered as important as the form of physical laws themselves, in a consistent and valid model of reality.

A deep conviction among scientists that perhaps might be considered a cornerstone in science is the universality of physical law, and hence there is a strong motivation to formulate physical theories that exhibit the characteristics of universality. This may be extended to the universality of fundamental constants of nature. Thus, the *electron charge* is considered identical for any two electrons even with lightyears of separation; or that the *speed of light* is the same today as it was 4.5 billion years ago when the solar system formed. Any observed variation of fundamental constants, then provides very stringent tests of existing theories and if established, would naturally inaugurate the search for new physics.

The previous two examples of fundamental constants that were invoked, the electron charge and the speed of light, are fundamental constants with dimensions or units. If a *dimensional* quantity is varying, there is no *operational* method of ascertaining if it is the measured quantity itself or the unit (or measuring rod so to speak) that is changing.[1] For this reason, if we are to seek variations in constants, it would be most convenient to probe dimensionless constants. Apart from a practical reason, *dimensionless* fundamental constants are regarded with universal significance in contradistinction to arbitrary, anthropically-derived units of measure.

There is an additional philosophical justification for considering dimensionless constants as more universal. There always has been an optimism, prevalent among scientists, of discovering the ultimate theory of everything, where it is expected or most desired to include a deterministic method to calculate the constants of nature. Einstein was one prominent example, where he expressed his hopes of the future elucidation of dimensionless fundamental constants, as mere combinations natural numbers and mathematical constants such as π and e.[*] However, as it stands at present, there is still no theory that predicts, or even restricts the values of the constants. A fundamental question then arises, if it is possible to ever give bounds or restrictions to possible values of the constants of nature *in our universe*. Fortunately, the answer turns out to be affirmative, relying on the fact that the subsequent evolution of the universe since the Big Bang is very sensitive to the balance of fundamental forces, the strengths of which are parameterized by the fundamental constants of nature. [†]

As an example to highlight the dramatic consequences of the specific values of fundamental constants, we take the nucleosynthesis of carbon and oxygen in stars. The formation of ^{12}C is a two-step process, first with the formation of ^{8}Be from the collision of two alpha particles (^{4}He nuclei), and a subsequent step where an additional alpha particle is captured. The observed ^{12}C abundance is found to be much higher than what could be expected from the non-resonant accumulation of alpha particles. Furthermore, the next step in the chain is the synthesis of ^{16}O, from the additional capture of ^{4}He, which further reduces the ^{12}C abundance. To account for the observed abundance of ^{12}C in the universe, Hoyle suggested that there must be a nuclear resonance in ^{12}C that enhances the triple-alpha process,[5] which has since been confirmed experimentally.[6,7] The energy position of the resonance depends on the balance between the strong nuclear force, which binds the nucleons, and electromagnetic force, which is responsible for the repulsion between the protons. The strengths of the strong nuclear force and the electromagnetic force depend on the strong-coupling constant α_s and the fine structure constant α, respectively. Oberhummer *et al.*[8] have calculated the change in the abundances of ^{12}C and ^{16}O when the strengths of these two forces are varied, as depicted in Fig.1.1. The calculated abundances X can be as low as a few thousandths of the observed ^{12}C and ^{16}O abun-

---

[*] Quoted in Ref. 2. See also Ref. 3.

[†] Indeed, there are modern theories, motivated by the inflationary Big Bang model, that propose the existence of a multitude of universes[4] that may have very different physical laws and constants of nature; therefore, the constants cannot be restricted in the method suggested.

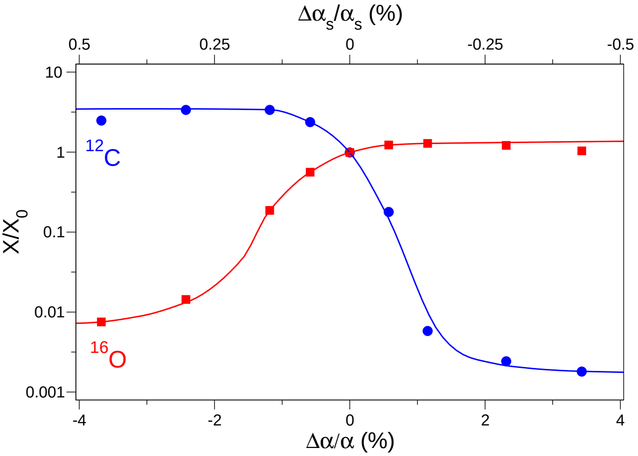

Figure 1.1 – *The relative abundance* X/X_0*, where* X_0 *is the standard value, of the* ^{12}C *and* ^{16}O *as a function of the variation in the coupling strengths of the strong nuclear interaction,* α_s*, and electromagnetic interaction,* α*. (Adapted from Ref. 8.)*

dances X_0, for a change in α_s of only a fraction of a percent or for a few percent in α. Clearly, this balance in the abundances of ^{12}C and ^{16}O has major implications for the subsequent organic chemistry in our universe, and hence by natural extension to the evolution of biological systems on earth.

The fine structure constant α

The fine structure constant α is truly a fundamental constant which permeates the whole of physics. It is related to other fundamental physical constants, and in S.I. units we have the relation

$$\alpha = \frac{e^2}{4\pi\epsilon_0 \hbar c},$$

where e is the electron charge, ϵ_0 is the electric permitivitty in vacuum, $\hbar$ is Planck's constant divided by 2π, and c is the speed of light. The fine structure constant first gained its significant position in the theory of Sommerfeld,[9] which is an extension of Bohr's atomic theory, thereby completing the so-called old quantum theory. Sommerfeld considered relativistic elliptical orbits, which effectively adds a second quantum number (corresponding to the second axis) to the principal orbital quantum number of Bohr. The classical electron speed for the first orbit is $v_1 = \alpha c$, and it is then natural to expect the relativistic energy correction to be expressed in terms of $\alpha = v_1/c$. It turns out that the Sommerfeld theory correctly accounts for the doublet structure of the hydrogen spectrum as well as that of the He^+ ion. These predictions were soon confirmed experimentally by Paschen in the optical and X-ray domain.[10] The successful resolution of these examples of atomic *fine structures*, hitherto unexplained by the Bohr theory, was acclaimed as a great success, and the parameter α was from then on to be known as the fine structure constant. Although the old quantum theory has been superseded by the quantum theory pioneered by Schrödinger, Heisenberg, and Pauli, it is remarkable that the completely relativistic Dirac model of the hydrogen atom arrives at the exact expression for the level energy as that of Sommerfeld's result. We refer to Ref. 11 for a historical exposition prior to Quantum Electrodynamics.

Indeed, α has transcended its strong association with spectroscopy and at present takes a central role in that most successful theory of Quantum Electrodynamics or QED. The fine structure constant is the coupling constant which quantifies the strength of the electromagnetic interaction. In fact, the very success of QED can be attributed to the small value of $\alpha \sim 1/137$, making it possible to express the QED contributions as a converging series in increasing powers of α, e.g. for a free electron in a magnetic field.[*] (This is not the case for the strong nuclear force where the strong coupling constant α_s is about two orders of magnitude larger that α, and hence of order $\alpha_s \sim 1$.) Additionally, α is considered to be a *running* constant and its value depends on the energy scale, so that the fine structure constant that we have been referring to, is actually the coupling constant at low energy. Incidentally, this is the mechanism that allows for the unification of the electromagnetic force and weak nuclear force to form a single electroweak force above 10^2 GeV. The unified electroweak force is expected to be further unified to the strong interaction (Grand Unification Theory or GUT) at a much higher energy scale estimated at $\sim 10^{15}$ GeV.[13]

The latest CODATA 2006 recommended value for the fine structure constant[14] is $\alpha = 1/137.035\,999\,679(94)$, which represents the average of the results from three different measurements, two based on the electron magnetic anomaly and the other based on the muon magnetic anomaly. The latest measurement of the group of Gabrielse[15] for the electron magnetic anomaly $a_e = (g-2)/2$ (where g is the electron spin g-factor) in combination of QED calculations, enables the currently most ac-

---

[*] For bound atomic systems, the QED contribution is expressed as a power series in $Z\alpha$, where Z is the charge number. Therefore, higher-order QED contributions fall off rapidly in light atoms such as hydrogen and helium. However, in high-Z ions, where $Z \sim 1/\alpha$, a perturbative expansion of the QED terms is not possible.[12]

curate determination of $\alpha = 1/137.035\,999\,084(51)$. Other independent techniques for determining α involve measurements of the recoil effects in cold ensembles of Rb[16,17] and Cs[18] atoms. These recoil techniques are an order of magnitude less accurate than the a_e-based, determination but have the advantage that it is practically independent of QED calculations.

The proton-to-electron mass ratio μ

As has been pointed out originally by Max Born,[19] the fine structure constant α and the proton-to-electron mass ratio $\mu = M_\mathrm{p}/m_\mathrm{e}$ are the only two dimensionless parameters that are needed for the description of the gross structure of atomic and molecular systems. The Bohr radius for the hydrogen atom scales as

$$a_0 \sim 1/(\alpha m_e), \tag{1.1}$$

while the size of the nucleus is determined by the effective distance of the strong nuclear interaction, e.g. given by the Compton wavelength of the nucleon (proton), $\lambda_p \sim 1/M_\mathrm{p}$. The ratio of the nuclear radius to the atomic radius is $\sim \alpha/\mu \sim 10^{-6}$. The smallness of this ratio is just a statement of the familiar structure of atoms, where the small well-defined nucleus is surrounded by a relatively large and diffuse electron cloud, with dramatic consequences for chemical processes.

One can extend this dimensional reasoning to solids, where one envisions an electron sea moving through islands of fixed ions.[20] Every ion in the lattice can then be considered as an independent harmonic oscillator with mass $\sim M_\mathrm{p}$, with a natural frequency ω. If the ion is displaced a distance x from the equilibrium position, the potential energy gained is $\sim (1/2)M_\mathrm{p}\omega^2 x^2$. The equilibrium distance between ions is $\sim a_0$, and as the displacement x of an ion approaches a_0, the bond breaks. The potential energy at this distance $x \to a_0$ is $\propto e^2/x \sim \alpha/a_0$. The mean-square momentum of the ions is

$$\left\langle p^2 \right\rangle \sim \alpha M_\mathrm{p} a_0^{-3} \left\langle x^2 \right\rangle$$

Invoking the Uncertainty Principle, we expect $\left\langle p^2 \right\rangle \sim \left\langle x^2 \right\rangle^{-1}$. If we compare this ion position uncertainty to that of the electron's $\langle x_e \rangle$ (in the order of $\sim a_0$) moving through the lattice, we get

$$\sqrt{\frac{\langle x^2 \rangle}{\langle x_e \rangle^2}} \sim \left(\frac{1}{\mu}\right)^{1/4} \ll 1$$

This expresses the fact that in relation to the electron positions, the ionic nuclei positions in the solid are well-defined. This dependence on μ highlights the importance of μ as a parameter which determines the stable configuration of solids. It seems that well-ordered and complex structures exist because of the smallness of $1/\mu$. In contrast, structures bound by the strong nuclear force do not have the same property since the nucleons have a mass ratio ~ 1, giving rise to spherically symmetric structures when viewed from the outside.

The validity of the Born-Oppenheimer approximation, that describes the gross structure of molecules, also relies on the fact that μ is large. Indeed, this approximation permits the separation of the electronic motion from nuclear motion, where the nuclei could vibrate, rotate or bend about the internuclear axes. This makes possible a convenient hierarchical classification of energies, where each electronic level has a set of vibrational energy levels, and each vibrational level has a set of rotational levels. Molecular vibrational level energies scale with $\sim \sqrt{1/\mu}$, while rotational level energies scale with $\sim 1/\mu$. These relations are actually exploited to probe a possible μ-variation, as will be discussed later.

Current theories attempt to explain the mechanism of how fundamental particles obtain mass itself. In electroweak unification, the Higgs mechanism is invoked to give rise to massive weak interaction bosons $W^{\pm}$ and Z^{0}. In the Standard Model, which includes the electroweak theory, a similar interaction with the Higgs field gives rise to the fundamental particle masses, e.g. the electron mass m_{e} or quark masses.[21,22] Since the proton is not a fundamental particle but is a composition of three quarks, the proton mass M_{p} depends on the strong interaction.[*] We emphasize this dependence on the strong interaction by noting that the total mass of the constituent quarks of the proton is just 1% of the proton mass, the rest is due to the binding energy. (In contrast, the binding energy of the electron in a Hydrogen atom is a very small fraction of the electron (rest) mass, in the order of $\alpha^2 m_{\mathrm{e}} c^2$.) In Grand Unified gauge theories, M_{p} (as well as the masses of other particles) is expressed in terms of the Quantum Chromodynamic (QCD) confinement parameter Λ_{QCD}. This means that μ contains physics from both the electroweak theory via m_{e}, and a strong interaction part via M_{p}.

The present value for μ recommended after the CODATA 2006 adjustments is $\mu = 1836.152\,672\,47(80)$.[14] This value is derived from the results of two separate experiments using Penning ion traps, where the electron and proton cyclotron frequencies were determined relative to a ^{12}C ion cyclotron frequency. The mass of the electron m_{e} was determined relative to a $^{12}\mathrm{C}^{6+}$ ion in Ref. 24, but a more recent determination, based on the the comparison of the experimental and theoretical val-

---

[*] Recently, *ab initio* lattice QCD calculations of M_{p} achieved accuracies of 1-2%.[23]

ues of the $^{12}C^{5+}$ g-factor as described in Ref. 25, yields the most accurate value of the electron mass, $m_e = 0.000\,548\,579\,909\,2(4)$ u. The mass of the proton M_p with respect to a $^{12}C^{4+}$ ion was measured in Ref. 26 to be $M_p = 1.007\,276\,466\,89(14)$ u.

In principle, a direct determination of mass ratio μ is also possible from highly-accurate measurements of molecular vibrational or rotational transitions. In this method, accurate theoretical calculations that include QED effects at the level of better than 10^{-10} would be necessary in addition. The electronic structure of the H_2 molecule is very complicated, and at present the calculation accuracy fails this requirement.[27] The calculations are simpler in principle, in the case of the one-electron hydrogen molecular ion H_2^+, and its isotopologues D_2^+ and HD^+, due the absence of electron correlation. Indeed, non-relativistic *ab initio* structure calculations for H_2^+ with a fractional accuracy of 8×10^{-30} have been achieved,[28] while that of D_2^+ and HD^+ is in the order of $\sim 10^{-14}$.[29,30] The important inclusion of relativistic effects have been tackled recently by Korobov,[31,32] who calculates ground state rovibrational transition frequencies with an accuracy in the order of $\sim 10^{-10}$. The spectroscopy of H_2^+ could therefore, in the foreseeable future, lead to an improved and direct determination of μ. Recently, high resolution spectra on rovibrational transitions of the HD^+ ion have been obtained from an ion trap[33] reaching the 2×10^{-9} relative accuracy, thus marking a first step in that direction.

1.2 Possible variation of the fundamental constants

Theoretical justifications

The possibility of a space-time variation of fundamental constants of nature inspired intense interest in physics, since an unambiguous experimental demonstration of such a variation would require adaptations in presently accepted theories. Moreover, variations in the fundamental constants would violate the equivalence principle, Einstein's starting point in the formulation of general relativity. The Einstein equivalence principle (EEP) states that: 1) the trajectory of a freely-falling test body is independent of its structure and composition (Weak Equivalence Principle WEP); 2) the outcome of any local, nongravitational test experiment is independent of the experimental apparatus' velocity relative to the gravitational field (local Lorentz invariance LLI); and 3) is independent of where and when in the gravitational field the experiment is performed (local position invariance LPI).[22,34] We can decompose the mass of a composite object, as the sum of the constituent particle masses and the binding energies of the constituent particles. Since the binding energies depend on the coupling constants, any change in the constants would then manifest itself as a change in the mass of matter, thus contradicting the equivalence principle. The Equivalence Principle has been continuously tested since Galileo's evocative free-fall experiment where he (allegedly) dropped two different masses and verified that the acceleration of both masses were identical. Since the masses of different materials do not have identical dependence on the coupling constants, the effect of the variation in the coupling constants may be seen as a difference in the acceleration of masses with different material compositions in the same gravitational field (violation of the universality of free-fall). Modern Eötvös-type experiments compare the acceleration of two masses of different compositions using a torsional balance; the most recent results give bounds in the level of 10^{-13}.[35] The Lunar Laser Ranging experiment, involving the free-fall of massive object, *i.e.* the Moon, also furnishes stringent bounds to the violation of EEP in the 10^{-13} level.[36]

Theoretical investigations have presented scenarios that predict or explain variation of the constants of nature. Besides the older Kaluza-Klein theories that relate such variations to compactified extra dimensions,[37,38] also modern superstring and M-theories predict similar variations.[39] If space has extra dimensions, then a true fundamental constant is an invariant over the whole multidimensional space, while the fundamental constant that we perceive is only the projection onto our 4-dimensional spacetime. If the compactified dimensions change, then the modulus of the true fundamental constant will also change, and in turn our perceived fundamental constant will correspondingly vary. Besides, as discussed earlier, the coupling constants are actually *running* constants depending on the momentum transfer, thus the concept of the variation of constants is not unexpected. For more extensive reviews on this rich subject we refer to Barrow[2] and Uzan.[40]

Barrow and coworkers[41,42] have developed a theoretical scenario that would allow for a variation of μ. In a *minimal theory*, where m_e varies while both α and M_p are kept constant, self-consistent extensions of general relativity are imposed to ensure energy and momentum conservation. We note that in a theoretical scenario it is very well conceivable that *dimensional* parameters vary, whereas in experiments only variation of *dimensionless* parameters can be probed. In the minimal variation models developed, constraints imposed by existing data supporting the weak equivalence principle then put a boundary on a possible variation of $|\Delta\mu|/\mu < 10^{-9}$.[41] Larger variations in μ cannot be accommodated for and would hint at variation in M_p. The work has been extended recently to postulate local space-time effects of cosmological variations induced by scalar fields (dilaton).[42] In addition, models based on dynamical scalar fields have been developed that account for dark energy and at the same time for varying couplings.[43,44]

It is interesting to note that there is a vigorous theoretical activity to connect possible variation of the two central dimensionless quantities α and μ. Within the framework of Grand Unification,[22,45–47] and also within string theories,[48] a proportionality relation is derived between possible changes of α and μ:

$$\frac{\Delta\mu}{\mu} = R\frac{\Delta\alpha}{\alpha} \tag{1.2}$$

While the signs resulting from the derivations may differ, the absolute value of the proportionality factor $|R|$ is usually large, *i.e.* varying between 20 and 40, although somewhat smaller values are reported as well.[49] Hence it is expected that if any variation of the constants occur, the variation in μ will be the largest. This makes the proton-to-electron mass ratio an important quantity for searching temporal variation of a constant *per se*. An intuitive justification of the correlation in the variation of α and μ in Eq. (1.2) can be presented as follows. The electron mass m_e and the quark masses, appearing in μ, are explained through the Higgs mechanism. The same mechanism is invoked in the electroweak theory to cause the W and Z bosons to become massive. The weak gauge bosons are naturally linked to the photon (before the symmetry-breaking of the electroweak gauge at lower energy scale), which is associated with the fine structure constant α. The proportionality constant R in Eq. (1.2) provides an experimental handle to decide which of the scenarios to explain variation of constants is realistic.

Historical perspective

Dirac[50] was among the first to cast doubt on the constancy of fundamental physical constants in connection with his Large Number Hypothesis. He considered three very large numbers: 1) the ratio of the size of the observable universe to the Bohr radius: $N_1 \sim 10^{40}$; 2) the ratio of the electromagnetic to gravitational force between an electron and a proton: $N_2 \sim 10^{40}$; and 3) the number of protons in the observable universe: $N \sim 10^{80}$. Dirac's Large Number Hypothesis states that these large numbers must have a simple relation to each other by numerical factors of the order 1, i.e. $N_1 \approx N_2 \approx \sqrt{N} \propto t$. The t-dependence is due to the increasing size of the *observable* universe with time. This leads to an inevitable conclusion that the combination of the constants of nature varies in time, i.e. $e^2/(GM_p) \propto t$, which Dirac attributed to a varying G.* Dirac's suggestion for a rather large temporal variation of the grav-

---

*The earliest speculation on the inconstancy of G was put forward by Milne,[51] in relation to considerations of cosmologies where gravitational processes progress according to a cosmic clock different to that for atomic processes.

itational constant G was elegantly refuted by Teller,[52] based on paleontological evidence. Dirac's proposal was deemed to be too *elegant* and *attractive* by Gamow, so that he proposed to rescue it by supposing that e varies instead of G,[53] however, this was soon proven to be untenable shortly afterwards.[54] We note that at present, from measurements on the cosmic microwave background and deductions on the baryon-to-photon ratio, combined with independent measurements of deuterium-hydrogen ratios from quasar absorption, a constraint on the possible variation of the gravitational constant G is set at the level of 15-20% since the Big Bang.[55] Even though Dirac's suggestion of varying constants was proven to be wrong, it then was established then that various paleontological or cosmological observations could be exploited to test for a possible variation of constants.

The lively discussions about the mysteriousness of the coincidences of Dirac's large number, led to Dicke's explanation[56] that the large number of protons in the *visible* universe is a direct consequence of the age of the universe to be that particular value when the universe would have evolved biological observers. Eventually, a generalization of this principle, the Weak Anthropic Principle (WAP), could also be invoked satisfactorily to explain other apparent coincidences in nature, such as the particular resonance in ^{12}C that was discussed earlier. As it turns out, Nature is replete with examples exhibiting extreme fine-tuning of the particular values of fundamental constants, that the number of *coincidences* triggers the strong suspicion that they cannot be entirely random. As Freeman Dyson once remarked: "*... it almost seems as if the Universe must in some sense have known that we are coming.*"[20] In its most basic sense, WAP is nothing but an expression of a systematic bias by observers whose very existence can only be possible if the values of the fundamental constants are what they are. In this trivial form, the anthropic principle is only a statement of caution, instead of scientific hypothesis in the Popplerian sense. A stronger version has been forwarded: the Strong Anthropic Principle[20] claims that the *allowed* physical laws and values of fundamental constants (and subsequent evolution) are those that *must ensure* the existence of conscious observers.[*]

A stringent constraint for the time variation of α was obtained from the study of remnants from the Oklo natural nuclear reactor in Gabon. This natural fission reactor was operating around 2 billion years ago and was made possible due to a series of remarkable geological coincidences.[2] Shlyakhter[57] first recognized that some of the nuclear byproducts, specifically Samarium $^{149}_{62}$Sm, are very sensitive to a neutron capture resonance. The resonance is due to the near cancellation of the electromagnetic force and the strong nuclear force, reminiscent of the ^{12}C synthesis resonance.

---

[*] This suspiciously reminds us of the Panglossian pronouncement that "the nose is formed for spectacles".

By comparing the reaction cross-sections at the time of the reactor activity, calculated from the observed nuclear product abundances, and the present cross-section values, constraints in α and/or α_s can be extracted. Recent extensive analysis of on the Oklo phenomenon was carried out by Fujii *et al.*[58] and by Gould *et al.*,[59] where both investigations obtain constraints for the variation in α that are consistent with the earlier analysis by Damour and Dyson.[60] The most recent constraint is $\Delta\alpha/\alpha = -0.65 \pm 1.7 \times 10^{-8}$ over the past 1.8 billion years,[59] which translates to $\dot{\alpha}/\alpha = -0.36 \pm 0.97 \times 10^{-17}$ per year, if a constant rate of change is assumed. There is actually a second possibility predicting a variation of $\Delta\alpha/\alpha = 8.2 \pm 1.1 \times 10^{-8}$, which is ruled out by Fujii *et al.* for the reason that the difference from the present-day resonance would be too large, which is not in itself a very satisfactory argument. We note that the α-constraints were obtained with the assumption that the strong interaction coupling constant does not vary. The resulting constraints of such investigations lead to the inescapable conclusion that if the constants of nature vary, the rate of change is extremely small.

Various other investigations are reviewed by Uzan,[40] which include geological studies of alpha and beta decay[61] as well as cosmological studies on the Cosmic Microwave Background[62] and Big Bang nucleosynthesis.[63,64] In general, these investigations have resulting constraints that are less stringent compared to those obtained from the Oklo studies or from spectroscopy-based approaches. The spectra of atoms, ions and molecules exhibit different dependencies on the fundamental constants α, μ, Rydberg constant R_∞ and nuclear g-factors g_I as shown in Table 1.1. From the ratios of the different types of transitions, *combinations* of the (dimensionless) parameters can be tested for variability, such as *e.g.* $g_p[\alpha^2/\mu]^\gamma$ in the microwave spectrum of the OH molecule,[65–68] with g_p the proton g-factor and γ a real number differing for each specific line; or from a combination of the 21-cm (hyperfine) line of H and UV absorptions (gross structure) of atoms and ions to constrain $g_p\alpha^2/\mu$.[69,70]

The inherent accuracy of spectroscopy then offers very good prospects for access to observations of possible variations of the constants. Indeed, comparisons of the laboratory and astrophysical spectra have been demonstrated to be a very sensitive probe, which we discuss in the next section. We emphasize at this point that in the search for possible variations of the constants, accuracies in the values of the constants do not limit the analyses. For example, note that the accuracy of recommended value[14] for α is in the order of 10^{-10}, while we have seen a much more stringent constraint that has been accessed from the Oklo observations for $\dot{\alpha}/\alpha \sim 10^{-17}$ per year.

Table 1.1 – *Dependence of atomic and molecular transitions on the constants* α, μ, g_I *(after Ref. 71).* $R_\infty c$ *expresses an energy scale in this table, and indeed maybe replaced by other combinations of constants (e.g.* $m_e c^2$*) or units (e.g. Joules).*

	Transition	Scaling
Atomic	Gross structure	$R_\infty c$
	Fine structure	$\alpha^2 R_\infty c$
	Hyperfine structure	$g_I(1/\mu)\alpha^2 R_\infty c$
Molecular	Electronic structure	$R_\infty c$
	Vibrational structure	$\mu^{-1/2} R_\infty c$
	Rotational structure	$(1/\mu) R_\infty c$

Recent interest

The revival and increased interest on the topic of possible variations of fundamental constants owes much to the recent findings by the Sydney-based group claiming a possible variation of the fine structure constant α.[72–77] These investigations are based on comparisons of laboratory spectra and absorption spectra of distant galaxies (with quasar radiation as the light source). The extreme sensitivity of this approach stems from the enormous 10^{10} years of time difference between the present-day lab spectra and the high-redshift astronomical spectra. (This time difference constitute a look-back time of almost 90% towards the time origin of the universe.) The quasar absorption spectra were collected with high resolution and accuracy ($\sim 10^{-6} - 10^{-7}$) using the HIRES spectrometer connected to the Keck telescope. The investigators employed the so-called *many-multiplet methods* (MM), where the transitions used in the comparisons are from a great number of atomic and ionic species. In addition to the improved precision over previous methods, the wide sampling of transitions and absorbing species (also the number of absorbing systems) of MM greatly suppresses the possibilities of systematic shifts that might mimic a variation in α. An important element that makes these comparisons possible are the accurate *ab initio* calculation of the sensitivity factors, which represent the induced shift of a spectral line as a function of the variation of α.[78,79] Such calculations involve an accurate quantitative assessment of the relativistic shift of atomic energy levels. Another important component in the analysis are the accurately calibrated laboratory spectra of atomic and ionic species; a compilation of the transitions used in MM can be found in Ref. 80. Our contribution to the MM-based studies is to provide highly-accurate laboratory calibrations of a number of transition wavelengths used in the analysis. In Chapters 5 and 6, we describe the calibration of the first two principal lines of Magnesium, while calibrations of transitions in Nitrogen are described in Chapter 8 and that for Oxygen transitions in Chapter 7. The wavelength calibration of spectral lines Carbon,[81] neutral Calcium[82] and ionic Calcium[83,84] have also been done in our group.

A comprehensive analysis by Murphy, Webb, and Flambaum,[76] has combined data from 143 quasar absorption systems over redshift ranges of $0.2 < z_{abs} < 4.2$. After addressing a large number of possible systematic effects, they claim a variation in α at the 5σ confidence level of $\Delta\alpha/\alpha = (-0.573 \pm 0.113) \times 10^{-5}$. Notwithstanding the detailed data reduction and error analysis, the findings of the Sydney-based group (for observations of quasars on the northern hemisphere) are disputed by other groups. The latter investigators[85–88] find essentially a null result from monitoring quasar absorption systems on the southern hemisphere using the Very Large Telescope of the European Southern Observatory. Recently, Murphy *et al.*[89] have reanalyzed the data of Chand *et al.*,[90] and argues that the null result obtained for the dataset collected by VLT/UVES by the latter investigators are due to a flawed data analysis procedure. Murphy *et al.*,[89] thus contend that the results of their reanalysis is not inconsistent with the previous Keck/HIRES results. A concise summary of all MM-based constraints of α is given in Figure 1 of Ref. 89.

Predating the many-multiplet method is the Alkali-Doublet (AD) method using spectral lines with fine structure splitting, which is proportional to α^2 (see Table 1.1). Actually, the MM method described earlier is a generalization of the doublet method. The AD method was originally developed by Savedoff[91] for probing variations of α from *emissions* in the galaxy. A similar method was used by Bahcall *et al.*[92] for detecting α-variation from Si II and Si IV quasar *absorption* features, which was recently applied by the Australian group in an investigation of Si IV absorption lines in new astrophysical observations.[93] A null result was obtained from the latter investigation, with a constraint for the variation of the fine structure constant of $\Delta\alpha/\alpha = (-0.5 \pm 1.3) \times 10^{-5}$. Chand *et al.*[90] reported a constraint of $\Delta\alpha/\alpha = (+0.15 \pm 0.43) \times 10^{-5}$ based on AD analysis of VLT/UVES data, over the range of $1.5 < z_{abs} < 3.0$. However, Murphy *et al.*[89] argue that it suffers from the same flaws as the MM-analysis of Ref. 87. These results are, in general, not in disagreement with the claims on α-variation derived from the many-multiplet method, since the AD-method is intrinsically less accurate than the MM-method by an order of magnitude.

Lab–Astrophysical comparisons for constraining μ-variation

Thompson[94] pointed out already in 1975, that absorption by molecules in interstellar clouds at high redshift in the line of sight of quasar sources could reveal possible variations in the proton-to-electron mass ratio μ over cosmological time; he identified the strong mass-dependence of quantized rotational and vibrational motion in the molecule, in particular the H_2 molecule, as a tool to search for variation of μ. Over the years this concept was pursued by a number of researchers. Alternative schemes to search for μ variation were proposed as well. Pagel[95] noted that the simultaneous detection of electronic isotope shifts in various atoms could also provide a bound on the variation of μ; this method is however less sensitive. Wiklind and Combes[96] invoked a method to constrain possible μ variation by comparing apparent redshifts from microwave transitions in different molecules (CO, HCN, HCO^+, H_2CO, N_2H^+) that were observed at redshifts in the range of $z = 0.2 - 0.9$. By invoking certain assumptions, Tzanavaris *et al.*[69] derived a constraint for the variation of μ from the constraint for $\alpha^2 g_p/\mu$, where g_p is the proton gyromagnetic ratio. Flambaum and Kozlov[97] proposed the analysis of the inversion spectra of NH_3 in quasar absorption spectra, since this tunneling transition is very sensitive to the change in μ. A recent analysis of an NH_3 absorber, with $z \sim 0.7$, by Murphy *et al.*[98] based on this proposal yield a tight constraint on μ-variation of $|\Delta\mu/\mu| < 1.8 \times 10^{-6}$ (over 6 billion years).

The μ-variation comparisons, e.g. based on the H_2 absorption features, run in a completely analogous fashion as that of the α-variation study, and relies on three main ingredients, namely: 1) high-quality quasar absorption spectra; 2) the (improved) calculation of the sensitivity parameters; and 3) the highly accurate H_2 laboratory database. We discuss this particular study in more detail, since it is of most relevance to the work presented in this thesis. Furthermore, we present this as a representative procedure, which should demonstrate the general features of the astrophysical comparisons.

Astronomical observations

Absorption spectra from the high-redshift galaxies are collected by the largest optical telescopes on Earth, e.g. the Keck telescope or the Very Large Telescope (VLT). The radiation source for the absorbing systems emanate from quasars (or quasi-stellar objects), with an emission spectrum depicted in Fig. 1.2 along with an absorption spectrum. Quasars are identified from the their characteristic spectrum which typically exhibit enormous redshifts $z = \lambda/\lambda_0 - 1$, where λ is wavelength of light collected by the telescope and λ_0 is the restframe wavelength as calibrated in the lab.

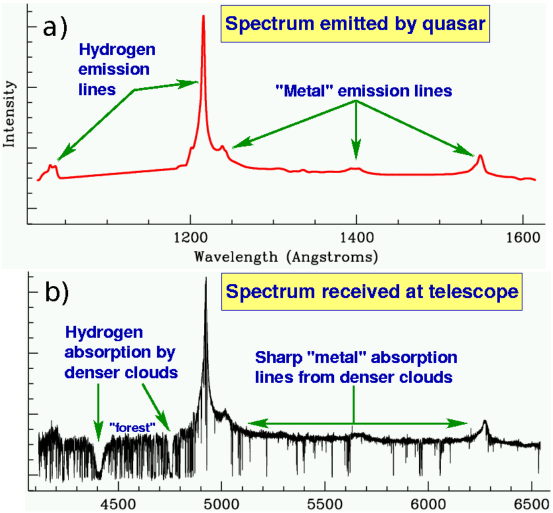

Figure 1.2 – *The quasar emission a) and absorption b) spectra collected by the telescopes.*

Fig. 1.2a shows the emission spectrum, the most intense line is the principal transition of the Hydrogen atom, called the Lyman-α transition with a rest wavelength of 1216 Å. The dense region of absorption lines to the left of the Ly-α emission in Fig. 1.2b, labeled as the *forest*, is due to the overlap of the different absorber systems with different redshifts. The broad absorption feature, referred to as damped Lyman systems, are caused by a high-density of H absorbers at a specific z. Thus molecular H_2 transitions are observed in this dense part of the region on account of the high density of atomic H, which is a prerequisite for molecular H_2 formation. Indeed, the difficulty in separating the H_2 transitions from the stronger H-lines is the main reason why only a tiny fraction of the whole set of observed quasar absorption systems can be used in H_2-based comparisons for μ-variation. Notice that the spectrum collected by the telescope in Fig. 1.2b, shows the Ly-α emission peak at around 4900 Å, corresponding to red-shift of around $z = 3$. The original UV transition wavelength has been stretched due to the expansion of the universe, and it is observed in the visible region when it reaches the earth. Such enormous cosmological redshifts imply that the astronomical object has a huge velocity component in the direction away from us. Taking into account Hubble's law, stating that the distance d of the astronomical object is proportional to its *recessional* velocity v ($d = vH_0$, with the Hubble constant H_0), we see that the object is very distant from earth and hence we are observing light from very deep into the past. The most distant quasar observed thus far were reported by Willot *et al.*,[99] with a redshift of $z = 6.43$ (corresponding to lookback time of 95% of the present age of the universe). Interestingly, since the intensity of an isotropic radiation source decreases as the inverse square of the distance from the source, it has been recognized that the great distance from the quasars imply that they are very intense radiation sources. For example, the quasar Q 0347-383, with $z = 3.23$, has an estimated luminosity of about $\sim 10^{13}$ times that of our sun.

Because of their enormous distance from Earth, quasars are very faint astronomical objects. Again taking Q 0347-383 as an example, its apparent magnitude is $V = 17.3$, which is about a million times fainter than Polaris. In addition to the relative faintness of the astronomical objects, the subsequent dispersion of the spectral components means that only a very tiny fraction of the incident radiation is detected on each pixel of the recording device. For such reasons, quasar radiation is collected using the biggest telescopes, such as the 10-m diameter Keck Telescope in Hawaii and the 8.2-m diameter VLT in Chile. The VLT and Keck Telescopes are equipped with high-resolution spectrometers, the Ultraviolet and Visible Echelle Spectrograph (UVES) and the High Resolution Echelle Spectrometer (HIRES), respectively. For the high-redshift absorption systems in the line of sight of the quasars Q 0347-383 and Q 0405-443 used in the $\Delta\mu$-analysis of Refs. 100 and 101, the VLT/UVES resolving power was at that time $R \sim 53{,}000$ with SNR$\sim 30 - 70$.[102] Absolute wavelength calibration is based on a Thorium-Argon lamp reference, with an accuracy ~ 2 mÅ.[102]* The achieved transition wavelength accuracies are in the order of $10^{-6} - 10^{-7}$ in the 329–451 nm range. The accuracies of the astrophysical observations actually limit the present comparisons between laboratory and astrophysical data. A recent preliminary application of frequency comb technologies in the calibration of astronomical spectra has been shown to improve the accuracy.[104]

Sensitivity coefficients

The set of sensitivity coefficients $\{K_i\}$ relate the shift in the transition frequency as a consequence of the change in the fundamental constant, in this case μ. For the Lyman and Werner transitions of H_2, that are used in the $\Delta\mu$ analysis, the calculations have been carried out in a semi-empirical fashion,[101] or by *ab initio* methods.[105] In the absence of any mass-dependent effects, the highly redshifted line positions λ_i

---

*An improved procedure for calibration of echelle spectra based on ThAr lines, to address possible systematic errors, has been proposed.[103]

relate to the wavelengths at zero-redshift λ_i^0 via:

$$\frac{\lambda_i}{\lambda_i^0} = (1 + z_\mathrm{Q}) \tag{1.3}$$

where z_Q is the redshift of the absorbing cloud in the line of sight of quasar Q. A possible mass dependence of a certain line can be added to this equation by the introduction of K_i for the i^{th} line to obtain the corresponding wavelength λ_i':

$$\frac{\lambda_i'}{\lambda_i^0} = (1 + z_\mathrm{Q})(1 + \frac{\Delta\mu}{\mu} K_i), \tag{1.4}$$

For the quantity $\Delta\mu = \mu_\mathrm{z} - \mu_0$, μ_0 is the proton-to-electron mass ratio in the present epoch, i.e. at zero redshift, while μ_z is the mass ratio in the absorbing cloud at high redshift. Taking the difference of Eqs. 1.3 and 1.4, to obtain the mass-dependent *reduced redshift* contribution, [*]

$$\frac{\Delta\lambda_i}{\lambda_i^0} = \frac{\lambda_i' - \lambda_i}{\lambda_i^0} = \frac{\Delta\mu}{\mu} K_i, \tag{1.5}$$

In Eq. 1.5, the K_i coefficients represent a sensitivity factor of the (mass-dependent) shift in the transition wavelength as a function of μ-variation. The amount of shift is determined by the magnitude of K_i and the direction of the shift by the sign of K_i. In Fig. 1.3, H_2 Lyman (L) and Werner (W) transition wavelengths, exhibiting different mass-dependent shifts, are shown for different values of $\Delta\mu/\mu$. We have greatly exaggerated the values of the μ-variation ($\Delta\mu/\mu = 0.25, 0.50, 0.75$) to demonstrate the differences in the magnitude and directions of the shifts.

The sensitivity coefficients K_i are implicitly defined for each spectral line in terms of the derivatives of energy or wavelength with respect to μ, and can be expressed in various forms:[106–108]

$$\begin{aligned} K_i &= \frac{\mu}{\lambda_i}\frac{d\lambda_i}{d\mu} = \frac{d\ln\lambda_i}{d\ln\mu} = -\frac{\mu}{\nu_i}\frac{d\nu_i}{d\mu} \\ &= -\frac{\mu}{E_\mathrm{e} - E_\mathrm{g}}\left(\frac{dE_\mathrm{e}}{d\mu} - \frac{dE_\mathrm{g}}{d\mu}\right) \end{aligned}$$

In the Born-Oppenheimer picture, we can express the energy of the molecule E into separate contributions of the electronic and nuclear motion as,

$$E = E_\mathrm{elec} + E_\mathrm{vib} + E_\mathrm{rot},$$

---

[*] The *reduced redshift* is denoted by ζ_i in Refs. 100 and 101.

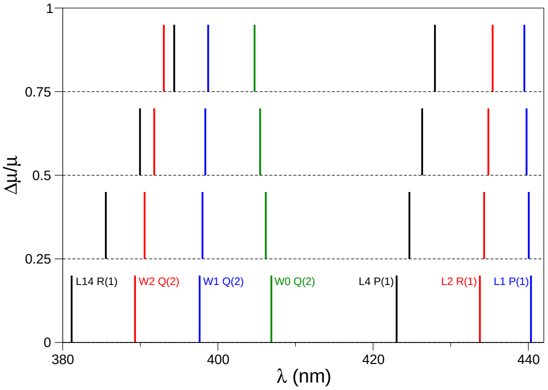

Figure 1.3 – *Some H_2 Lyman (L) and Werner (W) transition wavelengths for different values of $\Delta\mu/\mu$. The values of $\Delta\mu/\mu$ are greatly exaggerated to demonstrate the differences in the magnitude and direction of the shifts. The absorber redshift is taken to be $z_Q = 3$.*

where E_{elec} represents the electronic energy, while E_{vib} and E_{rot} represent nuclear vibrational and rotational energies, respectively. From Table 1.1, we see that E_{elec} has no μ-dependence while the nuclear motion contributions have μ-dependent scaling. The vibrational term scales as $E_{\mathrm{vib}} \propto \mu^{-1/2}$, analogous to a harmonic oscillator, and the rotational term as $E_{\mathrm{rot}} \propto \mu^{-1}$, analogous to a simple rotor. The same scaling or combinations thereof, then applies to transition energies. The change in the vibrational transition energy due to a change in μ is $\Delta E_{\mathrm{vib}}/E_{\mathrm{vib}} = -0.5\Delta\mu/\mu$, so that the sensitivity coefficient is -0.5. In a similar manner, the change in rotational energy due to a change in μ is $\Delta E_{\mathrm{rot}}/E_{\mathrm{rot}} = -\Delta\mu/\mu$, which yields a sensitivity coefficient of -1.0. For the rovibronic (combination of rotational, vibrational and electronic) transitions of H_2 used in the μ-variation analysis, the largest energy contribution comes from the electronic part which is μ-independent. Therefore, the relative change in transition energies due to a μ-variation is smaller ($< |0.1|$) compared to those in pure vibrational or rotational transitions. It is interesting to note that in the case of the tunneling transition in ammonia NH_3, the exponential dependence of tunneling process to mass results in a sensitivity coefficient of -4.2.[109]

In Ref. 100 and 101, the derivation of K-coefficients is semi-empirical and analogous to previous attempts,[106–108] but with improved accuracy. Improvements in this analysis over previous ones constitute three main points: the use of an improved set of data from the XUV-laser experiments; the inclusion of adiabatic shifts; and the accounting for non-adiabatic couplings in the model representation. The latter two effects go beyond the Born-Oppenheimer approximation, and the contributions to K_i can be as much as 1% for the adiabatic and 10% for the non-adiabatic effects. The accuracy of the semi-empirically determined K-coefficients are estimated to be 1% in the full range of K-values (between -0.01 and and 0.05). The semi-empirical calculation results are also consistent (within 1%) to results from an *ab initio* analysis.[105]

So far, we have discussed the two main ingredients in $\Delta\mu$-analysis based on quasar absorption lines of H_2, namely, the astrophysical observations and the sensitivity coefficients. The final ingredient in the $\Delta\mu$-analysis is an accurate database of laboratory transition wavelengths (λ^0), representing zero redshifts. The most accurate determination of the H_2 laboratory transition wavelengths is our contribution to $\Delta\mu$-studies. In Chapter 3 of this thesis, we describe the improved determination of the Lyman and Werner transition wavelengths, which can be considered exact in the context of comparisons with quasar absorption data.

Using these ingredients, the finding of an indication of a 0.002% *decrease* in μ in the last 12 billion years was reported in Refs. 100 and 101. The analysis was based on a comparison of prominent transitions in the Lyman and Werner bands of H_2 from two absorbers in the line of sight of two the quasars, with 39 transitions for the Q 0405-443 absorber and 37 transitions for the Q 0347-383 absorber. However, King *et al.*[110] recently raised a counterclaim of a null variation in μ after an inclusion of an additional absorber system, to those included in the analyis of Refs. 100 and 101. It is clear from the present debate in these comparisons that the acquisition of more data, from more absorber systems, with improved accuracies, will hopefully clarify the situation in the future.

If we extend these ideas to the logical limit, we are led in principle towards comparisons of the oldest observable radiation, that is, the Cosmic Microwave Background (CMB). Despite the enormous redshift $z \sim 1000$ of the CMB, the corresponding look-back time of 13.7 billion years is not a large difference in comparison to the 12 billion years of the quasar absorption systems. However, since the CMB represents the leftover radiation at the time when the universe was just cold enough to form atoms, it is actually very different from the comparisons of atomic or molecular absorptions that we have discussed. Nevertheless, CMB is indeed sensitive to the variation of α in two ways: 1) the strength of electromagnetic interaction affects the Thomson scattering cross-section (photon-electron scattering); and 2) the ionization fraction, which is related to the two-photon emission H 1S–2S and red-shift of H Ly-α lines.[40] The difficulty in this method is that a number of other parameters of the model can not be independently determined. In the end, these limitations render the CMB based constraints to be inferior compared to the quasar absorption comparisons.

Pure laboratory tests for variation

The main disadvantage of the tests for the variation of constants based on lab-astronomical spectra comparisons is the limited experimental handle on the astrophysical observations. In fact, the use of as many spectral lines simultaneously, is done to address possible systematic shifts, i.e. transitions used have different sensitivity coefficients. Pure laboratory tests, on the other hand, offer the possibility of experimental control, and hence reliability and reproducibility. A major drawback of the laboratory tests is the relatively short time difference, in period of years compared to $\sim 10^{10}$ years for the cosmological comparisons. Pure laboratory tests have recently become viable due to the impressive advance in time and frequency metrology that are now sensitive to variations in the order 10^{-17} per year. The recent metrology revolution is due to advances in atomic and single-ion optical clocks technology with *stabilities* in the order of $10^{-15}/\sqrt{\tau}$, with the measurement (averaging) time τ given in seconds. The *accuracies* of the best clocks are now better than $10^{-16}-10^{-17}$,[111,112] and now surpass atomic Cesium clock standards with accuracies $10^{-15}-10^{-16}$,[113] where the current definition of the *second* is based upon. Indeed, to measure clock accuracies surpassing that of the Cs standard, direct comparisons of the frequencies of two accurate clocks, each more accurate than a Cs clock, were performed.[111,112]

The recent time and frequency metrology revolution owes much to the invention and development of frequency combs.[114,115] Frequency comb technology has enabled the relatively convenient* link of optical frequencies to radio frequency where direct electronic frequency counting is possible (up to hundreds of GHz). For a review on frequency combs we refer to Ref. 117.

The state-of-the-art clocks probe (dipole-forbidden) optical transitions in either cold atomic ensembles or cold and trapped single ions. The most accurate frequency ratio was recently obtained by Rosenband *et al.*,[112] from the comparison of Hg^+ and Al^+ single-ion optical clocks, with a fractional uncertainty in the order of a few times 10^{-17}. Clock comparisons based on the Sr and Ca atomic clocks have also performed, with an obtained frequency ratio uncertainty of 1×10^{-16}.[111] These clock transitions depend on the constants, such as α or nuclear magnetic moment, as indicated in Table 1.1. Any variation of the transition frequencies over time may then be attributed to the variation of the constants. The most stringent constraint

---

*In comparison to frequency chains for example.[116]

for α is given by Rosenband *et al.*,[112] $\dot{\alpha}/\alpha = (-5.3 \pm 7.9) \times 10^{-17}$ per year. This value is the joint limit set by clock comparisons: Yb^+/Cs, Hg^+/Cs, and Al^+/Hg^+.

From the extreme precision obtained by Rosenband *et al.*,[112] Barrow and Shaw[118] investigated the seasonal variation of the previous measurements to extract bounds for the variation in α that could be attributed to the seasonal variation of the Sun's gravitational field. If the Equivalence Principle holds, a correlation of α-variation with the changing gravitational potential, due to Earth's elliptical orbit, should not be observed and so far there is the case. The constraints obtained from these single-ion clocks are (at present) less stringent but are consistent with Eötvös-type and Lunar ranging experiments.

In the case of pure lab test for the variation in μ, the comparison of the molecular rovibrational transition in SF_6 to the Cs standard yields a tight constraint for μ-variation of $\dot{\mu}/\mu = (-3.8 \pm 5.6) \times 10^{-14}$ per year.[119] It has also been proposed to extend the Sr atomic clock set-up, to perform photoassociation of cold Sr atoms to form cold Sr_2 molecules. Subsequent measurements of vibrational transitions in Sr_2 is projected to be able to constrain $\Delta\mu/\mu$ at the level of 10^{-15} per year.[120] Another proposal is to perform measurements of the tunneling frequency in ammonia NH_3 in a molecular fountain to probe for μ-variation, which is expected to be sensitive to changes at the level of 10^{-15} per year.[109]

A different approach is to find special atomic or molecular resonances that are nearly degenerate, which exhibit extreme sensitivity to the variation of constants. The accuracy requirement for these specific transitions are then relaxed because of *amplification effect* of the sensitivity coefficients K_i. In this manner, the temporal variation of α is constrained to $\dot{\alpha}/\alpha = (-2.7 \pm 2.6) \times 10^{-15}$ per year, from the measurements in atomic dysprosium (Dy).[121] Recently, the microwave spectroscopy of nearly degenerate molecular states in CO, has been proposed[122] to probe for μ-variation.

On the consistency of the results

The α-constraints derived from different techniques representing different epochs, *i.e.* from cosmological, geophysical, and present atomic clock investigations, do not give identical constraints for the α-variation. This might seem contradictory at first sight, however, it is not really necessary that the variation be linear in time, or that it be the same at every point in space. Sandvik, Barrow and Magueijo*et al.*[123] have extended the Bekenstein model of varying e,[124] with the result showing that α has changed throughout the cosmological evolution of the universe. The value of α

hardly varies through the early radiation-dominated phase, and then increases as the matter-dominated phase progresses, and finally stays constant again in the present vacuum energy-dominated epoch.[123]* Another model presented by Fujii[125,126] exhibits α-oscillations over the universe's cosmological history. The α-variation is due to changes in a (hypothetical) dilaton field, which is also invoked in this theory (and similar ones) to explain the present acceleration of the universe. At the moment, the α-constraints derived from all investigations do not discriminate between the different theories that have been put forward. In this context, all these investigations are complementary, and future refinements for both the laboratory-astronomical spectra comparison, pure laboratory tests, and possibly new experiments, are all equally important and necessary to probe for variations over spacetime.

1.3 Thesis outline

This thesis can be roughly subdivided into two parts: i) on the spectroscopy of atoms; and ii) on the spectroscopy on molecules. This subdivision also naturally separates the spectroscopic investigations in relation to either α- or μ-variation. The part on atomic spectroscopy contributes to the laboratory database of transitions that is used in the study of a possible variation of the fine structure constant α. The molecular spectroscopy on H_2 presented in this thesis, furnishes an improved database of Lyman and Werner transitions which are utilized in the study of detecting a possible variation of the proton-to-electron mass ratio μ. In addition, the high-precision measurements enable us to determine the ionization potential of H_2, an important quantity that provides a test on the validity of fundamental molecular theory. Our accurate measurements also enable the extraction of Born-Oppenheimer corrections in I_2, as well as permitting a detailed study of a local perturbation in N_2. We summarize the chapters in this thesis in the following.

Chapter 2 describes the measurement on the two-photon EF–X transitions of H_2. This chapter serves a detailed description of the experimental setup used for the different precision spectroscopic studies. Exploiting Doppler-free techniques and frequency comb calibration methods, we obtain relative accuracies which are better than 2×10^{-9}.

In Chapter 3, we present an improved calibration of the H_2 Lyman and Werner bands used in the μ-variation studies. The results were obtained from a combination of Deep UV spectroscopy of the H_2 EF–X system performed in Amsterdam, and separate Fourier Transform spectroscopy of the EF–B and I–C systems performed

---

[*] At present, the expansion of the universe is accelerating, which is attributed to the negative pressure of the vacuum energy.

in Orsay. The resulting database constitutes a better than an order of magnitude improvement over previous XUV spectroscopy with direct excitation of the Lyman B–X and Werner C–X systems. With the achieved accuracy of $\sim 5 \times 10^{-9}$, the laboratory data contibutes $< 2\%$ to the total uncertainty in the value for the constraint of the variation in the proton-to-electron mass ratio $\Delta\mu/\mu$.

We discuss the improved determination of the Ionization Potential (E_i) of H_2 in Chapter 4. This is obtained from the combination of the results from three separate high-precision spectroscopic investigations: i.e. 1) EF–X Deep UV 2-photon spectroscopy at around 202; 2) EF–55p (Rydberg state) spectroscopy at around 398 nm; and 3) high-np to I.P. spectroscopy by millimeter wave investigation. In this chapter our experimental determination of the second step, i.e. the H_2 EF–55p spectroscopy performed at ETH-Zurich is described. This enables the derivation of $E_\mathrm{i}(H_2)$ as well as the dissociation energy $D_0(H_2)$, with precisions that represent an improvement of better than an order of magnitude over previous experimental and theoretical results.

The second part of this thesis concerning spectroscopy on atomic species, starts with the frequency metrology on the first and second principal transitions in Magnesium. Chapter 6 contains a description of the determination of the Mg $3s^2\,{}^1S$ – $3s3p\,{}^1P$ transition at 285 nm; while Chapter 5 deals with the $3s^2\,{}^1S$ – $3s4p\,{}^1P$ transition at 202 nm. In addition to the highly accurate line positions, the isotope shifts have been determined, which is important in addressing issues on assumptions of extra-terrestrial isotopic abundance which might mimic an effect similar to that of α-variation. In Chapters 7 and 8, the frequency calibrations of transitions in atomic Oxygen and Nitrogen are presented, respectively, using the Amsterdam XUV source. These atomic lines are used in α-variation studies along with a great number of other atomic and ionic transitions.

On a slightly different theme in Chapter 9, the results of precision spectroscopy on the a$''$–X two-photon transitions of N_2 are presented, which enabled us to investigate in some detail a local perturbation in the energy level structure. In Chapter 10, we present our work on I_2 spectroscopy of the ${}^{129}I_2$ and ${}^{127}I{}^{129}I$, performed in collaboration with Universität Hannover, which provides additional transitions which can be exploited as a molecular frequency standard. We have used these results to extract Born-Oppenheimer corrections of the I_2 theoretical model as discussed in Chapter 11, resulting in the improved prediction accuracy in the extrapolation of the model.

Chapter 2

Frequency metrology on the EF $^1\Sigma_g^+ \leftarrow$ X $^1\Sigma_g^+$ (0,0) transition in H_2, HD, and D_2

We present a frequency metrology study on the lowest rotational levels of the hydrogen EF $^1\Sigma_g^+ \leftarrow X\,^1\Sigma_g^+$ *(0,0) two-photon transition near 202 nm. For this purpose the fourth harmonic of an injection-seeded titanium:sapphire pulsed oscillator is employed in a Doppler-free REMPI-detection scheme on a molecular beam of hydrogen. A frequency comb laser is used to perform the absolute frequency calibration on the CW laser that injection-seeds the oscillator. Chirp-induced frequency differences between the output of the pulsed oscillator and the seeding light are monitored on-line, while possible systematic shifts related to the AC-Stark and Doppler effects are addressed in detail. The transition frequencies of the Q(0) to Q(2) lines in* H_2 *and* D_2*, and the Q(0) and Q(1) lines in HD are determined with an absolute accuracy at the* 10^{-9} *level.*

This chapter is published as Physical Review A **74**, 062514 (2006).

2.1 Introduction

Accurate determination of the dissociation and ionization energies of the hydrogen molecule and its isotopomers is an important test ground for quantum *ab initio* calculations on molecular systems.[127,128] The pioneers in this field, Kołos[129] and Wolniewicz[27] calculated values for the ionization potential of H_2 ranging from 124 417.491 cm^{-1} to 124 417.496 cm^{-1}, including adiabatic, non-adiabatic, relativistic and radiative corrections to the Born-Oppenheimer results, believed to be accurate to within 0.01 cm^{-1}. The best theoretical value for the adiabatic dissociation limit is calculated to be 36 118.060 cm^{-1}.[27]

At the experimental side, different approaches have been adopted to retrieve increasingly accurate values for these two key quantities. Stoicheff and coworkers[130] directly excited the region near the $n = 2$ dissociation threshold resulting in a value for the ground state dissociation threshold $D_0(\mathrm{H}_2)$ with an accuracy of $0.08\,\mathrm{cm}^{-1}$. Eyler and coworkers showed that the region near the $n = 2$ threshold is prone to spin-orbit and hyperfine effects as well as perturbations between several electronic states, yielding an irregular structure of many resonances near threshold[131] and later obtained a value for $D_0(\mathrm{H}_2)$ in a two-step excitation process.[132]

The ionization potential in hydrogen can be determined from direct one-photon excitation of the *n*p Rydberg series and extrapolation to the series limit using multichannel quantum defect theory (MQDT). This approach was taken by Greetham *et al.*[133] to deduce a value for the ionization potential of HD. Alternatively the ionization potential may be derived from a number of consecutive excitation steps bridging the gap between the $\mathrm{X}\,^1\Sigma_g^+$, $v = 0, J = 0$ ground state and the ionization limit. One such route was explored by De Lange *et al.*[134] who calibrated a high-lying vibrational level ($v = 19$) in the $\mathrm{EF}\,^1\Sigma_g^+$ state and then connected to the ionization limit through the Fourier-transform infrared work on inter-Rydberg transitions by Jungen *et al.*[135] This scheme is fundamentally limited by the fact that a transition needs to be calibrated in the $\mathrm{B}\,^1\Sigma_u^+ \rightarrow \mathrm{X}\,^1\Sigma_g^+$ system, probing an upper state with a lifetime as short as 0.3 ns.

A promising multi-step scheme involves calibration of the lowest $\mathrm{EF}\,^1\Sigma_g^+$, $v = 0$ level (with a lifetime of 200 ns[136] and therewith allowing for precision spectroscopy), which can be reached in a two-photon transition allowing for Doppler-free excitation. This scheme was explored already some time ago by Glab and Hessler[137] and by Eyler and coworkers.[138–141] The concept of the multi-step scheme is to determine the ionization potential from accurate calibration of the $\mathrm{EF}\,^1\Sigma_g^+, v = 0, J = 0$ level, subsequently excite the long-lived *n*p Rydberg series and then extrapolate this series to the limit with the aid of improved Fourier-transform infrared transitions between high-*n* levels[142] and by millimeter wave transitions between very high-*n* levels.[143] A recent reinvestigation of the $\mathrm{EF}\,^1\Sigma_g^+ \leftarrow \mathrm{X}\,^1\Sigma_g^+(0,0)$ two-photon transition by Eyler and coworkers constitutes an important improvement to this approach. Transition frequencies at an absolute accuracy of $0.008\,\mathrm{cm}^{-1}$ were obtained,[144] that differed from earlier investigations by as much as three standard deviations. Such discrepancy warrants an independent validation by alternative methods, and that is the purpose of the present study.

In the present experimental investigation a pulsed laser source, tunable near 202 nm, is used for exciting the Q(0) to Q(2) lines of the $\mathrm{EF}\,^1\Sigma_g^+ \leftarrow \mathrm{X}\,^1\Sigma_g^+(0,0)$-band in H_2 and D_2, as well as the Q(0) and Q(1) lines in HD, in a two-photon Doppler-free resonance-enhanced multi-photon ionization (REMPI) scheme. Using a novel-design pulsed titanium:sapphire (Ti:sapphire) oscillator in the near infrared range, three stages of non-linear conversion are required to attain deep-UV wavelengths.[145] The frequency metrology is performed on the output of the continuous-wave (CW) laser, that seeds the oscillator cavity of the pulsed laser system, by referencing against a home-built frequency comb laser.[146,147] As is known from pulsed-dye laser systems, the amplification process can induce frequency excursions during the temporal evolution of the pulse (known as frequency chirp), which may cause a net shift between the center frequency of the pulse and the carrier-frequency seeding the pulsed amplifier.[148–150] For the absolute calibration of the Q(0), Q(1), and Q(2) transitions in the hydrogen $\mathrm{EF}\,^1\Sigma_g^+ \leftarrow \mathrm{X}\,^1\Sigma_g^+(0,0)$-band we have performed extensive measurements on these chirp effects and corrected for them. Although the underlying physics of the chirp process is somewhat different (frequency mode-pulling in a resonator vs. transient gain in a traveling-wave dye-amplifier) the phenomenology of the effect is similar. We followed strategies recently explored by White *et al.*[151,152] for determining chirp phenomena in an injection-seeded and pulsed optical parametric oscillator.

2.2 Experimental setup and procedures

The EF ← X two-photon resonances are detected using Doppler-free 2 + 1-REMPI. An excitation scheme including potential energy curves is given in Fig 2.1. The essential ingredients of the experimental components and the measurement procedures are described in detail in the following sections: 2.2 The geometrical layout of a molecular gas jet perpendicularly crossing a set of counter-propagating laser beams with 2 + 1-REMPI detection. A special interferometric alignment scheme was followed (based on the Sagnac geometry) to ensure exact overlap of the counter-propagating beams; 2.2 A novel-design tunable deep-UV laser system operating at 202 nm, involving fourth harmonic generation of the amplified output of an injection-seeded pulsed Ti:sapphire oscillator; 2.2 The absolute frequency calibration of the near-IR seeding light using a fs-laser frequency comb; 2.2 The assessment of the frequency chirp effect; 2.2 The assessment of possible shifts due to DC and AC-Stark effects; 2.2 Discussion of possible effects of phase distortions introduced by the Kerr effect in the nonlinear upconversion stages; 2.2 The integration of the three laser systems (the seed-laser, the pulsed oscillator, and the frequency comb laser) and the on-line chirp detection into a computer-controlled measurement system and the measurement procedures.

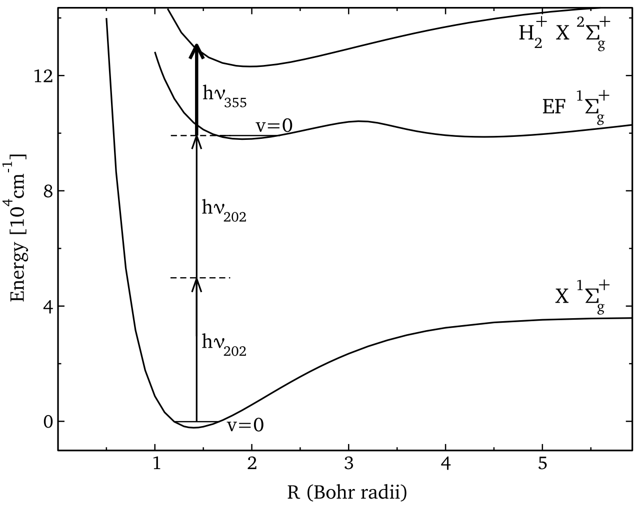

Figure 2.1 – *Potential diagram of molecular hydrogen and the applied 2 + 1-REMPI excitation scheme. The zero energy is identified with the ground state.*

Doppler-free 2 + 1-REMPI in a gas jet

A schematic overview of the molecular beam apparatus, including the excitation and time-of-flight (TOF) mass separation and detection zones is shown in Fig. 2.2. Molecular hydrogen is injected into the vacuum using a pulsed valve at a stagnation pressure of 3 bar. The TOF-chamber and the interaction chamber are both differentially pumped to a pressure of 10^{-7} mbar, which rises to about 10^{-6} mbar when the molecular beam is present. Under these conditions, essentially collision-free transition frequencies can be determined.

Although the technique of two-photon spectroscopy employing counter-propagating laser beams is known to be Doppler-free, a slight misalignment from an exact anti-parallel geometry can lead to Doppler shifts. In case of an angular mismatch $\delta \ll 1$, the effective Doppler-shift is:

$$\Delta\nu = \delta \frac{v}{\lambda} \tag{2.1}$$

at the two-photon level, where v is the velocity of the hydrogen molecules and λ the wavelength of the UV light used for two-photon excitation.

In order to minimize calibration uncertainties due to possible Doppler shifts, a collimated laser beam with about 1 mm diameter at the interaction zone was used.

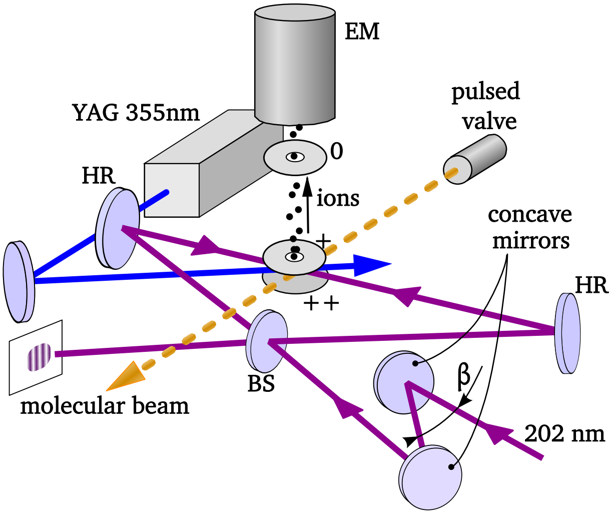

Figure 2.2 – *Experimental apparatus used for Doppler-free 2 + 1-REMPI detection on a molecular beam. The pulsed valve injects the gas directly to the interaction chamber in a free jet expansion. The laser beam is collimated using a telescope consisting of concave mirrors. A pair of counterpropagating beams is aligned in a Sagnac interferometer using a beamsplitter (BS) and highly reflective mirrors (HR). An auxiliary Nd:YAG laser operating at 355 nm serves to ionize the* H_2 *molecules excited to the EF state by the first laser.*

Since the UV light output of the laser system is astigmatic, a concave mirror telescope (see Fig. 2.2) is aligned under a certain angle β, making use of the aberration effects on spherical mirrors and thus compensating for the astigmatism. In a first alignment scheme the collimated light was sent to the interaction zone over a distance of 1.5 m, while a plain retro-reflecting mirror placed inside the vacuum on a pivoting mirror mount was aligned such that the counter-propagating beams are overlapped. During the alignment procedure a pinhole of 0.5 mm diameter was placed in the center of the forward directed beam. An overlap accuracy between the counter-propagating beams of about 0.3 mrad is achieved corresponding to a Doppler-shift of about 2.5 MHz at the two-photon energy level. A different, interferometric method has been employed during a later stage of the experiments based on the Sagnac geometry achieving a reproducible angular overlap of better than 0.1 mrad — or 0.8 MHz calibration uncertainty.[153] The stated uncertainty margins for the angular mismatch of the counterpropagating beams contain also an es-

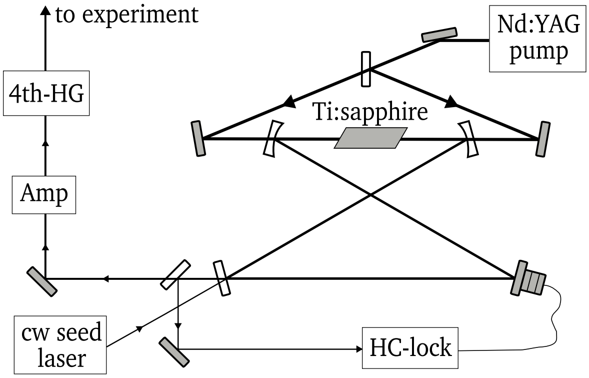

Figure 2.3 – *Schematic layout of the laser system used. The laser resonator contains a Ti:sapphire crystal as single active optical element. The cavity length is locked using Hänsch-Couillaud (HC) scheme.*[154] *The amplifier system (Amp) is a multi pass Ti:sapphire amplifier in a bow-tie geometry. The* 4^{th} *harmonic of the near-IR radiation is produced in three consecutive nonlinear crystals. For further details see text and Sneep et al.*[145]

timated contribution for the fact that the laser beam does not exhibit a perfectly Gaussian beam profile and features possible wavefront distortions.

The REMPI signals were induced either in a single-color (202 nm) excitation, or in a two-color-scheme. In the latter case a strong UV-laser pulse (at 355 nm, the third harmonic of an auxiliary pulsed Nd:YAG laser) serves to ionize the resonantly excited population in the EF-state. In particular for low-energy pulses ($< 10\,\mu$J) of the resonant laser, the ion signal significantly increases in the two-color scheme. The UV-ionization pulse was delayed by ≈ 50 ns with respect to the excitation laser in order to avoid inducing AC-Stark and population depletion effects.

The deep-UV laser source

For the production of laser light at 202 nm a tunable pulsed laser system at 10 Hz repetition rate is used. A schematic overview is given in Fig. 2.3. A gain-switched (passive) titanium:sapphire (Ti:sapphire) oscillator cavity is pumped by a Nd:YAG laser (Quanta Ray GCR 3). Upon injection seeding with the output of a CW Ti:sapphire ring laser (Coherent 899) at about 808 nm the pulsed oscillator produces a Fourier-limited linewidth at the seed wavelength with a pulse energy of 0.5 mJ. The pulsed oscillator output can optionally be enhanced in a bowtie Ti:sapphire amplifier up to 30 mJ. In order to produce the fourth harmonic at 202 nm, three consecutive nonlinear upconversion stages — BBO crystals cut at appropriate type-I phase matching angles — are used.[145] The pulse energy at 202 nm is varied from zero to maximum output by rotating the polarization of the third harmonic light in front of the fourth harmonic mixing crystal using a $\lambda/2$-waveplate. The laser system reaches maximum output energies of 0.2 mJ/pulse at 202 nm.

The pulse duration and the bandwidth of the Ti:sapphire pulsed oscillator are found to depend strongly on the pulse energy of the pump laser. Under conditions of optimum power production (at 6 mJ/pulse pump energy, limited by damage of the reflective optics of the resonator) pulse lengths of 20 ns are readily obtained; under these conditions the bandwidth at deep-UV wavelengths, after frequency quadrupling is about 40 MHz as can be estimated from the linewidth of the obtained two-photon resonances. By limiting the pulse energy the pulse duration can be extended to 40 ns. The bandwidth is then also reduced accordingly by a factor of two. In the stage of the experiment where the final calibrations were performed the Ti:sapphire pulsed oscillator was run in this mode delivering the narrowest linewidths.

Absolute calibration procedures

Absolute calibration is performed on the CW seeding light from the Ti:sapphire ring laser. For an absolute calibration with a frequency comb the CW frequency has to be known within a fraction of the frequency spacing of neighboring modes in the comb, which is equal to the repetition rate of the frequency comb, in this case ≈75 MHz.[147] At the time, when these measurements where started, the transition frequencies of the $\mathrm{EF}\,^1\Sigma_g^+ \leftarrow \mathrm{X}\,^1\Sigma_g^+(0,0)$ were known[141] to a 1σ accuracy of 0.003 cm^{-1}, which corresponds to 11 MHz accuracy in the infrared domain. In order to avoid any ambiguity on the specific mode, initial calibration experiments were performed with respect to the I_2 saturation standard in the near-infrared. An example of a recording of the Q(0) line in H_2 is shown in Fig. 2.4. The absolute frequency of the Q(0) is found at 99 164.787(1) cm^{-1} — an accuracy of 4 MHz in the infrared — by referencing it to the "t"-hyperfine component of the P(194) line in the $\mathrm{B}\,^3\Pi_u^+ - \mathrm{X}\,^1\Sigma_g^+\,(0,15)$ band of I_2 at 12 395.65082 cm^{-1},[155] with inclusion of chirp corrections. According to the discussion of the AC-Stark shift in section 2.2, its effect can be estimated to be about 2 MHz at the applied UV power levels for the precalibration. Hence, it can be neglected for the purpose of the mode identification.

For the final calibration measurements, part of the CW seed light is coupled through a 100 m single-mode optical fiber for transportation to another laboratory, where a phase and carrier-envelope stabilized femto-second frequency comb laser

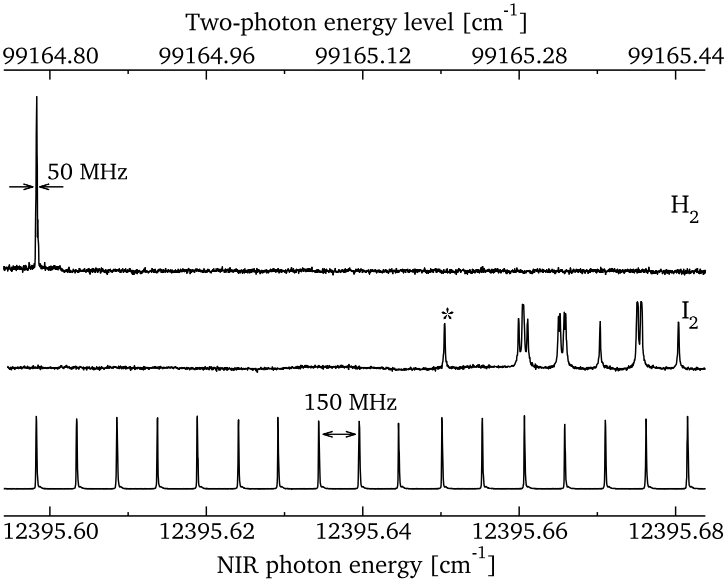

Figure 2.4 – *Simultaneous spectral recording of the EF* $^1\Sigma_g^+ \leftarrow X^1\Sigma_g^+$ *(0,0) Q(0) line of* H_2 *(via the one-color 2 + 1-REMPI scheme), and a saturated* I_2 *spectrum as well as etalon markers produced at the fundamental wavelength. The line marked with an asterisk is the "t"-hyperfine component of the P(194) line in the* $B^3\Pi_u^+ - X^1\Sigma_g^+$ *(0,15) band of* I_2 *at 12395.65048 cm*$^{-1}$*, used as an absolute reference. The indicated linewidth on the* H_2 *resonance depends on the specific settings on the Ti:sapphire pulsed oscillator (pulse duration and bandwidth) and is given for the two-photon level frequency.*

is installed.[146,147] The CW-light is heterodyned with the output of this frequency comb in a setup as depicted in Fig. 2.5, and the radio-frequency beatnote ν_{bn} is detected on an avalanche photodiode (PD). To increase the signal-to-noise ratio (s/n) on the photo-detector, a grating and lens are used to disperse the spectrum of the frequency-comb in a $4f$-configuration, so that a reduced number of modes is focused together with the CW mode on the PD. Typically, the beatnote detection reached a s/n of 45 db. The two main parameters of the frequency comb are its carrier-envelope phase offset frequency ν_{ceo} and its repetition rate ν_{rep}. Both are locked against a Rubidium-clock standard, which is further referenced to the global positioning system (GPS). From the locking characteristics, the stability of each single frequency of the comb around 808 nm is estimated to be better than 100 kHz for the typical averaging times of 1 s.

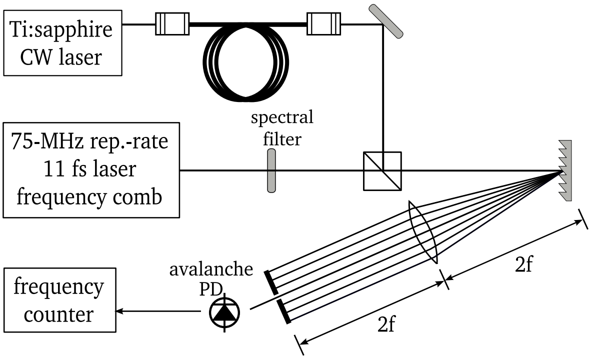

Figure 2.5 – *Schematic view of the setup for the detection of the beatnote with the fs-laser frequency comb.*

The transition frequency ν_Q is measured by determining all radio frequencies involved, via:

$$\nu_Q = \pm \nu_{bn} + \nu_{ceo} + n \times \nu_{rep} \tag{2.2}$$

where the mode number n follows from the initial calibration using the I_2 saturated spectroscopy. The $\pm$ sign of the beatnote frequency ν_{bn} is determined by scanning the cw-laser while monitoring the beatnote between frequency comb and cw-laser. When the cw-laser is scanned to shorter wavelengths and the beatnote increases accordingly the sign is $+$, and when the beatnote decreases the sign is $-$.

The beatnote between the frequency comb and the CW laser is kept at ≈ 22 MHz over the entire scan for convenient electronic filtering. To achieve that, the repetition rate of the frequency comb is correspondingly scanned as the CW laser is tuned over the molecular resonance. The wavelength tuning was sufficiently slow to ensure that the comb mode is correctly identified. In effect, an absolute calibration is performed for every scan step. In Fig. 2.6 the counted beatnotes between seeding light and frequency comb during a typical scan are shown. As pointed out before, the beatnote remains constant at around 22 MHz over the entire scan. In order to obtain a result with reasonable statistics, at each scan step the beatnote is counted 10 times. Each single count is acquired within a time gate of 0.1 s, so that the beatnote counting takes 1 s per scan step. The given error bars depicted in the zoomed inlay are taken from the standard deviation of the 10 beatnote frequency countings. Typical standard deviations are 0.5 MHz which is about a factor 5 larger than the

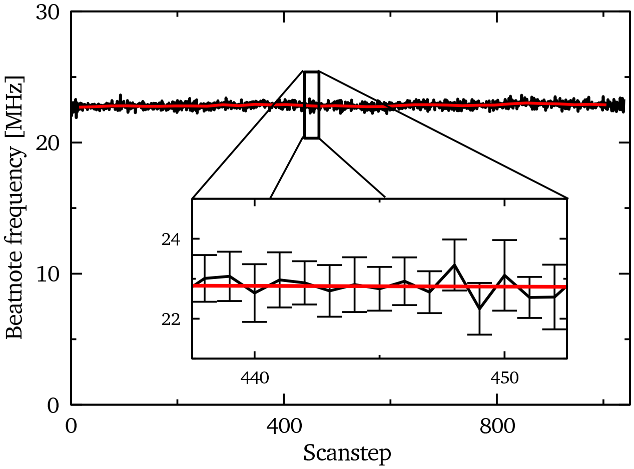

Figure 2.6 – *Frequency measurements via counting of* ν_{bn} *for a scan of a thousand frequency steps.*

stability of the frequency comb (< 100 kHz). The source of the fluctuations of the beatnote is predominantly due to frequency jitter of the seed laser.

Frequency-chirp induced offset

Since the spectroscopic experiment on the EF $^1\Sigma_g^+ \leftarrow X\,^1\Sigma_g^+(0,0)$ transitions is performed with the quadrupled output of the pulsed oscillator, while the frequency calibration procedures are performed on the CW seed-frequency, possible deviations between the two must be considered. Such offsets are common, investigated in detail for traveling-wave dye-amplifiers,[148–150] and recently also for optical parametric oscillators.[151,152] In the present case of a pulsed laser oscillator, containing only a Ti:sapphire crystal as an active optical element inside its resonator (see Fig. 2.3), the optical path length will depend on the rate of pumping by the Nd:YAG pump laser; a mode-pulling effect will result from the change in refractive index in the Ti:sapphire crystal during the time interval of population inversion.

This phenomenon is assessed experimentally in two steps. First, a possible net average offset between CW and pulsed output is measured using a confocal etalon in an experimental configuration as shown in Fig. 2.7. Both pulsed and CW beams are overlapped and propagated through a single mode fiber to ensure that they excite a common spatial mode in the etalon. Photodiodes detect fringe traces as in Fig. 2.7

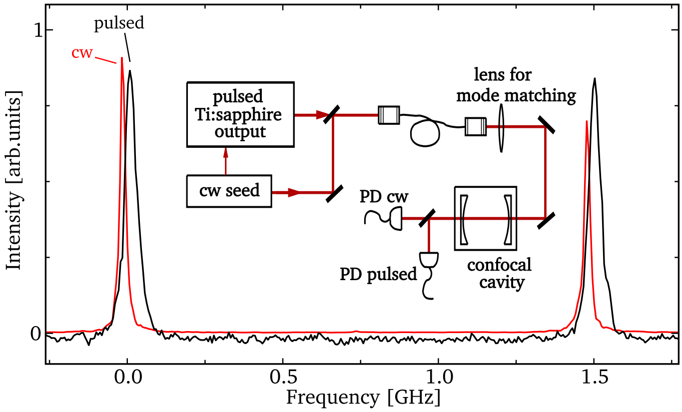

Figure 2.7 – *Frequency measurements via the output of the CW seed laser and that of the pulsed oscillator (for one specific setting of the Hänsch-Couillaud lock on the cavity). As the seed light is tuned the etalon fringes (FSR = 750 MHz) of the pulsed output are red-shifted from the CW-fringes by 20 MHz. The experimental setup is given as an inlay. Both the pulsed and the cw-light are superimposed and mode-matched by transmitting them through a single-mode fiber.*

for both the orthogonally polarized signals, when scanning the CW seed-frequency and keeping the etalon at fixed FSR. This procedure results in a quantitative value for the average frequency of the pulsed oscillator: its output is red-shifted by an amount of ≈ 20 MHz with respect to the CW carrier frequency. We note that this method of chirp detection does not allow for a single pulse assessment of this phenomenon, nor does it produce insight into the frequency excursions during the laser pulse. Rather it yields an averaged chirp-induced net shift between CW and pulsed outputs of the laser system.

Secondly the instantaneous frequency during the temporal evolution of the laser pulse is obtained by heterodyning methods previously described.[149–152] With the use of an acousto-optical modulator (AOM) a CW-light field shifted in frequency by 250 MHz is generated from the seed light. This frequency shifted light is heterodyned with the pulsed light, and the beatnote is detected on a fast photodiode detector (New Focus DC-1). For maximum beatnote contrast the two light fields must be well overlapped, which is achieved by coupling through a single-mode fiber.

The chirp beatnote is acquired on a fast oscilloscope (Tektronics TDS 7404; bandwidth: 4 GHz, sampling rate: 20 GSample/s) — from now on to be referenced as the "chirp scope" — and used to obtain the temporal evolution of the phase $\Phi(t)$, from

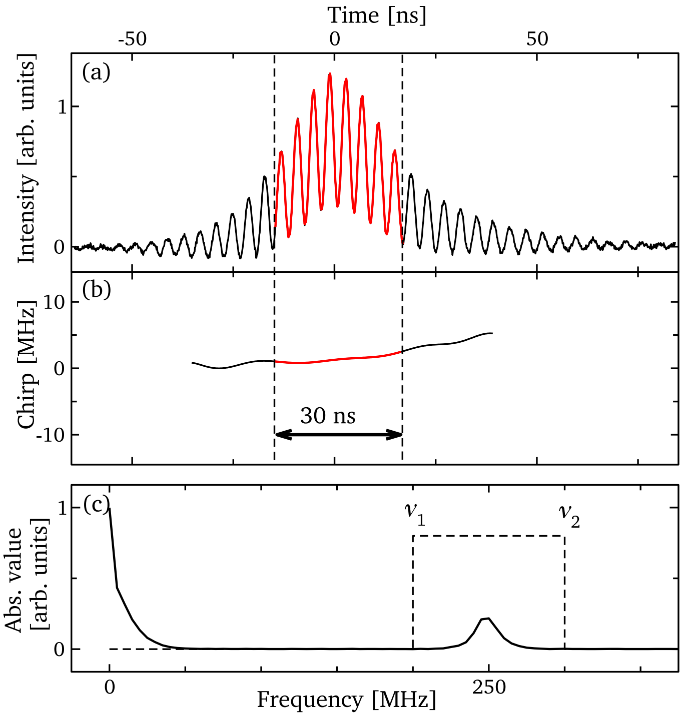

Figure 2.8 – *From the beatnote (a) a FFT is performed — the lowest graph (c) shows the corresponding power spectrum. Then the result is filtered and inverse Fourier-transformed. From the obtained temporal phase evolution the instantaneous frequency offset is calculated (b).*

which the instantaneous frequency is calculated by:

$$\nu_{\text{chirp}}(t) = \frac{1}{2\pi} \frac{d}{dt} \Phi(t) \tag{2.3}$$

In Fig. 2.8 typical pictures of the various steps in the chirp analysis of an acquired beatnote are shown.

First the beatnote transient $I(t)$ is Fourier-transformed to $\tilde{I}(\nu)$. In this case the power spectrum (Fig. 2.8c) contains two well separated peaks. The lower frequency peak is a result of the envelope of the beatnote signal, and the higher frequency peak at around 250 MHz contains the phase information, which allows for calculating a time dependent change of the instantaneous frequency of the pulse. For extracting the phase information from the beatnote frequency spectrum, the corresponding peak is filtered out by a gate-filter $F(\nu) = \Theta(\nu - \nu_1)\Theta(\nu_2 - \nu)$ — where $\Theta(x)$ is the Heaviside step function — shown in Fig. 2.8c. The imaginary part of the inverse Fourier-transformed filtered spectrum $\tilde{I}(\nu)F(\nu)$ gives a time dependent phase $\Phi(t)$, from which the phase evolution due to the AOM frequency has to be subtracted. Finally, the instantaneous frequency differences between the CW carrier and the pulsed output are reconstructed using Eq. (2.3). The evolution of the instantaneous frequency of the pulsed light can be described as $\Delta_f(t) = \overline{\Delta}_{f_0} + \Delta_{f_0}(t)$, where $\overline{\Delta}_{f_0} = \overline{f}_{\text{out}} - f_{\text{cw}}$ is called the net pulsed - CW frequency offset and $\Delta_{f_0}(t)$ a time dependent deviation from $\overline{\Delta}_{f_0}$. In Fig. 2.8 — which shows a typical result of the chirp analysis — one can see a shallow slope in $\Delta_f(t)$. The detection and analysis procedures of this dynamic chirp assessment are sufficiently fast to be able to run them online for each individual data point, while performing the hydrogen spectroscopic measurements.

An important finding is that the slope of $\Delta_f(t)$ (*cf.* Fig. 2.8b) can be reduced by lowering the pulse energies to pump the oscillator. Additionally, at low pump energy conditions the produced pulses are of longer duration and have a narrower line width. The narrow linewidth and the flat frequency chirp — typically 0 - 2 MHz on 30 ns — are particularly important for producing nearly Fourier-limited harmonics with a well defined frequency and will directly reduce the uncertainty budget on the absolute calibration. The lower pump energy of the pulsed oscillator can be compensated by additional amplification in the multi-pass amplifier system, when working in the saturated regime. It is verified that at the wavelengths used here, the amplifier changes the temporal evolution of the instantaneous frequency of the output pulses only slightly, which means it shifts the net frequency offset in the order of 2 - 4 MHz. Therefore the chirp analysis is performed on the output of the total infrared laser system so that the effect of the amplifier is always taken into account.

In contrast to changes in the pump power, the settings of the Hänsch-Couillaud feedback loop have only little influence on the chirp slope, but strongly affect the frequency offset $\overline{\Delta}_{f_0}$, which in fact can be tuned to any value in a range from -50 MHz to 20 MHz. This effect is due to cavity mode pulling: the Hänsch-Coulliaud setting changes the cavity length and hence the longitudinal mode structure of the cavity. As a result the pulsed output is pulled from the seeding frequency towards the closest cavity resonance. In order to check, whether the chirp analysis performs consistently, the EF ← X Q(1) line in H_2 was measured using different chirp offset frequency settings. If the chirp analysis is properly behaved, the transition frequency of the Q(1)-line should be independent of the chirp offset. In Fig. 2.9 the result of a series of scans over the resonance is shown. Each scan obtained at different Hänsch-Couillaud settings. For the resulting different frequency offsets, the

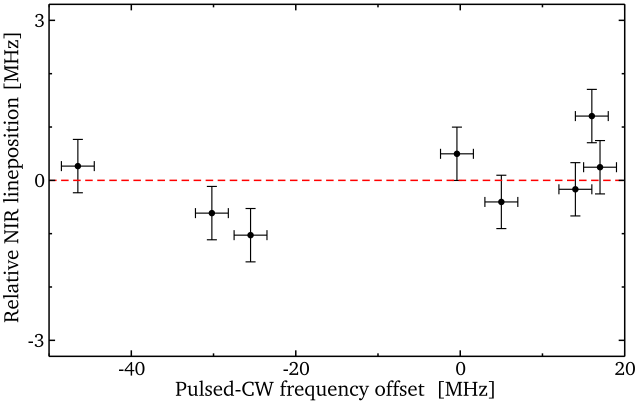

Figure 2.9 – *Sequence of spectroscopic scans performed on the EF$\leftarrow$X(0,0) Q(1) line in H_2 using different chirp frequency offsets ranging from -50 MHz to 20 MHz. The mean value of all acquired positions for the Q(1) line is 99109.7315 cm^{-1}. The y-axis shows the deviations of the line positions of the single scans from that mean value on the infrared frequency scale (around 12388.7165 cm^{-1}). The standard deviation is 0.7 MHz (cf. discussion in section 2.2).*

fitted transition frequencies are spread around 99109.7315 cm^{-1} with a standard deviation of 5.6 MHz. Correspondingly, the actual Ti:sapphire frequencies vary around 12388.7165 cm^{-1} with a standard deviation of 0.7 MHz. It should be noted, that both the spread and the mean line position for Fig. 2.9 are acquired using earlier, preliminary alignment and ionization methods, which where replaced by more accurate procedures afterwards — a Sagnac interferometer replaced a simple retroreflection on a plain mirror and a two-color REMPI replaced a one color scheme. Correspondingly, the spread in Fig. 2.9 is a combination of several statistical errors being larger than listed in Table 2.2. It includes larger Doppler uncertainties, larger AC-Stark influences, and more pronounced chirp influences than the ones achieved using the newer methods.

Though the check in Fig. 2.9 shows, that the actual frequency offset between pulsed and seed light does not affect the final result, the settings were selected such that the offset frequency remains about zero during a scan. In a forthcoming publication the characteristics of the pulsed laser are investigated in greater detail. It appears, that the zero-offset setting is also the most efficient for the energy conversion from the cavity pump to the Ti:sapphire near infrared output. That in turn allows for a further reduction of the pump energy, and consequently a reduction of the chirp. In Fig. 2.10 the obtained chirp-induced frequency offsets during one spec-

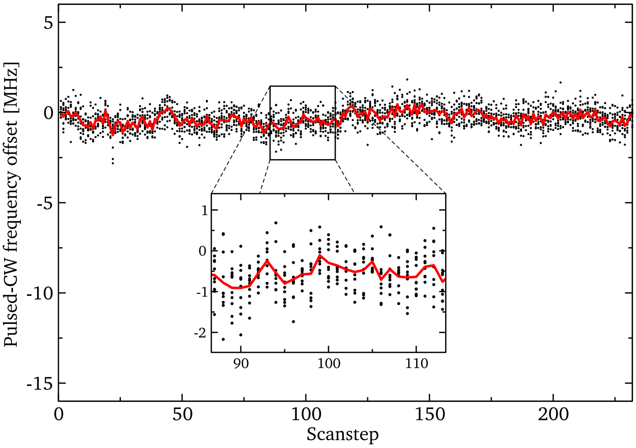

Figure 2.10 – *Online chirp analysis for a scan covering ≈ 260 seconds at 10 Hz of data for a specific setting of the pump energy for the Ti:sapphire oscillator. The locking point of the Hänsch-Couillaud feedback system was set such that the net shift* $\overline{\Delta}_{f_0}$ *equals zero.*

troscopic scan are displayed for a specific setting of the pump energy for the pulsed oscillator and the Hänsch-Couillaud locking point. The frequency offset is acquired for 10 pulses per scan step. From those 10 values per scanstep the mean values are calculated and shown as a solid line in the figure.

For the measurements displayed in Fig. 2.10 the Hänsch-Couillaud locking was set such that a net shift of $\overline{\Delta}_{f_0}$ is zero. This is a different setting than used for the data displayed in Fig. 2.7. It was verified however that the obtained mean values of about -15 MHz to -20 MHz obtained with the etalon method are consistent with the dynamic chirp measurements. The negative sign indicates, that the pulsed output has a smaller frequency than the seeding light. The chirp analysis gives information on the relative frequency jitter between seeding light and pulsed output of the Ti:sapphire oscillator.

DC and AC-Stark effects

In order to prevent DC-Stark effects shifting the transition frequency laser, excitation is performed under field-free conditions, while a pulsed extraction voltage ramp (1000 V) is switched 0.3 μs after the excitation to collect the ions produced via $2+1$-

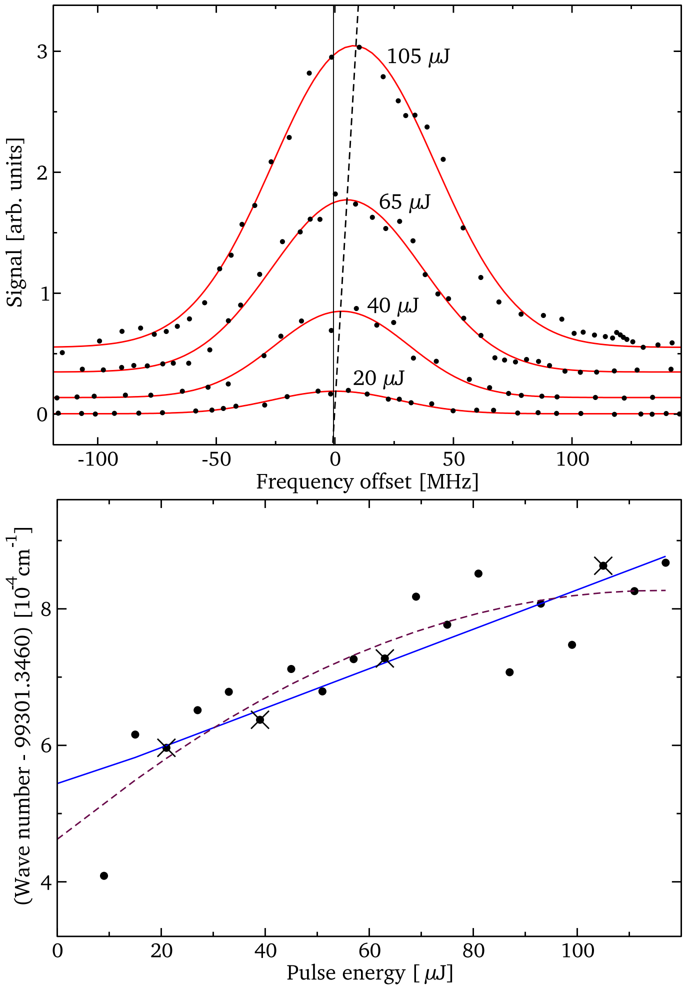

Figure 2.11 – *Assessment of the AC-Stark effect on the EF* $^1\Sigma_g^+ \leftarrow X\,^1\Sigma_g^+$ *(0,0) Q(0) line in HD by measurement of the transition frequency as a function of laser pulse energy with parameters: pulse length 12 ns (at 202 nm) and collimated beam diameter 0.04 cm. The upper graph shows data obtained at four different pulse energies for the deep-UV excitation laser, here used in the 2 + 1 one-color REMPI scheme. The line positions found for different data traces in the upper graph are marked with an X in the lower graph. Extrapolation by linear regression to the intercept yields a value of 99 301.34654(6)* cm^{-1} *for this specific measurements series and a value for the AC-Stark shift of 7 MHz/(MW/*cm^2*). A quadratic regression (dashed line) leads to an intercept of 99 301.34646(6)* cm^{-1}.

Table 2.1 – *Measured AC-Stark shifts on various EF* $^1\Sigma_g^+ \leftarrow X\,^1\Sigma_g^+$ *(0,0)-transitions in* H_2 *and HD given in MHz/(MW/cm*^{2}*).*

molecule	line	AC-Stark shift
H_2	Q(0)	13(7)
	Q(1)	6(4)
HD	Q(0)	5(3)
	Q(1)	6(3)

REMPI. For the $n = 2$ EF state in hydrogen possible stray electric fields at the level below 0.1 V do not affect the transition frequency at the present level of accuracy.

In order to assess the influence of the AC-Stark shift, the output energy of the laser was varied. Finally, the result on each transition frequency is retrieved from an extrapolation to zero pulse energy as shown in Fig. 2.11. Note that the AC-Stark effect parameter exhibits a different value for each transition. The absolute value for the AC-Stark shift parameter, being 7 MHz/(MW/cm^2) for the Q(0) line in HD, can be determined to within an accuracy of not better than 50 % in view of the uncertainties in the measurement of UV pulse energy and the size of the laser beam. The obtained values for the AC-Stark shift parameters are listed in Table 2.1. The present value for the AC-Stark parameter pertaining to the Q(1) line of H_2 is in reasonable agreement with that of Vrakking *et al.*,[156] who found 15 MHz/(MW/cm^2).

For the determination of AC-Stark free transition frequencies the extrapolations to zero intensities are relevant, irrespective of the absolute pulse intensity scale. In a first round of experiments the absolute transition frequencies of most of the lines were determined from such extrapolations of the measured frequencies in the one-color 2 + 1-REMPI scheme. A general result from the entire set of measurements on the assessment of the AC-Stark effect is that at the lowest laser intensities, corresponding to pulse energies ($< 4\,\mu$J) the AC-Stark shifts are lower than 1 MHz. Hence a second round of measurements was performed on all lines in H_2, HD and D_2 in which the excitation laser was kept below 4 μJ/pulse, and where the ionization was accomplished by a second intense UV-laser pulse (at 355 nm) that was temporally delayed by ≈ 50 ns. In this two-color REMPI scheme AC-Stark free measurements were performed resulting in the most accurate values for the transition frequencies. It was verified that the data of the extrapolated one-color experiments are consistent with those of the two-color pulse-delayed scheme.

Phase distortions in non-linear mixing

Additional effects of frequency chirp can be induced as a result of optical phase distortions in the processes of nonlinear mixing for the generation of harmonics. These issues and the consequences for frequency metrology on the basis of pulsed laser sources were discussed in detail by Gangopadhyay *et al.*[157] Firstly, the optical Kerr effect, modulating the index of refraction $n(t)$ with the laser intensity $I(t)$ during the pulse evolution via : $n(t) = n_0 + n_{\mathrm{Kerr}} I(t)$, may give rise to phase distortions of the size:[157,158]

$$\Phi(t) = -\frac{2\pi L \, n_{\mathrm{Kerr}} \, I(t)}{\lambda}, \tag{2.4}$$

where L is the length of the non-linear crystal, λ the wavelength, and n_{Kerr} the wavelength-dependent Kerr index for the used crystal.

The resulting chirp may be evaluated via Eq. (2.3). The Kerr index of BBO has been measured by Li *et al.*[159] at 1064 nm and 532 nm at different crystal axes. The obtained values vary between $4 \cdot 10^{-16}\,\mathrm{cm^2/W}$ and $5 \cdot 10^{-16}\,\mathrm{cm^2/W}$ and are given with a 20 % error margin. For the moment, the analysis is restricted to the Kerr effects induced in the stage of the second harmonic generation (SHG). In Fig. 2.12 an example for typically used infrared pulse intensities of $0.2\,\mathrm{GW/cm^2}$ in the SHG crystal is calculated. For obtaining the temporal intensity profile $I(t)$, shown in Fig. 2.12(b), the normalized signal of a fast photodiode (Thorlabs DET 210) with a response time of 1 ns was used. Using the chirp analysis system the corresponding instantaneous frequency evolution $\nu_{\mathrm{offs}}(t)$ in the SHG crystal was acquired — displayed in Fig. 2.12(a). From the calculation using Eq. (2.4) inserted into Eq. (2.3) it is apparent that the Kerr effect modulates the instantaneous frequency ν_{result} in an antisymmetric way around the maximum of $I(t)$. At the rising side the instantaneous pulse frequency is shifted to higher frequencies and the at the falling side to negative frequencies. Possible deviations from a perfect antisymmetric behaviour resulting from an asymmetric temporal pulse profile $I(t)$ could produce net frequency shifts affecting the absolute calibration. Based on a simulation the net frequency shift $\overline{\Delta}_{f_0}$ was calculated both with and without the Kerr effect. As a result of the nearly antisymmetric evolution of $\nu_{\mathrm{Kerr}}(t)$, the difference between the two net shifts proved to be insignificant, as the net Kerr shift is several orders of magnitude below the uncertainties of the chirp analysis of section 2.2.

The fact, that the instantaneous our effect of the Kerr induced phase distortions, is quasi-antisymmetric over the temporal profile of the pulse — also for the subsequent stages of third and fourth harmonic generation — their net effect on the frequency calibration is far below other sources of calibration uncertainties. In principle, at the following sum frequency mixing stages, the Kerr effect could indeed cause

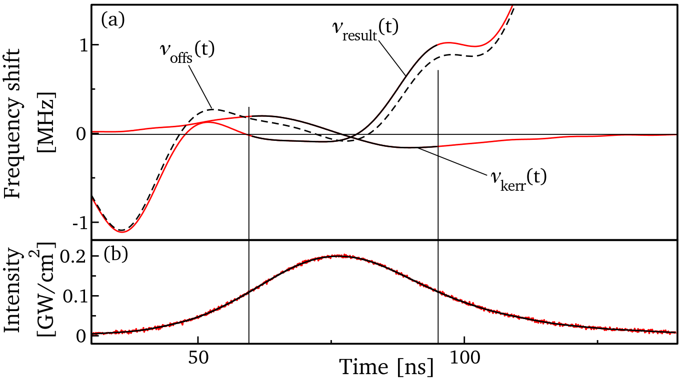

Figure 2.12 – *The influence of the Kerr effect on the instantaneous frequency evolution in the SHG crystal calculated for a typical infrared pulse of 0.2 GW/cm^2 peak intensity and 35 ns duration.* ν_{offs} *: pulsed – CW frequency offset measured in front of the SHG crystal,* ν_{kerr} *: instantaneous frequency shift caused by the Kerr effect,* ν_{result} *: the sum of* ν_{offs} *and* ν_{kerr}*.*

frequency shifts, when a time delay between the two contributing input beams was introduced. However with typical pulse lengths of 20 ns as used here, careful alignment of the lengths of the beam branches in the upconversion stages prevents such problems efficiently.

A second phenomenon resulting in chirp from phase distortions in non-linear mixing is associated with a deviation from optimum phase-matching.[157,160] We decided to assess the effects of non-perfect phase-matching via an experimental approach. The entire optical layout, in particular involving the alignment of the beam propagation and the adjustment of the phase-matching angles, was set up from scratch in a number of separated measurement days focusing on a few transitions. After the complete daily realignment procedure both the phase-matching angles of the upconversion crystals and the dark fringe at the exit port of the Sagnac interferometer were readjusted for each single scan. During those procedures indeed statistical day-to-day excursions in the determined transition frequencies were obtained with a standard deviation of about 2.5 – 6 MHz depending on the isotopic species and particular line; these excursions are somewhat larger than the 1σ spread of results obtained during a measurement series of one day, which was limited to 2 – 3 MHz. These excursions are attributed to the combined effect of Doppler shifts, phase distortions in non-linear mixing, day-to-day beamprofile variations, and varying wavefront distortions. Particular the latter two effects are more dependent on the daily full realignment of the optical layout.

Integrated setup and measurement procedures

The three different laser systems, the CW Ti:sapphire seed laser and the Ti:sapphire pulsed oscillator-amplifier system in one laboratory, and the frequency comb lasers in another laboratory separated by 100 m, and the vacuum and detection equipment are assembled into one experiment of which a schematic overview is shown in Fig. 2.13. In laser-lab-I, where the spectroscopic data are recorded, master computer PC1 takes control of all tasks during the experiment. The frequency of the seed laser is driven, via its external voltage scan port, by an arbitrary waveform generator (Agilent AWG 33250A) connected via GPIB to PC1. The "chirp scope" is triggered by a photodiode detecting the 202 nm light. The sample beatnote waveforms (as in Fig. 2.8) are transferred via GPIB to PC1, where the chirp analysis is carried out. Finally, the REMPI-TOF signal is registered on an electron multiplier tube and digitally integrated using a LeCroy WaveRunner oscilloscope (the "TOF scope"). The "TOF scope" is triggered by the external trigger interface of the "chirp scope". This combined trigger acquisition ensures that all possible data is acquired from each pulse following the 10 Hz repetition rate of the laser: the chirp parameters, the relative UV power and the REMPI signal. This pulse-correlated acquisition allows for using binning and filtering techniques for data analysis, of which some are performed off-line. By this means correlations between power fluctuations of the pump laser, the chirp/frequency-pulling characteristics, and the UV output power can be investigated. Also, the AC-Stark induced frequency shifts resulting from UV-power fluctuations can be used to derive the AC-Stark parameter.

In the femto-lab (*cf.* Fig. 2.13), where the frequency comb is operated, PC2 is responsible for the frequency comb laser control and data acquisition. The beatnote signal detected on the avalanche photodiode (Fig. 2.5) is filtered via an RF-band pass filter to remove signal from higher order beatnotes, amplified, processed via a discriminator and counted on a frequency counter (Agilent 53132A Universal Counter) connected to PC2 via GPIB. The repetition rate of the frequency comb — actually its 140th harmonic — is locked to a frequency of about 10 GHz. This frequency is generated by a radio frequency synthesizer (Agilent PSG-L F8241A), which is locked to a Rubidium clock standard. The set frequency of the synthesizer is controlled by PC2 via GPIB bus. In order to maintain synchronous operation in the two labs PC2 stays in connection with PC1 via a server client protocol running on top of the ethernet. PC2 initiates beatnote counting on PC1's request. Further-

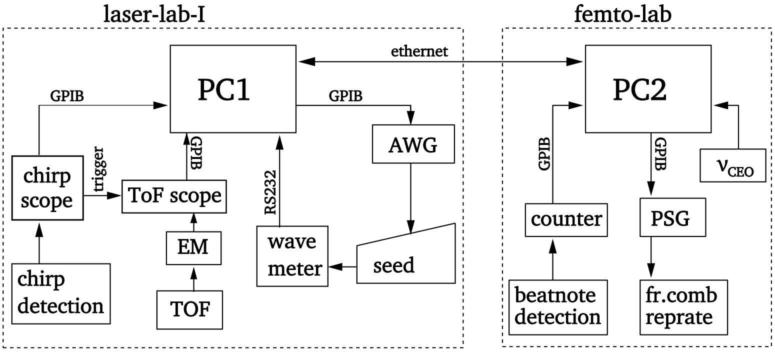

Figure 2.13 – *Flow control scheme and overview of the experimental components. PC1 is the master system, taking control of the laser scan and requesting data from frequency comb server PC2 in the femto-lab. PC2 initiates the beatnote counts, but also maintains the beatnote within a frequency window by controlling the repetition rate of the comb. AWG: arbitrary waveform generator. DAC: GPIB signal acquisition interface. PSG: signal generator.* ν_{ceo}*: the carrier envelope offset frequency is read via GPIB from the wave form generator that provides the reference signal for the corresponding feedback loop.*

more PC2, depending on the actual beatnote readout, adjusts the repetition rate of the frequency comb in order to maintain the beatnote within a frequency window of 21 MHz – 24 MHz which is the working range of the final low-pass filter in front of the frequency counter.

The wavelength of the seed light is continuously monitored by an ATOS LM 007 wavemeter and sent to PC1 through a RS 232 serial connection. Although its long-term stability is about 30 MHz in the near infrared, during the time-span of an experiment it remains reproducible to within 3 MHz. This auxiliary instrument is used for pre-calibration, for detection of possible mode-hops of the CW seed laser, and for establishing the sign of the beatnote frequency between frequency comb and seed light.

The experimental procedure is as follows: After the precalibration is finished using iodine saturation spectroscopy (*cf.* Fig. 2.4) the actual frequency comb measurement is performed. First the seed laser is tuned to the start frequency which is chosen roughly 30 MHz next to the two-photon resonance. Then the repetition rate of the frequency comb is set such that the beat note frequency between seed and frequency comb is 22 ± 2 MHz (within the accepted range of the band pass filter in use). Furthermore the sign of the beatnote frequency must be established. Then the scan is started: using the AWG connected to PC1 the laser is scanned with a fixed

Table 2.2 – *(A) Estimated systematic error budget for the frequency calibrations of the* $EF\,^1\Sigma_g^+ \leftarrow X\,^1\Sigma_g^+$ *(0,0)-transitions in hydrogen. (B) The experimentally obtained statistical spread listed for each line.*

(A) Systematics	Detail	Value (MHz)
(i) Doppler	H_2	0.75
	HD	0.6
	D_2	0.5
(ii) Calibration	Frequency comb	< 0.1
(iii) Chirp	In Ti:sapphire oscillator	2
(iv) Chirp	In nonlinear mixing	< 0.01
(v) AC Stark	In two-color scheme	< 1.0
Estimated systematic error budget[a]		3.2
(B) Statistics[b]	H_2 Q(0),Q(2)	3.3
	H_2 Q(1)	5.4
	HD Q(0),Q(1)	6.0
	D_2 Q(0),Q(1)	2.4
	D_2 Q(2)	2.1

[a] Quadrature summation of errors (i-iv) and adding (v) linearly to the result.

[b] (1σ) standard deviation of all results (10 to 15 scans per line) obtained over several days.

voltage step per scan step. On each scan step the beatnote frequency between seed and frequency comb is counted. If the frequency comb would run at fixed settings and no band pass filter was used — depending on the sign of the beatnote frequency — the beatnote frequency would increase until reaching half the repetition rate ν_{rep} and decrease again, or it would decrease until a zero beatnote is reached and then increase again. In order to avoid inevitable assignment problems at beat note frequencies close to zero or $\nu_{\text{rep}}/2$, the beatnote is quasi-locked around the start value. This is achieved by steadily adjusting ν_{rep} at each scan step after finishing the beatnote frequency counting.

Each scan covers a range of about 70 MHz (in the near infrared) and consists of about 300 equidistant voltage steps. On each step PC1 first requests PC2 to start the beatnote frequency counting in the femto-lab. Then the "chirp scope" and "TOF scope" are triggered ten times so that the data of ten pulses are obtained. After that PC1 requests PC2 to send all relevant data from the frequency comb, ν_{rep}, ν_{ceo} and ν_{bn}. The software written on both computers is based on the Python programming language. The mathematically more involved part of the chirp analysis is written using the SciPy[161] package.

Uncertainty budget for the transition frequencies

In this section, the final contributions to the uncertainty budget for the present calibration study on $\mathrm{EF}\,^1\Sigma_g^+ \leftarrow \mathrm{X}\,^1\Sigma_g^+(0,0)$ lines are compiled. The estimated values, discussed extensively in the previous subsections are listed in Table 2.2. The major contributions are associated with the chirp characteristics of the pulsed oscillator — documented in section 2.2 — and with the non-perfect overlap of the two counter-propagating laser beams pumping the two-photon resonance. In the present experiment an almost negligible uncertainty is associated with the absolute frequency scale by using a frequency comb laser. The estimate on the AC-Stark effect pertains to the two-color $2+1$-REMPI scheme, in which pulse energies of less than 4 μJ are used for the two-photon excitation. The resulting final estimate for the uncertainty of a transition frequency, including all systematics is evaluated at 3.2 MHz. The statistical spread (1σ) in the data for measurements recorded under identical conditions on the same day is limited to 2 MHz for H_2 and D_2 and to 3 MHz for HD — for the latter lower beam densities were applied yielding lower s/n ratios. These uncertainties are consistent with the final systematic estimate as listed in Table 2.2 A. However, the spread (1σ) over varying conditions of several days measurements can be as large as 5.4 MHz for H_2 Q(1) and 6 MHz for HD (*cf.* Table 2.2 B), but is smaller in other cases. We do not know the exact origin of these somewhat larger variations. Since the known sources of systematic uncertainties lead to a smaller value, the day-to-day variations are treated as statistical uncertainties. In the final listing of the transition frequencies in Table 2.3, the estimated systematical error budget of 3.2 MHz or 0.00011 cm^{-1} (Table 2.2 A) is considered as lower uncertainty limit.

One possible contribution to statistical variation not discussed so far is the non-linear curve fitting for obtaining the line positions. In the present study, we have not elaborated on line shape models, because all spectral lines, recorded at low intensity, could be fitted to purely Gaussian line profiles. A typical example of a recorded line is shown in Fig. 2.14. Each scan consists of about 2000 to 3000 datapoints and spans about 300 MHz at the two photon level. The obtained fitting uncertainties for the line center positions are about 0.4 MHz for each single scan and all measured lines, which is to small to explain the discrepancy between estimated error budget and experimentally observed spread.

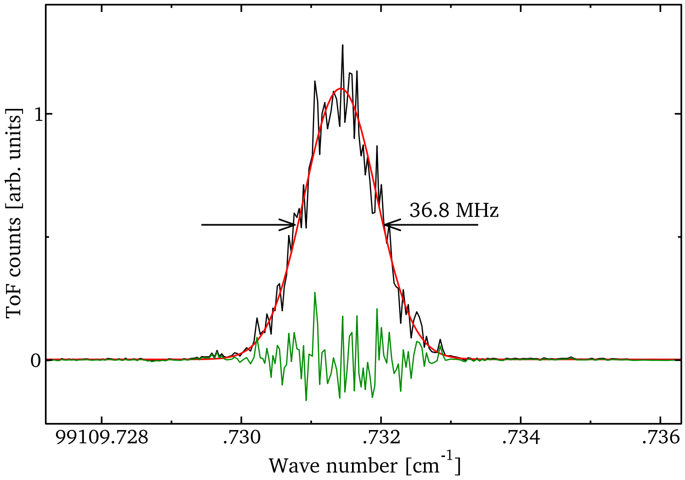

Figure 2.14 – *Scan on the EF* $^1\Sigma_g^+ \leftarrow X\,^1\Sigma_g^+$ *(0,0) Q(1) line in* H_2*. This spectrum was recorded under low pulse energy pumping conditions for the Ti:sapphire pulsed oscillator delivering the narrowest bandwidth output. Each datapoint represents an average over 10 shots. The line width obtained in this spectrum is 36.8 MHz. The smooth line corresponds to a Gaussian function fitted to the observed spectral data; residuals are shown as well.*

2.3 Results and conclusions

The present study involves a highly accurate frequency measurement of eight spectral lines in the EF $^1\Sigma_g^+ \leftarrow X\,^1\Sigma_g^+(0,0)$ band of H_2, HD, and D_2 by Doppler-free two-photon excitation in the collision-free conditions of a molecular beam. As a typical example, in Fig. 2.14 a scan over the Q(1) line in H_2 under conditions of a narrowband excitation pulse in the two-color 2 + 1-REMPI scheme is shown. Resulting values for the transition frequencies are listed in Table 2.3. Values for the AC-Stark shift were derived and are given in Table 2.1. In the two-color REMPI scheme the AC-Stark effect was reduced to a sub-MHz level. An absolute accuracy of 2×10^{-9} on the transition frequencies is achieved, thanks to the implementation of several new technologies. A pulsed Ti:sapphire oscillator laser was designed to produce Fourier-transform limited narrowband pulses of which the chirp was measured on-line at high precision. For the first time a frequency comb, referenced to a Rb-atomic clock and to the GPS, was implemented in a spectroscopic measurement chain for calibrating chirp-controlled nanosecond pulses.

Table 2.3 – *The two-photon energy values in various hydrogen isotopomers for* $EF\,^1\Sigma_g^+ \leftarrow X\,^1\Sigma_g^+$ *(0,0)-transitions and a comparison with results by Yiannopoulou et al.*[144] Δ *represents the deviation between presently obtained values and those of Yiannopoulou et al.*[144] *The numbers given in parentheses in column "this work" are the final estimates of the uncertainty as discussed in section 2.2. All values in* cm^{-1}.

species	line	this work	Ref. 144	Δ
H_2	Q(0)	99164.78691(11)	99164.7871(8)	−0.0002
	Q(1)	99109.73139(18)	99109.7316(8)	−0.0002
	Q(2)	99000.18301(11)		
HD	Q(0)	99301.34662(20)	99301.3461(8)	+0.0005
	Q(1)	99259.91793(20)	99259.9184(8)	−0.0005
D_2	Q(0)	99461.44908(11)	99461.4490(8)	+0.0001
	Q(1)	99433.71638(11)	99433.7166(8)	−0.0002
	Q(2)	99378.39352(11)	99378.3937(8)	−0.0002

The present results are in excellent agreement with a previous set of measurements on the same lines, performed at the 8×10^{-9} accuracy level. It is important to note that the study of Yiannopoulou *et al.*[144] involves an entirely different setup and measurement procedures. Hence it is more than comforting that the deviations between the two experiments are much less than expected based on the quoted uncertainties. The combined results of the present study and those of Yiannopoulou *et al.*[144] form an essential ingredient for a future determination of a value of the ionization potential in H_2 and the other hydrogen isotopomers at an accuracy of $0.001\,cm^{-1}$.

Acknowledgment

We thank Dr. Knöckel (Hannover) for lending us a cell to perform I_2 saturation spectroscopy in the near-infrared region, and Dr. E. E. Eyler (Connecticut) for discussing results obtained by his group prior to publication. The Netherlands Foundation for Fundamental Research on Matter (FOM) is gratefully acknowledged for financial support.

Chapter 3

Improved laboratory values of the H_2 Lyman and Werner lines for constraining time variation of the proton-to-electron mass ratio

Two distinct high-accuracy laboratory spectroscopic investigations of the H_2 molecule are reported. Anchor lines in the EF $^1\Sigma_g^+$ – X $^1\Sigma_g^+$ system are calibrated by two-photon deep-UV Doppler-free spectroscopy, while independent Fourier-transform spectroscopic measurements are performed that yield accurate spacings in the B $^1\Sigma_u^+$ – EF $^1\Sigma_g^+$ and I $^1\Pi_g$ – C $^1\Pi_u$ systems. From combination differences accurate transition wavelengths for the B – X Lyman and the C – X Werner lines can be determined with accuracies better than $\sim 5 \times 10^{-9}$, representing a major improvement over existing values. This metrology provides a practically exact database to extract a possible variation of the proton-to-electron mass ratio based on H_2 lines in high-redshift objects. Moreover, it forms the rationale for equipping a future class of telescopes, carrying 30-40 m dishes, with novel spectrometers of higher resolving powers.

This chapter is published as Physical Review Letters **101**, 223001 (2008).

3.1 Introduction

Fundamental physical constants may be subject to change on cosmological time scales. For the fine structure constant α, evidence for a temporal drift with a 5σ significance has been reported.[76] Recently, an indication of a possible decrease of the dimensionless proton-to-electron mass ratio $\mu = m_p/m_e$ was reported at $\Delta\mu/\mu = (2.45 \pm 0.59) \times 10^{-5}$ over a time interval of 12 billion years, based on a comparison of spectra of molecular hydrogen.[100,101] The latter findings require three crucial input ingredients. First, a theory is required that relates possible changes in μ to observable shifts in the spectrum of H_2. For this purpose sensitivity coefficients $K_i = \mathrm{d}\ln\lambda_i/\mathrm{d}\ln\mu$, which indicate how each line in the H_2 spectrum would drift as a result of a variation in the mass ratio μ, can be deduced either in a semi-empirical fashion[101] or through quantum chemical *ab initio* calculations.[105] The second ingredient is the accurate determination of spectral line positions at high redshifts. Of the thousands of known quasar systems at redshifts $z > 2$, H_2 absorptions features have only been observed in some 10 to 15 systems thus far. Of these, only Q0405-443 and Q0347-383 have high-quality and well-calibrated spectra containing many H_2 lines,[102] which formed the basis of the finding on $\Delta\mu/\mu$.[100] Recently, HE0027-184 was established as another system with many resolved H_2 lines,[162] and hence a potential source in deriving further constraints on $\Delta\mu$. The final ingredient is a database comprising of high-precision laboratory measurements that represent present-day ($z = 0$) H_2 spectra. The limited amount of available astrophysical data accentuates the need for a set of laboratory data that would not contribute to the uncertainties in estimating a possible drift in μ.

The principle behind the novel determination of laboratory transition wavelengths in the B $^1\Sigma_u^+$ – X $^1\Sigma_g^+$ Lyman and the C $^1\Pi_u$ – X $^1\Sigma_g^+$ Werner band systems is depicted in Fig. 3.1. Two entirely independent experiments are performed. First, the level energies of the lowest rotational states in EF $^1\Sigma_g^+, v = 0$ with respect to X $^1\Sigma_g^+, v = 0$ are determined by deep-UV (DUV) two-photon laser excitation as depicted in Fig. 3.1(a). The EF $v = 0, J = 0, 1$ rotational levels then assume the role of anchors, on which all determinations of excited level energies will be based. A second experiment measures the energy differences between nearby lying levels in the B $^1\Sigma_u^+$ and C $^1\Pi_u$ states with respect to the EF anchor levels. As an illustration, two sets of transitions involving the B – EF systems are highlighted in Fig. 3.1(b). The set represented by the solid arrows provides a measurement of the B vibrational energy levels relative to the anchor EF $v = 0$ level. In an analogous scheme, the transitions represented by the dashed arrows relate the upper EF levels to an arbitrary B vibrational level ($v = 4$) and hence can be used for the absolute calibration of the EF upper levels via the energy spacing between the B, $v = 4$ and the EF, $v = 0$ anchor.

3.2 H_2 EF←X DUV spectroscopy

The deep-UV spectroscopic determination of the EF – X (0,0) rotational transitions have been described in detail by Hannemann *et al.*[163] The experiment involves 2+1

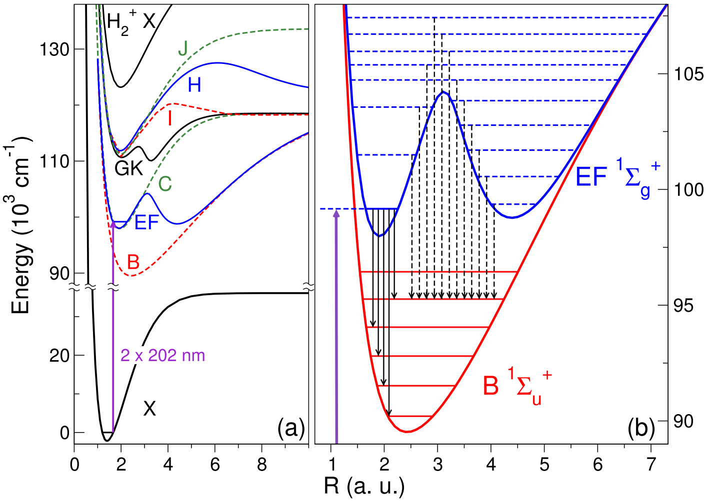

Figure 3.1 – *Schematic of the combination differences exploited in this work. First, the two-photon frequency measurement (at* ∼ 2 × 202 *nm) on the EF – X (0,0) system is used as the anchor to perform subsequent absolute calibrations, as indicated in (a). Two sets of transitions connecting the EF and B states are depicted in (b) to illustrate the technique. The transitions indicated by the solid arrows all originate from the EF* $v = 0$ *level and access different vibrational levels of B, leading to the calibration of the B levels. In a similar manner, the transitions indicated by the dashed arrows enable the calibration of the EF energy levels.*

Resonance-Enhanced Multiphoton Ionization (REMPI) spectroscopy of H_2 at 202 nm; the deep-UV radiation is obtained from the frequency-quadrupling of the IR output from an injection-seeded Ti:Sa oscillator-amplifier laser.[164] The first order Doppler shift is minimized by utilizing the Doppler-free two-photon technique on a H_2 molecular beam (where the laser excitation beams are oriented perpendicular to the H_2 beam). Minimization of the residual Doppler *shift* is accomplished by exploiting a Sagnac interferometric alignment of the counter-propagating laser beams.[165] The high-resolution frequency calibration is achieved by referencing the cw-seeding radiation of the Ti:Sapphire oscillator to a stabilized frequency comb referenced to a (GPS-disciplined) Rb-clock standard. Frequency offsets between the cw-seeding radiation and the IR pulse output of the oscillator are measured and corrected for in every laser pulse. In Fig. 3.2 typical two-photon spectra of the Q0 and Q5 lines are displayed. The accuracy in frequency determination is estimated to be better than 2×10^{-9}.[163] The data set of H_2 EF – X (0,0) Q0 to Q2 lines from[163] has

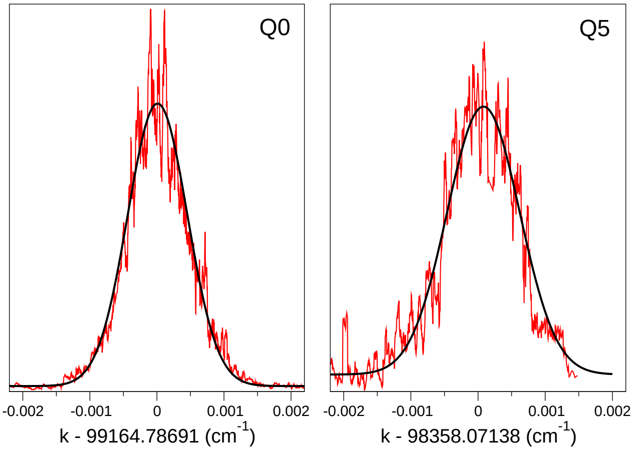

Figure 3.2 – *Recorded spectra of the Q0 and Q5 lines in the EF - X (0,0) band using the methods discussed in the text.*

now been extended to include the transitions: Q3 at $\nu = 98837.24717(15)$ cm^{-1}; Q4 at $\nu = 98622.52699(10)$ cm^{-1}; and Q5 at $\nu = 98358.07138(15)$ cm^{-1}.

3.3 Fourier-Transform spectroscopy

The second experiment entails high-resolution Fourier-Transform (FT) spectroscopy, in a low pressure discharge of hydrogen, spanning a wide wavelength range from the mid-infrared (5.5 μm) all the way to the violet (450 nm). The spectrum was obtained by a Bruker IFS 120 in four portions using appropriate filters and detectors (LN$_2$ cooled InSb photodiode, LN$_2$-cooled InGaAs photodiode, an avalanche silicon photodiode and a photomultiplier tube). As an example we show in Fig. 3.3 a spectrum at around 800 nm displaying the H_2 discharge emission lines from many band systems, including the e $^3\Sigma_u^+$ – a $^3\Sigma_g^+$ triplet systems that were reported recently in,[166] where a detailed discussion about the FT experimental setup can be found.

The Fourier-transform spectra provide a database with a large information content. Because all relevant B $^1\Sigma_u^+, v, J$; C $^1\Pi_u, v, J$; and EF $^1\Sigma_g^+, v, J$ ro-vibrational quantum levels are interconnected via 10 or more spectral transitions, a consistent framework of level energies with high accuracy can be constructed from the entire spectrum. For example, the rotational level energies in B $^1\Sigma_u^+, v = 2$ were deter-

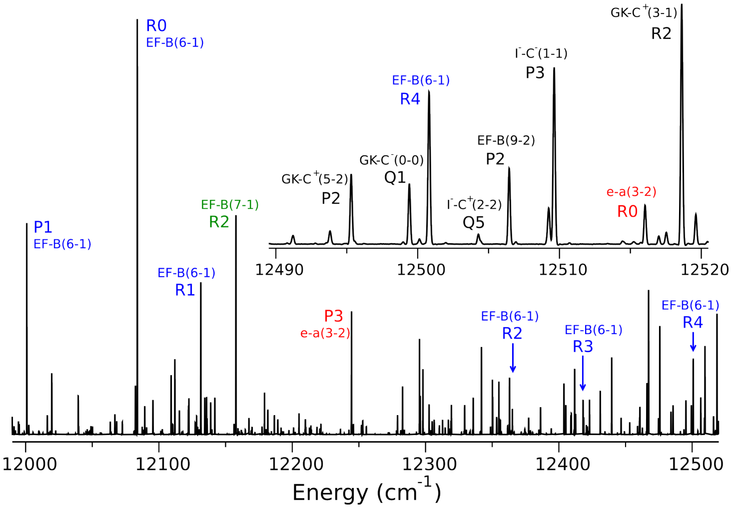

Figure 3.3 – *Sample spectrum obtained from the high-resolution Fourier Transform spectroscopy. The inset shows a smaller portion in detail.*

mined from the analysis involving 13 different bands in the EF – B system. The relative positioning of ro-vibrational level energies in the B state are determined from the analysis of several bands EF – B and GK $^1\Sigma_g^+$ – B, while those of the C state result from the analysis involving the I $^1\Pi_g$ – C, J $^1\Delta_g$ – C, H $^1\Sigma_g^+$ – C and GK $^1\Sigma_g^+$ – C systems. The potential energy curves of the relevant excited states are depicted in Fig. 3.1(a). The bands connecting the C-state are generally weaker than the bands belonging to the EF – B system, and consequently, the reduced signal-to-noise ratio (SNR) leads to a greater uncertainty in the corresponding Werner lines.

Although all lines are Doppler-broadened ($\Delta\nu_D = 0.02 - 0.2$ cm^{-1}, depending on the wavelength), the high SNR and the large amount of spectral information enables a statistical analysis that results in absolute accuracies of 10^{-4} cm^{-1} for the best lines. The spectra were recorded multiple times at slightly varying conditions of pressure and discharge power. Each spectrum was calibrated against reference standard lines of CO[167] and Ar,[168] for which purpose traces of CO and Ar were added in the discharge. Since the deduced level energies are obtained through transitions from many bands occurring at vastly different wavelengths in the FT-spectra, the absolute calibrations depend on a wide range of CO and Ar reference lines. For this reason, the wavelength calibration is considered to be included in the statistical averaging

Table 3.1 – *Level energies ν_0 of the rotationless ($J = 0$) quantum states in $B\,^1\Sigma_u^+$ and ($J = 1$) $C\,^1\Pi_u$ as obtained from the comprehensive analysis of the FT-data. The number N in BN and CN refers to the vibrational level, while the (+) and (-) refer to the Λ-doubling in the C state. The reference energy level is that of the EF, $v = 0, J = 0$ state. All values in cm^{-1}.*

Level	ν_0	Level	ν_0
B0	-8961.28713 (09)	B10	2700.14738 (65)
B1	-7642.96287 (40)	B11	3692.23944 (49)
B2	-6361.48656 (10)	B12	4654.73466 (46)
B3	-5114.77698 (12)	$C0^+$	-12.72964 (48)
B4	-3901.75984 (28)	$C0^-$	-13.93600 (25)
B5	-2721.76001 (24)	$C1^+$	2292.7827 (38)
B6	-1574.25568 (33)	$C1^-$	2291.55606 (45)
B7	-458.77970 (30)	$C2^+$	4463.8750 (13)
B8	625.13263 (30)	$C2^-$	4463.0752 (10)
B9	1677.94489 (16)		

process performed over the data ensemble. This comprehensive analysis leads to a highly accurate set of level energies of excited states that may be referenced to the EF $^1\Sigma_g^+, v = 0$ quantum states, with $J = 0$ for parahydrogen and $J = 1$ orthohydrogen. In Table 3.1, the level energies of the rotationless quantum states of B $^1\Sigma_u^+, v$ and C $^1\Pi_u, v$ levels are listed. The FT-analysis includes a great number of quantum states, with vibrational quantum numbers covering $v = 0 - 12$ for the Lyman band and $v = 0 - 2$ for the Werner band. Most of these vibrational bands cover the range $J = 0 - 7$, with up to $J = 10$ for some strong bands.

3.4 Combining FT and DUV spectroscopy data

Since the energies of rotationally excited states in the EF $^1\Sigma_g^+$, v=0 band can be determined independently using either the FT- or DUV two-photon- data sets, this allows for an independent check on the accuracy and consistency of each data sets separately. The subsequent analysis of the relative level energies obtained from FT spectroscopy requires the X $^1\Sigma_g^+$ ground state level energies which are derived from the accurate far-infrared studies of Jennings *et al.*[169] Relative to the lowest rotational state $J = 0$, we adopt X-state rotational excitation energies of 118.48684(10) cm^{-1} for $J = 1$; 354.37354(21) cm^{-1} for $J = 2$; 705.51906(19) cm^{-1} for $J = 3$; 1168.79827(22) cm^{-1} for $J = 4$; and 1740.18930(19) cm^{-1} for $J = 5$. Using these ground state energy split-

Table 3.2 – *Comparison of the ($J = 2-5$) rotational level energies of the EF* $^1\Sigma_g^+$ *– X* $^1\Sigma_g^+$ *system obtained from direct DUV two-photon spectroscopy* E_{DUV}*, and those obtained from the indirect determination* E_{FT} *using the combined results of FT spectroscopy and Q0- and Q1-derived anchor lines from DUV spectroscopy. The difference,* $\Delta = E_{FT} - E_{DUV}$*, is also tabulated. All energies are expressed in* cm^{-1}.

J	E_{DUV}	E_{FT}	Δ
0	99164.78691 (16)	para anchor	
1	99228.21823 (19)	ortho anchor	
2	99354.55655 (24)	99354.55631 (13)	-0.00024
3	99542.76623 (24)	99542.76597 (19)	-0.00026
4	99791.32526 (25)	99791.32506 (15)	-0.00020
5	100098.26068 (24)	100098.26083 (17)	0.00016

tings in combination with the Q0 and Q1 lines of EF – X (0,0), the anchor levels are determined for the para and ortho series, respectively. Performing a similar procedure with Q2 through Q5, obtained directly from the DUV spectroscopy, an independent determination of the EF ($v = 0, J = 2-5$) rotational energy levels E_{DUV} is obtained. A comparison of E_{DUV} to energy levels derived from the FT combination differences (referenced to the EF anchor lines) E_{FT} is shown in Table 3.2. The difference $\Delta = E_{FT} - E_{DUV}$ falls within the stated 1σ uncertainty in E_{DUV}, where there is a considerable contribution due to the uncertainties in the ground state level energies. This comparison provides a strong verification of the accuracy of the separate (DUV- and FT-) data sets. Most importantly, this demonstrates the validity of the calculated values from the combination-difference method presented here.

3.5 Lyman and Werner transition wavelengths

From the large set of level energies of B $^1\Sigma_u^+, v, J$ and C $^1\Pi_u, v, J, (\pm)$ quantum states with respect to the X $^1\Sigma_g^+, v = 0, J = 0$ ground level, transition frequencies or wavelengths in the B – X Lyman and C – X Werner bands can then be calculated from the inter-combination differences, taking into account the uncertainties deriving from both experiments. The R- and P-transition wavelengths for the lowest ortho and para rotational states in the Lyman band are listed in Table 3.3, and a comprehensive list of the derived transitions is supplied in.[170]

For the Lyman lines an average relative uncertainty of $\Delta\lambda/\lambda = 4.6 \times 10^{-9}$ is obtained, while the average for the Werner lines is $\Delta\lambda/\lambda = 1.7 \times 10^{-8}$. The derived transition wavelengths, compared to those obtained from direct extreme ultraviolet XUV laser excitation,[100,171–173] are listed in Table 3.3. As these example transitions demonstrate, there is good agreement between the present set of transition values and previous values from direct XUV measurements. However, the XUV-data are subject to a systematic shift towards longer wavelengths at the 1σ level, with the L5–L8 bands having the largest discrepancies. We suspect that this may be attributed to some unaccounted systematic shifts in the direct XUV data set due to chirp effects in the pulsed-dye amplifier or in the harmonic conversion process in the Xenon nonlinear medium.[150]

If we consider only the 56 transitions (48 Lyman- and 8 Werner-lines) used in the recent $\Delta\mu/\mu$ analysis,[100] the new set of wavelengths represents a 21-fold improvement for the Lyman lines and a 7-fold improvement for the Werner lines. Where the previous set of data, obtained from direct XUV laser spectroscopy at an accuracy of $\Delta\lambda/\lambda \sim 5.4 \times 10^{-8}$ (Refs. 100,171–173) contributed for some 11% to the error budget in the $\Delta\mu/\mu$ analysis, the uncertainty contribution of the presently derived data set is only 1.7%, where half of this value is due to the 9 transitions that are outside the range of the present data set, where the XUV results are still used. Performing an identical analysis using the updated laboratory data yield $\Delta\mu/\mu = (2.74 \pm 0.59) \times 10^{-5}$.

3.6 Conclusion

In conclusion, we make available a laboratory data set of Lyman and Werner absorption bands in H_2, with a close-to-exact accuracy for the purpose of comparisons with high redshift astrophysical data, to extract a possible variation of the proton-to-electron mass ratio. The order-of-magnitude improvement in the laboratory metrology will reduce the uncertainty contribution of the laboratory data to less than 2%, and any improvement on the derivation of the $\Delta\mu/\mu$ will fully depend on astrophysical observations using current telescope technology. Now that a new generation of telescopes with 30-40 m dishes are in the design stage, the present data may add to the scientific rationale for equipping these systems with spectrometers of much higher resolution than the existing ones.

Table 3.3 – *Comparison of combination-difference derived transition wavelengths λ_{FT} and direct XUV determination λ_{XUV}* [100,171–173] *for the first transitions of the Lyman v = 0–10 bands, expressed in nm. The difference, $\Delta = \lambda_{\mathrm{XUV}} - \lambda_{\mathrm{FT}}$ is in 10^{-6} nm. A full list of the derived data set is provided in.* [170]

Line	λ_{FT}	λ_{XUV}	Δ
L0 R(0)	110.812 731 72 (16)	110.812 733 (7)	1.3
L0 P(1)	111.006 255 79 (28)	111.006 251 (6)	-4.8
L1 R(0)	109.219 519 99 (31)	109.219 523 (8)	3.0
L1 P(1)	109.405 195 65 (54)	109.405 198 (6)	2.4
L2 R(0)	107.713 865 76 (17)	107.713 874 (5)	8.2
L2 P(1)	107.892 540 43 (27)	107.892 547 (5)	6.6
L3 R(0)	106.288 206 97 (21)	106.288 214 (5)	7.0
L3 P(1)	106.460 532 74 (27)	106.460 539 (5)	6.3
L4 R(0)	104.936 738 53 (22)	104.936 744 (4)	5.5
L4 P(1)	105.103 245 71 (39)	105.103 253 (4)	7.3
L5 R(0)	103.654 567 53 (20)	103.654 581 (4)	13.5
L5 P(1)	103.815 704 53 (34)	103.815 713 (4)	8.5
L6 R(0)	102.437 374 37 (49)	102.437 386 (5)	11.6
L6 P(1)	102.593 518 51 (41)	102.593 535 (6)	16.3
L7 R(0)	101.281 294 56 (51)	101.281 303 (5)	8.4
L7 P(1)	101.432 716 35 (44)	101.432 724 (5)	7.6
L8 R(0)	100.182 374 21 (33)	100.182 387 (5)	12.8
L8 P(1)	100.329 650 33 (37)	100.329 662 (5)	11.7
L9 R(0)	99.137 884 96 (28)	99.137 891 (5)	6.0
L9 P(1)	99.280 962 53 (26)	99.280 968 (5)	5.5
L10 R(0)	98.143 871 05 (76)	98.143 871 (5)	0.1
L10 P(1)	98.283 529 70 (66)	98.283 533 (5)	3.3

Chapter 4

Determination of the ionization and dissociation energies of the hydrogen molecule[*]

The transition wave number from the EF $^1\Sigma_g^+(v=0,N=1)$ *energy level of ortho-*H_2 *to the* $54p1_1(0)$ *Rydberg state below the* $X^+\ ^2\Sigma_g^+(v^+=0,N^+=1)$ *ground state of ortho-*H_2^+ *has been measured to be* $25209.99756 \pm (0.00022)_{statistical} \pm (0.00007)_{systematic}$ cm^{-1}. *Combining this result with previous experimental and theoretical results for other energy level intervals, the ionization and dissociation energies of the hydrogen molecule have been determined to be* 124417.49113(37) cm^{-1} *and* 36118.06962(37) cm^{-1}, *respectively, which represents a precision improvement over previous experimental and theoretical results by more than one order of magnitude. The new value of the ionization energy can be regarded as the most precise and accurate experimental result of this quantity, whereas the dissociation energy is a hybrid experimental-theoretical determination.*

This chapter has been accepted for publication in the Journal of Chemical Physics (2009).

4.1 Introduction

The hydrogen molecule is an important system for testing molecular quantum mechanics. Both the ionization energy (E_i) and the dissociation energy (D_0) of H_2,

---

[*] The work presented in this chapter is a collaborative effort with the group of Prof. F. Merkt at the Laboratory for Physical Chemistry at the ETH Zürich, with an important contribution made by Dr. J. Liu.

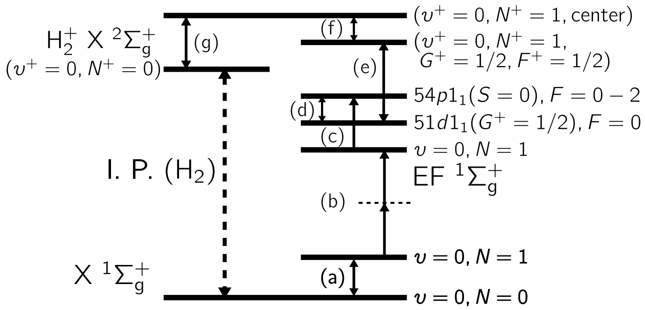

Figure 4.1 – *Energy level diagram and determination of $E_i(H_2)$. The energy separations are not drawn to scale, with corresponding numerical values given in Table 4.2. Intervals (b) and (c) represents the two-step excitation scheme used in the present experiment.*

related to each other by

$$E_\mathrm{i}(H_2) = D_0(H_2) + E_\mathrm{i}(H) - D_0(H_2^+), \tag{4.1}$$

are benchmark quantities for *ab initio* calculations. The comparison of the calculations and the measurements have played a fundamental role in the validation of molecular quantum mechanics and quantum chemistry, thereby elucidating the real nature of chemical bonds.[174] The precision of both quantities has been improved by more than an order of magnitude over the past three decades (Refs. 132,134 and references therein), and the latest experimental values[132,134] ($E_\mathrm{i}(\mathrm{H}_2)_\mathrm{exp}$=124417.476(12) cm^{-1} and $D_0(\mathrm{H}_2)_\mathrm{exp}$=36118.062(10) cm^{-1}) are compatible with the latest theoretical ones: $E_\mathrm{i}(\mathrm{H}_2)_\mathrm{th}$=124417.491 cm^{-1} and $D_0(\mathrm{H}_2)_\mathrm{th}$=36118.069 cm^{-1}.[27] A new measurement of either $E_\mathrm{i}(\mathrm{H}_2)$ or $D_0(\mathrm{H}_2)$ with improved precision would be highly desirable to test current and future theoretical calculations of either $E_\mathrm{i}(\mathrm{H}_2)$ or $D_0(\mathrm{H}_2)$.

In this chapter, we report on a new experimental determination of the ionization energy of ortho-H_2 as a sum of three energy intervals: the first between the $X\ ^1\Sigma_g^+(v = 0, N = 1)$ and the $EF\ ^1\Sigma_g^+(v = 0,\ N = 1)$ levels of ortho-H_2 (99109.73139(18) cm^{-1}),[163] the second between the $EF\ ^1\Sigma_g^+(v = 0,\ N = 1)$ and $54p$ Rydberg states belonging to series converging on the $X^+\ ^2\Sigma_g^+(v^+ = 0, N^+ = 1)$ level of ortho-H_2^+, and the third between the selected $54p1_1(0)$ Rydberg state and center of gravity of the $X^+\ ^2\Sigma_g^+(v^+ = 0, N^+ = 1)$ ionic level (37.50902(2) cm^{-1}).[143] We present here a measurement of the second energy interval, which, when combined with the other two, enables us to derive a more precise value of the ionization energy of ortho-H_2. The ionization energy $E_\mathrm{i}(\mathrm{H}_2)$ and the dissociation energy $D_0(\mathrm{H}_2)$ of para-H_2 can be derived by from this new measurement by including previous results of the ionization energy of the hydrogen atom,[175] the dissociation energy of H_2^+,[27] and the rotational energy level intervals for the lowest vibronic states of the neutral molecule and the cation.[31,32,169,176]

4.2 Experiment

The experiment was carried out using a two-step excitation scheme (represented as intervals (b) and (c) in Fig. 4.1). A pulsed supersonic beam of molecular hydrogen (2 bar stagnation pressure) was collimated by a 0.5-mm-diameter skimmer before it entered a differentially pumped (∼10^{-7} mbar) interaction region, where it was crossed at right angles by two laser beams. In the first step, H_2 was excited from the X $^1\Sigma_g^+(v = 0, N = 1)$ level to the EF $^1\Sigma_g^+(v = 0, N = 1)$ level in a nonresonant two-photon process using a UV laser (wavelength 202 nm, bandwidth ∼0.4 cm^{-1}, pulse length ∼10 ns, pulse energy ∼20 μJ). The UV radiation was generated by frequency upconversion of the output of a pulsed dye laser in two β-barium borate (BBO) crystals. The broad bandwidth served the purpose of exciting all Doppler components of the transition and so avoiding the systematic shift of the wave numbers of the transitions from the EF $^1\Sigma_g^+(v = 0, N = 1)$ state to the high Rydberg states that would result from selecting a subset of the hydrogen molecules with nonzero Doppler shifts. A possible residual effect caused by an asymmetric intensity profile across the Doppler lineshape would in any case cancel out when determining the transition frequencies as the average of two measurements carried out with counterpropagating beams (see below).

In the second step, H_2 was excited from the EF $^1\Sigma_g^+(v = 0, N = 1)$ level to the $54p$ Rydberg states using a second UV laser (wavelength 397 nm, bandwidth ∼20 MHz, pulse length ∼50 ns, pulse energy ∼40 μJ). The UV radiation for the second step was the second harmonic of the output of a pulsed titanium-doped sapphire (Ti:Sa) amplifier.[177,178] The single-mode output of a Ti:Sa cw ring laser was shaped into pulses by an acousto-optic modulator (AOM) and used as the seed source of the Ti:Sa amplifier. The 397 nm laser was delayed by 50 ns with respect to the 202 nm laser. To measure the Doppler shift resulting from the small nonorthogonality between the molecular hydrogen beam and the 397 nm laser beam, the 397 nm laser beam was split into two components by a 50% beamsplitter. A dichroic mirror was used to overlap one of the two components with the 202 nm laser, while the other was introduced into the interaction region in a counterpropagating configuration. The difference between the transition wave numbers measured by the

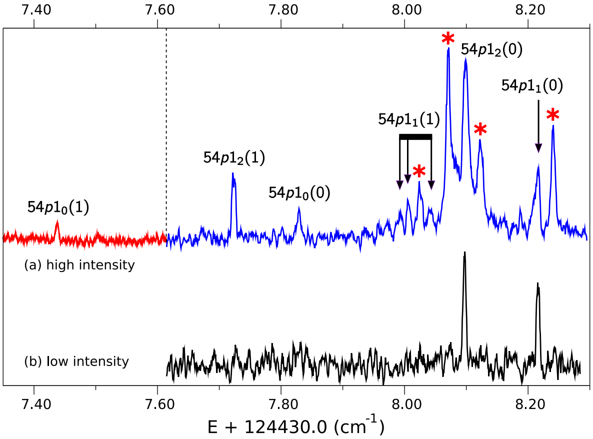

Figure 4.2 – *Field ionization spectra of H_2 in the region of transitions to the 54p Rydberg states with 397 nm laser pulse energy of 700 μJ (a) and 40 μJ (b). The vertical dashed line indicates the junction point of two different scans. The scan on the low wave number side was taken with smaller step size and more averaging for each data point to increase the signal-to-noise ratio. The wave numbers are given relative to the position of the X* $^1\Sigma_g^+(v=0, N=0)$ *ground state of para* H_2.

two components represents twice the Doppler shift, which can be eliminated by taking the average value of the two measurements. Both the 202 nm and 397 nm laser beams were slightly focused to a spot size of ~1 mm^2 in the interaction region. The molecules in Rydberg states created by the two-step excitation were ionized by applying a pulsed voltage delayed by 150 ns with respect to the 397 nm laser pulse across a set of seven resistively coupled metallic plates. H_2^+ was extracted by the same pulsed electric field and detected by a microchannel plate (MCP) detector. The experimental region was surrounded by a double layer of mu-metal magnetic shielding to eliminate stray magnetic fields.[179]

4.3 Results

The $54p1_1(0) \leftarrow EF\,^1\Sigma_g^+(v=0, N=1)$ transition

Fig. 4.2 shows two field ionization spectra of H_2 in the region of the transitions from the EF $^1\Sigma_g^+(v=0,\ N=1)$ level to the $54p$ Rydberg states, located below the $X^+\,^2\Sigma_g^+(v^+=0, N^+=1)$ ionic state, recorded with pulse energies of 700 μJ (panel a) and 40 μJ (panel b). The final states of these transitions are labelled using the notation $nlN_{\rm N}^{+}(S)$ where the quantum numbers have their usual meaning.[143] The wave numbers are given relative to the $X\ ^1\Sigma_g^+(v=0, N=0)$ ground state and correspond to the sum of the wave number intervals between the $N=0$ and $N=1$ rotational levels of the $X\ ^1\Sigma_g^+(v=0)$ ground state, 118.48684(10) cm^{-1},[169] between the $X\ ^1\Sigma_g^+(v=0, N=1)$ and the $EF\ ^1\Sigma_g^+(v=0,\ N=1)$ levels, 99109.73139(18) cm^{-1},[163] and between the $EF\ ^1\Sigma_g^+(v=0,\ N=1)$ level and the 54p Rydberg states. In the spectrum recorded at high laser power (Fig. 4.2a) more lines are observed than in that recorded at low power (Fig. 4.2b). The additional lines in Fig. 4.2a correspond to very weak transitions, for instance, transitions to triplet Rydberg levels. Most of the observed lines could be assigned by comparing with the results of MQDT calculations.[143] The assignment of the four lines marked by asterisks remains uncertain and requires further calculations. Only two lines are observed at low laser power. These two lines can be unambiguously assigned to the two allowed transitions to the $54p1_2(0)$ and $54p1_1(0)$ levels. For the present determination of the ionization energy of H_2, we chose to use the latter transition because the binding energy of the $54p1_1(0)$ level was determined with an absolute accuracy of ∼600 kHz in Ref 143.

For the calibration procedure, part of the output of the cw Ti:Sa laser was directed into an I_2 cell and through a high-finesse Fabry-Pérot (FP) étalon. The absolute frequency was calibrated by recording, simultaneously with each spectrum, the Doppler-free saturation absorption spectrum of I_2 using a 75-cm-long cell heated to 900 K.[163,180] The frequencies of the hyperfine components of the I_2 transitions were determined with an accuracy of better than 100 kHz by comparing with positions measured using a frequency comb[163] in a separate measurement. The H_2 spectra were linearized using the transmission signal through the FP étalon by cubic spline interpolation. The FP étalon was locked to a polarization-stabilized He-Ne laser and its free spectral range (FSR) was determined with an accuracy of 3 kHz using two iodine lines.

To compensate for a possible chirp or shift of the NIR pulse arising in the multipass amplification in the Ti:Sa crystals, we have carried out a measurement of the frequency evolution during the pulse by monitoring the beating of the pulsed amplified beam with the CW NIR output of the ring laser as explained in Ref. 177 and determining the optical phase evolution following the procedure described in Ref. 181. The measurement yielded a frequency shift of -4.76(60) MHz with no significant chirp during the pulse. We attribute this shift to an optical effect caused by the depletion of the excited state population by the NIR radiation. Numeri-

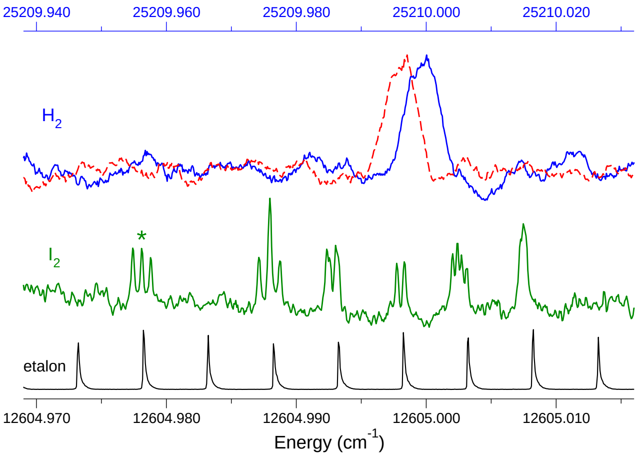

Figure 4.3 – *Spectrum showing the transition from the EF* $^1\Sigma_g^+(v = 0, N = 1)$ *level to the* $54p1_1(0)$ *level with the* I_2 *calibration and étalon traces. The* H_2 *spectra shows a pair of traces obtained from each of the counter-propagating laser beams. The position of the* a_2 *hyperfine component (*) of the P157, B – X(1-15) rovibronic transition was determined to be at* 377886781.37(10) *MHz using a frequency comb.*

cal modelling of the frequency characteristics of the pulse following the procedure discussed in Ref. 149 and using optical data on Ti:Sa crystals from Refs. 182,183 reproduced the observed shift (and the absence of a chirp) semiquantitatively. Indeed, our numerical simulation predicted a shift of about -3 MHz under our experimental conditions. The missing factor of about 1.6 could be explained by the uncertainty in the Nd:YAG pump fluence. The fact that we observed a frequency shift rather than a chirp under the present experimental conditions is attributed to the nearly constant rate of depopulation of the excited state by the NIR radiation. The constancy of this depopulation rate is itself a consequence of the moderate amplification per pass when a sufficiently low pump power is used.

The centers of the lines in the H_2 spectra were determined by fitting a Gaussian lineshape function to each transition. An example illustrating the calibration of the transition to the $54p1_1(0)$ level is shown in Fig. 4.3. Sixteen pairs of measurements were carried out on four different days, each pair consisting of two scans, one recorded with the 397 nm laser beam propagating parallel to, the other antiparallel to the 202 nm laser beam. The transition frequencies determined from these mea-

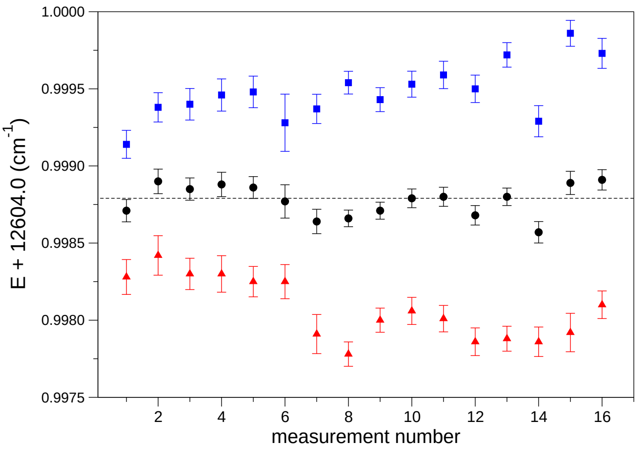

Figure 4.4 – *Distribution of the calibrated fundamental wave numbers for the transition to the* $54p1_1(0)$ *level. Triangles and squares are measurements with either of the two counterpropagating 397-nm laser beams. The filled circles are the average values of the measurement pairs, with the dashed line marking the position of the overall mean value* (12604.99880(10) *cm*$^{-1}$) *for this transition.*

surements are plotted with their uncertainties in Fig. 4.4, which also illustrates how the center frequency of the transition was obtained.

The frequency difference between the two scans of each pair amounted to ~2×50 MHz and the mean wave number of the transition to the $54p1_1(0)$ level was determined to be 2×12604.99880(10) cm^{-1}, where the number in parentheses represents one standard deviation in units of the last digit.

Additional corrections to the calibrated frequency listed above and the associated uncertainties had to be considered. (i) A possible frequency shift arising in the doubling crystal as a result of the Kerr effect[159] and/or a phase-mismatch in the crystal.[149,184] The shift resulting from these two effects under our experimental conditions (pulse length of ~70 ns, crystal length of 5 mm, and peak intensity in the NIR of 2.4×10^7 W/cm^2) is -1 kHz for the Kerr effect and less than ±350 kHz for the frequency shift caused by phase-mismatch, assuming the phase-mismatch Δk <0.3 mm^{-1} which corresponds to a 20% decrease of the conversion efficiency from its maximum value. (ii) The AC Stark shift induced by the 397 nm laser was determined by varying the laser pulse energies and extrapolating the transition frequencies. Because the 202 nm laser pulses preceded the 397 nm laser pulses, no AC Stark shift needed to be considered for this laser. (iii) The DC Stark shift resulting from residual stray electric fields was measured by applying different offset voltages to the metallic plates surrounding the photoionization region. The magnitude of the stray field and the DC Stark shift were deduced from the second-order polynomial fit of the frequency shift as a function of the offset voltages.[185,186] (iv) The pressure shift was estimated to be less than 0.1 MHz from the pressure-shift coefficient of Rydberg states of H_2 reported by Herzberg and Jungen[187] [5.7 ± 0.5 cm^{-1}/amagat (1 amagat=2.6867774(47) $\times 10^{19}$ cm^{-3})] and the local concentration ($\sim 10^{13}$ cm^{-3}) of the hydrogen molecules in the interaction region under the present experimental conditions. The uncertainties of the AC and DC Stark shifts and pressure shift were assumed to be half the absolute value, which represents a very conservative estimate. Other sources of errors and uncertainties related to the frequency calibration were also taken into account as indicated in Table 4.1. The wave number of the $54p1_1(0) \leftarrow EF\ ^1\Sigma_g^+(v = 0, N = 1)$ transition was determined to be $25209.99756 \pm (0.00022)_{\text{statistical}} \pm (0.00007)_{\text{systematic}}$ cm^{-1}, which represents the main experimental result of this article. This result includes the -10.4 MHz correction resulting from the systematic shifts listed in Table. 4.1. By adding the statistical and systematic errors, the result can be given as 25209.99756(29) cm^{-1}. The experimental precision is limited mainly by the statistical uncertainty in the determination of the centers of the H_2 lines and the systematic uncertainty in the frequency shift arising in the Ti:Sa amplifier.

The ionization energy of H_2

Fig. 4.1 illustrates the energy level diagram used in the determination of the ionization energies of ortho- and para-H_2. The numerical values of all relevant wave number intervals are listed in Table 4.2 and lead to a value of 124357.23797(36) cm^{-1} for the ionization energy of ortho-H_2. This value corresponds to the center of gravity of the hyperfine structure components of the $N^+ = 1$ level of H_2^+.[188] (Note that the hyperfine structure of the $N = 1$ level of both X and EF states is negligible.) The $54p1_1(0)$ level has three hyperfine components, separated by ~ 0.00011 cm^{-1} and ~ 0.00005 cm^{-1} as determined from the transition frequencies in Ref. 143, and were not resolved in the present experiment. Their mean value has been used in the present calculation, resulting in an uncertainty of much less than 0.0001 cm^{-1}. The three hyperfine components of the $X\ ^1\Sigma_g^+(v = 0, N = 1)$ level are split by less than 500 kHz;[189] the hyperfine splittings of the $EF\ ^1\Sigma_g^+(v = 0, N = 1)$ level are assumed to be equally small and thus negligible in the present analysis. The overall uncertainty in the ionization energy of ortho-H_2 is determined as quadrature summation of the uncertainties of all energy level intervals. Using the energy separations be-

Table 4.1 – *Error budget. Individual corrections and errors were determined for the frequency of the cw Ti:Sa laser and are thus multiplied by two.*

statistical uncertainties:	value (MHz)
uncertainty in the determination of the line centers:	
I_2 spectra	$\pm 0.36 \times 2$
H_2 spectra	$\pm 3.0 \times 2$
nonlinearity of the ring laser scans	$< \pm 1.1 \times 2$
residual Doppler shift	$< \pm 0.32 \times 2$
sum in quadrature	± 6.5

systematic shifts and uncertainties:	value (MHz)
error in linearization due to uncertainty of FSR	$\pm 0.012 \times 2$
uncertainty in the positions of the I_2 reference lines[163]	$< \pm 0.1 \times 2$
frequency shift in the Ti:Sa amplifier	$(-4.76 \pm 0.60) \times 2$
frequency shift in the doubling crystal	$< \pm 0.35$
AC Stark shift by the 397 nm laser	$(-1.27 \pm 0.64) \times 2$
DC Stark shift by the stray electric field	$(+0.77 \pm 0.39) \times 2$
pressure shift	$< +0.10 \pm 0.05$
sum in quadrature	-10.4 ± 2

tween $N = 0$ and $N = 1$ levels of the $X\ ^1\Sigma_g^+(v = 0)$ state of H_2[169] and that between $N^+ = 0$ and $N^+ = 1$ levels of the $X^+\ ^2\Sigma_g^+(v^+ = 0)$ state of H_2^+,[31,32,176] the ionization energy of para-H_2 is be determined to be 124417.49113(37) cm^{-1}.

The precision of the present value exceeds that of the latest theoretical results.[27] Our new result thus represents a test for future calculation of $E_i(H_2)$, and also of $D_0(H_2)$ in combination with precise values of $E_i(H)$ and $D_0(H_2^+)$ as is explained in more detail in the next subsection.

The dissociation energy of H_2

The relationship between the dissociation energy $D_0(H_2)$ and ionization energy $E_i(H_2)$ of molecular hydrogen (see Eq. 4.1) is depicted graphically in Fig. 4.5. As part of our procedure to obtain an improved value of $D_0(H_2)$ from our new exper-

Table 4.2 – *Energy level intervals and determination of the ionization energy of* H_2 *in* cm^{-1}.

	energy level interval	wave number (cm^{-1})	Ref.
(a)	$X\ ^1\Sigma_g^+(v=0,N=1)$—$X\ ^1\Sigma_g^+(v=0,N=0)$	118.48684(10)	169
(b)	$EF\ ^1\Sigma_g^+(v=0,N=1)$—$X\ ^1\Sigma_g^+(v=0,N=1)$	99109.73139(18)	163
(c)	$54p1_1(S=0,\mathrm{center})$—$EF\ ^1\Sigma_g^+(v=0,N=1)$	25209.99756(29)	this work
(d)	$54p1_1(S=0),F=1$—$51d1_1(G^+=1/2),F=0$	4.79180	143
(e)	$54p1_1(S=0),F=0$—$51d1_1(G^+=1/2),F=0$	4.79191	143
(e)	$54p1_1(S=0),F=2$—$51d1_1(G^+=1/2),F=0$	4.79196	143
(e)	$X^+\ ^2\Sigma_g^+(v^+=0,N^+=1,G^+=1/2),F^+=1/2$—$51d1_1(G^+=1/2),F=0$	42.270539(10)	143
(f)	$X^+\ ^2\Sigma_g^+(v^+=0,N^+=1,\mathrm{center})$—$X^+\ ^2\Sigma_g^+(v^+=0,N^+=1,G^+=1/2),F^+=1/2$	0.03037961	188
(g)	$X^+\ ^2\Sigma_g^+(v^+=0,N^+=1,\mathrm{center})$—$X^+\ ^2\Sigma_g^+(v^+=0,N^+=0)$	58.2336751(8)	31,32,176
$E_\mathrm{i}(\text{ortho-H}_2)$=(b)+(c)-(d)+(e)+(f)=124357.23797(36)			
$E_\mathrm{i}(\mathrm{H}_2)\equiv E_\mathrm{i}(\text{para-H}_2)$=(a) + $E_\mathrm{i}(\text{ortho-H}_2)$ - (g)=124417.49113(37)			

imental value for $E_{\mathrm{i}}(\mathrm{H}_2)$, we have reevaluated the ionization energy of atomic hydrogen $E_{\mathrm{i}}(\mathrm{H})$ and the dissociation energy of the hydrogen molecular cation $D_0(\mathrm{H}_2^+)$ using the most recent values of fundamental constants recommended by CODATA 2006,[14] i.e., $R_\infty = 109\,737.315\,685\,27(73)$ cm^{-1} for the Rydberg constant and $\mu = M_p/m_e = 1836.152\,672\,47(80)$ for the proton-to-electron mass ratio, and the global average for the fine structure constant $\alpha = 1/137.035\,999\,679\,082(45)$ including the results of the most recent measurements.[14–18,190,191] The uncertainties in the values of $E_{\mathrm{i}}(\mathrm{H})$ and $D_0(\mathrm{H}_2^+)$ make a negligible contribution to the final uncertainty of $D_0(\mathrm{H}_2)$, which is dominated by the experimental uncertainty of $E_{\mathrm{i}}(\mathrm{H}_2)$.

The atomic ionization energy $E_{\mathrm{i}}(\mathrm{H})$ is defined as the energy interval between the ionization limit and the atomic ground state $1\,^2\mathrm{S}_{1/2}$ without the effects of the hyperfine interactions.[175] The center-of-gravity of the hyperfine structure of the $1\,^2\mathrm{S}_{1/2}$ ground state of H lies $1\,065\,304.313\,8260(75)$ kHz ($= (3/4)\Delta_{\mathrm{hfs}}$) above the lowest ($F = 0$) hyperfine level. To obtain this value we have used the hyperfine splitting Δ_{hfs} reported in Ref. 12. The present method of determining the $E_{\mathrm{i}}(\mathrm{H})$ represents the inverse of the method used in the determination of the Rydberg constant from the spectroscopic measurements on atomic hydrogen as discussed by Biraben.[192] The atomic level energy is expressed as the sum of three terms:

$$E_{n,l,j} = E_{n,j}^{\mathrm{Dirac}} + E_n^{\mathrm{Recoil}} + L_{n,l,j} \tag{4.2}$$

The first term, $E_{n,j}^{\mathrm{Dirac}}$, is the Dirac energy eigenvalue for a particle with a reduced mass $m_r = m_e(1+m_e/M_p)^{-1}$. The second term, E_n^{Recoil}, is the first relativistic recoil correction associated with the finite mass of the proton. $L_{n,l,j}$ is the Lamb shift term accounting for all other additional corrections, including QED corrections, higher-order relativistic corrections and the effects resulting from the proton structure. The atomic level energy (relative to the ionization limit) obtained from the non-relativistic Schrödinger equation is:

$$E_n^{\mathrm{NR}} = -\frac{Z^2}{n^2} hcR_\infty \tag{4.3}$$

where Z is the charge number of the nucleus (1 in this case), and n is the principal quantum number. To account for the finite mass of the proton, the electron mass m_e is replaced by the reduced mass m_r, resulting in the Dirac eigenvalue with the reduced mass correction[14,175]

$$E_{n,j}^{\mathrm{Dirac}} = \left(\frac{m_r}{m_e}\right) E_n^{\mathrm{NR}} \left(1 - \left[1 + \left(\frac{Z\alpha}{n-\delta}\right)^2\right]^{-\frac{1}{2}}\right) \frac{2n^2}{(Z\alpha)^2} \tag{4.4}$$

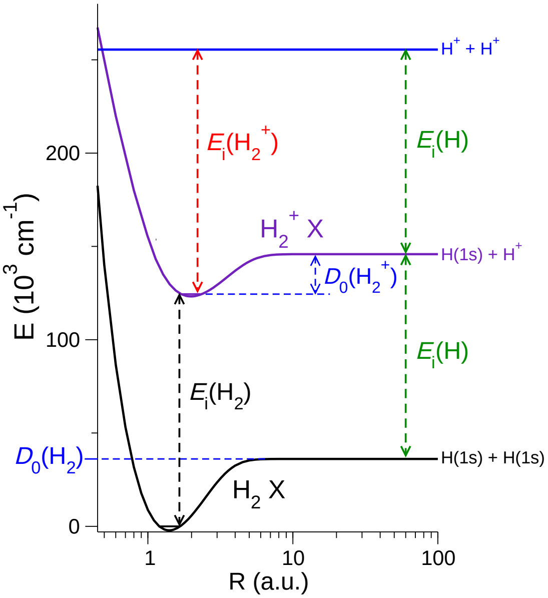

Figure 4.5 – *Potential energy diagram of the neutral molecular hydrogen and molecular ion electronic ground states, showing the relationship of the various ionization and dissociation energies.*

where $\delta = (j+1/2) - \sqrt{(j+1/2)^2 - (Z\alpha)^2}$. The first relativistic correction due to the proton recoil can be written as,[175,192]

$$E_n^{\mathrm{Recoil}} = E_n^{\mathrm{NR}} \frac{m_r^2}{m_e(m_e+M_p)} \left(\frac{Z\alpha}{2n}\right)^2 \tag{4.5}$$

All other higher-order relativistic recoil corrections (e.g. of the QED terms) are included in the Lamb shift term.

We have recalculated the Lamb shift corrections using the formulae detailed in CODATA 2006[14] and the values of fundamental constants mentioned above, and find the following contributions to the binding energy ($-E_\mathrm{i}(H)$) of the "hyperfine-less" $1\,^2\mathrm{S}_{1/2}$ ground state,

$$E_{1\mathrm{S}_{1/2}}^{\mathrm{Dirac}} = -\quad 109\,679.043\,564\,75(73) \quad \mathrm{cm}^{-1}, \tag{4.6}$$

$$E_{1\mathrm{S}_{1/2}}^{\mathrm{Recoil}} = -\quad 0.000\,794\,3407 \quad \mathrm{cm}^{-1}, \tag{4.7}$$

$$L_{1\mathrm{S}_{1/2}} = \quad 0.272\,616\,53(67) \quad \mathrm{cm}^{-1}, \tag{4.8}$$

where the uncertainty in the recoil term is on the order of 4×10^{-13} cm^{-1}, and thus entirely negligible. The uncertainty in the Lamb shift term is dominated by the uncertainty contributions of R_∞ and the proton charge radius. The updated atomic hydrogen ionization energy is thus

$$E_\mathrm{i}(\mathrm{H}) = 109\,678.771\,7426(10) \quad \mathrm{cm}^{-1} \tag{4.9}$$

The present value for E_i(H) is comparable with that of Wolniewicz (109 678.7717 cm^{-1}),[27] where no uncertainty was indicated. Wolniewicz used a recent value for R_∞, with an unspecified value, in order to correct (or rescale) the 1977 tabulated value of Erickson (109 678.773 704(3) cm^{-1}),[175] the uncertainty of which only includes the estimated uncertainty in the Lamb shift calculation but does not include the uncertainty of 8.3×10^{-3} cm^{-1} in the R_∞ value used.

The one-electron molecular ion H_2^+ is the simplest test system of the *ab initio* molecular quantum theory. In the non-relativistic approximation the level energies have been calculated to precisions of up to 10^{-30} hartrees (E_h).[28] Despite its simplicity, the three-body system represents a formidable problem which poses particular difficulties in accounting for relativistic and radiative corrections to the level energies. The dissociation energy $D_0(\mathrm{H}_2^+)$ is defined relative to the hyperfineless ground state ($v = 0, N = 0$) of the molecular ion H_2^+. We used the formulae developed by Korobov[31,32,176] to determine the H_2^+ ground state ($v = 0, N = 0$) energy relative to the onset of the dissociation continuum, which should result in a slight improvement over the calculations of Moss.[193] In these *ab initio* calculations, the level energies are determined relative to $E_\mathrm{i}(\mathrm{H}_2^+)$, the ionization energy of the molecular ion H_2^+. Included in the present reevaluation are the energy corrections comprising relativistic and radiative terms up to $\mathcal{O}(\alpha^5 R_\infty)$ from Refs. 31,32,176. We used the same values for the fundamental constants as in the reevaluation of E_i(H) descibed above, and obtained

$$E_\mathrm{i}(\mathrm{H}_2^+) = 131\,058.121\,975(49) \quad \mathrm{cm}^{-1} \tag{4.10}$$

The indicated uncertainty is not limited by the uncertainty contributions of the fundamental constants used, but by the fact that higher-order terms were neglected. The uncertainties obtained for molecular rovibrational transitions are much more accurate (see, e.g., Ref. 31), since contributions of the neglected terms are almost equal for different rovibrational states and therefore largely cancel.

Using the relation $E_\mathrm{i}(\mathrm{H}_2^+)$=$D_0(\mathrm{H}_2^+)$+$E_\mathrm{i}(\mathrm{H})$ (see 4.5), we obtain a value for the dissociation energy of the molecular ion,

$$D_0(\mathrm{H}_2^+) = 21\,379.350\,232(49) \quad \mathrm{cm}^{-1} \tag{4.11}$$

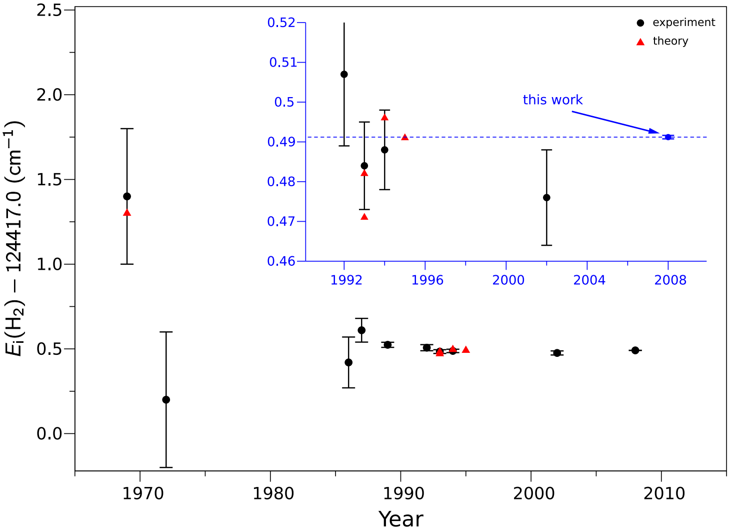

Figure 4.6 – *Values for the ionization energy of H_2 as determined in various studies or combinations thereof. The inset is an enlargement providing a better view of the evolution over the past 20 years.*

where the uncertainty of $E_i(H)$ makes a negligible contribution to the final uncertainty. The present value of $D_0(H_2^+)$ agrees well with that previously derived by Moss (21 379.3501(1) cm^{-1}).[193]

Using the calculated values for $E_i(H)$, $E_i(H_2^+)$, $D_0(H_2^+)$ and the experimental value of $E_i(H_2)$, we derive the dissociation limit of the neutral molecule $D_0(H_2)$ from either Eqs. 4.12 or 4.13,

$$\begin{aligned} D_0H_2) &= E_i(H_2) + D_0(H_2^+) - E_i(H) && (4.12)\\ &= E_i(H_2) + E_i(H_2^+) - 2 \times E_i(H) && (4.13)\\ &= 36\,118.069\,62(37) \quad \mathrm{cm}^{-1} && (4.14) \end{aligned}$$

The final uncertainty in $D_0(H_2)$ is entirely limited by the experimental uncertainty of the $E_i(H_2)$, and indeed we would have obtained the same value had we used the values of $D_0(H_2^+)$ and $E_i(H)$ reported in Refs. 27,175,193 rather than the updated values given in Eqs. 4.11 and 4.9.

The present value of the dissociation energy of $D_0(H_2)$ is consistent with, but more precise than, the result of the *ab initio* calculations of Wolniewicz[27] which

Table 4.3 – *$E_i(H_2)$ as determined in various experimental and theoretical studies or combinations thereof in cm^{-1}.*

year	experimental	theoretical	Ref.
1969	124418.4(4)		194
1969		124418.3	194
1972	124417.2(4)		187
1986	124417.51(22)		195
1987	124417.61(7)		137
1987	124417.42(15)		195, revised in 138
1987	124417.53(7)		137, revised in 138
1989	124417.524(15)		139
1990	124417.501(17)		135
1992	124417.507(18)		140
1993		124417.471	196
1993	124417.507(12)		139, revised in 141
1993	124417.484(17)		135, revised in 141
1993		124417.482	197
1994	124417.488(10)		198
1994		124417.496	129
1995		124417.491	27
2002	124417.476(12)		134
2008	124417.49113(37)		this work

yield $D_0(\mathrm{H}_2)_{\mathrm{th}} = 36118.069\ \mathrm{cm}^{-1}$, and the most recent experimental result of Zhang *et al.*[132] with $D_0(\mathrm{H}_2)_{\mathrm{exp}} = 36118.062(10)\ \mathrm{cm}^{-1}$.

4.4 Conclusions

Table 4.3 and Fig. 4.6 summarize the results of determinations, by various methods, of the ionization energy of para-H_2 over the past 40 years. Because of the relationship between the dissociation and ionization energies of H_2 (Eq. 4.1), the recommended value of the dissociation energy has evolved in a very similar manner. Earlier determinations of the dissociation energy have been summarized in Ref. 174. Compared to previous experimental values of the dissociation and ionization energies of H_2, the present values: $D_0(\mathrm{H}_2) = 36118.06962(37)\ \mathrm{cm}^{-1}$ and $E_{\mathrm{i}}(\mathrm{H}_2) = 124417.49113(37)$, are more precise by a factor of ~ 30.

As part of the procedure of determining the dissociation energy, we have attempted to reevaluate the ionization energy of H and the dissociation energy of H_2^+ using the latest values of the fundamental constants α, M_p/m_e, and R_∞. The main result in this reevaluation is that the current uncertainties in this quantities make a negligible contribution to the uncertainty of the dissociation energy of H_2, which is entirely determined by the uncertainty of the ionization energy of H_2.

Our new values of the ionization and dissociation energies of molecular hydrogen are in excellent agreement with the latest theoretical result, 124417.491 cm^{-1} for the ionization energy and 36118.069 cm^{-1} for the dissociation energy,[27] which included adiabatic, nonadiabatic, relativistic, and radiative corrections to the Born-Oppenheimer energies and are believed to be accurate to within 0.01 cm^{-1}. The new value of the ionization energy can be regarded as the most precise and accurate experimental result of this quantity, whereas the dissociation energy is a hybrid experimental-theoretical determination. Because of their higher precision, the present results represent an incentive to improve calculations of the ionization and dissociation energies beyond the current limits.

Acknowledgements

The authors thank Dr. H. Knöckel (Hannover) for providing us with the iodine cell and for elucidating discussions on frequency calibration issues. This work was financially supported by the Netherlands Foundation for Fundamental Research of Matter (FOM), the Swiss National Science Foundation under project No. 200020-116245, and Laserlab-Europe (RII3-CT-2003-506350).

Chapter 5

Frequency metrology on the Mg $3s^2\,{}^1S \rightarrow 3s4p\,{}^1P$ line for comparison with quasar data

We report a frequency metrology study on the Mg $3s^2\,{}^1S \rightarrow 3s4p\,{}^1P$ transition near 202.5 nm. For this purpose, the fourth harmonic of the output from an injection-seeded Ti:Sa pulsed laser is employed in a Mg atomic beam experiment with LIF-detection. Absolute frequency calibration with a frequency comb laser is performed on the CW-seeding radiation, while the chirp induced frequency shift between the pulsed output and the seed light is monitored on-line. The resulting transition frequency for the main isotope ^{24}Mg is determined at 49346.756809(35) cm^{-1}. This value is three orders of magnitude more precise than the best value in literature. The line positions of the other isotopes ^{25}Mg and ^{26}Mg are also measured at comparable accuracy, giving rise to very exact values for the isotopic shifts. The achieved precision for the transition frequency at 7×10^{-10} level, makes this second resonance line of Mg I an additional candidate for inclusion in many-multiplet methods, aimed at detecting a possible temporal variation of the fine structure constant α from comparison with quasar spectra. The isotopic shifts obtained are also important to correct for possible systematic shifts due to evolution of isotopic abundances, that may mimic α-variation effects.

This chapter is published as Physical Review A **74**, 012505 (2006).

5.1 Introduction

The recent findings[72] claiming a possible variation of the fine structure constant $\alpha = e^2/4\pi\epsilon_0\hbar c$ touch upon the very foundations of physics. In a recent analysis by Murphy et al.[76] combining data from 128 quasar absorption systems over redshift ranges of $0.2 < z_{abs} < 3.7$ show $\Delta\alpha/\alpha = (-0.543 \pm 0.116) \times 10^{-5}$, a result at the 5σ confidence level. Notwithstanding the detailed data reduction and error analysis[74] the findings of the Australian based group, using the Keck telescope for observations of quasars on the northern hemisphere, are disputed by other groups, using the Very Large Telescope of the European Southern Observatory, monitoring quasar absorption systems on the southern hemisphere.[85,86]

The method used to extract information on a possible variation of α, the many-multiplet (MM) method,[78] includes a number of atomic (and ionic) fine-structure splittings in a comparison between quasar and zero-redshift absorption features. The method requires extensive first principles atomic-structure calculations of relativistic corrections to level energies, resulting in characteristic q-factors for each atomic transition that represent the sensitivity for a certain spectral line to depend on a variation of α. The q-factors for a number of atomic and ionic spectral lines including magnesium have been calculated.[79] For the transition frequencies at $z = 0$ the most accurate literature values are used in the comparisons, but for many lines the uncertainties in the laboratory spectra are equally large, or even larger, than those of the quasar features. Recently Berengut *et al.*[80] have produced a list of lines that could be implemented in the MM-method to improve constraints on variation of α, if improved laboratory data would become available. The $3s^2\,{}^1S \rightarrow 3s4p\,{}^1P$ transition in Mg I was identified as one that needed a more accurate rest-frame frequency determination.

In addition, because isotope abundances in the early universe and at distant locations in space may differ from those on Earth, accurate measurements of isotope shifts are required to quantify systematic effects and to prevent varying isotope abundances from mimicking variations of α. In particular for magnesium, contributing several lines to the MM-methods with large isotopic shifts, there exists an ongoing dispute on the isotopic evolution of the abundance ratio and its consequences for variations of α.[199–201] For these reasons a renewed interest has arisen in the determination of isotope shifts through refined *a*b initio calculations.[202,203]

In view of the need for improved spectral data the Mg I $3s^2\,{}^1S \rightarrow 3s4p\,{}^1P$ spectral line near 202 nm is reinvestigated. The most accurate determination of the transition frequency for this second resonance line in the singlet system of magnesium dates back to the classical study of Risberg.[204] While the $3s^2\,{}^1S \rightarrow 3s3p\,{}^1P$ first resonance line has been the subject of many high resolution investigations, focusing on the absolute transition frequency,[205,206] the isotope shift,[207–209] and even the hyperfine structure of ^{25}Mg,[210] such detailed studies have not been performed for the 4p level.

In the present experimental investigation, a pulsed laser source, tunable near 202 nm, is used for exciting the $3s^2\,{}^1S \rightarrow 3s4p\,{}^1P$ in Mg. This approach, with the unavoidable intrinsic broadening due to the pulse structure of the light source, is chosen because of the difficulty in producing radiation in the deep-UV via nonlinear conversion with continuous-wave lasers. Using a novel-design pulsed titanium:sapphire (Ti:Sa) oscillator in the near infrared range, three stages of nonlinear conversion are required to attain deep-UV wavelengths.[145] The frequency metrology using a home-built frequency comb laser setup[147,211] is performed on the output of the continuous-wave (CW) laser, which also seeds the oscillator cavity of the pulsed laser system. As is known from pulsed-dye laser systems, frequency excursions during the temporal pulse evolution (known as frequency chirp) may cause a net shift between the center frequency of the pulse and the CW-frequency seeding the pulsed amplifier.[148–150] For the calibration of the singlet 3s4p level in Mg extensive measurements on these chirp effects were performed. It turned out that they are a limiting factor to the attainable accuracy in the transition frequency.

5.2 Experimental setup and procedures

Mg atomic beam setup

Fig. 5.1 depicts the term levels of the singlet system in Mg which are relevant for the excitation and detection scheme used in the present study. The excited 3s4p state has a lifetime of 14 ns[212] and decays back to the ground state via three channels. While the resonant decay has a branching ratio[213] of ≈ 85 %, both of the remaining two channels — 2 % via 3s4s, 13 % via 3s3d — decay to the 3s3p level that eventually emits 285 nm light upon relaxation to the ground state. This allows for off-resonant fluorescence detection at 285 nm with the advantage of efficient filtering of the 202 nm background with a Schott UG5 color filter.

A schematic of the atomic beam apparatus including the laser excitation and laser-induced fluorescence (LIF) detection zone is shown in Fig. 5.2. Magnesium pellets are heated in an oven to about 700 K producing an effusive atomic beam that is collimated downstream by two skimmers (S1: 0.5 mm diameter and S2: 2 mm diameter) to reduce the transversal velocity spread. The line broadening due to the transversal velocity spread of the skimmed atomic beam is about 20 MHz.

Any deviation from perpendicular alignment of the atomic and laser beams will result in a Doppler shift. To address this issue, the laser beam is split into two paths and then aligned such that the laser beams are counterpropagating collinearly as they cross the atomic beam. As long as the two laser beams are exactly counterpropagating, the first-order Doppler shifts in both beams will be of opposite signs and the unshifted line position can be obtained by taking the average of the line

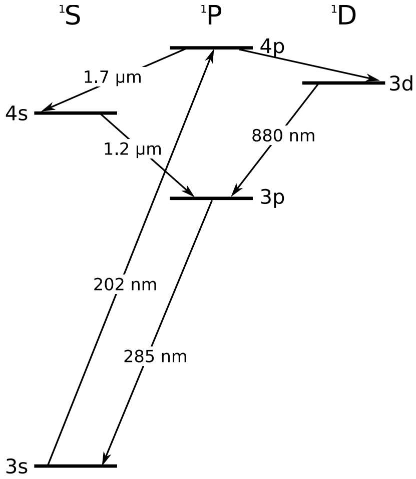

Figure 5.1 – *Term level scheme of the singlet system of Mg showing the excitation and decay channels of the 3s4p ^{1}P level investigated. The laser excitation is at 202 nm and the 285 nm fluorescence from the 3s3p to the ground state is monitored in the experiment.*

positions resulting from either laser path. The burden of establishing perpendicular atomic and laser beam alignment is then transposed to ensuring that the counter-propagating laser beams are perfectly aligned. However, it should be noted, that the laser beams are aligned preferably perpendicularly to the atomic beam in order to achieve maximum signal to noise ratio.

An interferometric alignment technique is employed in order to align the counterpropagating beams to less than $\delta = 0.1$ mrad misalignment, which corresponds to a Doppler shift of about 350 kHz in the deep-UV. As shown in Fig. 5.2, the excitation laser beam is split into two paths and then recombined to form a Sagnac interferometer. Special care was taken to ensure that the distances between beam splitter and interaction region are equally long for both light branches and that the two arms are of comparable intensity. Moreover the light is collimated with a beam diameter of about 1 mm at the interaction region. The advantage of the Sagnac setup is its robustness against acoustic disturbances which modulate the arm length of the interferometer. Since those disturbances affect both counter-propagating light beams in the same way, the path difference and likewise the interference pattern remains unchanged. In fact the interference pattern is predominantly influenced by the angle δ between the two contributing arms. When δ is lowered to zero the in-

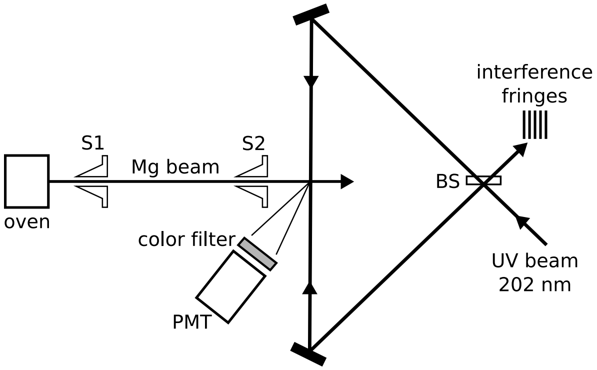

Figure 5.2 – *Experimental arrangement of the off-resonance laser-induced fluorescence detection using a collimated Mg atomic beam. The excitation laser beam is split and the two paths are aligned to be perfectly counterpropagating, making use of the Sagnac-interferometer configuration. S1 and S2 – skimmers; BS – beam splitter; PMT – photomultiplier tube.*

terference will show a dark fringe, which is especially useful as a sensitive alignment technique. In a two beam interference pattern the relation between fringe periodic distance L and the angular misalignment θ of the two interfering beams is given by:

$$\frac{\lambda}{L} = \sin\theta \approx \theta = 2\delta. \tag{5.1}$$

Geometric consideration shows that an angular mismatch δ between the counterpropagating beams within the Sagnac interferometer will lead to an angle $\theta = 2\delta$ on the screen. The attainable accuracy for the angular alignment is restricted by the beam diameter, because it determines the spot size on the screen and likewise the maximum resolvable fringe period L. Identifying the fringe period L with the beam diameter $d = 1\,\text{mm}$ yields the aforementioned possible misalignment of $\delta = 0.1\,\text{mrad}$. Since the interferometer alignment does not drift from dark fringe to the first order fringe pattern showing up on the screen the accuracy for δ is actually better. Still this uncertainty level is kept as a conservative measure. A more detailed discussion of the interferometric alignment to eliminate first-order Doppler shifts is given in Ref. 165.

The deep-UV laser source

A schematic representation of the laser system and frequency metrology setup is shown in Fig. 5.3. The UV laser source has been described in some detail before.[145]

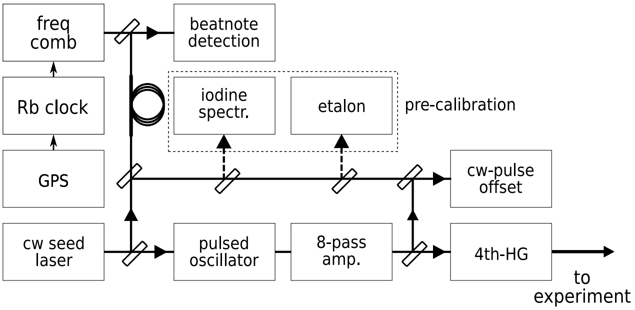

Figure 5.3 – *Schematic representation of the experiment. The amplified output of a Ti:Sa pulsed oscillator is upconverted to the 4th harmonic, and the resulting 202.5 nm light is used in the atomic beam setup as depicted in Fig. 5.2. The CW–pulse frequency offset is monitored throughout the measurement. The frequency of the CW Ti:Sa seed radiation is measured with a fs-frequency comb, which is referenced to a Rb-frequency standard with GPS time correction. A pre-calibration with an I_2 saturation set-up is performed to determine the correct mode of the frequency comb.*

The system consists of a Ti:Sa pulsed oscillator that is injection-seeded with light from a CW Ti:Sa ring laser and is actively locked using the Hänsch-Couillaud (HC) scheme. The pulsed oscillator produces Fourier-limited pulses of 20 MHz linewidth centered at the CW-seed wavelength of about 810 nm, with a typical pulse energy of 0.1 mJ. The pulses are subsequently sent through an 8-pass amplification stage to enhance the pulse energy to about 8 mJ. In order to produce the fourth harmonic at 202.5 nm, three consecutive nonlinear upconversion stages — BBO crystals cut at appropriate type-I phase matching angles — are used.[145] The resulting radiation near 202.5 nm has a repetition rate of 10 Hz, bandwidth 40 MHz, and a typical pulse length of about 15 ns. The pulse energy of the excitation laser beam can be chosen by varying the pump power sent to the multi-pass amplifier. The laser system reaches maximum output energies of 0.2 mJ/pulse at the 4th harmonic. However, in order to reduce saturation effects typical pulse energies of not more than 0.1 μJ were applied, corresponding to an intensity of about 1 kW/cm^2 at the interaction zone. Observed linewidths were about 50 MHz, which corresponds to the width one expects when convoluting the laser linewidth, the residual Doppler broadening and the natural linewidth of the $3s^2\,{}^1S \rightarrow 3s4p\,{}^1P$ transition.

Since the absolute frequency calibration is performed on the CW Ti:Sa seeding radiation, it is necessary to assess the possible frequency difference between the pulsed output and the injected seeding light. Such frequency offsets might be caused by frequency excursions during the temporal pulse evolution (chirp) due to the intensity-dependent refraction index of the lasing medium [148–150] and by dynamical mode-pulling effects in the pulsed oscillator resonator. In order to address both effects, strategies were followed recently explored by White *et al.*[151,152] for determining chirp phenomena in an injection-seeded and pulsed optical parametric oscillator. A more extensive description of the CW – pulse frequency offset characterization is given in Chap. 2 (or Ref. 163).

It is possible to adjust the CW – pulse offset and set it close to zero by changing parameters of the pulsed oscillator HC-lock. The frequency chirp is minimized by lowering the pump power to the pulsed oscillator. Typically, the CW – pulse frequency offset is centered around zero and has a standard deviation of less than 0.5 MHz, for the entire duration of the measurement. During the spectroscopic scans a multitude of data from each single pulse is registered. We use a single oscilloscope to measure the LIF signal, the UV power, and the net CW – pulsed frequency difference from each laser pulse acquired. This correlated acquisition technique allows for data filtering in the analysis procedure. Thus it is possible to use the power fluctuations of the UV-laser output, simply by taking many data points during one scan. The acquired data is subsequently binned with respect to the UV pulse intensity. By this means possible excitation intensity dependent line shifts can be assessed during the scans.

Absolute calibration procedures

The absolute calibration is performed on the CW seeding light from the Ti:Sa ring laser. Part of the CW seed light is coupled through a 100 m single-mode optical fiber towards the lab where a frequency comb reference laser [147] is located. The CW-light is heterodyned with the output of this frequency comb and the radio-frequency beat-note is detected in a spectrometer setup using an avalanche photodiode (PD). Typically, the beat-note detection reached a s/n of 45 db. The two main parameters of the frequency comb are its carrier-envelope phase offset frequency ν_{ceo} and its repetition rate ν_{rep}. Both are locked to a Rubidium-clock standard, which is further referenced to the synchronization signal of the global positioning system (GPS). From the locking characteristics, and from the fact that a scan over one isotopic line takes about two minutes the precision of the calibration with the frequency comb is estimated to be better than 25 kHz — which corresponds to an accuracy of $<$ 100 kHz in the deep-UV.

An absolute calibration with a frequency comb requires the frequency to be known in advance within a fraction of the frequency spacing of neighboring modes in the comb, which is equal to the repetition rate of the laser ($\nu_{\text{rep}} \approx 75\,\text{MHz}$). Since the $3s^2\,{}^1S \rightarrow 3s4p\,{}^1P$ transition frequency is only known[204] within $0.07\,\mathrm{cm}^{-1}$, a precalibration procedure is required. For that purpose, part of the CW seeding light is used to perform iodine saturation spectroscopy in a setup developed by the Hannover group[180] specially suited for the near-infrared wavelength region. It consists of an iodine cell which is heated to about 900 K in order to populate high rovibrational levels in the $X\,{}^1\Sigma^+_g$ ground state of I_2. For reducing the pressure in the cell, it has a cold finger extension which is temperature stabilized at room temperature. After the precalibration the transition frequency of the Mg $3s^2\,{}^1S \rightarrow 3s4p\,{}^1P$ line is known to a 10 MHz level of accuracy, which is sufficient for the final calibration using the frequency comb.

Measurement procedures

Since the frequency comb laser is situated in a different laboratory, the data acquisition and scan control software is divided on two separate PCs which are linked via TCP/IP on a 100 Mbit/s ethernet connection. (A more detailed discussion is given in Chap. 2 (or Ref. 163).) In short, the PC in the spectroscopy lab runs the actual laser scan and acquires and stores all retrieved data. On each scan step it sends a beatnote count request to the PC which controls the frequency comb, and receives the essential data from the frequency comb: the repetition rate ν_{rep}, the carrier envelope offset frequency ν_{ceo}, and the measured beatnote frequency ν_{bn} between frequency comb and CW-seed light.

The experimental procedure is as follows: The seed laser is tuned stepwise in frequency with an external control voltage provided by an arbitrary waveform generator (Agilent AWG 33250A). Each scan is about 200 MHz wide (in the deep-UV) and consists of about 300 equidistant voltage steps. While the CW-laser frequency is scanned the beatnote between frequency comb and CW-light changes likewise. In order to keep the beatnote frequency within a range of (21.7 ± 2) MHz — which is the working range of a frequency band pass filter in the electronic beatnote frequency counting circuitry — the repetition rate of the frequency comb is adjusted after each scan step, so that the frequency components of the comb spectrum follow the seed light scan.[163] At each scan step the acquisition software obtains the relative UV-power, the CW – pulse frequency offset, and the LIF signal of 10 laser shots. At the same time the computer which controls the frequency comb counts the beatnote frequency 10 times per scan step within time gates of 0.1 s for each individual count. From those 10 frequency counts the average value is used for the calibration, while the standard deviation is a measure for the short term frequency jitter of the seed laser, which is about 1 MHz.

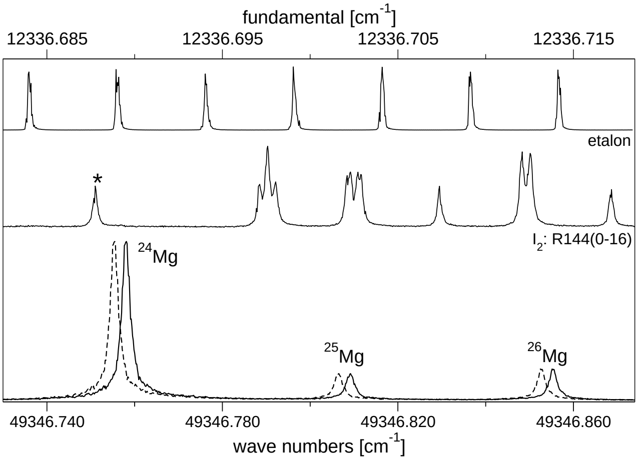

Figure 5.4 – *The 3s^2 ^{1}S → 3s4p ^{1}P Mg spectrum showing the isotope splittings. A fraction of the seeding radiation at the fundamental wavelength is used to record the I_2 saturation signal and etalon markers (150 MHz-FSR) for pre-calibration. The Mg spectrum obtained for the counter-propagating laser beam is drawn with a dashed curve. The t-hyperfine component of the R144 line in the B – X (0-16) band, predicted*[155] *at 12336.68774 cm^{-1}, is marked by an asterisk.*

5.3 Results

The Mg spectrum with the I_2 calibration line and the etalon markers are shown in Fig. 6.1. The spectrum obtained from the counter-propagating beam is also indicated in the same figure. The angle between the light beam and the atomic beam was purposely misaligned from the near-perpendicular orientation to demonstrate a clear separation of the line centers obtained from either light beam paths. For the subsequent calibrations using the frequency comb, the light beams were aligned back to the perpendicular setting. The positions of the hyperfine components of the I_2 R144 (0-16) rovibrational line of the B – X transition used for the calibration were taken from the prediction software developed by the Hannover group.[155] The CW – pulse offset was set to be around zero throughout the measurements.

First calibration scans on the most abundant isotope ^{24}Mg were performed. In order to obtain a Doppler-free frequency value for the 3s^2 ^{1}S → 3s4p ^{1}P transition, the Sagnac interferometer is first aligned until dark fringe is achieved. Then for each of the two light branches of the interferometer two scans are performed — one by tuning the laser from lower to higher frequencies and another scan with opposite

Table 5.1 – *The line positions of the Magnesium isotopes for the $3s^2\,{}^1S \rightarrow 3s4p\,{}^1P$ transition. The isotopic shifts obtained from the experiment are compared to ab initio calculations by Berengut et al.*[203] *The given uncertainty intervals for the experimental values represent the final uncertainties as listed in Table 6.2.*

isotope	position (cm^{-1})	shift from ^{24}Mg (MHz) exp	shift from ^{24}Mg (MHz) calc[203]
^{24}Mg	49346.756809(35)	–	–
^{25}Mg	49346.807724(40)	1526.4(1.2)	1530(50)
^{26}Mg	49346.854173(40)	2918.9(1.2)	2950(50)

tuning direction. For each of the four scans, a center line position is obtained by nonlinear least square fitting. Their arithmetic average gives the final transition frequency.

In order to check the reproducibility of the calibration the full procedure has been repeated 5 times. After each of the four-scan measurements not only the Sagnac dark fringe was realigned, but also the phase-matching of the upconverting nonlinear crystals has been checked and optimized. Hence possible systematic frequency shifts, as a result of imperfectly aligned phase-matching angles or Sagnac dark fringe acquire a statistical characteristic. Additionally, the relative UV excitation intensity has been changed by one order of magnitude, without showing any significant effect on the calibrated line position. In Table 5.1 the average value of the 5 calibrations is given. The contributions to the uncertainty budget are discussed below.

For the ^{25}Mg and ^{26}Mg isotopes two complete scan sets consisting of 4 scans each were registered. The obtained frequencies are also given in Table 5.1. Additionally, since the isotopic shifts can be obtained from relative measurements, after performing one complete scan set on ^{24}Mg the Sagnac interferometer was not realigned. Instead the seed laser was directly tuned to the other isotopic lines where spectroscopic scans were performed and frequency differences obtained by comparing the line positions from a single interferometer arm only. The line positions for the less abundant isotopes given in Table 5.1 result from combined averaging of the two absolute calibrations and a number of relative measurements. The slightly larger uncertainties are due to the lower signal to noise ratio on the LIF signal of the weaker isotopes.

The scans on ^{25}Mg did not give significantly different measured linewidths compared to the even isotopes, which points to the fact that a possible hyperfine splitting on the odd isotope is very small. *A*b initio calculations of the hyperfine constant *A*

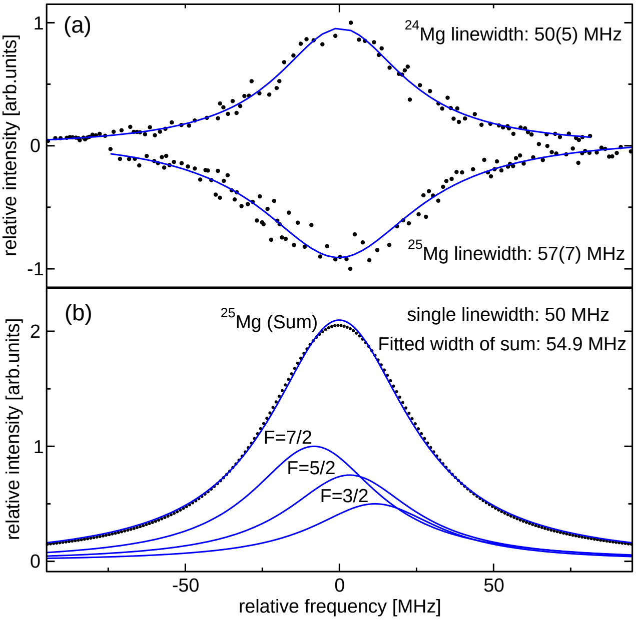

Figure 5.5 – *(Color online) Comparison of the observed lineshapes of the main* ^{24}Mg *isotope and the odd* ^{25}Mg *isotope (a). In the lower part (b) the three single hyperfine contributions with a linewidth as found on the main isotope (50 MHz) are separately depicted. The calculated sum of the three overlapping features is also shown as dotted curve and a fit against the result is performed and depicted as solid line. Even though the hyperfine splitting between the F=7/2 and F=3/2 is about 20 MHz, the linewidth of the sum is only marginally larger than a single peak linewidth.*

for the 3s4p ^{1}P state yield a value of $A = -3.3\,\text{MHz}$,[214] which would lead to the hyperfine levels $\Delta E_{\text{hfs}} = (-8.25, 3.3, 11.55)\,\text{MHz}$ for $F = (7/2, 5/2, 3/2)$. With an observed linewidth of 50 MHz for the main ^{24}Mg isotope — which is the convoluted linewidth of the instrumental width and the natural linewidth of the $3s^2\,{}^1S \rightarrow 3s4p\,{}^1P$ transition — it is impossible to resolve such a hyperfine structure, which is in agreement with the experiment.

In order to assess a possible line broadening for the observed ^{25}Mg lineshape as a result of the calculated hyperfine splitting, a superposition of the three hyperfine lines is simulated using the observed linewidth of the ^{24}Mg isotope (see Fig. 5.5). In the upper part (a) of the figure, averaged data is shown as dots for the main ^{24}Mg and the ^{25}Mg isotope. Each dot represents an average of 4 pulses on the ^{24}Mg data and of 7 pulses on the ^{25}Mg data. The solid curves depict fitted Lorentzian lines. The

Table 5.2 – *Error budgets on the absolute calibration given in kHz at the deep-UV energy scale. The total confidence interval is obtained by taking the quadrature sum of the errors* $i - vi$ *and linear summation of the result with the errors* v–vii. *Errors* iii *and* iv *represent the* 1σ-*uncertainties of the nonlinear least square fit.*

	Error	kHz
i	1st order Doppler	350
ii	frequency comb	< 100
iii	fit error ^{24}Mg	200
iv	fit error ^{25}Mg,^{26}Mg	450
v	ac-Stark	100
vi	CW - pulse offset	500
vii	2nd order Doppler	8
	total ^{24}Mg	1050
	total ^{25}Mg,^{26}Mg	1200

given linewidths in part (a) of the figure represent average values from a multitude of spectroscopic scans. There is no significant difference in the observed lineshapes of the ^{24}Mg and the ^{25}Mg isotopes as the small suggested difference can be explained by noise broadening — the observed linewidth of ^{26}Mg is 60(9) MHz. Figure 5.5(b) shows the three simulated hyperfine lines (Lorentzian shape) which are intensity weighted by their multiplicities. The sum of the hyperfine lines is depicted as a dotted curve, which is fitted by another Lorentzian curve shown as solid line. Even though the hyperfine splitting between $F = 7/2$ and $F = 3/2$ is about 20 MHz the resulting superposition gives only a small additional line broadening by about 5 MHz, which would not be visible in our experiment. It should be noted that the line center of the fitted curve in Figure 5.5(b) is found exactly on the center-of-gravity of the simulated hyperfine structure. We conclude that the calculated hyperfine splitting constant $A = -3.3$ MHz fits well within our observed linewidth.

The contributions to the experimental error budget are listed in Table 6.2. The table is split into two parts. Since the errors i–iv have statistical characteristics and are not related, quadrature summation is applied on them. It should be noted that error iv is only relevant for the isotopic shifts. The errors v and vi are of systematic character and estimated as maximum possible deviations. Error vii (second order Doppler) is also systematic, but very small and can be neglected. For the total error budget the quadrature sum over errors i - iv has been added to the linear summation of errors v and vi. It represents a final uncertainty for the resulting values for the absolute calibration and isotopic shifts.

As discussed earlier for the 1st order Doppler error (position i in Table 6.2) a conservative budget is given. In practice it turns out that the dark fringe alignment is quite stable and does not drift to a bright interference maximum during the measurements. Moreover the persistent realignment of the Sagnac interferometer for each measurement procedure turns this possible systematic error into a statistical one, and can hence be reduced when taking more spectroscopic scans. The actual experimental spread ($1\,\sigma$) for the ^{24}Mg linecenter frequencies is 510 kHz and about 600 kHz for the isotopic shifts, which is well below the given total error bars in Table 6.2. The ac-Stark effect was too weak to be measured at the power levels used in a range 0.03 – 0.3 μJ/pulse. We estimate an upper limit to the ac-Stark shift based on the obtained statistics. For a more elaborate treatment of the CW – pulse frequency deviations as a result of chirp, we refer to Hannemann *et al.*[163] The frequency comb measurements result in line positions which are about 15 times more accurate compared to the I_2 pre-calibration procedure.

The final value for the transition frequency of the $3s^2\,{}^1S \rightarrow 3s4p\,{}^1P$ line entails an improvement of about 3 orders of magnitude from the results of classical spectroscopy by Risberg.[204] To our knowledge, the present experiment is the first to resolve the isotopic shifts for this transition. The precision of the isotopic shifts is comparable to those obtained by Hallstadius[207] for the $3s^2 \rightarrow 3s3p$ transition. We also tabulate the calculated isotopic shift using the parameters from Berengut *et al.*[203] The comparison shows very good agreement between the experimental and the theoretical results.

It should be noted that the red shifted quasar absorption spectra do not resolve the isotopic structure of the $3s^2\,{}^1S \rightarrow 3s4p\,{}^1P$ line. Instead the resolution is given[76] as FWHM $\approx$ 6.6 km/s which corresponds to 33 GHz at 202 nm. Using our results and the natural isotopic abundances on Earth as found in Rosman *et al.*[215] — ^{24}Mg: 78.99(4) %, ^{25}Mg: 10.00(1) %, ^{26}Mg: 11.01(3) % — a merged line is simulated using the three isotopic lines each having a FWHM of 33 GHz. The resulting line center is found at 49346.77252(7) cm^{-1}. This value, folded over the isotopic components, agrees within the 1σ uncertainty limit with the value reported by Risberg: 49346.729(70) cm^{-1}. During the review of this paper we learned about another spectroscopic study of the $3s^2\,{}^1S \rightarrow 3s4p\,{}^1P$ transition in Mg I. Aldenius *et al.*[216] measured 49346.771(3) cm^{-1} based on Fourier-transform spectroscopy in which the isotopic components are not resolved. This value is a factor of 20 more accurate than the value of Risberg, and is in perfect agreement (within 1σ limits) with the present value of the folded line.

5.4 Conclusion

We have performed an accurate determination of the $3s^2\,{}^1S \rightarrow 3s4p\,{}^1P$ transition frequencies of the three Magnesium isotopes — ^{24}Mg, ^{25}Mg and ^{26}Mg. This investigation is motivated by current studies on the absorption spectra of extragalactic gas clouds at high redshift to probe a possible variation of the fine-structure constant α. With the frequency determination at the level of 7×10^{-10}, the Mg $3s^2\,{}^1S \rightarrow 3s4p\,{}^1P$ line may represent a welcome addition to the set of transitions used in the many-multiplet analysis in the search for a variation of α.

The isotope shift obtained at an 1 MHz accuracy should be helpful in assessing systematic effects that imitate an α-variation due to the possible evolution of isotopic abundance.[200] For example, when taking the possible change in α as:

$$\frac{\Delta\alpha}{\alpha} = (-0.543 \pm 0.116) \times 10^{-5} \tag{5.2}$$

from Kozlov *et al.*[200] and $q = 87\,\mathrm{cm}^{-1}$ for the $3s^2\,{}^1S \rightarrow 3s4p\,{}^1P$ transition in Mg as given in Berengut *et al.*,[80] the transition frequency ν_{Mg} (unresolved for the isotopic contributions) should have been different by

$$\Delta\nu_{\mathrm{Mg}} \;=\; 2q\frac{\Delta\alpha}{\alpha} = -28.3(6.1)\,\mathrm{MHz} \tag{5.3}$$

10^{10} years ago. With the isotopic shift obtained from this experiment a comparable change in ν_{Mg} could be mimicked by a 1% different abundance of ^{24}Mg in the isotopic composition of the magnesium used in the lab and existing at the point in space-time, where the quasar absorption spectra were imprinted.

In addition, the values of the isotopic shifts for this transition are found to be in good agreement with the *a*b initio calculations of Berengut *et al.*[203] It is reassuring that the theoretical predictions are in such good agreement, since the sensitivity coefficients q for possible variations of α (Refs, 78,79) are calculated within the same framework.

Acknowledgment

We thank Dr. H. Knöckel (Hannover) for providing us with the I_2-cell for near-IR saturation spectroscopy, Dr. L. Veseth (Oslo) for calculating the hyperfine constant in ^{25}Mg, Dr. J. Berengut (Sydney) for valuable discussions, and Dr. M. T. Murphy (Cambridge) for sending us the manuscript on the recent Fourier-transform measurements prior to publication.

Chapter 6

Isotopically-resolved calibration of the 285-nm Mg I resonance line for comparison with quasar absorptions

We have performed high-precision spectroscopy on the $3s^2\,{}^1S \rightarrow 3s3p\,{}^1P$ *first resonance line of Mg I at 285 nm. This measurement is motivated by the recent studies comparing observed quasar absorption lines with laboratory measurements in the search for a possible variation of the fine structure constant* α*. The Mg transition is excited using the upconverted radiation of an injection-seeded Ti:sapphire pulsed laser system, while the frequency of the cw-seed light is measured using a femtosecond frequency comb laser. The line positions of the isotopes are fully resolved and have accuracies better than* 8×10^{-9}*. Using terrestrial abundances for the Mg isotopes* ^{24}*Mg:*^{25}*Mg:*^{26}*Mg being* 78.99 : 10.00 : 11.01*, we determine the composite line wavenumber to be* 35051.2808(2) *cm*$^{-1}$*, which can be compared to the astronomical observations where the isotopic shifts are unresolved.*

This chapter is published as Monthly Notices of the Royal Astronomical Society **373**, L41–L44 (2006).

6.1 Introduction

There is a resurgent interest in the possibility of a variation of fundamental constants, like the fine structure constant $\alpha = e^2/4\pi\epsilon_0\hbar c$ (Refs. 72 and 73) and the proton-to-electron mass ratio $\mu = M_p/m_e$.[100] The possible variation of such constants has far-reaching implications for modern physical theories, see for example Ref. 40 for a recent review. The magnitude of such variations and their effect on the wavelengths of spectral lines of atoms, ions and molecules are expected to be minute, so that it is necessary to employ extremely precise spectroscopic techniques to probe for such effects. One approach is to measure very narrow transitions in atoms or ions over time intervals of months to years at accuracies of $\sim 10^{-15}$/year.[217] Another approach is to compare spectra taken over extremely large time intervals, comparing spectra in cold absorbing interstellar clouds at high redshift in the line-of-sight of quasars (providing look-back times of ∼10 billion years) and present-day measurements in the laboratory. The advantage of the latter approach is that the absolute differences are greater, thus the demands on the spectral accuracy is less stringent compared to that of the first approach.

The most accurate method for probing possible changes in α, based on a comparison of quasar-absorption data and lab spectra, is the many-multiplet (MM) method.[78] Performing the MM analysis on data from quasar absorption systems that are observed with the Keck/HIRES telescope in the northern hemisphere indicates that α was smaller at earlier epochs, with the most recent result of the variation at $\Delta\alpha/\alpha = (-0.57 \pm 0.10) \times 10^{-5}$.[218] However, when other groups[85,86] applied the same method to data gathered from the Very Large Telescope VLT/UVES in the southern hemisphere, they found a null result. Refs. 75 and 219 extensively studied possible sources of systematic errors that could explain this discrepancy, however, none could be found to date. The reliability of the results obtained from the MM method can be improved by maximizing the number of transitions that are included in the analysis, as well as improving the lab frequency calibrations (at zero redshift) so that those can be considered exact for the purpose of the comparisons. Berengut *et al.*[80] have provided a list of spectral lines that require better laboratory calibrations for inclusion in the MM method.

The Mg I $3s^2\,{}^1S \rightarrow 3s3p\,{}^1P$ transition at 285 nm is one of several lines of atomic or ionic magnesium that are used in the MM method. Beverini *et al.*[205] have previously calibrated this line using cw-excitation of an atomic beam, resolving all the naturally-occuring isotopes. Pickering *et al.*,[206] and more recently Aldenius *et al.*,[216] performed calibrations using Fourier Transform Spectroscopy (FTS) without resolving the isotopic substructure due to Doppler-broadening. Isotope shifts have been determined by Hallstadius,[207] Le Boiteux *et al.*,[208] as well as Beverini *et al.*[205]

The ^{25}Mg isotope has a nuclear spin of 5/2, and from the hyperfine structure constants obtained by Kluge and Sauter,[210] the total splitting between the three hyperfine components can be calculated to be less than 50 MHz. However, the hyperfine structure cannot be resolved since the lifetime of $3s3p\,{}^1P$ state is (1.99 ± 0.08) ns,[220] corresponding to a natural linewidth of about 80 MHz.

Following our recent measurements of the Mg I $3s^2\,{}^1S \rightarrow 3s4p\,{}^1P$ transition near 202 nm,[153] we present here our frequency calibration of the Mg I $3s^2\,{}^1S \rightarrow 3s3p\,{}^1P$ transition with the isotopes fully resolved. Using a similar system consisting of

Table 6.1 – *The line positions of the Mg isotopes for the $3s^2\,{}^1S \rightarrow 3s3p\,{}^1P$ transition. The resulting isotope shifts are compared to previous determinations by Refs. 205, 207 and 208, as well as the theoretical calculations from Ref. 203. The uncertainties are shown in between the parentheses.*

isotope	absolute position (cm^{-1})	relative shift from ^{24}Mg (MHz) this expt.	Ref. 205 [a]	Ref. 207	Ref. 208	Ref. 203[b]
^{24}Mg	35051.27311(17)	–	–	–	–	–
^{25}Mg	35051.29784(25)	744.1(7.5)	743.8(3.0)	728 (12)	720(27)	740(30)
^{26}Mg	35051.32015(25)	1413.8(7.5)	1415.3(5.0)	1412(21)	1391(30)	1420(30)

---

[a] Ref. 205 give the ^{24}Mg position of 35051.272 cm^{-1}, where an experimental uncertainty of 0.005 cm^{-1} and a calibration confidence of 0.004 cm^{-1} are specified.

[b] theoretical results

a Ti:sapphire-based pulsed laser system, we performed laser induced fluorescence (LIF) spectroscopy on a Mg atomic beam and obtained frequency calibrations with a stabilized femtosecond frequency comb laser.

6.2 Experimental

A pulsed laser source is used because of the relative ease and efficiency in the up-conversion process towards the deep UV region. We employed an almost identical system to that of the Mg I $3s^2\,{}^1S \rightarrow 3s4p\,{}^1P$ measurements except that the 3rd harmonic of the fundamental is used instead of the 4th harmonic. Here, we present a concise description of the experimental setup and procedures. For an extensive and detailed discussion of the experiment as well as the resulting uncertainty evaluations, we refer to our previous publication.[153]

The laser system consists of a 10-Hz repetition rate Ti:sapphire pulsed oscillator, which is injection-seeded with radiation from a tunable cw Ti:sapphire laser. The oscillator output pulse is centered around the cw-seed frequency at ∼856 nm. The required 285-nm UV excitation light is produced after two frequency upconversion stages in BBO crystals, involving second-harmonic generation and a subsequent frequency-mixing process to produce the third harmonic.

We excite an effusive Mg atomic beam that is skimmed to reduce the transversal velocity spread, resulting in a residual Doppler width of about 15 MHz for the 285-nm transition. The laser-induced fluorescence, which is at the same wavelength as the excitation, is collected with a photomultiplier tube. In order to minimize the Doppler shift due to an imperfect alignment of the UV excitation and Mg atomic beams, an interferometric technique is employed. A Sagnac interferometer is set-up by splitting the UV beam and then recombining the paths, thus creating exactly

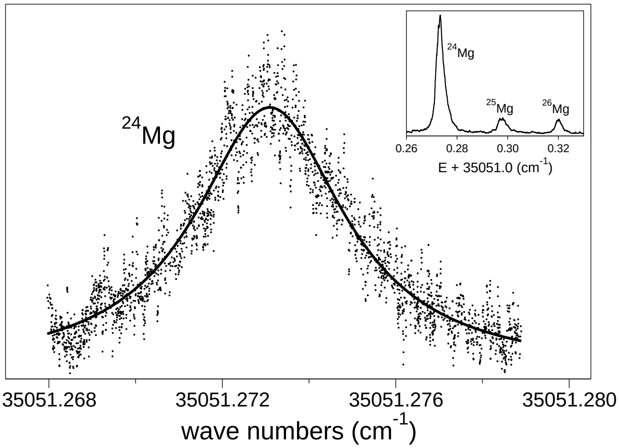

Figure 6.1 – *A recording of the* ^{24}Mg *resonance with the fitted Lorentzian profile. Each data point represents a 0.1-sec measurement for every laser shot. (Inset) An overview spectrum of the Mg* $3s^2\,{}^1S \rightarrow 3s3p\,{}^1P$ *transition with the* ^{24}Mg, ^{25}Mg *and* ^{26}Mg *isotopes resolved.*

counter-propagating beams that cross the atomic beam. Successive measurements for the each of the counter-propagating beams are performed separately and by taking the mean of the spectral line positions obtained from either beam paths, the resulting Doppler error is reduced to < 300 kHz.

Frequency calibration is performed on the cw-seed radiation using a stabilized femtosecond frequency comb.[114,115] The frequency comb is referenced to a Rb-clock standard and approaches a stability in the order of 10^{-12} over a 10-sec averaging time.[211] However, there can be a shift between the center frequency of the pulse and that of the cw-seed radiation caused by frequency excursions during the temporal evolution of the pulse due to the frequency chirp in the Ti:sapphire gain medium and by dynamical mode-pulling effects in the pulse oscillator cavity. In order to characterize these effects, we employed procedures similar to those used by[151,152] to assess chirp phenomena in an injection-seeded and pulsed optical parametric oscillator. Using this method, we measure and correct for the frequency offset between the cw-seed radiation and the amplified pulse generated for every laser shot.

6.3 Results and discussion

A recording of the ^{24}Mg line with a Lorentz fit superimposed is displayed in Fig. 6.1. A recorded resonance consists of about 2500 data points, with each point represent-

Table 6.2 – *Uncertainty budget for the absolute calibration at the deep-UV energy scale. The total uncertainty is obtained by taking the quadrature sum of the errors* $i - iv$ *and linear summation of the result with the errors* $v - vi$.

	Error	MHz
i	1st-order Doppler	0.3
ii	frequency comb	< 0.1
iii	fit error ^{24}Mg	2.0
iv	fit error ^{25}Mg,^{26}Mg	4.5
v	ac-Stark	0.5
vi	cw – pulse offset	2.5
	total ^{24}Mg	5.0
	total ^{25}Mg,^{26}Mg	7.5

ing a 0.1-sec measurement. The observed linewidth is about 120 MHz, which is close to the expected width taking into account the natural linewidth of 80 MHz, the laser linewidth of about 35 MHz, and the residual Doppler width of 15 MHz. The signal-to-noise ratio (SNR) is low because we reduced the intensity of the UV excitation in the measurements to the lowest possible value in order to avoid power shifts. We typically used peak intensities of less than 100 W/cm^2 (pulse length ~20 ns), and we do not detect any power shifts at higher laser peak intensities (~1 kW/cm^2). An isotope-resolved overview recording of the Mg I $3s^2\,{}^1S \rightarrow 3s3p\,{}^1P$ transition is shown as an inset in Fig. 6.1.

We list the absolute line positions that we obtained for the different isotopes in Table 6.1. An uncertainty budget for the calibration is presented in Table 6.2 and we refer to Ref. 153 for a more detailed discussion of the uncertainty estimates. The lower accuracy we obtained for the present measurements compared to that of the 202-nm line can be attributed to the larger natural linewidth, the worse SNR since resonance fluorescence is detected, and the more severe frequency chirp in the Ti:sapphire pulsed oscillator at the fundamental wavelength of ~856 nm. The first two factors increase the uncertainty in the determination of the line center (errors iii and iv), while the last factor increases the error in the correction of the cw–pulse frequency offset (error vi).

Our value for the ^{24}Mg line position is in good agreement with that obtained by Beverini *et al.*[205] of 35051.272(5)(4) cm^{-1}, where the first number in parentheses refers to the experimental uncertainty and the second number refers to the confidence in the reference standard used for calibration. The isotope shifts are also listed

Table 6.3 – *Comparison of the transition centre-of-gravity with previous determinations where the isotopes were not resolved. We use the terrestrial isotopic abundance ratio* ^{24}Mg:^{25}Mg:^{26}Mg *of* 78.99 : 10.00 : 11.01, *to weight the isotopic line centers for comparison with the composite line positions given by Refs. 216, 206 and 204. The values are given in* cm^{-1}.

	this expt.	Aldenius	Pickering	Risberg
composite line	35051.2808(2)	35051.280(2)	35051.277(1)	35051.26(4)

in Table 6.1, along with some previous determinations.[205,207,208] It is satisfying to see that the values obtained from different measurement techniques are consistent with each other. In addition, the result of the *ab initio* calculations of Berengut *et al.*[203] for the isotope shifts are in good agreement with the experimental results. The relative uncertainty for the ^{24}Mg line position is $< 5 \times 10^{-9}$, while it is $< 8 \times 10^{-9}$ for the less abundant isotopes. The present values constitute a more than an order of magnitude improvement on the absolute frequencies of the isotope-resolved transition. The relative isotope shift determination of Beverini*et al.*[205] are slightly more accurate than our values since they employed cw-laser excitation.

We use the weighted sum of the isotopic line positions using the terrestrial isotopic abundances to obtain the centre-of-gravity of the transition in order to compare our measurements with the composite line obtained by Aldenius *et al.*,[216] by Pickering *et al.*[206] and by Risberg,[204] as shown in Table 6.3. (Ref. 215 provide values for the terrestrial Mg isotopic abundances of 78.99(4)% for ^{24}Mg, 10.00(1)% for ^{25}Mg, and 11.01(3)% for ^{26}Mg.) The centre-of-gravity that we obtain is in agreement with the value obtained by Aldenius *et al.*[216] and that of Risberg.[204] It has been pointed out by Aldenius *et al.*[216] that there is a systematic offset of -0.003 cm^{-1} between their results and those of Pickering *et al.*[206] due to the use of new and improved calibration values for the (Ar II) reference standard in the more recent FTS measurements. If the results of Pickering *et al.*[206] are recalibrated with respect to the improved reference standard, then the values are consistent.

The isotopic structure is not resolved in the quasar absorption spectra with a typical linewidth of 0.78 cm^{-1} for this transition (corresponding to a velocity spread of 6.6 km/s). In general, the lineshapes and linewidths should be taken into account in synthesizing a composite line for comparison with the absorption spectra. However, for the large linewidths in the quasar absorption data, the difference from our centre-of-gravity value can be neglected. Hence, the centre-of-gravity value that we provide here could be used directly in the comparison with quasar-absorption spectra.

There is an implicit assumption in the MM method that the terrestrial isotopic abundances also hold in the absorption systems studied. The possibility that a variation in isotopic abundance might mimic an α-variation has been discussed in a number of papers.[75,199–201] Systematic shifts attributable to variations in isotopic abundance are more pronounced for the light species such as Mg, because the isotope shifts are larger relative to the expected spectral line shift induced by a changing α. For the Mg I $3s^2\,^1S \rightarrow 3s4p\,^1P$ transition, the isotopic shifts are more than twice that of the $3s^2\,^1S \rightarrow 3s3p\,^1P$ transition, however, the sensitivity coefficients to the variation of α of both transitions are almost equal.[200] It might be possible to evaluate or correct for any systematic effect related to the isotopic abundance by comparing the spectral shifts of both transitions. The highly accurate spectroscopic data produced in our laser experiments may assist in resolving these issues.

6.4 Conclusion

We have reinvestigated the Mg I $3s^2\,^1S \rightarrow 3s3p\,^1P$ transition and obtained the line positions of the ^{24}Mg,^{25}Mg and ^{26}Mg isotopes with unprecedented accuracies of better than 8×10^{-9}. This transition is seen in quasar absorption spectra and is used in the many-multiplet method to probe for a possible variation in the fine structure constant α. Using the terrestrial isotopic abundance ratio ^{24}Mg:^{25}Mg:^{26}Mg of 78.99:10.00:11.01, we evaluate the centre-of-gravity of the transition to be 35051.2808(2) cm^{-1}. This value for the composite line including all three isotopes is in agreement with the values obtained by Aldenius *et al.*[216] and the older measurements of Risberg;[204] it also agrees with that of Pickering *et al.*[206] if the corrections for the FTS absolute calibrations are taken into account. Our more accurate absolute frequency determination of the ^{24}Mg line is in agreement with the previous measurements of Beverini *et al.*[205] The isotope shifts that we obtained are also consistent with the previous determinations of Refs. 207, 208, and 205. Furthermore, the experimental results agree very well with the recent *ab initio* calculations of the isotope shifts by Berengut *et al.*[203] The transition centre-of-gravity that we provide can be used in the comparison with the quasar-absorption spectra, where the isotopic structure is unresolved. In addition, our isotopically-resolved frequency determinations of the $3s^2\,^1S \rightarrow 3s3p\,^1P$ and $3s^2\,^1S \rightarrow 3s4p\,^1P$ (Ref. 153) transitions in Mg I might be helpful in resolving the issue of isotopic abundance evolution in the MM analysis that mimics an α-variation.

Chapter 7

Extreme-ultraviolet laser metrology of O I transitions

Some 16 transitions in atomic oxygen originating from its ^3P ground state were measured using a tunable narrow-band extreme-ultraviolet laser source, with an unprecedented accuracy of $\Delta\lambda/\lambda = 8 \times 10^{-8}$. The results are relevant for comparisons with spectral absorption features observed in the line of sight of quasars, in order to test a possible variation of the fine-structure constant α on a cosmological time scale.

This chapter is published as Monthly Notices of the Royal Astronomical Society **389**, L4–L7 (2008).

7.1 Introduction

The search for a variation in fundamental constants on a cosmological time scale of $\sim 10^{10}$ years is a topic of strong interest. The method employed is based on a comparison between spectral absorption lines at high redshift, observed in the line of sight of quasar systems, with the same transitions observed at zero redshift in the laboratory. Currently two different approaches are pursued. One is the search for a variation in the dimensionless proton-electron mass ratio μ, which employs transitions associated with the Lyman and Werner band of molecular hydrogen,[100] its isotopologue HD (Ref. 221) and the inversion splitting in ammonia.[97] The other addresses the fine structure constant $\alpha = e^2/(4\pi\epsilon_0\hbar c)$, and is based on a comparison between atomic and ionic spectral absorption lines[72,73] that all depend in a different way on a possible variation in α. Various spectral transitions have been included in a comprehensive analysis, dubbed the many-multiplet (MM) method.[78] The astrophysically observed transitions falling in the atmospheric transmission window of visible and near-ultraviolet wavelengths correspond to laboratory wavelengths (*i.e.* zero-redshift) in the deep-ultraviolet and extreme-ultraviolet (XUV) wavelength ranges, if redshifts of $z > 2$ are probed. The implementation of the MM-method is most effective if transitions associated with various elements at different degrees of ionization, covering a broad dynamic range of absorption strengths, are probed in the same highly redshifted absorbing clouds in the line of sight of quasars. For the purpose of such a comparison a list of transitions that require improved laboratory wavelength metrology has been identified.[80]

In a program to provide accurate laboratory measurements of relevant spectral transitions in the XUV wavelength range for the purpose of comparison with quasar absorption data, we have previously investigated transitions in C I,[81] N I,[222] molecular hydrogen[171,172] and its isotopologue HD.[221] Using a tunable, narrow-band laser source in the range 90-110 nm, transition wavelengths could be determined with an absolute accuracy of 0.000 008 nm or $\Delta\lambda/\lambda = 8 \times 10^{-8}$. In this paper we extend these studies to the oxygen atom for which we report the accurate wavelength measurement of 16 transitions from the ground state to various excited states of O I. Some of these transitions are contained in the Berengut list.[80]

The extreme-ultraviolet absorption spectrum of O I has been obtained by classical means with Doppler-broadening present, the first detailed study being that by Huffman *et al.*[223,224] The absolute calibration uncertainties in their measured wavelengths were estimated to be about ±0.002 nm or ±2 cm^{-1}, although the relative uncertainties were considerably less. The most recent atomic database compilation is that of Morton,[225] for which the O I data are taken from Moore[226]. Inspection of the data in the latter compilation shows that the term values for the final states accessed in our present absorption measurements derive from Eriksson and Isberg.[227,228] The tabulated values are theoretical ones, calculated by these authors, and are deemed to be accurate to ±0.00005 nm, but have never been confirmed with experimental observations at that accuracy. With the present laser-based sub-Doppler measurements the accuracy of these term values is improved considerably. To obtain improved experimental excited-state level energies, the highly accurate data from a far-infrared study by Zink *et al.*[229] on the splittings between the fine-structure components in the ^{3}P ground state of O I are employed. These data are also used to verify the consistency of our results. In a later Letter[230] the ground-state splittings in the oxygen atom, again obtained by employing far-infrared spectroscopy, essentially confirmed the previous findings[229] within our stated accuracy.

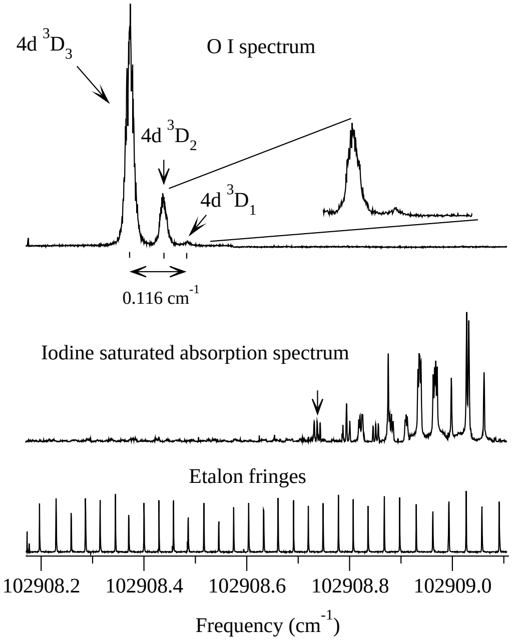

Figure 7.1 – *Recording of the ($^4S^o$) $^3P_2$ →($^4S^o$) 4d $^3D^o$ triplet in atomic oxygen performed* via *1 XUV+1' UV ionization spectroscopy. The middle and the lower trace show the I_2-saturation spectrum used for absolute calibration and the markers of an actively stabilized étalon used for relative calibration. The marked iodine line is the t-hyperfine component of the B–X(18,2) R(109) rotational line in I_2 at* 17151.45606 *cm*$^{-1}$.

7.2 Experiment

The operation and characteristics of the tunable, narrow-band extreme-ultraviolet laser source and its application in spectroscopic studies have been described previously.[231] In short, laser and non-linear optical techniques are combined to generate ∼ 5 ns pulses of tunable XUV radiation. A continuous wave (cw) seed beam produced in the visible spectral range, is pulse-amplified, frequency-doubled in a KD*P-crystal, and subsequently tripled in frequency in a gas jet to produce coherent radiation with a bandwidth ($\Delta\lambda_{bw}$) of 250 MHz, yielding $\Delta\lambda_{bw}/\lambda \sim 10^{-7}$. Spectroscopic measurements are performed in a crossed-beam configuration, where the collinear XUV and UV laser light is perpendicularly intersected with an atomic beam, providing a largely reduced Doppler width. A pulsed-discharge source based on either pure oxygen or a 1:2 oxygen/helium mixture is used to produce ground-state oxygen atoms in a beam. The procedure is similar to that employed to produce carbon[81] and nitrogen[222] atoms in their respective ground states. The detection scheme involves resonant excitation of the oxygen atoms, subsequent UV-induced photo-ionization, followed by mass selection in a time-of-flight (TOF) setup and time-gated detection of the resulting ions. In our experiments only the arrival of ^{16}O ions is detected. Hence, our spectroscopic results should be assigned to the pure ^{16}O isotope, rather than to naturally occurring oxygen as is usually the case in the classical absorption experiments.

Frequency or wavelength calibration is performed by referencing the cw-seed radiation against an I_2 molecular standard,[232] while also employing an interpolation between frequency markers of a stabilized étalon. A typical example of an observed O I transition together with the I_2 and étalon marker traces is presented in Figure 1. The instrumental line width is mainly determined by residual Doppler broadening in the crossed-beam setup, and by the bandwidth of the XUV radiation, yielding a total of ~500–600 MHz. The absolute accuracy of the wavelength positions of the O I transitions is determined by a number of factors, where a systematic uncertainty due to the frequency chirp in the dye-amplification system gives the largest contribution.[231] For all observed transitions we estimate the relative uncertainty to be $\Delta\lambda/\lambda \sim 8 \times 10^{-8}$.

7.3 Results and discussion

Atomic oxygen is produced in its ^{3}P ground state, in each of the well-known fine-structure components $^3P_{2,1,0}$. The $^3P_2$ component is lowest in energy, with $^3P_1$ and $^3P_0$ 158.268741(5) and 226.985249(8) cm^{-1} above it, respectively.[229] The population of the three fine-structure components depends on the details of the oxygen atom production in the discharge. Since only ^{16}O (which has a nuclear spin zero) is studied in this work, hyperfine splittings are absent. Because the spin-orbit coupling in atomic oxygen is small, the one-photon selection rules $\Delta J = 0, \pm 1; \Delta S = 0$ and $\Delta l = \pm 1$ hold. The excited states accessed are O $(1s)^2(2s)^2(2p)^3(^4S^o)$ 3d, 4d and 5d $^3D^o_{3,2,1}$ with 6 possible transitions each, O $(1s)^2(2s)^2(2p)^3(^2D^o)$ 3s' $^3D^o_{3,2,1}$ with 6 possible transitions, and O $(1s)^2(2s)^2(2p)^3(^4S^o)$ 5s and 6s $^3S^o_1$ with 3 possible transitions each. Not all possible transitions are observed in this work. The reasons for this are the following: (i) the $^3P_0$ and $^3P_1$ levels of the ground state multiplet are probably less populated than $^3P_2$; (ii) considering the degeneracy factors, the transitions originating from $^3P_0$ and $^3P_1$ are expected to be weaker than those from $^3P_2$; (iii) the fine-structure splittings in higher Rydberg states decrease, and can no longer be resolved in the case of the O $(1s)^2(2s)^2(2p)^3(^4S^o)$ 5d $^3D^o_{3,2,1}$ level. Since the line

Table 7.1 – *Observed line positions (in cm^{-1} and nm) of transitions originating from the ground-state multiplet of oxygen atoms (^{16}O isotope). Since the systematic errors exceed the statistical ones, for all transitions an uncertainty of* ±0.008 *cm^{-1} or* ±0.000008 *nm is estimated.*

Initial state	Final state	Frequency (cm^{-1})	Wavelength (nm)
$^3P_0$	$(^4S^o)\ 3d\ ^3D^o_1$	97 261.383	102.815 729
$^3P_1$	$(^4S^o)\ 3d\ ^3D^o_1$	97 330.100	102.743 139
$^3P_1$	$(^4S^o)\ 3d\ ^3D^o_2$	97 330.159	102.743 077
$^3P_2$	$(^4S^o)\ 3d\ ^3D^o_1$	97 488.369	102.576 339
$^3P_2$	$(^4S^o)\ 3d\ ^3D^o_2$	97 488.429	102.576 276
$^3P_2$	$(^4S^o)\ 3d\ ^3D^o_3$	97 488.530	102.576 170
$^3P_1$	$(^2D^o)\ 3s'\ ^3D^o_2$	100 989.248[a]	99.020 442[a]
$^3P_2$	$(^2D^o)\ 3s'\ ^3D^o_3$	101 135.394	98.877 352
$^3P_2$	$(^2D^o)\ 3s'\ ^3D^o_2$	101 147.517	98.865 502
$^3P_0$	$(^4S^o)\ 5s\ ^3S^o_1$	102 184.994[a]	97.861 727[a]
$^3P_1$	$(^4S^o)\ 5s\ ^3S^o_1$	102 253.710[a]	97.795 962[a]
$^3P_2$	$(^4S^o)\ 5s\ ^3S^o_1$	102 411.979	97.644 827
$^3P_0$	$(^4S^o)\ 4d\ ^3D^o_1$	102 681.512[a]	97.388 515[a]
$^3P_1$	$(^4S^o)\ 4d\ ^3D^o_2$	102 750.181[a]	97.323 430[a]
$^3P_1$	$(^4S^o)\ 4d\ ^3D^o_1$	102 750.229[a]	97.323 384[a]
$^3P_2$	$(^4S^o)\ 4d\ ^3D^o_3$	102 908.382	97.173 814
$^3P_2$	$(^4S^o)\ 4d\ ^3D^o_2$	102 908.449	97.173 751
$^3P_2$	$(^4S^o)\ 4d\ ^3D^o_1$	102 908.498	97.173 705
$^3P_0$	$(^4S^o)\ 6s\ ^3S^o_1$	104 938.226[a]	95.294 159[a]
$^3P_1$	$(^4S^o)\ 6s\ ^3S^o_1$	105 006.943[a]	95.231 799[a]
$^3P_2$	$(^4S^o)\ 6s\ ^3S^o_1$	105 165.211	95.088 479
$^3P_0$	$(^4S^o)\ 5d\ ^3D^o_1$	105 182.024	95.073 279
$^3P_1$	$(^4S^o)\ 5d\ ^3D^o_{1,2}$	105 250.733	95.011 214
$^3P_2$	$(^4S^o)\ 5d\ ^3D^o_{1,2,3}$	105 409.010	94.868 551

[a] Calculated using a measured transition and the known ground-state level splittings.

Table 7.2 – *Experimental term energy values for the ^{16}O isotope of atomic oxygen and comparison with calculated values from Moore's Tables. The uncertainties are given in brackets.*

Level	Energy(cm^{-1})	Moore(cm^{-1})
($^4S^o$) 3d $^3D^o_1$	97 488.368(3)	97 488.378
($^4S^o$) 3d $^3D^o_2$	97 488.428(4)	97 488.448
($^4S^o$) 3d $^3D^o_3$	97 488.530(8)	97 488.538
($^2D^o$) 3s' $^3D^o_3$	101 135.394(8)	101 135.407
($^2D^o$) 3s' $^3D^o_2$	101 147.517(8)	101 147.526
($^4S^o$) 5s $^3S^o_1$	102 411.979(8)	102 411.995
($^4S^o$) 4d $^3D^o_3$	102 908.382(8)	102 908.374
($^4S^o$) 4d $^3D^o_2$	102 908.449(8)	102 908.443
($^4S^o$) 4d $^3D^o_1$	102 908.498(8)	102 908.489
($^4S^o$) 6s $^3S^o_1$	105 165.211(8)	105 165.232
($^4S^o$) 5d $^3D^o_{1,2,3}$	105 409.010(8)	105 409.008

widths for the transitions arising from the $^3P_1$ and $^3P_2$ ground-state fine-structure components are observed to be ~ 0.015 cm^{-1}, this value constitutes an upper limit on these splittings. A total of 16 transitions are observed in this study. Another 8 are calculated combining the present measurement with the ground-state data from the literature.[229] The results are summarized in Table 7.1.

The measurements were taken during several runs on different days. The statistical errors in a certain run were small and of the order of 0.0015 cm^{-1} (0.0000015 nm). However, systematic errors between runs, probably associated with minor day-to-day differences in alignment and chirp, were significantly larger. Hence, on the basis of the error budget we attribute an uncertainty of ±0.008 cm^{-1} (±0.000008 nm) to each transition in Table 7.1. All wavelengths pertain to vacuum.

The assignments of the various transitions are straightforward and are based on literature data.[226] Since the fine-structure splittings in the ^{3}P ground state are known to extremely high accuracy,[229] they can be used, together with our precise transition frequencies, to determine the energies of the final excited states with unprecedented accuracy. In Table 7.2 the excited-state energies of the levels studied in this work are summarized. These energies are given with respect to the $^3P_2$ ground-state level of the oxygen atom. By considering different combinations of measured transitions and ground-state splittings leading to the same upper state, the uncertainties in some term energies are reduced. A comparison with the calculated values from Moore's Tables shows typical deviations in the order of 0.02 cm^{-1} (0.00002 nm) or less. This

Table 7.3 – *Calculated frequency splittings of the excited-state fine-structure components. The uncertainties are shown in brackets.*

Level	J	Energy(cm^{-1})
(^{4}S^o) 3d ^{3}D^o	1	0.0
	2	0.060(2)
	3	0.161(2)
(^{2}D^o) 3s' ^{3}D^o	3	0.0
	2	12.123(1)
	1	–[a]
(^{4}S^o) 4d ^{3}D^o	3	0.0
	2	0.067(3)
	1	0.116(3)

[a] Transitions to (^{2}D^o) 3s' ^{3}D$^o_1$ have not been observed.

supports the claim of Eriksson and Isberg[228] that their calculated values are accurate to ±0.00005 nm.

The chirp effects and possible remaining Doppler shifts represent by far the largest contributions to the total error budget. Since for transitions in narrow wavelength ranges the contributions of these effects are virtually identical, the frequency splittings between excited-state fine-structure components can be determined more accurately. In Table 7.3 these splittings are presented with respect to the lowest lying component of each multiplet. Since the relevant errors are now statistical rather than systematic, they are shown in brackets in the table.

It should be noted that the multiplet splittings associated with the (1s)^2(2s)^2(2p)^3(^{4}S^o) 3d ^{3}D^o and 4d ^{3}D^o levels have opposite signs. This is probably due to slightly different spin-orbit-mediated interactions with the (1s)^2(2s)^2(2p)^3(^{4}S^o) 3d and 4d ^{5}D^o quintuplet levels, located slightly below the corresponding triplets.[226]

Since our results are exclusively for the ^{16}O isotope, their relevance for a comparison with quasar data, based on the isotopic composition of atomic oxygen in distant cosmic clouds, should be discussed. Hence, the role of the other stable isotopes ^{17}O and ^{18}O should be considered. Their possible importance depends on their isotope shifts compared to ^{16}O and their abundances. For atomic oxygen there are two main contributions to the isotope shift: the Normal Mass Shift (NMS), also called Bohr's shift, and a Specific Mass Shift (SMS). For a light atom as oxygen the volume shift may be neglected. Hence, for every energy level one obtains:[233]

$$E_M = \frac{M}{(1+M)}E_\infty + \frac{M}{(1+M)^2}S_{SMS}$$

where E_M is the energy level corresponding to a finite mass M (in units of electronic mass m_e), and E_∞ is the (negative) energy eigenvalue of the infinite nuclear mass problem. Also

$$S_{SMS} = -\langle \Psi_\infty | \Sigma_{i<j} \nabla_\mathrm{i} . \nabla_\mathrm{j} | \Psi_\infty \rangle$$

The effect of the first term (NMS) shifts the levels of the various isotopes by different amounts that can be easily calculated when the excited-state energy is known. For the excited states addressed in this study these different amounts lie in the range $0.36 - 0.40$ cm^{-1}. The SMS depends on the excited-state wave function for the infinite mass problem, and even its sign is not known *a priori*. However, it can be safely stated that the overall isotope shifts between the various stable isotopes of atomic oxygen for the excited states under consideration will not amount to more than 0.7 cm^{-1}.

For a comparison with quasar data the isotopic abundances in the cosmic clouds should be considered as well. ^{16}O is a principal product of stellar evolution, primarily produced at the end of the helium burning in stars, and therefore very abundant in the Universe. In contrast, the production of ^{17}O and ^{18}O secondary isotopes requires pre-existing seed nuclei. Hence the abundances of ^{17}O and ^{18}O are low, with terrestrial abundances of typically 0.0372(4) and 0.200004(5) %,[215] respectively. Employing these values and assuming a realistic line width for the astronomical measurements to be $\sim$ 1 cm^{-1}(taken on the XUV scale, hence for a resolving power of 100 000), we performed simulations for a range of isotope shifts to determine whether the simultaneous observation of all isotopes would shift the line position of a natural O-sample from the presently determined lines for ^{16}O. Our results show a maximum deviation of 0.0002 cm^{-1}, negligible compared to the uncertainties obtained with telescope systems currently in use for high redshift observations (HIRES-Keck and UVES-VLT). A comparison with our ^{16}O results is therefore valid.

7.4 Conclusion

Experimental transition energies to highly-excited states in atomic oxygen were obtained with a tunable narrow-band extreme-ultraviolet laser source at an unprecedented accuracy of $\Delta\lambda/\lambda \sim 8 \times 10^{-8}$. A comparison with previously calculated term values of the excited states accessed in the present experiments shows deviations of up to 0.02 cm^{-1} (0.00002 nm). The present values can be used in comparisons with astrophysically observed O I transitions, in order to establish a possible variation in the fine-structure constant α over a time span of $\sim 10^{10}$ years.

Chapter 8

High precision frequency calibration of N I lines in the XUV domain

With the use of a narrowband and tunable extreme ultraviolet laser source transition frequencies in the spectrum of neutral atomic nitrogen were measured for transitions originating from the $(2p^3)\,^4S_{3/2}$ *ground state to twelve levels in the* $2p^23d$ *and* $2p^24s$ *configurations in the wavelength range* 95.1 − 96.5 *nm. The present laboratory calibrations, performed at an absolute accuracy of* 0.005 *cm*$^{-1}$ *or* 5×10^{-8}, *should be useful for comparison with nitrogen absorption features observed in quasars for assessment of possible temporal variation of the fine structure constant. Simultaneous recordings of spectra for both* ^{14}*N and* ^{15}*N yield accurate values for transition isotope shifts, that reveal large specific-mass shifts almost to the extent of canceling the isotope shifts.*

This chapter is published as Journal of Physics B **38**, L383-L387 (2005).

8.1 Introduction

With the recent claims on a possible variation of the fine structure constant $\alpha = e^2/4\pi\epsilon_0\hbar c$ on a cosmological time scale, deduced from comparisons between laboratory spectra and high-resolution data from quasi-stellar objects,[72,76] a renewed interest has arisen in obtaining transition frequencies of the strong resonance lines of atoms and ions measured at the highest precision. Although the claim of variablity of α has been disputed, based on differing findings on the northern[72,76] and southern hemispheres,[85,86] this issue which touches upon the very foundations of physics is sufficiently important to be pursued in all details. With the use of the many-multiplet method, adding lines to the comparison-database may result in improved constraints on the temporal behaviour of α, particularly when these lines have a spread in relativistic fine structure splittings. But as was noted, the laboratory (or zero-redshift) values for quite a number of spectral lines is not known at sufficient precision for reliable comparison with astrophysical data.[80] After a similar investigation on the C I line at 94.5 nm achieving an absolute accuracy of 4×10^{-8} with the use of the Amsterdam narrowband and tunable extreme ultraviolet (XUV) laser system,[81] we now turn to a high-accuracy calibration study of twelve resonance lines in the spectrum of N I near 95–96 nm, including a determination of the isotope shift. Neutral nitrogen has been observed in so-called damped Lyman-α systems, where the nucleo-synthetic origin of ^{14}N is a matter of controversy.[234]

The XUV spectrum of N I was investigated in the early days of quantum mechanics by Compton and Boyce,[235] who covered the entire range of 50–120 nm. Since then a number of investigators focused on the nitrogen spectrum. Herzberg performed a high-resolution investigation, probing levels of the $(2p^2 4s)\ ^4$P and $(2p^2 3d)\ ^4$D manifolds directly in emission at an absolute accuracy of of 0.0002 Å or 0.02 cm^{-1}. Alternatively the level energies of the highly excited states were derived from the investigation of combination differences after measuring large numbers of spectral lines in the visible and near-infrared ranges. On the basis of the spectra of Eriksson and coworker,[236,237] as well as from some new measurements, Kaufman and Ward succeeded in determining the level energies of all levels included in the present study to an accuracy of 0.04 cm^{-1}.[238]

The aim of the present investigation is to further improve upon the calibration accuracy of the resonance lines in the XUV-domain such that in comparison with quasar and other astrophysical data the laboratory or rest-frame frequencies can be considered exact. The use of the Amsterdam narrowband and tunable XUV laser-setup has been described extensively, including its limitations in providing frequency calibrations. For discussions on the effects of frequency chirp in pulsed dye amplifiers used in the production of highly energetic laser pulses; the generation of narrowband XUV-radiation; the method of 1 XUV + 1 UV photoionization detection; possible effects of residual Doppler and AC-Stark shifts; and the frequency calibration against the Doppler-free I_2-standard in the visible range, we refer to Ref. 150. The operation of the same system for a calibration of C I lines (for both ^{12}C and ^{13}C) was demonstrated recently.[81]

8.2 Experiment

A beam of atomic nitrogen was produced in a pulsed expansion from a source equipped with a high-voltage discharge as described in Ref. 239. About 20% of N_2 in He was used for optimal discharge operation, where the nitrogen part was

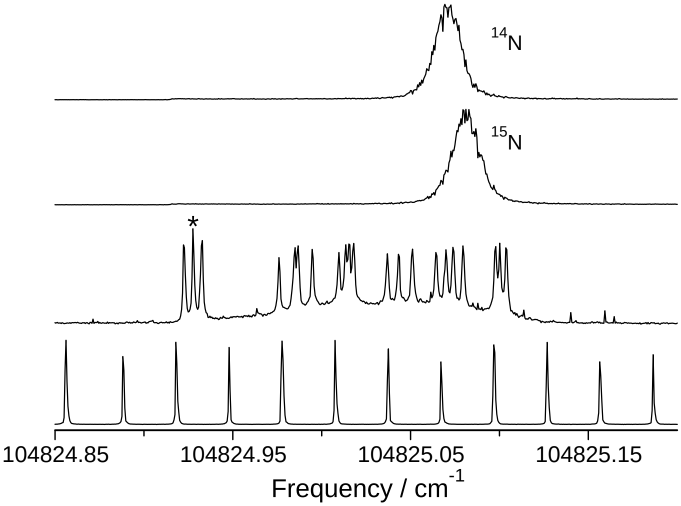

Figure 8.1 – *Recordings of the* $(2p^3)^4\mathrm{S}_{3/2}$ - $(2p^2 3d)^4\mathrm{P}_{5/2}$ *transition for* ^{14}*N and* ^{15}*N. The calibration line marked with an asterisk is the t-hyperfine component of the P43 line in the B–X(18–1) band of* I_2 *at* 17 470.821 290 *cm*$^{-1}$ *measured by saturated absorption spectroscopy. The lower trace represents markers of an étalon used for the frequency calibration procedure.*

premixed from naturally-occuring nitrogen $^{14}\mathrm{N}_2$ with a sample of 99% isotopically enriched $^{15}\mathrm{N}_2$ in a 50%/50% mixture. The nozzle-discharge expansion was positioned at a distance of 10 cm from a skimmer to obtain a highly collimated atomic beam which is perpendicularly crossed with the laser beams to obtain Doppler-free spectra. An example of recordings of the $(2p^3)^4\mathrm{S}_{3/2}$ - $(2p^2 3d)^4\mathrm{P}_{3/2}$ transition for both ^{14}N and ^{15}N is shown in Fig. 8.1. The spectra are obtained by laser excitation combined with time-of-flight mass separation. By this means the spectra for ^{14}N and ^{15}N are recorded simultaneously from the same atomic beam, although the spectral traces for both isotopes appear distinct, as shown in Fig. 8.1. The transition frequencies were determined by line-fitting with the use of frequency markers from a calibrated and stabilized étalon, and the simultaneous measurement of I_2 calibration lines, recorded at the fundamental wavelength of the laser system at $6 \times \lambda_{\mathrm{XUV}}$.

8.3 Results and discussion

In Table 8.1, the resulting transition frequencies are listed with the uncertainties, including a statistical error from averaging over at least three recordings and esti-

Table 8.1 – *Resulting frequency calibration for transitions from the* $(2p^3)\,^4\mathrm{S}_{3/2}$ *electronic ground state in the N atom to the listed excited states, with uncertainties given in parentheses. For* ^{14}*N a comparison is made with literature values from Refs. 238,240. All values in cm*$^{-1}$*.*

Excited state	^{14}N (Obs.)	Δ (Ref. 240)	Δ (Ref. 238)	^{15}N (Obs.)
$(2p^24s)\,^4\mathrm{P}_{1/2}$	103 622.477 3 (50)	−0.009 (20)	−0.052 (40)	103 622.482 5 (40)
$(2p^24s)\,^4\mathrm{P}_{3/2}$	103 667.121 4 (50)	−0.021 (20)	−0.053 (40)	103 667.125 5 (40)
$(2p^24s)\,^4\mathrm{P}_{5/2}$	103 735.452 7 (50)	−0.020 (20)	−0.042 (40)	103 735.457 2 (40)
$(2p^23d)\,^2\mathrm{F}_{5/2}$	104 810.332 4 (50)		−0.045 (40)	104 810.342 9 (40)
$(2p^23d)\,^4\mathrm{P}_{5/2}$	104 825.069 9 (50)		−0.051 (40)	104 825.084 4 (40)
$(2p^23d)\,^4\mathrm{P}_{3/2}$	104 859.695 2 (50)		−0.051 (40)	104 859.709 4 (40)
$(2p^23d)\,^4\mathrm{P}_{1/2}$	104 886.068 7 (50)		−0.051 (40)	104 886.082 8 (40)
$(2p^23d)\,^4\mathrm{D}_{1/2}$	104 984.323 8 (50)	−0.007 (20)	−0.062 (40)	104 984.339 1 (40)
$(2p^23d)\,^4\mathrm{D}_{3/2}$	104 996.234 3 (50)	−0.001 (20)	−0.056 (40)	104 996.248 7 (40)
$(2p^23d)\,^4\mathrm{D}_{5/2}$	105 008.514 1 (50)	−0.004 (20)	−0.048 (40)	105 008.529 7 (40)
$(2p^23d)\,^2\mathrm{D}_{3/2}$	105 119.841 9 (50)		−0.054 (40)	105 119.854 1 (40)
$(2p^23d)\,^2\mathrm{D}_{5/2}$	105 143.679 9 (50)		−0.046 (40)	105 143.691 3 (40)

mating the systematic uncertainty.[81,150] The accuracy of the absolute calibrations in the present study is at the 5×10^{-8} level, and hence a factor of 4 and 8 more accurate than the previous classical studies.[238,240] These uncertainties are mainly determined by systematic effects related to frequency chirp in the dye amplifiers, the possible first-order Doppler shifts as a result of imperfect perpendicular alignment of the laser and atomic beams, and the AC-Stark effect. These effects were estimated and treated experimentally by methods described before.[150] The present data on the transition frequencies are on average lower in energy by -0.010 cm^{-1} with respect to the values of Ref. 240, in agreement with the cited error of 0.020 cm^{-1}. Similarly the present values for the twelve transitions are on average -0.051 cm^{-1} lower than those of Ref. 238, therewith slightly exceeding the cited uncertainty of 0.040 cm^{-1}.

The linewidths of the atomic resonances are in the range 450 – 650 MHz, larger than the bandwidth of the XUV source (≈ 300 MHz). In the chosen geometry of the beam configuration, Doppler broadening adds slightly to the instrument width. For the upper states in the 4*s* and 3*d* manifolds of N I lifetimes of 11 ns and 7 ns are reported,[225,241] giving rise to lifetime broadenings of 14 and 22 MHz, so only

Table 8.2 – *Resulting isotope shifts from relative frequency measurements for transitions from the* $(2p^3)\,^4S_{3/2}$ *electronic ground state in the N atom to the listed excited states, with uncertainties given in parentheses. Values are given in MHz.*

Excited state	$\Delta_{IS}\,(^{15}N - ^{14}N)$
$2p^24s\,^4P_{1/2}$	160 (60)
$2p^24s\,^4P_{3/2}$	130 (40)
$2p^24s\,^4P_{5/2}$	140 (50)
$2p^23d\,^2F_{5/2}$	310 (20)
$2p^23d\,^4P_{5/2}$	320 (20)
$2p^23d\,^4P_{3/2}$	340 (20)
$2p^23d\,^4P_{1/2}$	320 (30)
$2p^23d\,^4D_{1/2}$	440 (20)
$2p^23d\,^4D_{3/2}$	430 (20)
$2p^23d\,^4D_{5/2}$	470 (20)
$2p^23d\,^2D_{3/2}$	370 (20)
$2p^23d\,^2D_{5/2}$	340 (30)

marginally contributing to the observed widths in the present experiment. This is in contrast to the investigation of the C I resonance line,[81] where lifetime broadening was the dominant broadening effect. The $(2p^3)\,^4S_{3/2}$ ground state in ^{14}N is split into a hyperfine triplet spanning 42 MHz, while in ^{15}N it is split into a doublet spanning 29 MHz[242] by the magnetic dipole interaction term. For the $4s$ and $3d$ excited states no information exists for the hyperfine structure, but for the $(2p^2)3s\,^4P$ level hyperfine constants of 61 MHz (^{14}N) and 45 MHz (^{15}N) were determined.[243] Such effects of hyperfine structure should not be observable in the present XUV excitation scheme, at least not in terms of splittings or asymmetries, but might add somewhat to the linewidths.

Since the ^{14}N and ^{15}N spectra are recorded simultaneously under identical conditions, the isotope shifts (IS) can be derived from relative frequency measurements, which are not affected by most of the systematic contributions to the uncertainty in the absolute calibration. Hence, the uncertainties in the values for the IS, depend mainly on the statistical uncertainties related to the fitting of the line profiles and the determination of line centres. The values are listed in Table 8.2 in units of MHz. The ^{15}N - ^{14}N isotope shifts are in the range between 120 and 470 MHz, or 0.004 and 0.016 cm^{-1}, where the Bohr shift (or the normal mass-shift contribution to the IS) for these XUV-transitions should amount to 0.27 cm^{-1}. Hence, the specific mass-shift (SMS) contribution to the isotope shift for these lines is negative, exceeds 7.5 GHz, and almost cancels the effect of the Bohr shift. This implies that in astrophysical observation of these lines the ^{15}N component will always be fully overlapped. This large and negative SMS-contribution in nitrogen is consistent with previous measurements on isotope shifts in the near-infrared spectral range. In the case of the $(2p^2 3s)^4$P - $(2p^3)^4$P transitions SMS contributions of -2.5 GHz were found to give rise to negative isotope shifts in the nitrogen atom.[243] So far no isotope measurements involving the $2p^2 4s$ and $2p^2 3d$ configurations, nor results on *ab initio* calculations of IS in atomic nitrogen, have been reported.

8.4 Conclusion

In conclusion, we report on a frequency calibration in the XUV-domain of twelve resonance lines in the spectrum of N I, for both ^{14}N and ^{15}N isotopes, at the 5×10^{-8} accuracy level. These results should be useful for comparison with highly redshifted quasar absorption lines of atomic nitrogen in order to test a possible variation of the fine structure constant, and may encourage performing first principle calculations on the anomalous isotope shift behaviour in this atom.

Acknowledgement

We wish to thank the Netherlands Foundation for Fundamental Research of Matter (FOM) and the Space Research Organisation Netherlands (SRON) for financial support.

Chapter 9

High-resolution 2+1 REMPI study of the $a''^1\Sigma_g^+$ state in N_2

We reinvestigated the 2+1 REMPI Q-branch spectrum of the $a''^1\Sigma_g^+$–$X^1\Sigma_g^+$ *system of* N_2 *at around 202 nm in a Doppler-free configuration with counter-propagating laser beams. Highly accurate absolute calibrations were performed using either an* I_2 *reference standard or a frequency comb reference laser. The observed rotational series shows a clear effect of a perturbation in terms of an anti-crossing located at* $J = 26$*. In addition to the improved set of molecular constants for the* $a''^1\Sigma_g^+$ *state, we tentatively assign the perturber state to be the* $^1\Sigma_g^+$*(II) state of* N_2*.*

This chapter is published as Journal of Physical Chemistry A **113**, 2383 (2009).

9.1 Introduction

The quantum energy level structure of homonuclear molecules such as N_2 can be subdivided into two non-interacting components, one of *gerade* and one of *ungerade* molecular inversion symmetry, defined in the body-fixed frame of the molecule. The connection between the sub-compartments is made through electronic dipole-allowed transitions in the spectrum. The level structure of the u symmetry excited states has been investigated in detail through classical spectrographic studies, either in absorption[244] or emission,[245] by synchrotron absorption studies,[246] by extreme ultraviolet (XUV) laser studies[247] and by fragment kinetic energy studies.[248,249] The structure in this u-manifold above 100 000 cm^{-1} is one of severe complexity. The seemingly erratically ordered singlet states have been unraveled through the semi-empirical work of Stahel *et al.*,[250] who assigned the mutually interacting Rydberg and valence states $^1\Sigma_u^+$ and $^1\Pi_u$ symmetry. Adding to this complex behavior is the coupling of the singlet states to triplet states, that cause further perturbations in the level structure as well as predissociation.[251,252]

Prominent quantum states of g symmetry, besides the $X^1\Sigma_g^+$ ground state, are the $a^1\Pi_g$ state, observed in the relatively weak Lyman-Birge-Hopfield system[253] and the $a''^1\Sigma_g^+$ state, which is the subject of the present study. The $a''^1\Sigma_g^+$ Rydberg state was first identified via pressure-induced excitation in the dipole-forbidden $g - g$ transition by Dressler and Lutz.[254] Later Ledbetter identified the $a''^1\Sigma_g^+$ state as the lower level in an infrared emission system, also providing information on the rotational constants.[255] Using a combination of pulsed-electron excitation and laser-induced fluorescence the lifetime of the $a''^1\Sigma_g^+$ state was determined to be 3.49 ± 10 μs;[256] this implies that spectroscopic studies at very high resolution are possible upon excitation of the $a''^1\Sigma_g^+$ state.

2+1 resonance enhanced multi-photon ionization (REMPI) on the $a''^1\Sigma_g^+ - X^1\Sigma_g^+$ system was performed by a number of groups prior to the present high-resolution study. After an initial study by Lykke and Kay,[257] Hanisco and Kummel[258] improved the resolution and wavelength calibration, and also detected the (1,1) and (2,2) bands. Later Rijs *et al.*[259] performed 2+1 REMPI on the $a''^1\Sigma_g^+ - X^1\Sigma_g^+$ system, upon photodissociation of N_2O, allowing them to probe the $(0,0)$ and $(1,1)$ bands for rotational quantum numbers as high as $J = 94$, albeit at a lower wavelength accuracy.

At higher excitation energies there exist numerous additional states of singlet and *gerade* symmetry. Kaplan observed the states labeled as $x^1\Sigma_g^-$, $y^1\Pi_g$, and $z^1\Delta_g$, in transitions that are now referred to as the Kaplan systems.[260] More recently de Lange *et al.*,[261] using a laser-based double-resonance scheme, observed a large number of novel bands and quantum states. Although through the double-resonance scheme the rotational structure could be fully unraveled, the vibronic assignment of the observed structures is still pending.

Ab initio calculations by Ermler *et al.*[262] predict that there exists a valence state $^1\Sigma_g^+$(II), at much larger internuclear separation than the $a''^1\Sigma_g^+$ state. In the adiabatic potential picture these states of equal symmetry interact and form an $a''^1\Sigma_g^+ -$ $^1\Sigma_g^+$(II) double-well structure with an outer well minimum at ~ 11 eV and an inner well minimum at ~ 13 eV. Bominaar *et al.*[263] recently performed a two-photon excitation study with a powerful tunable excimer-laser system and they could observe a vibrational level in the outer well, which they tentatively assigned as $v' = 32$. Until now this is the only level observed in the outer well.

Table 9.1 – *Absolute frequency positions of* $B^3\Pi(0_u^+)$ - $X^1\Sigma_g^+$ *transitions in* I_2 *used in the subsequent* N_2 *calibrations. The positions are listed for the a1 (for even-J) or a2 (for odd-J) hyperfine component, also referred to as the t-component. The values are expressed in MHz.*

Line	Position
P125 (0–16) a2	370 380 996.21 (30)
R134 (0–16) a1	370 372 289.78 (30)
P135 (0–16) a2	370 321 305.18 (30)
P127 (0–16) a2	370 278 962.40 (30)
P128 (0–16) a1	370 227 354.33 (30)
P211 (0–15) a2	370 198 437.93 (30)

In the present study, we reinvestigate the 2+1 REMPI spectrum of the $a''^1\Sigma_g^+$–$X^1\Sigma_g^+$(0,0) band in N_2 under largely improved resolution and absolute wavelength calibration. The precision obtained allows us to deperturb a local perturbation in the rotational structure of the $a''^1\Sigma_g^+$, $v' = 0$ manifold. However, the information does not allow for an unambiguous identification of the symmetry of the perturber state as either $^1\Sigma_g^+$ or $^1\Pi_g$. We tentatively assign the perturber as a vibrational level in the $^1\Sigma_g^+$(II) outer well state of N_2.

9.2 Experimental methods

The method of 2 + 1 resonance-enhanced multi-photon ionization (REMPI) spectroscopy used in the present experiment is essentially similar to that of previous studies in Refs. 257–259. However, some features were implemented that allow for higher experimental resolution and accuracy in the experiment. First of all, a laser source was used that delivers laser pulses, tunable near 202 nm, at a much reduced bandwidth of ∼ 40 MHz. This system, based on an injection-seeded pulsed Titanium-sapphire oscillator-amplifier system, and three stages for frequency upconversion, has been documented elsewhere.[164] A crucial improvement is the implementation of 2+1 REMPI with counter-propagating laser beams, thus allowing for Doppler-free spectroscopy. The alignment procedure using a Sagnac interferometer has been applied to produce exactly counter-propagating laser beams.[165] Further methods employed in the present experiment are similar to the ones used in the study of the $EF^1\Sigma_g^+$ - $X^1\Sigma_g^+$ system in H_2 and we refer to that study for all details leading to high resolution and accuracy,[163] in particular including the on-line frequency-chirp analysis of the pulsed laser.

The absolute calibration was based on a two-step procedure. First, some hyperfine components in the saturated absorption spectrum of the B–X system in I_2, at the fundamental near-infrared wavelength (808 nm), were calibrated at sub-MHz accuracy against a frequency comb laser that is stabilized against a Rb-clock and GPS-corrected. Six calibrated I_2 hyperfine resonances, listed in Table 9.1, were then used as a secondary frequency reference standard during most spectroscopic measurements on N_2. The transmission fringes of an actively stabilized etalon (against a stabilized HeNe laser) provided the relative frequency markers. At the avoided crossing at $J = 26$, absolute frequency calibrations were performed directly using the frequency comb laser, in a similar fashion to previous studies on the calibration of H_2 lines.[163]

Nitrogen molecules were excited downstream in an effusive expansion from a pulsed jet (General Valve). Under normal operation, this yields a low rotational temperature and only population of the lowest rotational states is found. Varying settings of pulse delays (between nozzle and laser pulses), of nozzle opening times, and of backing pressures made it possible to observe N_2 in rotational quantum states up to $J = 28$.

9.3 Results and discussion

The 2+1 REMPI lines of the Q-branch in the $a''^1\Sigma_g^+ - X^1\Sigma_g^+(0,0)$ band of N_2 were measured several times and calibrated against the pre-calibrated hyperfine components in the I_2 reference transitions. Typical spectra of the Q(0) and Q(1) lines are displayed in Fig. 9.1(a), demonstrating the improved resolution with respect to previous studies[257,258] in which these Q-branch lines were unresolved. A sample spectrum of the Q(26) transition that was calibrated directly against a frequency comb, is shown in Fig. 9.1(b), showing the typical linewidths of ∼ 70 MHz. The result of the calibrated line positions, including the estimated uncertainties are listed in Table 9.2. In addition to the Q-branch rotational states from $J = 0 - 28$ of the $a''^1\Sigma_g^+$ state, the $J = 26$ transition belonging to a perturber state was also calibrated; this is the only level associated with the perturber state that is actually observed. The estimated uncertainties for most of the lines were limited by statistics (*i.e.*, number of measurements). The uncertainties of the two Q(26) lines are significantly smaller than the other transitions on account of the direct calibration.

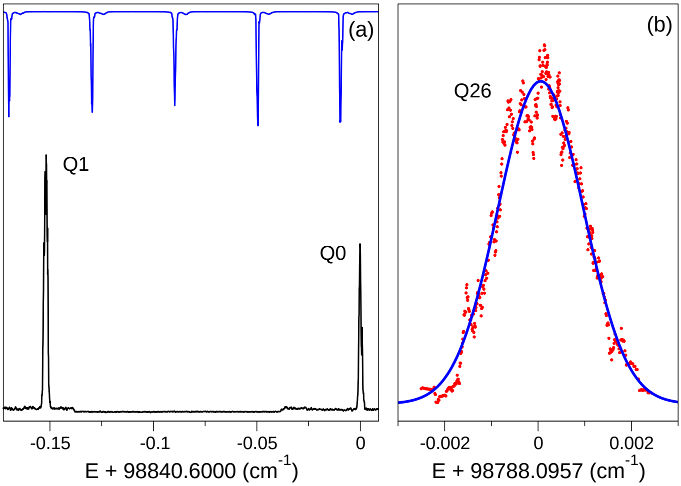

Figure 9.1 – *2 + 1 REMPI spectrum of the* $a''^1\Sigma_g^+$ *–*$X^1\Sigma_g^+$*(0,0) band of* N_2*. (a) Relative frequency calibrations of the Q(0) and Q(1) transitions using the etalon markers (top trace) with respect to an* I_2 *resonance (not shown). (b) The absolute frequency calibration of one of the Q(26) transitions, where the maximum perturbative shift occurs, was performed directly against a frequency comb.*

For the analysis of the spectrum, we adopted a representation for the energy $T_X(J)$ of the rotational levels in the $X^1\Sigma_g^+$, $v'' = 0$ ground state to be:

$$T_X(J) = B''[Y] - D''[Y]^2 + H''[Y]^3, \tag{9.1}$$

with $Y = J(J+1)$. We used the rotational constants derived by Trickl,[264] from a comprehensive re-evaluation of all available literature on the ground state: $B'' = 1.989\,5776(10)$ cm^{-1}, $D'' = 5.74137(100) \times 10^{-6}$ cm^{-1}, and $H'' = 4.843(1.000) \times 10^{-12}$ cm^{-1}.

For the $a''^1\Sigma_g^+$, $v' = 0$ excited state we take a similar expression:

$$T_{a''}(J) = \nu_{a''(0)} + B'[Y] - D'[Y]^2, \tag{9.2}$$

with $\nu_{a''(0)}$ representing the band origin.

A perturbation is found to occur in the vicinity of $J = 26$, and we take this perturbation into account in the subsequent analysis. We invoke a perturbing state where its rotational energy levels $T_{\text{pert}}(J)$ were calculated using an analogous expression to that of Eq. (9.2), following the procedures as described in Ref. 265, with ν_{pert}, B'_{pert}, and D'_{pert}. The effect of the perturbation can be calculated by diagonalizing

Table 9.2 – *Transition frequencies (in cm^{-1}) as observed in the* $a''^1\Sigma_g^+$–$X^1\Sigma_g^+$*(0,0) band of* N_2.

J	Q(J)	J	Q(J)
0	98 840.6000 (3)	15	98 822.3750 (10)
1	98 840.4485 (3)	16	98 819.9424 (4)
2	98 840.1449 (4)	17	98 817.3576 (10)
3	98 839.6895 (3)	18	98 814.6201 (10)
4	98 839.0822 (4)	19	98 811.7298 (10)
5	98 838.3234 (4)	20	98 808.6860 (10)
6	98 837.4126 (7)	21	98 805.4885 (10)
7	98 836.3497 (5)	22	98 802.1374 (10)
8	98 835.1354 (8)	23	98 798.6322 (10)
9	98 833.7688 (3)	24	98 794.9710 (5)
10	98 832.2501 (10)	25	98 791.1482 (10)
11	98 830.5796 (10)	26	98 788.09569 (15)[a]
12	98 828.7568 (10)	26	98 785.74370 (10)[b]
13	98 826.7822 (10)	27	98 783.1185 (30)
14	98 824.6546 (10)	28	98 778.8312 (30)

[a] $a''^1\Sigma_g^+$ state: frequency comb calibration

[b] Perturber state: frequency comb calibration

the matrix for each value of J:

$$\begin{pmatrix} T_{a''(0)}(J) & H_{\text{int}} \\ H_{\text{int}} & T_{\text{pert}}(J) \end{pmatrix} \tag{9.3}$$

A priori, the symmetry of the perturbing state is not known, but in view of the *ab initio* calculations by Ermler *et al.*[262] on the $^1\Sigma_g^+$(II) state, and the observation of the $v' = 32$ level in this outer well,[263] we assume that the perturbation is due to a lower-lying vibrational level in the outer well. Hence, the perturber is assumed to be of $^1\Sigma_g^+$ symmetry, and in such a case, the interaction is characterized by a homogeneous perturbation where the off-diagonal matrix element H_{int} is independent of rotational quantum number J.[265] We have performed extensive least-squares analyses to extract information on the molecular constants for the a″ state as well as those of the perturber state, and the the interaction strength parameter H_{int}. For the sake of completeness, we also performed minimization using a heterogeneous perturbation model. This model would represent the perturber state to be of $^1\Pi_g$ symmetry,

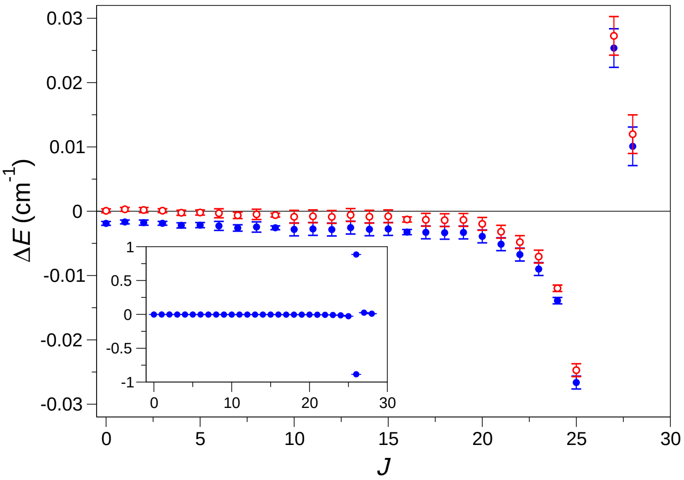

Figure 9.2 – *The perturbative shifts on the Q-branch transitions of* $a''^1\Sigma_g^+$–$X^1\Sigma_g^+$*(0,0) system. The filled circles (blue) represent the shifts in the case of a homogeneous perturbation while the unfilled circles (red) represent those in the case of heterogeneous perturbation. The inset shows an overview to include the* $J = 26$ *transitions, with the upper point representing the transition belonging to the perturber state.*

and the off-diagonal matrix element in this case of a heterogeneous perturbation should be J-dependent: $H_{\text{int}} = H'\sqrt{J(J+1)}$.

In the fitting procedures, we chose to fix the ground state molecular constants to the accurately known values of Ref. 264, since each ground rotational state is accessed once (except for $J = 26$) for the Q-branch series; thus in reality, we can only access the difference of the upper and lower state constants. In addition, the small size of the dataset limits the number of variable parameters that can be used. Nevertheless, after the optimum parameter set for the upper states was obtained, we tried to vary the ground state parameters (keeping the other parameters fixed) but this did not yield any improvements in the goodness of fit.

The perturbative shifts ΔE are calculated by subtracting the perturbed level energies from the unperturbed $a''^1\Sigma_g^+$ series using the constants of Table 9.3 and setting $H_{\text{int}} = 0$. The resulting perturbative shifts are displayed in Fig. 9.2, yielding a clear graphical representation of the avoided crossing. The relatively weak interaction causes shifts of < 0.03 cm^{-1} except at $J = 26$, where the shift amounts to 0.8 cm^{-1}. This marked offset at $J = 26$ had already been observed by Hanisco and Kummel.[258]

Table 9.3 – *Obtained molecular parameters for the* $a''^1\Sigma_g^+$ *state of* N_2 *(in* cm^{-1}*), and the value for the interaction parameter with a perturber state; calculations are performed both with the assumption of perturber state of* $^1\Sigma_g^+$ *(homogeneous interaction) or of* $^1\Pi_g$ *(heterogeneous interaction) symmetry. We also include the values obtained by Hanisco and Kummel*[258] *for comparison.*

	Homogenous	Heterogenous	Ref. 258
$\nu_{a''(0)}$	98 840.60189 (15)	98 840.59993 (15)	98 840.59 (12)
B'	1.9137062 (15)	1.9137062 (15)	1.9143 (2)
D'	6.0000 (25) $\times 10^{-6}$	6.0000 (25) $\times 10^{-6}$	6.6 (2) $\times 10^{-6}$
H_{int}	1.13933 (17)	0.043020 (6)	–

The quality of the present experimental results makes it possible to see the subtle progression of the shifts starting already at $J = 15$.

The results from the least-squares fit are collected in Table 9.3 for both cases of a homogeneous and a heterogeneous perturbation. Despite the high accuracy of the data, it was not possible to determine which of the two models is best suited to describe the perturber state. In both models convergence to $\chi^2 \approx 8$ was achieved, which is very satisfactory for a fit with over 20 degrees of freedom. Highly accurate molecular parameters for the $a''^1\Sigma_g^+$ state are obtained, as well as a highly accurate value for the interaction parameter H_{int}. However, the parameters for the perturber state (ν_{pert}, B'_{pert}, and D'_{pert}) exhibit extremely strong correlations, while the error landscape is riddled with a great number of local minima close to $\chi^2 \approx 8.3$. This gives rise to a dependence of the least-squares fit on the starting values, in particular for the band origin ν_{pert}. For starting values of ν_{pert} in the wide range of 99100 to 99900 cm^{-1} the lowest local minimum was found near $\nu_{\mathrm{pert}} = 99502$ cm^{-1}. However, the neighboring local minima ($\nu_{\mathrm{pert}} = (99495 - 99505)$ cm^{-1}) in the error landscape do not differ at a statistically significant level ($\Delta\chi^2 < 0.01$). Hence, we conclude that we cannot unambiguously determine the symmetry of the perturber nor a reliable value for the band origin. At the lowest minimum with $\chi^2 = 8.3$, we obtain $\nu_{\mathrm{pert}} = 99502.31(1)$ and $B'_{\mathrm{pert}} = 0.96606(2)$, where we have fixed D'_{pert} to zero since the inclusion of this parameter does not significantly lower the χ^2 value.

This result is somewhat surprising, when comparing with the analysis of a perturbation in the $K^1\Sigma^+, v = 0$ state of $^{13}C^{18}O$, in which 28 quantum levels were detected at an accuracy of only 0.05 cm^{-1}.[265] That analysis resulted in an unambiguous

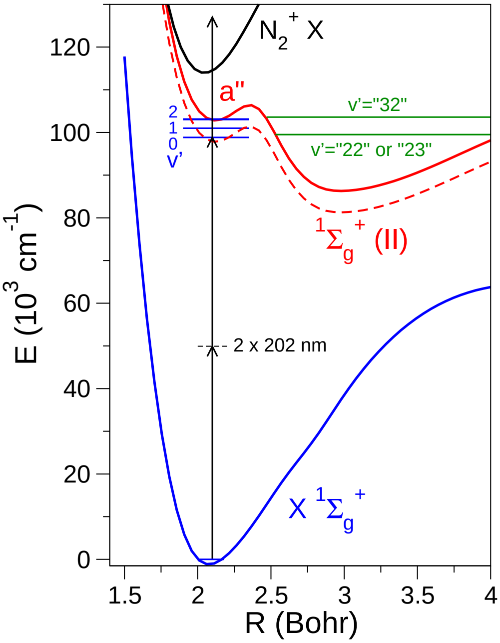

Figure 9.3 – *Potential energy curves for* N_2. *In the adiabatic picture, a double-well potential is formed from the interaction of the* a″$^1\Sigma_g^+$ *and* $^1\Sigma_g^+$*(II) states. While solid curve for the* a″/$^1\Sigma_g^+$(II) *represents the data from Ermler* et al.,[262] *the dashed curve is the potential that was shifted down by Bominaar* et al.,[263,266] *to match the a″(0) level with observations. The horizontal lines indicate the experimentally-observed energy levels clearly demonstrating the inaccuracy of the potential.*

identification of the the symmetry of the perturber and an accurate determination of molecular constants of the perturber state, even without having observed a single level of that perturber. In the present example, level energies are determined at almost two orders of magnitude higher accuracy, and in addition, one perturber level has been detected (at $J = 26$). The strength of the interaction for the example of Ref. 265 is much larger ($H_{\text{int}} = 1.018$ cm^{-1} for a heterogeneous perturbative interaction) and the band origins are closer, resulting in 27 levels with shifts much greater than the experimental uncertainty. We conclude that this strong interaction, imparts more information about the perturber state and thus convergence towards a global minimum is possible in the case of Ref. 265, whereas it is not possible in the present example.

Bominaar *et al.*[263] have calculated level energies for a sequence of vibrational levels in the $a''^1\Sigma_g^+$ – $^1\Sigma_g^+$(II) double-well potential obtained from *ab initio* calculations by Ermler *et al.*[262] They have tentatively assigned the $v' = 32$ level to the band origin found at 103621 cm^{-1}, while the calculations yield $\nu_{32} = 103497$ and $\nu_{33} = 103876$ cm^{-1}. In the calculations of Ref. 263 a prediction is made for vibrational level energies of $\nu_{22} = 99239$ cm^{-1} and $\nu_{23} = 99839$ cm^{-1}. In the present analysis we cannot determine unambiguously the symmetry of the perturber state, but in view of the fact that vibrational levels pertaining to $^1\Sigma_g^+$(II) must exist in this energy range we tentatively assign the observed perturber state to either $v' = 22$ or $v' = 23$.

The comparison of the experimental results and the calculated band origins in Ref. 263, based on the *ab initio* potential of Ermler *et al.*,[262] strongly suggests that the potential is far from spectroscopic accuracy. For clarity, we have reproduced the *ab initio* potential,[262] including the experimentally-determined[258,263] levels in Fig. 9.3. The $a''^1\Sigma_g^+$ $v' = 1$ level is predicted at 100827 cm^{-1} (with $B' = 1.442$cm^{-1}), while the experimentally-determined value of the $a''^1\Sigma_g^+$ $v' = 1$ level energy[258,264] is 100985.2(2) cm^{-1} (with $B' = 1.882(1)$ cm^{-1}). In fact, both the observed $a''^1\Sigma_g^+$ $v' = 0, 1$ levels are below the minimum of the inner part of the calculated potential energy curve. Indeed, this discrepancy has been noted Bominaar *et al.*,[263] where they have set the $a''/^1\Sigma_g^+$(II) $v' = 21$ level to be identical to $a''^1\Sigma_g^+ v' = 0$, to arrive at the values indicated in Table 2 of Ref. 263. This global offset effectively shifts the $a''/^1\Sigma_g^+$(II) potential down[266] by 5012 cm^{-1} as indicated by the dashed curve in Fig. 9.3. However, this correction is not entirely satisfactory, since the $a''^1\Sigma_g^+$ $v' = 2$ level (experimental level energy[258,264] at 103090.0(2) cm^{-1}) is then above the potential barrier. This contradicts the experimental results for the rotational constant $B' = 1.820(1)$ cm^{-1} from Ref. 258, which clearly indicate that $v' = 2$ level should be confined inside the inner well. It is then not surprising that the band origins of the outer well, for example in Bominaar *et al.*[263] as well as the perturber state in the present experiment, do not coincide with the predicted values. Improved *ab initio* calculations of the $^1\Sigma_g^+$ potentials should help in clarifying these issues.

9.4 Summary and conclusion

We have performed a high-resolution reinvestigation of the $a''^1\Sigma_g^+$– $X^1\Sigma_g^+$ system of N_2. The accuracy of most two-photon Q-branch lines at ≤ 0.001 cm^{-1}, shows a clear effect of a perturbation with a maximum shift at $J = 26$. However, the interaction is relatively weak, such that even with the present accuracy, we cannot satisfactorily resolve the issue whether the perturber state is of ${}^1\Sigma_g^+$ or of ${}^1\Pi_g$ symmetry. Based on the fact that the ${}^1\Sigma_g^+$(II) state is known to exist in this energy range we tentatively assign the perturber as either $v' = 22$ or $v' = 23$ of this outer well state of N_2.

Acknowledgement

We thank Dr. G.C. Groenenboom for clarifications on the *ab initio* calculations of the band origins, and the referees for their helpful remarks. This research was supported by the Netherlands Foundation for Fundamental Research of Matter (FOM).

Chapter 10

The hyperfine structure of $^{129}I_2$ and $^{127}I^{129}I$ in the $B^3\Pi_{0_u^+}$-$X^1\Sigma_g^+$ band system

In a double saturation spectroscopy experiment, using the radiation from one single frequency cw laser, the spectra of $^{129}I_2$ *and* $^{127}I^{129}I$ *from one saturation setup were recorded simultaneously and with respect to the spectrum of* $^{127}I_2$ *from another setup while tuning the laser. The hyperfine patterns of* $^{129}I_2$ *and* $^{127}I^{129}I$ *were analysed to determine the nuclear electric quadrupole interaction and the nuclear spin-rotation interaction parameters. Models are presented describing the observations and giving reliable predictions for the hyperfine parameters of all isotopomers.*

This chapter is published as Molecular Physics **104**, 2641–2652 (2006).

10.1 Introduction

The visible $B^3\Pi_{0_u^+} - X^1\Sigma_g^+$ system of molecular $^{127}I_2$ is widely used as a convenient reference spectrum for spectroscopic purposes, because the experimental setups to create iodine spectra are simple and the precision of 10^{-7} or sometimes better is sufficient for many purposes. Spectra for comparison with observed ones are available in form of the iodine atlas by Gerstenkorn and Luc[267–270] for linear absorption spectra, or from Doppler free spectroscopy in the atlas by Katô *et al.*[271]

Recently, some of the present authors were involved in proposing model descriptions for the rovibrational[180] and for the hyperfine structure[272] of the $B^3\Pi_{0_u^+}$–$X^1\Sigma_g^+$ system of $^{127}I_2$. Combining such models it is possible to identify observed iodine spectral lines and to predict their frequencies to better than 2 MHz in large frequency ranges. Both models have also been included in a program to predict frequencies of iodine lines, which then can be used for calibration.[273] The models are based on the data available from literature (see Ref. 272) at that time, which put restrictions on the ranges of validity, e.g. $v' = 43$ being the uppermost vibrational level in the B state.

In the meantime Chen *et al.*[274] have reported measurements beyond $v' = 42$ to higher v' in the B state for the isotopomer $^{127}I_2$. They also applied successfully a different approach to the description of the rovibrational dependence of the hyperfine parameters, which accounts for the dependence of the hyperfine interactions on the internuclear distance averaged over the vibrational motion. In that framework observations close to the dissociation limit could be modelled by including distinct electronic states sharing the same asymptote, and the resulting perturbations in the upper levels of the $B^3\Pi_{0_u^+}$.[275]

Thus new data are available offering the possibility to extend models of the hyperfine structure in the B–X system. The ultimate goal of the present study is, however, to help providing an accurate spectroscopic frequency standard based on the $B^3\Pi_{0_u^+} - X^1\Sigma_g^+$ band system for the three iodine molecular isotopomers; such a reference standard would be a factor of three more dense than the one solely based on the $^{127}I_2$ species. In addition more reliable information on the rovibronic structure of the excited $B^3\Pi_{0_u^+}$ state for those isotopomers is obtained, for the purpose of a better determination of the Born-Oppenheimer corrections, which could not be determined sufficiently precise in a previous paper.[180]

The $^{129}I_2$ and $^{127}I^{129}I$ molecules have been studied previously, although in much less detail than the main $^{127}I_2$ isotopomer. Cerny *et al.* presented an analysis of the rotational structure of the B – X system for both ^{129}I-containing isotopomers, based on a laser-induced fluorescence Fourier-transform spectroscopic study.[276] Previously, information on two excited vibrational levels in the B state of the $^{127}I^{129}I$ isotopomer had been obtained,[277] while also the hyperfine structure near 633 nm had been unravelled.[278] High precision splittings of few lines around 633 nm are tabulated in Ref. 279. Recently, in a study focusing on Raman lasing at 532 nm in I_2 some accurate information on the level structure of $^{129}I_2$ and $^{127}I^{129}I$ was obtained.[280]

In the present paper we report on systematic investigations of iodine spectra of the isotopomers $^{129}I_2$ and $^{127}I^{129}I$ covering a set of vibrational levels in the B state between $v' = 8$ and $v' = 20$ and in the ground state between $v'' = 0$ and $v'' = 5$. In these experiments hyperfine structures of many lines of the homonuclear $^{129}I_2$ and the heteronuclear $^{127}I^{129}I$ isotopomer were recorded simultaneously with $^{127}I_2$ for calibration in a double spectrometer.

The paper is organized as follows: in the next section we shall give a short outline of the experiment. A section discussing the description of the hyperfine structure follows, after which the measurements and the results on the different isotopomers will be presented. In the analysis section improved model descriptions for the hyperfine interactions are presented, which, for easy application in prediction of transition frequencies, are based on the simple Dunham series approach like in Ref. 272. While in Ref. 272 no data of the isotopomers $^{129}I_2$ or $^{127}I^{129}I$ had been included, the models presented here have been extended for use with all isotopomers. A discussion and conclusion will summarize the achievements of the paper.

10.2 Experimental

A schematic layout of the setup is shown in Figure 11.1. A stabilized cw ring-dye-laser (Spectra Physics 380D) is used as the radiation source. The dye laser is operated with Rhodamine 6G dye to access the wavelength range of 573 nm to 583 nm, while Rhodamine B dye is used for the range 610 nm to 615 nm and for some measurements near 633 nm.

Two saturated absorption setups allow for the simultaneous recording of the spectra obtained from a vapor cell containing the $^{129}I_2$ and $^{127}I^{129}I$ isotopomers with that of the main $^{127}I_2$ isotopomer in another cell. By means of this double saturation setup, the spectra of the $^{129}I_2$ and $^{127}I^{129}I$ isotopomers can be calibrated on an absolute scale using the $^{127}I_2$ resonances that have been measured at high accuracy before.[232,281] Although for the present article, focusing on the hyperfine structure of the $^{129}I_2$ and $^{127}I^{129}I$ molecules, a relative frequency calibration would suffice, the data on the ^{129}I containing species are calibrated on an absolute scale in view of a subsequent paper on a description of the rovibronic structure of the iodine molecule for all three isotopomers.

A 10-cm vapor cell containing 100% $^{127}I_2$ is used in one of the saturation setups, identical to the one used in the previous studies discussed in Refs. 281 and 232. Differential absorption is monitored, where one of the probe beams is crossed at a slight angle ($<$14 mrad) with the saturation beam. The saturating beam is modulated by a mechanical chopper at around 700 Hz and lock-in signal detection is employed. The $^{127}I_2$ cell is used at room temperature vapor pressure.

A 5-cm cell containing $^{129}I_2$ and $^{127}I^{129}I$ is used in the other saturation setup. The pump-offset saturation spectroscopy technique[282,283] is used to maximize the signal detection sensitivity. The first-order diffraction beam from an acousto-optic modulator (AOM) shifted by +75 MHz is used as the saturating beam. As a consequence of the 75-MHz frequency offset of the saturating beam with respect to the probe beams, the saturation resonances are shifted by 37.5 MHz from the real line positions.[282,283] Differential absorption signals were acquired, with one of the probe

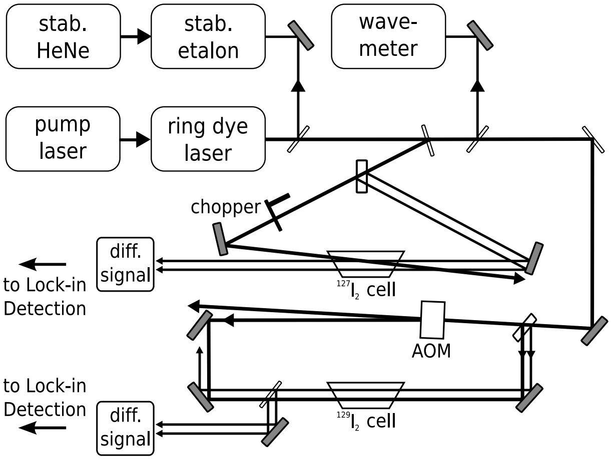

Figure 10.1 – *The experiment consists of parallel saturation spectroscopy measurements on two vapor cells, one containing* $^{129}I_2$ *(and* $^{127}I^{129}I$ *and traces of* $^{127}I_2$*) and the other containing* $^{127}I_2$*. The positions of the* $^{129}I_2$ *and* $^{127}I^{129}I$ *resonances are determined relative to the position of* $^{127}I_2$ *lines by means of a stabilized étalon.*

beams overlapped collinearly with the saturating beam. A 50-kHz modulation was imposed on the amplitude of the saturating beam and the saturation signal is retrieved by lock-in detection. The inherent sensitivity of the pump-offset technique combined with the fast modulation of the AOM results in a high detection sensitivity. With such a scheme, we could detect the strong transitions of the $^{127}I_2$ molecules that are also present in trace amounts inside this cell. These weak $^{127}I_2$ signals are compared to that obtained from the parallel $^{127}I_2$ saturation setup in order to check for possible frequency shifts between the two saturation setups.

A wavemeter is used to coarsely tune the laser to the resonances. Relative frequency calibrations are carried out by employing the transmission peaks of a 50-cm Fabry-Perot étalon. The étalon temperature and pressure is stabilized and its length is actively locked to the wavelength of a Zeeman-stabilized He-Ne laser. The étalon free spectral range FSR is measured at the start of every measurement session, which has a typical value of 148.96(1) MHz with small day to day variations. For the absolute frequency calibration of the of the $^{129}I_2$ and $^{127}I^{129}I$ lines a nearby lying $^{127}I_2$ line was chosen as reference, which has been measured previously in Refs. 281 and 232. Since the largest separation was less than thirty étalon fringes, this procedure results in a sub-MHz frequency uncertainty, in addition to the uncertainty of the $^{127}\mathrm{I}_2$ calibration, which is typically 1 MHz (1σ). The relative frequency scale is mainly determined by some remaining non-linearity of the laser scan, that is left over after a computerized linearisation procedure; it is also of sub-MHz order.

10.3 Hyperfine structure

Basic considerations

The hyperfine structure of the iodine molecule is described by an effective Hamiltonian:[284]

$$H_{\mathrm{hfs,eff}} = H_{\mathrm{NEQ}} + H_{\mathrm{SR}} + H_{\mathrm{SS}} + H_{\mathrm{TS}}. \tag{10.1}$$

$H_{N\mathrm{EQ}}$, H_{SR}, H_{SS} and H_{TS} represent the (effective) nuclear electric quadrupole, the nuclear spin-rotation, the scalar nuclear spin-spin and the tensorial nuclear spin-spin interactions. The matrix elements of each of these terms can be separated into a product of a geometrical factor g_i and a hyperfine parameter, i.e. eqQ, C, δ or d:

$$\langle \alpha', F | H_{\mathrm{hfs,eff}} | \alpha, F \rangle = eqQ \cdot g_{eqQ} + C \cdot g_{\mathrm{SR}} + \delta \cdot g_{\mathrm{SS}} + d \cdot g_{\mathrm{TS}} \tag{10.2}$$

α represents a set of quantum numbers characterising the molecular level, which will be specified later, and F is the total angular momentum. The g_i are functions of appropriate angular momentum quantum numbers of the system, and can be calculated with spherical tensor algebra. The hyperfine parameters are usually determined experimentally from the measured hyperfine structure of a rovibrational transition.

For calculation of the factors g_i different coupling schemes were applied. The homonuclear molecules $^{127}\mathrm{I}_2$ and $^{129}\mathrm{I}_2$ are characterized by a wave function $|\Omega v(I_1 I_2) IJFM_F >$.[284] The two nuclear spins $\vec{I}_1$ and $\vec{I}_2$ couple to a total nuclear spin $\vec{I}$, which is then coupled with the rotational angular momentum $\vec{J}$ to give a total angular momentum $\vec{F}$. Ω is the projection of the total electronic angular momentum on the internuclear axis and characterizes the electronic state, while v is the vibrational quantum number. Here the computer code described in more detail in Ref. 285 was applied.

For the spectra of the heteronuclear species a coupling scheme corresponding to the notation $|\Omega v(JI_1)F_1 I_2 FM_F >$ is used, and all simplifications due to symmetry like in the homonuclear case are absent. Moreover, for each nucleus appropriate hyperfine parameters must be used, which means $eqQ^{(127)}$, $eqQ^{(129)}$, $C^{(127)}$, $C^{(129)}$, ... values for each electronic state. An appropriate computer code was available.

The corresponding matrix elements are taken from Ref. 286. The nuclear spin-spin interactions are not included. Due to its small contribution of not more than 400 kHz to the hyperfine splitting and in view of the limited signal-to-noise ratio in our spectra this neglect does not change the results on the molecular parameters.

Providing the hyperfine parameters for both states, and the rotational angular momentum quantum number J'' and J', the computer codes calculate the hyperfine splitting frequencies and also relative intensities of the hyperfine lines, using for the dipole matrix element the eigenvectors determined during the diagonalisation of the hyperfine interaction matrix for each state, extending the rotational space up to $\Delta J = 0, \pm 2$.

It was verified, that the code for heteronuclear species gives the same results within numerical accuracy as the code for the homonuclear species for situations, where the results should coincide.

Rovibrational dependence of the hyperfine parameters

The hyperfine parameters are products of an electronic part and the expectation value of the corresponding nuclear moment. The electronic part depends on the vibrational and rotational quantum numbers of the levels involved. The form for the rovibrational dependence is based on that used in Ref. 272. For convenience we give a short outline of the nomenclature.

The functional forms of the effective hyperfine parameters were explicitly given by Broyer *et al.*[284] Following their paper we use for both the ground state $X^1\Sigma_g^+$and the exited state $B^3\Pi_{0_u^+}$, which are Ω=0 states, representations of the form:

$$\chi(v,J) = \chi^{(1)}(v,J) + \sum_p \frac{\chi^{(p)}(v,J)}{\Delta E^J_{v,v_p}} \cdot \langle v|v^{(p)}\rangle \tag{10.3}$$

where χ stands for eqQ, C, δ or d. $\chi^{(1)}$ is the first order contribution of the discussed electronic state (B or X) and $\chi^{(p)}$ is a second order contribution from a perturbing state p with energy difference $\Delta E_{v,v_p}$ between the levels (v,J) and (v_p,J) and the overlap integral $\langle v|v_p\rangle$ of the two vibrational states. This form is a simple approximation for the case where the electronic matrix element will have only a weak dependence on the nuclear separation. $\chi^{(1)}$ is the expectation value of the generally R dependent interaction for the specific rovibrational state (v,J). This is represented here in the form of a Dunham series in v and J,

$$\chi(v,J) = \sum_{l,k} \chi_{lk} \cdot (v+1/2)^l \cdot [J(J+1)]^k \tag{10.4}$$

Few members of this series are usually sufficient for describing the set of experimental data. The coefficients χ_{lk} can also be related to the potential of the electronic state, and a power expansion of χ with the internuclear distance R can be derived. Such approach was recently used by Chen *et al.*[274,275] and earlier by Spirko.[287] For the sake of simplicity of recalculation by other researchers, however, we shall follow the Dunham approach.

The sum over the perturbing states contains two different categories: In the first one, where the electronic state p is close by, the energy denominator plays an important role in the functional form of the parameter. In the second one, the perturbing state is so far away that its contribution does not vary significantly with v_p, so that this part is barely distinguishable from the functional form of $\chi^{(1)}(v,J)$. In the iodine molecule the states mainly perturbing the $X^1\Sigma_g^+$share the same atomic asymptote as X and are weakly bound. Thus the energy denominator can be approximated by $\Delta E^J_{v,vp} \approx E_{vJ} - \overline{E}_p(3/2,3/2)$, where $\overline{E}_p$ is an average of the perturbing levels and will have a value close to that of the atomic asymptote ${}^2P_{3/2}+{}^2P_{3/2}$. Also the overlap integral $\langle v|v_p\rangle$ will not vary strongly with v_p in this case, because the part of the wave function for small nuclear separation will almost stay constant while varying v_p up to the dissociation limit, so that $\chi^{(p)} \cdot \langle v|v_p\rangle$ can be approximated by a short Dunham expansion.

Quite similarly we approximate the functional form of the hyperfine parameters of the B state, the dissociation asymptote now being ${}^2P_{1/2}+{}^2P_{3/2}$ of iodine, and again we introduce as an average energy for the perturbing state $\overline{E}_p(1/2,3/2)$. In total, we get for the nuclear electric quadrupole interaction ($\chi = eqQ$) and for the nuclear spin-rotation interaction ($\chi = C$) the formula

$$\chi(v,J) = \sum_{lk} \chi^{(1)}_{lk} \cdot (v+1/2)^l \cdot [J(J+1)]^k + \sum_p \frac{\sum_{lk} \chi^{(p)}_{lk} \cdot (v+1/2)^l \cdot [J(J+1)]^k}{E_{vJ} - \overline{E_p}}, \tag{10.5}$$

$\overline{E_p}$ stands for $\overline{E}_p(3/2,3/2)$ or $\overline{E}_p(1/2,3/2)$.

The derivation in Ref. 284 of the second order contributions of the scalar and tensorial spin-spin interactions, i.e. the parameters δ and d, reveals that they have common contributions due to the perturbing states involved. Here we have to consider $\Omega_p = 0$ and 1. In the former case both contributions differ in sign, in the latter case by a factor of 1/2. This gives the following formulae for the two interaction parameters

$$\begin{aligned}\delta = &\sum_{lk} \delta_{lk} \cdot (v+1/2)^l \cdot [J(J+1)]^k \\ &+ \frac{\sum_{lk} \chi_{lk}^{(\Omega=0)} \cdot (v+1/2)^l \cdot [J(J+1)]^k}{E_{v,J} - \overline{E_{\Omega=0}}} \\ &+ \frac{\sum_{lk} \chi_{lk}^{(\Omega=1)} \cdot (v+1/2)^l \cdot [J(J+1)]^k}{E_{v,J} - \overline{E_{\Omega=1}}} \\ &+ \eta \cdot e^{-\frac{(E_{v,J}-E_c)^2}{W}}\end{aligned} \tag{10.6}$$

$$\begin{aligned}d = &\sum_{lk} d_{lk} \cdot (v+1/2)^l \cdot [J(J+1)]^k \\ &- \frac{\sum_{lk} \chi_{lk}^{(\Omega=0)} \cdot (v+1/2)^l \cdot [J(J+1)]^k}{E_{v,J} - \overline{E_{\Omega=0}}} \\ &+ \frac{1}{2}\frac{\sum_{lk} \chi_{lk}^{(\Omega=1)} \cdot (v+1/2)^l \cdot [J(J+1)]^k}{E_{v,J} - \overline{E_{\Omega=1}}} \\ &+ \frac{\eta}{2} \cdot e^{-\frac{(E_{v,J}-E_c)^2}{W}}\end{aligned} \tag{10.7}$$

where the second and third terms in each equation describe the effective perturbations due to $\Omega = 0$ states and $\Omega = 1$ states. The fourth terms in both equations were introduced in Ref. 272 as a simplified Gaussian representation with an amplitude η and a width of $\sqrt{W}$ for the local perturbation of the $B^3\Pi_{0_u^+}$ crossed by a nonbinding $1_u(^1\Pi)$ state (see e.g. Refs. 288,289) at E_c ≈16800 cm^{-1}. This is the only local perturbation accounted for explicitly in the formulas.

The above representation does not explicitly show the dependence on the nuclear moments. No distinction was made yet for including different isotopomers. The extension of the above set of formulae to the case of different isotopomers can be done by splitting off the nuclear moments from the rovibrational representations. The Dunham theory for the rovibrational motion also reveals dependences of the expansion parameters on the reduced mass. For the hyperfine parameters this is not straightforward. We checked the importance of mass corrections and found that within the present data set the results are not influenced by a Dunham-like dependence of the χ_{lk} on the reduced masses. Thus it is omitted in the formulas given earlier. The energies $E_{v,J}$ are calculated from the Dunham parameters in Ref. 290

Table 10.1 – *Ratios of nuclear moments used in the fits of the hyperfine parameters*

nuclear moment	value	reference
$\mu^{(127)}$	2.8090(4)[a]	Ref. 291
$\mu^{(129)}$	2.6173(3)[a]	Ref. 291
$\frac{^{129}Q}{^{127}Q}$	0.701213(15)	Ref. 292
$\gamma_\mu^{(127)}$	1	
$\gamma_\mu^{(129)}$	0.6655	
$\gamma_Q^{(127)}$	1	
$\gamma_Q^{(129)}$	0.701213	

[a] in units of μ_N (nuclear magneton)

for the case of $^{127}I_2$ and are used without mass relations for all isotopomers. $\overline{E_p}$, $E_{v,J}$ and E_c are referred to $E_{v''=0,J''=0}$ of the ground state.

The isotopic dependence by the nuclear moments is conveniently included by writing the hyperfine parameters $\chi^{(i)}$ for the isotope i in the following form:

$$\chi^{(i)}(v,J) = \chi^{(ref)} \cdot \gamma^{(i)}_{Q,\mu} \tag{10.8}$$

where $\chi^{(ref)}$ is the corresponding parameter for the reference isotopomer $^{127}I_2$ and $\gamma^i_Q = \frac{Q^{(i)}}{Q^{(ref)}}$ and $\gamma^i_\mu = \frac{\mu^{(i)}/I_1^{(i)}}{\mu^{(ref)}/I_1^{(ref)}}$ are the ratios of the nuclear electric quadrupole moments and of the nuclear dipole moments referred to the nuclear spin quantum numbers I_1. The numerical values are given in Table 10.1.

In this way the numbers given later can be used directly for $^{127}I_2$ with $\gamma = 1$, while for the other isotopomers the factors γ are different from one. These modifications are applied to the nuclear electric quadrupole and the nuclear spin-rotation interaction, where the nuclear moments enter linear. The nuclear spin-spin interaction is a product of two matrix elements containing a nuclear magnetic moment. So here the square of the ratio, $(\gamma^{(i)}_\mu)^2$, must be used.

Finally, we point out that by measuring optical transitions usually (for $J \geq 10$) only differences between the hyperfine parameters of X and B state can be determined, because the corresponding parameters of the two states are strongly correlated, if derived from transitions with selection rules $\Delta F = \Delta J$, which is the case for most of the existing data. By fitting spectra one obtains differences

$$\begin{aligned} \Delta eqQ &= eqQ_{\mathrm{B}} - eqQ_{\mathrm{X}} \\ \Delta C &= C_{\mathrm{B}} - C_{\mathrm{X}} \\ \Delta \delta &= \delta_{\mathrm{B}} - \delta_{\mathrm{X}} \\ \Delta d &= d_{\mathrm{B}} - d_{\mathrm{X}} \end{aligned} \tag{10.9}$$

The correlation can be broken, however, if hyperfine structures of low J'' lines are measured, or the signal-to-noise ratio is sufficient to observe the weak $\Delta F = 0$ and $\Delta F = -\Delta J$ transitions, or cross-over resonances of saturation spectroscopy. Such data were included in Ref. 272 and are included also in the data sets used here. This makes it possible to distinguish the hyperfine interaction of upper and lower electronic state as is done in this paper.

Due to the nuclear spins $I_1 = \frac{5}{2}$ for $^{127}\mathrm{I}$ and $I_1 = \frac{7}{2}$ for $^{129}\mathrm{I}$, the full hyperfine pattern of a transition with selection rule $\Delta F = \Delta J$ of $^{127}\mathrm{I}_2$ exhibits 15 hyperfine components when J'' is even and 21 when J'' odd, for $^{129}\mathrm{I}_2$ we have 28 resp. 36 components. Transitions of the mixed isotopomer $^{127}\mathrm{I}^{129}\mathrm{I}$ always have 48 hyperfine components, independent of J'' even or odd. The hyperfine components in the spectra are assigned by labels a_1 to a_n from lower to higher frequencies, n being the maximum number of components depending on J'' even or odd and on the isotopomer.

10.4 Measurements and results

Spectra from both saturation setups were observed simultaneously, with the issue to cover as many bands as possible in the range supplied by the laser available. In different periods of measurements, ranges around 633 nm and 612 nm, additionally from 610 nm to 615 nm and from 573 nm to 583 nm were recorded and lines of rovibronic bands were observed involving v'' from 0 to 5 and v' from 9 to 20 for all three isotopomers. An example of a simultaneously recorded spectrum is shown in Figure 11.2. As discussed in Section 11.2 the ranges were selected such that in each scan a hyperfine component with a known absolute frequency calibration was included.[232,281] First, a relative frequency scale was established from the markers of the stabilized Fabry-Perot cavity by performing a spline-fit and a linearisation procedure to the series of markers. Subsequently, this scale was converted into an absolute frequency scale by linking it to one of the hyperfine components known at high accuracy.

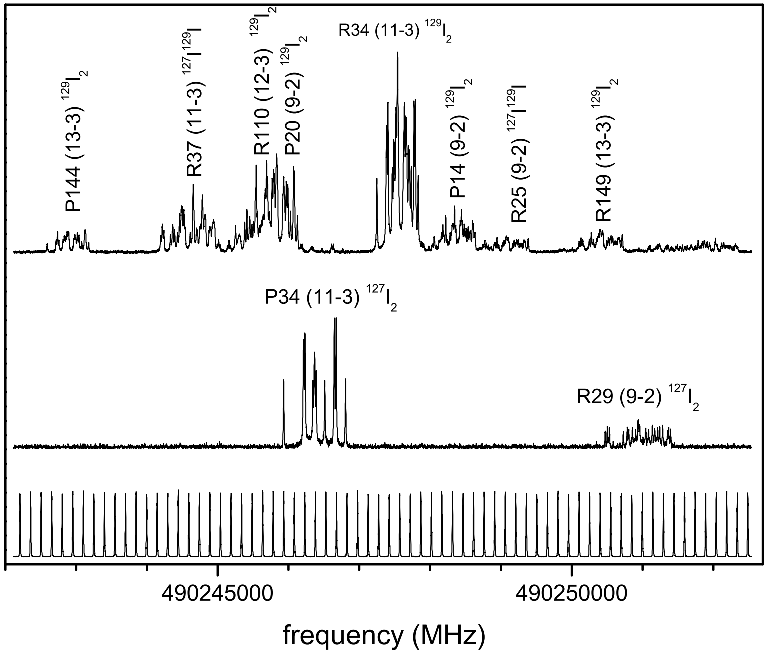

Figure 10.2 – *Example of spectra at 611 nm, recorded around P34 (11-3) of* $^{127}I_2$. *The lowest trace shows the markers used for the frequency scale, the middle trace is the pure* $^{127}I_2$ *spectrum, while the upper trace is from the* $^{129}I_2$ *cell and shows in addition lines due to the mixed isotopomer and weak signals from* $^{127}I_2$

.

Fitting of the hyperfine structures of the transitions was performed by programs, in which the hyperfine codes described in Section 10.3 were embedded to create calculated spectra from the list of hyperfine splittings and relative intensities. Each hyperfine component is represented by a standard line shape profile[285] of the form

$$f(x) = \frac{1}{1 + a(x - x_0)^2 + (1 - b - a)(x - x_0)^4 + b(x - x_0)^6} \tag{10.10}$$

with $x = \frac{2\nu}{\Delta\nu}$ as a reduced frequency variable and $\Delta\nu$ being the full width at half maximum (FWHM), and $x_0 = \frac{2\nu_0}{\Delta\nu}$ is the line position. Having calculated a hyperfine pattern by giving values to a, b, FWHM, and the hyperfine parameters for each state, additional parameters are necessary for intensity scaling and background of the calculated structure for best coincidence with the observed pattern.

Fitting of the hyperfine parameters is done using the MINUIT package,[293] which minimizes the function

$$\chi^2 = \sum_i w_i \cdot (obs_i - calc_i)^2 \tag{10.11}$$

by adjusting the variable parameters: obs_i is the measured signal at position i, $calc_i$ the corresponding calculated one, w_i is the weight for that data point. The weights are determined by the program from a part of the spectrum with only background, in order to take the signal to noise ratio of the measurement into account, and is usually the same for all i. It can be set to zero within a fit for chosen data points to be excluded from the fit. Such approach was used in cases when the line to be fitted was blended with one or more other transitions.

For all of our measurements, the selection rule $\Delta F = \Delta J$ applies, so that mainly the differences of the hyperfine parameters are significant, as explained in Section 10.3. For good starting values, we calculated the ground state hyperfine parameters using the formulas given in Ref. 272 with isotopic corrections according to Equation (10.8) and kept them fixed. Moreover, checking the frequency contributions by the nuclear spin-spin interaction to the hyperfine splitting in the range of quantum numbers relevant in our present measurements, they turn out to be less than 400 kHz. This is significantly smaller than the experimental uncertainty of the present experiment, typically about 2 MHz, so we cannot expect any reliable determination of such parameters from our spectra. Therefore, again applying the formulas given in Ref. 272 and isotopic corrections we calculated the nuclear spin-spin parameters also for the upper state and kept them fixed for the homonuclear case in all fits, while in the heteronuclear case this interaction was not taken into account at all. Similarly the number of the other parameters could be reduced. It turned out that *b* of the line shape (Equation 10.10) is not significant, so it was set to zero. Only the parameters *a* and FWHM needed to be adjusted, and the intensity scaling and background, and a global frequency shift as well.

For $^{127}I_2$ we had a fairly long cell available. So the pump beam is attenuated due to Doppler-broadened linear absorption until it crosses with the probe beam. Thus in the peak region of the Doppler broadened line the pump beam is weaker than in the wings, giving less saturation. Also the probe beams are attenuated by the same phenomenon, and this was not fully compensated in the experimental setup. As can be seen in Figure 11.3, the hyperfine components are sitting on some wider background, and moreover the saturation signals are weaker in the middle of the structure than expected when compared to calculated ones or to the corresponding line in the atlas by Katô *et al.*[271] For correction of the background of the probe beam a Gaussian function was introduced with a FWHM comparable to the width of the Doppler broadened absorption line. For additional correction of the intensity attenuation of the pump beam another Gaussian function, sharing the parameter center frequency and FWMH with the background correction of the probe beam, but with an independent intensity factor, was multiplied with the calculated intensities of the hyperfine components. With these additional means good agreement between observed and calculated spectra for $^{127}I_2$ could be achieved. In Figure 11.3 a transition with even J'' is shown, which exhibits 15 hyperfine components. For the fit in Figure 11.3 all of the above mentioned corrections to background and intensity have been applied. The lower trace displays $(obs. - calc.)$ and one can see small deviations, especially around the component of lowest frequency, while other components fit better. Such behaviour was observed sometimes even more pronounced, and also for the other isotopomers. We attribute this to slight nonlinearities in the frequency scale, caused by deviations of the laser scan from linearity between two markers separated by 150 MHz, which we cannot correct for.

We checked the effect of the background and intensity correction on the determination of the hyperfine parameters. It is smaller than the scatter of the parameter values derived from different records of the same line, so that any residual effect can be considered as being absorbed by the experimental uncertainty for cases when this correction was not applied. In Figure 11.4 a fit of the R34 (11-3) line of $^{129}I_2$ is shown. The lower trace shows that the fit is as good as in Figure 11.3. The total extension of the structure is narrower than in the $^{127}I_2$ case, as the hyperfine interaction is smaller. Here no frequency dependent background or intensity corrections were necessary due to the short length of the cell used. An even J'' results in a structure consisting of 28 components, of which not all are resolved. Figure 11.5 displays the fit of the R37 (11-3) line of $^{127}I^{129}I$. Only very slight deviations are shown by

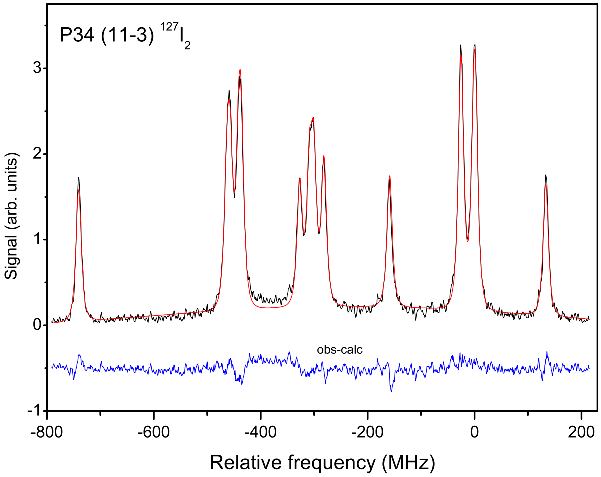

Figure 10.3 – *Fit of P34 (11-3) line of* $^{127}I_2$*. A difference between observed and calculated spectrum is only obvious around -400 MHz. The lower trace shows the residuals from the fit, shifted down from zero for better visibility.*

the lower trace displaying the residuals from the fit. This structure has 48 components independent of J'' even or odd, which overlap to a large degree, indicating directly the need of line profile fitting for the hyperfine analysis. Again in this case no frequency dependent background or intensity corrections were applied.

The bands observed in this work cover vibrational levels $8 \leq v' \leq 20$ in the upper state and $0 \leq v'' \leq 5$ in the lower state. The range of the rotational quantum number J'' is from 10 to 150 for the $^{129}I_2$ isotopomer, while the ranges for $^{127}I_2$ and $^{127}I^{129}I$ are a bit smaller. Altogether, more than 120 eqQ_B parameters of $^{127}I_2$, more than 200 for $^{129}I_2$ and more than 170 for $^{127}I^{129}I$ have been determined. The same numbers apply to new C_B values.

The tables of the individual hyperfine parameters will not be included here due to their length. The eqQ data are given in part 1 of the electronic supplement,[294] while the new data of the spin-rotation parameter C are collected in part 2. The values in the lists are given as ΔeqQ and ΔC according to Equations (10.9), respectively.

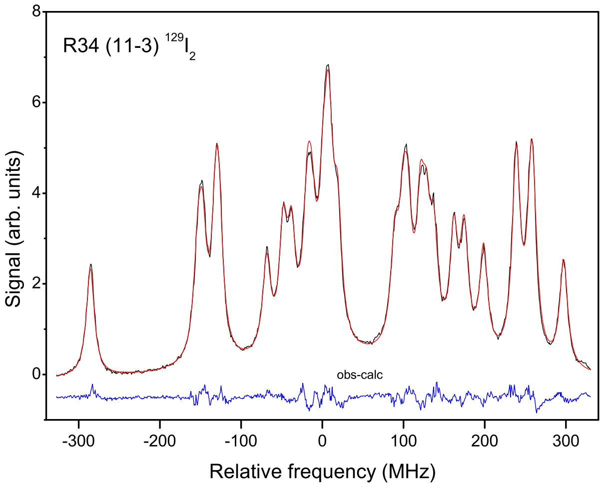

Figure 10.4 – *Fit of R34 (11-3) band of* $^{129}I_2$. *The lower trace shows the residuals from the fit, shifted down from zero for better visibility.*

When a certain line was recorded more than once, we averaged the resulting eqQ_B and C_B and give the standard deviation as the uncertainty. For hyperfine parameters inferred from single measurements we give uncertainties which are estimated by comparison with typical cases of the previously described situation of more than one line, according to the signal to noise ratio of the experimental spectrum and the quality of the fit, which also accounts for blends with other lines. Typical uncertainties for ΔeqQ are 2 MHz and for ΔC are 2 kHz.

10.5 Analysis of hyperfine functions

The new data of this paper and recent data from literature[274,295–298] have been used to derive a set of formulas, describing the rovibrational dependence of the hyperfine parameters. Based on the data given in Ref. 272, improved data sets have been established. As far as the original frequencies were given in literature, the hyperfine parameters were refitted using our own hyperfine code.

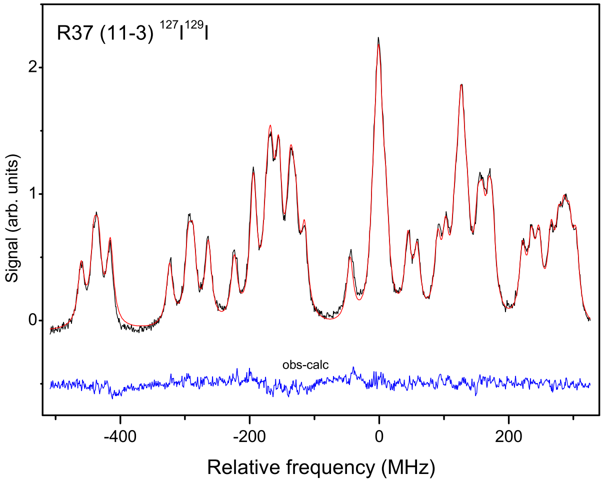

Figure 10.5 – *Fit of R37 (11-3) band of* $^{127}I^{129}I$. *The lower trace again indicates the residuals from a fit, shifted down from zero for better visibility.*

Usually, we found good agreement with the residuals and the hyperfine parameters given in the original papers. Only in the case of R121 (35-0) of $^{127}I_2$ given in Ref. 296 we found a deviation. We were able to fit all components including a_8 and a_{12} with a reasonable standard deviation of 2.2 kHz. This is in contrast to the fit given in that paper, where these two components show deviations of about +40 MHz and -40 MHz, respectively. These deviations might be an artefact of the program code used there.

The data by Chen *et al.*[274] extend the range of quantum states in the upper state substantially, so they will extend the validity of the models to higher vibrational levels. However, for levels higher than $v' = 55$ perturbations were observed,[274] which have been attributed to electronic states sharing the same asymptote as the B state. Actually even for $v' = 42$ and higher levels some irregularities were observed by increased standard deviations of their fits and attributed to local perturbations by the $1_g(^1\Pi_g)$ state, but they were still small.

The perturbations cannot be described by our simple models, so for the sake of reliable prediction covering a large range as reference spectra, we prefer to keep some distance to the more heavily perturbed vibrational quantum numbers range. Thus

Table 10.2 – *Parameters for representation of* δ_{B} *and* d_{B} *according to eqs. (10.6,10.7) from the combined fit of scalar and tensorial nuclear spin-spin-interaction parameters. For the ground state* δ_{X}*=3.705 kHz,* d_{X}*=1.524 kHz are used.*

parameter	value	unit
δ_{00}	20.88	kHz
d_{00}	25.93	kHz
$\chi_{00}^{(\Omega=0)}$	39698	kHz/cm^{-1}
$\chi_{21}^{(\Omega=0)}$	$0.2475 \cdot 10^{-3}$	kHz/cm^{-1}
$\chi_{00}^{(\Omega=1)}$	106923	kHz/cm^{-1}
$\chi_{21}^{(\Omega=1)}$	$0.1712 \cdot 10^{-3}$	kHz/cm^{-1}
η	-22.41	kHz
$\overline{E}_{\Omega=0}$	19973	cm^{-1}
$\overline{E}_{\Omega=1}$	20534	cm^{-1}
E_c	16787	cm^{-1}
W	260267	(cm^{-1})^2

we restrict here the ranges of our description to vibrational levels $0 \leq v'' \leq 17$ for the $\mathrm{X}^1\Sigma_g^+$state and $0 \leq v' \leq 53$ for the $\mathrm{B}^3\Pi_{0_u^+}$state.

Nuclear spin-spin interaction

Several new measurements around 532 nm, all of bands with $32 \leq v' \leq 36$ have been published,[295–298] and new data are available for $v' \geq 42$.[274] From the frequency tables in Ref. 279 hyperfine parameters for $^{129}\mathrm{I}_2$ were fitted, but only the data for the P69 (12-6) line of $^{129}\mathrm{I}_2$ are sufficiently accurate and complete for fitting reliable nuclear spin-spin parameters. These were also introduced to the data set. No parameters from the present measurements were included, because they could not be determined precisely enough. At the expense of two addional parameters for the upper state compared to our previous formulas (remark: erroneously the formulas (12) and (13) in Ref. 272 read $\Delta\delta$ and Δd, they should, however read δ_{B} and d_{B}), all data up to $v' = 53$ can be described by formulas (10.6) and (10.7), using the parameters listed in Table 11.1.

The ground state parameters were not changed, due to lack of new information on the ground state, δ_{X}=3.705 kHz, d_{B}=1.524 kHz are used. The value of δ_{B} of R30 (42-0) has been excluded from the fit,[274] because due to its different sign compared to the other ones it seems to be perturbed. The data were weighted with their experimental uncertainties, the standard deviation of the fit is 1.6 kHz. To estimate the contributions of the nuclear spin-spin interactions to the total hyperfine splitting, we give rules of thumb for $^{127}I_2$ here. The contributions of the nuclear spin-spin interaction increase in magnitude with the level energy increasing towards the dissociation limit. While the total contribution to e.g. the component a_2 is 200 kHz for $v' = 11$, it amounts to 1.1 MHz for the same component of P89 (53-0), which is the transition with the highest level in the fit. Similar magnitudes are calculated for a_{20}, while the contribution to a_{13} is about a factor of two less. This applies to the mentioned hyperfine components for odd J''. For even J'' the corresponding components are a_1, a_{10} and a_{15}, the contributions are of similar order. This is the magnitude of error one has to take into account if the interaction is completely neglected, as was done sometimes in literature.

Looking at the fit residuals, despite overall good agreement few larger deviations of about 10 kHz occur. Taking such value as an uncertainty of prediction of $\Delta\delta$ or Δd, the resulting frequency uncertainty would be not larger than 65 kHz for component a_1 (a_2), 25 kHz for $a_{10}(a_{13})$ and 50 kHz for $a_{15}(a_{20})$ for even J''(odd J'') in the range of quantum numbers given above.

Nuclear spin-rotation interaction

There are the new high precision data from literature[274,279,295–299] and new data from the present measurements. The data set for the fit comprises about 640 C_B and ΔC values of $^{127}I_2$, $^{127}I^{129}I$ and $^{129}I_2$. For the X ground state no new data exist, so those parameters are unchanged compared to Ref. 272, and were kept fixed in the fit. For the upper state we had to introduce two new parameters in the rovibrational dependence of the terms describing the perturbation from the electronic states sharing the same asymptote with the B state, in order to obtain a convincing fit. The parameters for representations of C_X and C_B due to Equation (10.5) are listed in Table 10.3. In order to give practical estimations of the prediction uncertainties, the sensitivity of different hyperfine components to changes of the nuclear spin-rotation interaction parameter was inspected for the main isotopomer $^{127}I_2$. Least sensitive are components $a_1(a_2)$, $a_{10}(a_{13})$ and $a_{15}(a_{20})$ in case of even (odd) J''. The contribution of the spin-rotation interaction increases with v' towards the dissociation limit. However, for P89 (53-0), which involves the highest level in the fit, the total contribution of the nuclear spin-rotation to a_2 is only 1.2 MHz, to a_{13} is 3.2 MHz and for a_{15} we find 6.3 MHz. Taking an experimental uncertainty of 1 kHz for ΔC, even for the lines with highest upper levels a frequency uncertainty amounts to changes of less than 15 kHz for those hyperfine components. Thus these are recommended for the pur-

Table 10.3 – *Parameters for representation of* C_X *and* C_B *according to eq. (10.5) from the fit of nuclear spin-rotation-interaction parameters.*

parameter	value	unit
$X^1\Sigma_g^+$:		
$\chi_{00}^{(1)}$	1.9245	kHz
$\chi_{10}^{(1)}$	0.01356	kHz
$\chi_{00}^{(p)}$	-15098	kHz/cm^{-1}
E_p	12340	cm^{-1}
$B^3\Pi_{0_u^+}$:		
$\chi_{00}^{(1)}$	28.89	kHz
$\chi_{10}^{(1)}$	$0.9234 \cdot 10^{-1}$	kHz
$\chi_{01}^{(1)}$	$0.2241 \cdot 10^{-2}$	kHz
$\chi_{11}^{(1)}$	$0.1027 \cdot 10^{-4}$	kHz
$\chi_{00}^{(p)}$	36672	kHz/cm^{-1}
$\chi_{10}^{(p)}$	-3388	kHz/cm^{-1}
$\chi_{01}^{(p)}$	9.7985	kHz/cm^{-1}
$\chi_{11}^{(p)}$	-0.2201	kHz/cm^{-1}
E_p	20140	cm^{-1}

pose of calibration. In contrast, the most sensitive components are $a_2(a_1)$ for even (odd) J'', where the contribution of the nuclear spin-rotation interaction, e.g. for P89 (53-0), a_1, is in total 217 MHz.

Nuclear electric quadrupole interaction

The new high precision data from literature[274,279,295–299] have been included in the data set, together with new data from the present investigations, for the fit of the rovibrational dependence of the interaction parameters. To account properly for data with largely different uncertainty, a weighted least squares fit was used. Altogether more than 650 eqQ_X, eqQ_B and ΔeqQ values for all three isotopomers have been included in the new data set. For the upper state we need to introduce two more parameters to cover the extended vibrational range with good accuracy. The ground state parameters were also fitted, which improved the χ^2 of the fit by a factor of two. The results for $eqQ_X(v'',J'')$ and $eqQ_B(v',J')$ are given in Table 10.4. The standard deviation of the fit is 13 kHz, mainly determined by the high precision

Table 10.4 – *Parameters for representation of* eqQ_X *and* eqQ_B *according to eq. (10.5) from the fit of the nuclear quadrupole interaction parameters. For the ratios of nuclear quadrupole moments see Table 10.1*

parameter	value	unit
$X^1\Sigma_g^+$:		
$\chi_{00}^{(1)}$	-2452.285	MHz
$\chi_{10}^{(1)}$	-0.5474	MHz
$\chi_{20}^{(1)}$	$0.4487 \cdot 10^{-1}$	MHz
$\chi_{01}^{(1)}$	$-0.2089 \cdot 10^{-3}$	MHz
$\chi_{11}^{(1)}$	$0.6965 \cdot 10^{-5}$	MHz
$B^3\Pi_{0_u^+}$:		
$\chi_{00}^{(1)}$	-488.086	MHz
$\chi_{10}^{(1)}$	-1.83777	MHz
$\chi_{30}^{(1)}$	$0.99774 \cdot 10^{-4}$	MHz
$\chi_{50}^{(1)}$	$0.80818 \cdot 10^{-8}$	MHz
$\chi_{01}^{(1)}$	$-0.14020 \cdot 10^{-3}$	MHz
$\chi_{11}^{(1)}$	$-0.32217 \cdot 10^{-5}$	MHz
$\chi_{21}^{(1)}$	$0.2716 \cdot 10^{-7}$	MHz
$\chi_{02}^{(1)}$	$-0.3377 \cdot 10^{-9}$	MHz

data. In Figure 11.6 the fit residuals are shown. We have restricted them to the high precision data only for better overview. Most of the data deviate from the fit by less than 0.5 MHz. Two of the measurements by Ref. 299 (P78 (1-9), R113 (3-10)) of $^{127}I_2$ were excluded, as the deviations were about 10 times their claimed accuracy. If the deviations were due to perturbations, they could not be described with our models.

Overall, the fit of eqQ describes the high precision data fairly well. The same applies to the data gathered in this work. For all three isotopomers, they generally agree very well with the model description within their uncertainty limits.

For using the formulas above for prediction of hyperfine splittings, we give an estimation of the expected prediction uncertainty for $^{127}I_2$. From the discussion on the nuclear spin-rotation interaction in Section 10.5 the hyperfine components $a_1(a_2)$, $a_{10}(a_{12})$ and $a_{15}(a_{20})$ were identified and recommended as being least sensitive to uncertainties of ΔC. Out of these, the component $a_{10}(a_{12})$ for even(odd J'') lines are those with smallest energy contribution by the nuclear electric quadrupole in-

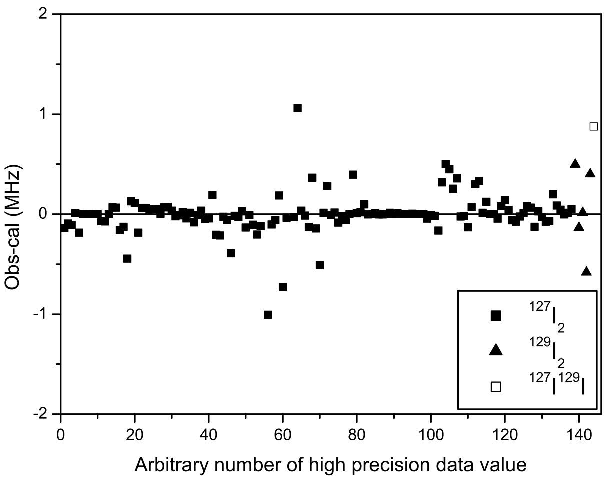

Figure 10.6 – *Fit residuals of fit of nuclear electric quadrupole interaction, ordered by number of data value. The values from 76 to 97 correspond to the high precision data from around 532 nm and have the highest weight in the fit.*

teraction, which is roughly around 100 MHz. Typical values of ΔeqQ are 2000 MHz for $^{127}I_2$. Thus the uncertainties in the prediction of ΔeqQ will convert to frequency uncertainties of that hyperfine component by dividing by about a factor of 20, and factors of 4 and 5 for $a_1(a_2)$ and $a_{15}(a_{20})$. Thus a change of ± 1 MHz of ΔeqQ gives ± 0.25 MHz for $a_1(a_2)$, ± 0.05 MHz for $a_{10}(a_{13})$ and ± 0.2 MHz for $a_{15}(a_{20})$ in the range of vibrational quantum numbers specified.

Combining the uncertainties for the hyperfine interactions, finally an uncertainty of less than 60 kHz can be expected for the prediction of component a_{10} (even J'') resp. a_{13} (odd J''), which is the best one of those recommended for calibration purposes.

10.6 Discussion and conclusion

The hyperfine structures of rovibronic lines of the $B^3\Pi_{0_u^+} - X^1\Sigma_g^+$ system of the isotopomers $^{127}I_2$, $^{127}I^{129}I$ and $^{129}I_2$ have been recorded by saturation spectroscopy. The parameters of the relevant hyperfine interactions have been extracted by combined fits of calculated spectra to the measured ones. The hyperfine parameters obtained have been used together with data known from literature in models, which describe the dependence of the hyperfine parameters on vibration and rotation in both electronic states for all three isotopomers with good precision. The models predict hyperfine parameters which can be used to calculate line positions within a hyperfine pattern. For reference purposes the components a_1,a_{10}, and a_{15} for (even J''), and a_2, a_{13}, and a_{20} for (odd J'') of $^{127}I_2$ are recommended, because they have only small dependence on the magnetic hyperfine interactions. The uncertainty of those lines is governed by the uncertainty of the description of the nuclear electric quadrupole interaction, and as a rule of thumb will be less than 60 kHz for a_{10} or a_{13} in case of even J'' or odd J''. This is sufficiently precise for prediction of frequencies of hyperfine transitions, which reach few MHz accuracy when combined with appropriate models for the rovibronic structure of the electronic states. Such models will be presented in a future paper. For the isotopomers $^{129}I_2$ and $^{127}I^{129}I$ prediction uncertainty is less due to only few high precision measurements available in literature. The combined evaluation of all isotopomers with the models presented transfers precision to the other isotopomers. From the fits of the new measurements presented here, applying similar estimations as before in Section 10.5 for $^{127}I_2$, we expect a prediction uncertainty of hyperfine splittings of $^{129}I_2$ and $^{127}I^{129}I$ not larger than 1 MHz. This is still sufficiently precise for a total prediction uncertainty of few MHz for rovobronic transitions including hyperfine structure. A drawback of these isotopomers for use as high reference spectra might be the overlap of many hyperfine components. Only for $^{129}I_2$ and even J'' one hyperfine component, a_1 is sufficiently separated from the other ones to be used as a reference line free from overlap. For calibrations, which do not require highest precision, also the overlapped structures can be used.

Acknowledgement

This study is supported by the European Community, Integrated Infrastructure Initiative action (RII3-CT-2003-506350) and by the Netherlands Foundation for Fundamental Research of Matter (FOM).

Chapter 11

Improved potentials and Born-Oppenheimer corrections by new measurements of transitions of ^{129}I$_2$ and ^{127}I^{129}I in the $B^3\Pi_{0_u^+} - X^1\Sigma_g^+$ band system

The light from one single frequency cw laser was employed in a double saturation spectroscopy experiment to record high resolution spectra of $^{129}I_2$ *and* $^{127}I^{129}I$ *together with spectra of* $^{127}I_2$ *which is used as a simultaneous frequency reference. Two separate saturation spectroscopy set ups were used. The frequencies of lines of* $^{129}I_2$ *and* $^{127}I^{129}I$ *were determined with respect to lines of* $^{127}I_2$*. More than 380 frequency differences between lines of* $^{127}I_2$ *and of the other isotopomers have been included in the data set. By a direct potential fit a precise description of the potential energy curves of the B and the X state and of effective Born-Oppenheimer correction functions valid for all three isotopomers of* I_2 *are given.*

This chapter is published as European Physical Journal D **47**, 171–179 (2008).

11.1 Introduction

The $B^3\Pi_{0_u^+} - X^1\Sigma_g^+$ spectrum of the iodine molecule has long been employed as a frequency reference. The simplicity of just using a room temperature cell filled with iodine vapor for observation of spectra together with a proper laser source and the high density of lines in the spectrum led to many applications of laser stabilization to iodine absorption lines. Several of those lines are recommended as secondary frequency standards.[279] Additionally, systematic measurements of frequencies of iodine lines were performed by various laboratories, either in the form of spectral atlases[267–271] or in the form of tables of selected lines of vibrational bands (see e.g. Refs. 232,281,300). Moreover, many measurements of selected iodine lines have been contributed by various authors. For a more complete list of papers before 2004 on measurements of iodine lines, see Ref. 180 and references therein. The precision of the transition frequencies is very high, a few lines have sub-MHz accuracy and more than 1500 have an accuracy in the range of a few MHz.

Thus this very precise data set is attractive for investigating small contributions to the molecular binding energies, like e.g. breakdown of the Born-Oppenheimer approximation, which is accounted for as additional terms in the Schrödinger equation.[301]

The structure of the iodine B-X spectrum was modeled by Gerstenkorn et al.[290] with a Dunham parameter approach based on the frequencies of the lines in their atlases. Extensive Fourier-transform laser induced fluorescence spectra were taken and modeled in Dunham based descriptions by Cerny et al.[276] for the three isotopomers $^{127}I_2$, $^{129}I_2$ and $^{127}I^{129}I$. However, the width of the lines was determined by the resolution of the Fourier-transform spectrometer, thus the precision was limited to a few times 10^{-3} cm^{-1}, and did not allow them to quantify effects of breakdown of the Born-Oppenheimer approximation.

High precision model descriptions of the $B^3\Pi_{0_u^+}$ - $X^1\Sigma_g^+$ spectrum have been proposed in previous papers,[180,272,302] based on data of own investigations in the near infrared spectral region and on data from the literature. The task of accurately modeling the Doppler-free iodine spectrum has two distinct aspects. In addition to the electronic and rovibrational structure the iodine lines exhibit hyperfine structure. Models for the latter have been proposed[272] and were refined using new data of the other isotopomers in Ref. 302, yielding precise and concise formulas representing the dependence of the hyperfine parameters on the vibrational and rotational quantum numbers for $^{127}I_2$, which are valid for the other two isotopomers as well. For the rovibronic structure a global model description based on directly fitted potential energy curves was used in Ref. 180. There it turned out that for a precise modeling of the transition frequencies, also Born-Oppenheimer correction (BOC) functions for adiabatic and nonadiabatic corrections had to be included in the Hamiltonian which determines the level energies involved in the optical transitions.

However, while the nonadiabatic centrifugal distortion correction (also called nonadiabatic BOC) can in principle be derived from one isotopomer alone, provided that data of a sufficiently large span of rotational lines are available, the adiabatic BOC can in principle only be determined when data of more than one isotopomer are included.

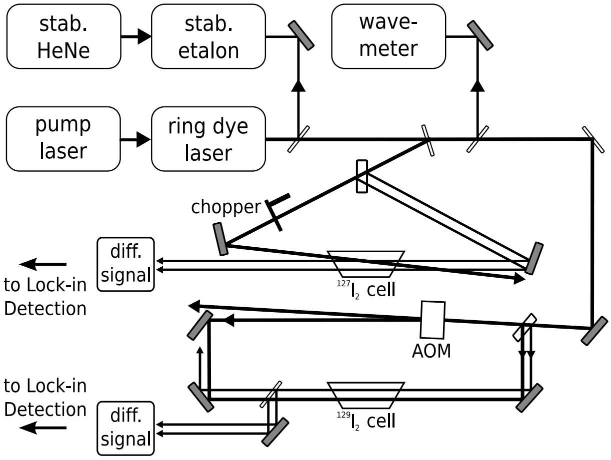

Figure 11.1 – *Scheme of the experimental setup. It consists of two parallel saturation spectroscopy measurements on two distinct vapor cells. One cell contains about 85% of* ^{129}I *and about 15% of* ^{127}I*, giving rise to spectra of* $^{129}I_2$ *(and* $^{127}I^{129}I$ *and weak* $^{127}I_2$*). The other cell contains pure* $^{127}I_2$*. The positions of the* $^{129}I_2$ *and* $^{127}I^{129}I$ *resonances are determined with respect to the position of* $^{127}I_2$ *lines by means of a HeNe-stabilized étalon used as a ruler.*

At the time when this model was developed, only six very precise transition frequencies from saturation spectroscopy for $^{129}\mathrm{I}_2$ and only one for $^{127}\mathrm{I}^{129}\mathrm{I}$ existed in the literature.[279] Despite their high precision, this information about isotopic effects was not sufficient for a satisfactory determination of the complete BOC. Thus it was not clear at the end of Ref. 180, how reliable the BOC functions would be, especially because a comparison of the expectation values of the nonadiabatic BOC calculated with the vibrational eigenfunctions did not agree well with the experimentally determined g_J factors (see section 4 of Ref. 180).

With the very precise data on the iodine B-X system we have in principle a data set with which one can investigate how precisely the BOC parameters can be evaluated for such a heavy system. However, to that end more data of high accuracy from other isotopomers are necessary. Therefore, a joint effort between VU Amsterdam and Leibniz University of Hannover undertook to measure a substantial amount of transition frequencies for the homonuclear isotopomer $^{129}\mathrm{I}_2$ and the mixed one $^{127}\mathrm{I}^{129}\mathrm{I}$. Here we report on the rovobronic transition frequencies of these measurements. In Section 11.2 we describe the experimental procedure applied. In Section 11.3 details of the measurements and in 11.4 of the evaluation procedure are presented. In Section 11.5 we discuss the model fit and its results. A conclusion will summarize the "take home message" of the paper*.

11.2 Experimental

A schematic layout of the experimental setup is shown in Figure 11.1. A stabilized, tunable cw ring-dye-laser (Spectra Physics 380D) is used as the common radiation source. The dye laser is operated with Rhodamine 6G dye to access the wavelength range from 573 nm to 583 nm, while Rhodamine B dye is used for the range 610 nm to 615 nm and for some measurements near 633 nm.

Two distinct saturated absorption setups allow for the simultaneous recording of the spectra obtained from a vapor cell containing the isotopomers $^{129}I_2$ and $^{127}I^{129}I$ together with that of the main isotopomer $^{127}I_2$ in another cell. By means of this double saturation setup, the spectra of the isotopomers $^{129}I_2$ and $^{127}I^{129}I$ can be referred to the $^{127}I_2$ resonances that have been measured at high accuracy before.[232,281] With reference to this spectrum, the data on the ^{129}I containing species can be calibrated on a relative scale and on an absolute scale as well.

A 10-cm vapor cell containing 100% $^{127}I_2$ is used in one of the saturation setups, identical to the one used in the previous studies discussed in Refs. 232 and 281. Differential absorption by two probe beams is monitored, while one of them is crossed at a slight angle (<7 mrad) with the saturation beam, leading to a contribution to the Doppler width of about 2.5 MHz. The saturating beam is modulated by a mechanical chopper at around 700 Hz and lock-in signal detection is employed. The $^{127}I_2$ cell is used at room temperature, corresponding to a vapor pressure of about 27 Pa.[303]

A 5-cm cell containing mainly ^{129}I and a small amount of ^{127}I is used in the other saturation setup. The pump-offset saturation spectroscopy technique[282,283] is applied to maximize the signal detection sensitivity. The first-order diffraction beam from an acousto-optic modulator (AOM) shifted by +75 MHz is used as the saturating beam. As a consequence of the 75-MHz frequency offset of the saturating beam with respect to the probe beams, the saturation resonances are shifted by 37.5 MHz from the real line positions[282,283] to lower frequencies of the laser. Differential absorption signals were acquired, with one of the probe beams overlapped collinearly with the saturating beam. A 50-kHz modulation was imposed on the amplitude of the saturating beam and the saturation signal is retrieved by lock-in detection. The inherent sensitivity of the pump-offset technique combined with the fast modula-

---

*the data set and the potential parameters are available online at www.epj.org tion of the AOM results in a high detection sensitivity. With such a scheme, we could also detect the strong transitions of the $^{127}I_2$ molecules that are present, but only in trace amounts, inside this cell. These weak $^{127}I_2$ signals are compared to those obtained from the parallel $^{127}I_2$ saturation setup in order to check for possible frequency shifts between the two saturation setups.

A wave meter is used to coarsely tune the laser to the resonances. Difference frequency measurements are carried out by employing the transmission peaks of a calibrated 50-cm Fabry-Perot étalon. The étalon temperature and pressure is stabilized and its length is actively locked to the wavelength of a Zeeman-stabilized He-Ne laser. The étalon free spectral range FSR is measured at the start of every measurement session, and has a typical value of 148.96(1) MHz with small day-to-day variations. For the absolute frequency calibration of the $^{129}I_2$ and $^{127}I^{129}I$ lines a nearby $^{127}I_2$ line was chosen as reference which had been measured previously in Refs. 232 and 281. Since the largest separation was less than thirty étalon fringes, this procedure results in a 1 MHz uncertainty of frequency differences.

11.3 Measurements

With the goal to cover as many rovibronic bands as possible in the ranges available by the tuning range of the dye laser we observed simultaneously saturated absorption spectra from both setups. In different periods of measurements ranges around 633 nm, from 615 to 610 nm, and from 583 to 573 nm were chosen. The hyperfine structures of lines of rovibronic bands for v" ranging from 0 to 5, for v' ranging from 9 to 20, and J" ranging from 23 to 128 were recorded for all three isotopomers. An example of such recorded spectra is given in Figure 11.2. The upper trace (a) shows the saturation spectrum from the frequency reference setup with the $^{127}I_2$ cell. The middle trace (b) shows that for the ^{129}I cell. In the lowest trace the frequency markers from the reference cavity are shown. The individual frequency sweeps were selected such that in each scan at least one hyperfine component with an absolute frequency already known from Refs. 232 and 281 was located. Thus an absolute frequency calibration of the recorded spectra is easily possible. A relative frequency scale was established from the markers of the Fabry-Pérot cavity applying a spline fit and a linearisation procedure to the series of markers. After that this relative scale was converted to an absolute one by linking it to one of the hyperfine components known with high accuracy. For the record of Figure 11.2 e.g. the lowest frequency hyperfine component a_1 (sometimes also called 't' component) of the line P(72) (11-3) served as the calibration line for the absolute frequency.

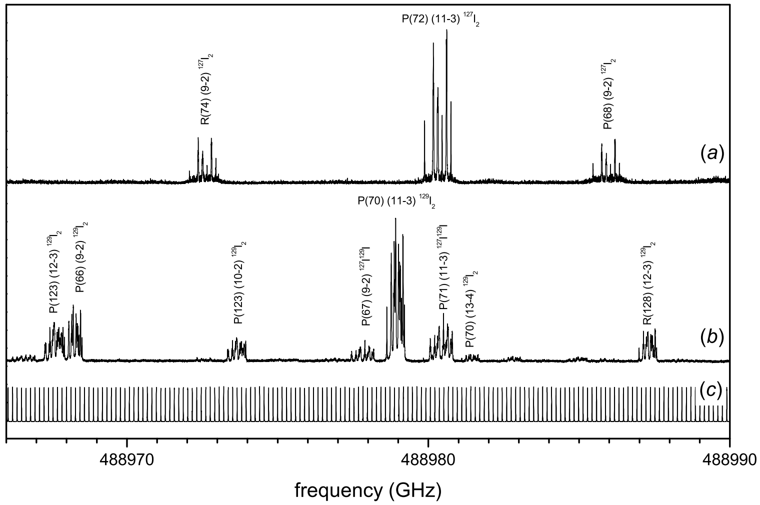

Figure 11.2 – *Typical spectra recorded while tuning the laser frequency. The trace (a) corresponds to the setup with a cell containing natural iodine, which is composed of 100% of* ^{127}I *cell. Trace (b) corresponds to the* $^{129}I_2$ *cell. With its content of few % of* ^{127}I *also lines of* $^{127}I^{129}I$ *appear, and moreover, weak lines of* $^{127}I_2$*. The lines of trace (b) are shifted by 37.5 MHz to lower frequencies due to the AOM frequency of 75 MHz. The lower trace (c) shows marker peaks from the stabilized étalon, which is used for interpolation of frequency differences.*

For obtaining the pure rovibronic transition frequencies, first the hyper-fine structure was fitted and the hyper-fine-free transition frequency determined from the fit. The details of the hyperfine structure models have been discussed in Ref. 302 and will not be repeated here. For more information about the hyperfine structure fits of the different isotopomers, taking into account a residual Doppler background and absorption in the case of the longer $^{127}I_2$ cell, the reader is referred to that paper.

From such evaluation on a relative frequency scale the absolute calibration of the frequencies of the lines of all isotopomers is possible. However, frequency differences between lines are more precise because only the uncertainty coming from the calibration of the stabilized reference cavity has to be taken into account, while for an absolute calibration the uncertainty of the reference line also must be accounted for. Therefore, in most cases we determined difference frequencies of $^{129}I_2$ and $^{127}I^{129}I$ with respect to chosen lines of $^{127}I_2$ from the other setup. Such differences were corrected for the systematic shift of 37.5 MHz of the spectra from the different setups due to the use of the AOM. In order to detect other possible systematic shifts between the different setups, we verified this procedure for the shifts of lines of the main isotopomer $^{127}I_2$ in cases where its lines could be identified in spectra recorded in the setup for the other isotopomers. The typical uncertainty of the absolute calibration by $^{127}I_2$ lines is 1 MHz (1σ). The residual uncertainty of the frequency differences is mainly determined by some uncorrected non-linearities or non-uniformity of the laser scan between two markers, which cannot be detected due to the marker separation and which is left after the computerized linearisation procedure; it is assumed to be not larger than 1.5 MHz.

Altogether more than 290 difference frequencies for $^{129}I_2$ and more than 90 difference frequencies for $^{127}I^{129}I$ were acquired. An overview of the quantum number range in the upper state is shown in Figure 11.3. The crosses mark data for the homonuclear isotopomer $^{129}I_2$, while the dots give the data field for the mixed $^{127}I^{129}I$. Vibrational quantum numbers for the lower state range from v"=0 to v"=5. The data for the main isotopomer $^{127}I_2$ span the range of vibrational quantum numbers $0 \leq$ v' ≤ 43 for the upper and $0 \leq$ v" ≤ 17 for the lower state.

11.4 Modeling of the spectra

The observed spectra will be modeled as in our recent paper Ref. 180, with the physical approach of describing each electronic state directly by a potential, and the energies of the levels being determined as the eigenvalues of the Schrödinger equation solved with these potentials. The potentials are represented in a parametrized form involving parameters which are fitted. We will model the case of single state (Born-Oppenheimer) potentials, allowing only for the lowest order corrections of the Born-Oppenheimer approximation. The data range is selected such that local perturbations by other electronic states, which are known to occur close to the dissociation limits[274,304,305] of the ground or excited state, are kept outside the selected energy ranges. For the levels of the B state which are in the region of known predissociation caused by the repulsive $^1\Pi_u$ state crossing the B state,[289,306,307] we neglect any local effect of level shifts. The levels in the data set are from high resolution experimental observations and the observed spectra showing narrow lines and regular intensities in the hyperfine patterns certify that the degree of predissociation should be small enough that such shifts will be absorbed in the present single state model within the presently obtainable precision.

Several representations of the potentials in such direct potential fits have been proposed in the literature, like e.g. the expanded Morse oscillator[308] or modified

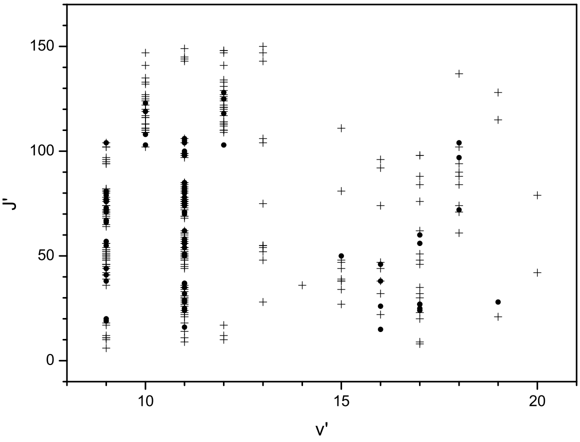

Figure 11.3 – *Data field in terms of the upper vibrational and rotational quantum numbers of the transitions of the isotopomers of* I_2*. Crosses mark the data of* $^{129}I_2$*, while dots mark data of the mixed isotopomer* $^{127}I^{129}I$*. The vibrational quantum numbers of the ground state levels range from v"=0 to v"=5.*

Lennard-Jones potential.[309] These were developed to describe the whole potential from short to large internuclear separations in a single expression which can be designed so that also the asymptotic behavior at large internuclear distance is described correctly (see e.g. Ref. 310). Other approaches like the spline interpolated numerical potential by Pashov et al.[311] use a flexible spline based representation for the range of intermediate nuclear distances for which data are available, and apply smoothly analytical extensions for the short and long range parts which are not supported by data.

We will follow here our previous approach in Ref. 180 and use potentials in the so called "X-representation". The potential is composed of three sections. The central well, which will determine the energy eigenvalues of the observed levels, is written as a truncated power series of the form

$$V(R) = \sum_i a_i \cdot X^i, i = 0, 1, 2, ... \tag{11.1}$$

with

$$X = \frac{R - R_m}{R + b \cdot R_m} \tag{11.2}$$

The parameters a_i are adjusted in a fit, R is the internuclear distance and R_m is an arbitrarily chosen expansion center close to the equilibrium nuclear distance of the electronic state. The parameter b allows us to vary the nonlinear mapping function $X(R)$, and is adjusted only once for a best fit of the potential representation (11.1) to the potential to start with.

Sufficiently far out of the range of internuclear distances in which the potential is determined by experimental data, the intermediate potential is continued to smaller and to larger internuclear distances by physically appropriate extension functions. For the inner branch $R < R_I$, R_I being the joining abscissa with the intermediate part, an exponential

$$V(R) = A_I \cdot exp(-B_I \cdot (R - R_I)) \tag{11.3}$$

is used. The parameters A_I and B_I are adjusted to give a smooth and differentiable connection at R_I after each modification of the central part of the potential. The outer branch at $R > R_O$, R_O being the joining point with the intermediate part, is extended with functions representing dispersion interactions

$$V(R) = D_e - \sum_n \frac{C_n}{R^n} - A_O \cdot exp(-B_O \cdot (R - R_O)) \tag{11.4}$$

The parameters D_e and C_n are taken from literature,[312–314] and the same values are taken for all isotopomers. This is justified because this part of the long range extension is far enough from the levels determined by the data that small changes like the atomic isotope shift do not introduce significant changes of the eigenvalues in the central part $R_I \le R \le R_O$ of the potential within the present accuracy. The numerical values so determined are given in Table 11.1. The exponential term is used to insure smoothness and differentiability at the connection R_O, and its parameters are adjusted accordingly after each modification of the central part of the potential. Thus, it does not have a physical meaning of an exchange term.

Small energy contributions which are neglected within the Born-Oppenheimer approximation ("Born-Oppenhei-mer corrections", BOC) are considered because of the very accurate data. A complete set of BOC would include an adiabatic correction V_{corr} of the potential, a nonadiabatic correction term α(R) in the rotational Hamiltonian and a nonadiabatic contribution $\beta(R)$ to the kinetic energy operator. For a homonuclear molecule these corrections depend on the ratio $\frac{m_e}{\mu}$ of the electron mass m_e and the reduced mass μ of the molecule. Watson[301,315] showed, that only two of these corrections can be determined simultaneously. Moreover, due to the mass dependence the contributions by β are expected to be very small.[316] Thus we chose $\beta = 0$ in our approach; contributions of it will be absorbed in effective BOC functions V_{corr}(R) and α(R), and the effective Hamiltonian for the radial motion is written as Refs. [180,315,316]:

$$\begin{aligned} \mathbf{H}_{eff} &= -\frac{\hbar^2}{2\mu}\frac{\partial^2}{\partial R^2} + V(R) + V_{corr}(R) \\ &\quad + \frac{\hbar^2 \cdot [1+\alpha(R)] \cdot J(J+1)}{2\mu R^2} \end{aligned} \tag{11.5}$$

For both V_{corr} and α we employ functions of the internuclear distance R represented as a truncated power series in X:

$$\alpha(R) = \frac{\mu_{ref}}{\mu} \cdot V_{nad} \tag{11.6}$$

with

$$V_{nad} = \frac{2R_m}{R+R_m} \sum_i \alpha_i \cdot X^i, i = 0, 1, 2, ... \tag{11.7}$$

and

$$V_{corr}(R) = (1 - \frac{\mu_{ref}}{\mu}) \cdot V_{ad} \tag{11.8}$$

with

$$V_{ad} = (\frac{2R_m}{R+R_m})^l \sum_i v_i \cdot X^i, i = 0, 1, 2, ... \tag{11.9}$$

with μ_{ref} being the reduced mass of the selected reference isotope $^{127}I_2$ and l being the power of R in the leading term of the dispersion interaction of Equation 11.4. The adiabatic correction V_{corr}(R) can only be determined if data of different isotopic species of the molecule are included. This ansatz should consider the asymptotic behaviour of the correction V_{corr}=V_{corr}(B)-V_{corr}(X) such that it asymptotically corresponds to the atomic isotope shift[317] of the $^2P_{1/2}$ - $^2P_{3/2}$ transition of iodine. However, to our knowledge this isotope shift is not yet known experimentally, but it is expected to be small because the transition is only due to a change in the fine structure level. Thus here we force the asymptotic value of V_{corr} to zero at infinity. The influence of this choice on the eigenvalues is negligibly small as the energies of the highest levels described with the model are still far from the dissociation energy. For the adiabatic and the nonadiabatic corrections the representations of Equations (11.7) - (11.9) were used for the full range of R without any extensions such as those for the potential function model.

During the fit the eigenvalues for the lower and the upper levels are calculated for each optical transition using the Numerov method[318] with the respective potentials, and their difference "cal" is subtracted from the measured frequency "obs". The parameters a_i, α_i and v_i are adjusted searching for a minimum of χ^2

$$\chi^2 = \sum_j \left(\frac{\mathrm{obs}_j - \mathrm{cal}_j}{\Delta \mathrm{obs}_j} \right)^2 , \tag{11.10}$$

$\Delta\mathrm{obs}_j$ is the uncertainty of the experimental value. The fitting strategies for this nonlinear problem are provided by the MINUIT program package.[293]

11.5 Results and discussion

Some frequency differences between $^{127}I_2$ lines were also derived from the new recordings and included in the data set, and moreover, the recent absolute frequency measurements of the P(62) line of the (4-5) band at 661 nm by Badr et al.,[319] of the P(80) (21-1) at 564 nm and the P(10) (14-1) at 585 nm by Reinhardt et al.[320] and of the P(42) (1-14) at 735 nm and R(114) (2-11) at 735 nm recently by Reinhardt et al.[321] were added to the data set. As for the near infrared range, also new frequencies of lines of high J" of the (0-15) band determined recently with a frequency comb in Amsterdam have been included. If the new literature data contained a sufficient number of hyperfine components, the hyperfine structure was fitted, and then the contribution of the hyperfine interaction was subtracted to yield the frequency of the rovibronic transition. In the other cases the hyperfine splitting was calculated taking the models from Ref. 302 and subtracted to yield the hyperfine-structure-free frequencies. The uncertainty introduced by this prediction of hyperfine splitting is less than 60 kHz.[302]

Together with the data base from Ref. 180, now more than 1900 frequencies or frequency differences were available, of which about 290 are for the homonuclear isotopomer $^{129}I_2$ and 90 are for the mixed species $^{127}I^{129}I$, for which a range of vibrational quantum numbers $9 \leq v' \leq 21$ is covered in the upper state and $0 \leq v'' \leq 5$ for the lower state.

Table 11.1: *Potential data of the upper state* $B^3\Pi_{0_u^+}$ *and lower state* $X^1\Sigma_g^+$ *and of the BOC functions* $\alpha(R)$ *and* $V_{ad}(R)$ *for the reference isotopomer* $^{127}I_2$.

parameter	upper state $B0_u^+$	lower state $X^1\Sigma_g^+$
R_m [Å]	3.02669183	2.66638233
b	-0.75	-0.60
a_0 [cm^{-1}]	15769.067837	0.0
a_1 [cm^{-1}]	0.813930E+01	0.155389E+00
a_2 [cm^{-1}]	0.850290979E+04	0.492601477E+05
a_3 [cm^{-1}]	0.695677594E+04	0.213629963E+05
a_4 [cm^{-1}]	0.995264129E+03	-0.18173865E+05
a_5 [cm^{-1}]	-0.556338644E+04	-0.49468474E+05
a_6 [cm^{-1}]	-0.1074389661E+05	-0.71353991E+05
a_7 [cm^{-1}]	-0.1685419562E+05	-0.10110925E+06
a_8 [cm^{-1}]	-0.1533164368E+05	-0.7156108E+05
a_9 [cm^{-1}]	0.4315045697E+05	0.4710538E+06
a_{10} [cm^{-1}]	0.6251096110E+05	-0.2904654E+06
a_{11} [cm^{-1}]	-0.38914630400E+06	-0.73300648E+07
a_{12} [cm^{-1}]	-0.43219553147E+06	0.22578115E+07
a_{13} [cm^{-1}]	0.27235279905E+07	0.38250822E+08
a_{14} [cm^{-1}]	0.32186808611E+07	
a_{15} [cm^{-1}]	-0.127338590547E+08	
a_{16} [cm^{-1}]	-0.172752514874E+08	
a_{17} [cm^{-1}]	0.425255265406E+08	
a_{18} [cm^{-1}]	0.712695731657E+08	
a_{19} [cm^{-1}]	-0.9130578539938E+08	
a_{20} [cm^{-1}]	-0.2108682403457E+09	
a_{21} [cm^{-1}]	0.9267186544061E+08	
a_{22} [cm^{-1}]	0.4132330557779E+09	
a_{23} [cm^{-1}]	0.6085337864116E+08	
a_{24} [cm^{-1}]	-0.4879703383624E+09	
a_{25} [cm^{-1}]	-0.3052394100029E+09	
a_{26} [cm^{-1}]	0.2691855865112E+09	
a_{27} [cm^{-1}]	0.3494609136897E+09	
a_{28} [cm^{-1}]	0.2771015696362E+08	
a_{29} [cm^{-1}]	-0.1333716748717E+09	
a_{30} [cm^{-1}]	-0.7655507971445E+08	
a_{31} [cm^{-1}]	-0.1366495310913E+08	
α_0	-0.23586E-03	*

*no parameter included in fit, see text

Table 11.1 – Continued from previous page

parameter	upper state $B0_u^+$	lower state $X^1\Sigma_g^+$
α_1	0.23445E-04	*
α_2	-0.43703E-03	*
α_3	-0.39630E-03	*
α_4	-0.10191E-02	*
α_5	-0.16462E-03	*
v_0 [cm^{-1}]	-0.209726E+00	*
v_1 [cm^{-1}]	-0.668183E+01	*
v_2 [cm^{-1}]	0.154676E+01	*
v_3 [cm^{-1}]	-0.286898E+01	*
l	5	
extension data used		
R_I [Å]	2.64700	2.40000
A_I [cm^{-1}]	0.19605269E+05	0.45809329E+04
B_I [Å^{-1}]	0.13736027E+01	0.90168320E+01
R_O [Å]	4.90000	3.30000
A_O [cm^{-1}]	-0.8105289769E+01	0.1053614048E+04
B_O [Å^{-1}]	0.9347221716E+01	0.1259030368E+01
D_e [cm^{-1}]	20150.317[313]	12547.340[313]
C_5 [cm^{-1}Å^5]	0.3161E+06[314]	–
C_6 [cm^{-1}Å^6]	0.1506E+07[314]	0.148E+07[312]
C_8 [cm^{-1}Å^8]	0.2480E+08[314]	0.386E+08[312]
C_{10} [cm^{-1}Å^{10}]	0.4200E+09[314]	0.10E+09[312]
range of turning points of data set [Å]	2.650 – 4.589	2.427 – 3.079
$R_e(^{127}I_2)$ [Å]	3.0264	2.6664
$T_e(^{127}I_2)$ [cm^{-1}]	15769.0659	0.0000

In our previous paper BOC parameters were only taken into account for the excited B state. The BOC contributions to the low levels of the ground state involved here were expected to be small, because other states contributing to BOC are energetically far off and the energy interval of the observations in the X state is small.

In principle these arguments still apply to the present data set, but with the highly accurate data it is worthwhile to check whether BOC for the ground state can be determined now with some significance. Thus we ran a number of different fits on the same data set. Again, as in our previous paper,[180] the minimum uncertainty of the absolute data was set to 3 MHz, in order to avoid placing too much weight on the most precise data. For the frequency differences gathered in the present work we chose an uncertainty of 2.1 MHz. A set of distinct fits was run:

1. with the same parameter set as before in Ref. 180: a_0-a_{31} and BOC parameters α_0-α_4 and v_0-v_2 for the B state, a_0 to a_{13} and no BOC parameters for the X state.
2. Case (1) parameters plus the leading nonadiabatic BOC parameter α_0 for the ground state,
3. Case (1) plus the leading adiabatic BOC parameter v_0 for the ground state,
4. Case (1) plus BOC parameters α_0 and v_0 for the ground state,
5. Case (1) plus BOC parameters α_5 for the upper and v_0 for the ground state.
6. Case (1) plus two additional BOC parameters α_5 and v_3 for the B state,
7. Case (1) plus two additional high-order potential parameters a_{32} and a_{33} for the B state.

A fit to Case (1) yields χ^2=1128 as a reference. Allowing for one or two additional BOC parameters, χ^2 of the fits was always reduced with respect to the first case. However, adding two potential parameters (Case (7)), gave no significant decrease of χ^2. This is not surprising, because the radial range is not increased with the new data of the present work as compared to Ref. 180. However, this also shows that the improvement of χ^2 is not a result of adding two arbitrary parameters to the fit, and supports the importance of the resulting BOC functions from this evaluation. The smallest χ^2 was achieved with either the lowest order nonadiabatic BOC parameter α_0 for the ground state (case (2)), with two BOC parameters of lowest order for the ground state (case (4)), or with two additional BOC parameters for the upper state (case (6)). These results were practically of the same statistical significance, with a reduction of χ^2 by about 5% with respect to the first case above, corresponding to a dimensionless root-mean-square standard deviation $\sigma = \sqrt{\frac{\chi^2}{N-M}} = 0.75$. Here N is the total number of data and M the number of free parameters in the fit.

Inspection of the covariance matrix for the case of BOC parameters for the ground state reveals a correlation coefficient of 0.55 for the correlation of α_0 of the ground state with α_0 of the upper state. Also correlation coefficients larger than 0.1 for correlation with the other nonadiabatic BOC parameters of the upper state appear, while other correlations are less than 0.06. A similar correlation is observed for v_0 of the ground state for correlations with the corresponding BOC parameters of the upper state. The parameter v_0 represents the shift of the corresponding potential at R_m depending on the isotopomer. Hence one can already expect that only the differences can be determined, but not the individual well depths. The correlation between the BOC parameters of the upper and lower state confirms, that a physical distinction between the values of upper and lower state parameters is not reached yet, and is consistent with the observation, that the fit results for cases (2), (4), and (6) are essentially equivalent.

Consequently, we apparently cannot determine the significance of the BOC parameters for the ground state because of the correlation between lower and upper state BOC parameters. Thus we prefer to give as the final result the parameters from the fit of case (6), in which one additional parameter each for nonadiabatic and adiabatic BOC for the upper state was adjusted. The parameters for the potentials, the nonadiabatic and adiabatic Born-Oppenheimer corrections and all other parameters used in the fit are given in Table 11.1. At the end of the table the conventional parameters R_e and T_e for the resulting potentials are given for convenience.

The distribution of the relative fit residuals, being the residuum (obs - cal) divided by the experimental uncertainty of the datum, is shown by the histogram in Figure 11.4. A Gaussian function was fitted to the distribution and is displayed as the black curve. Its full width at half maximum (FWHM) is close to 1, which means that 66% of the residuals fall within an interval of ±0.5 around the center. The center is slightly displaced by 0.029, corresponding to about 82 kHz for the data with highest precision, which means the minimum uncertainty of 3 MHz here. This shift is small and can be neglected for prediction of line frequencies from the parameters in Table 11.1.

The new data on the isotopomers $^{129}I_2$ and $^{127}I^{129}I$ are of similar precision compared to those of the main isotope and cover now a fairly broad range of vibrational quantum numbers in the upper and in the lower state. As discussed above, it turns out that two additional parameters for both the adiabatic and the nonadiabatic BOC functions improve the fit. The resulting BOC functions (nonadiabatic and adiabatic corrections) are displayed in Figures 11.5 and 11.6. We give for comparison also the functions reported in Ref. 180. In the earlier work the results of the adiabatic correction were based only on 5 frequencies of the other isotopomers. The vertical (blue) lines mark the range of turning points of the vibrational motion of the nuclei, which is supported by the data. Within this range the nonadiabatic BOC function in Figure 11.5 has changed only slightly, its magnitude has decreased by about $0.3 \cdot 10^{-4}$ compared to the old curve, and also the shape is nearly the same. The adiabatic contribution is close to the old function in the vicinity of the equilibrium internuclear

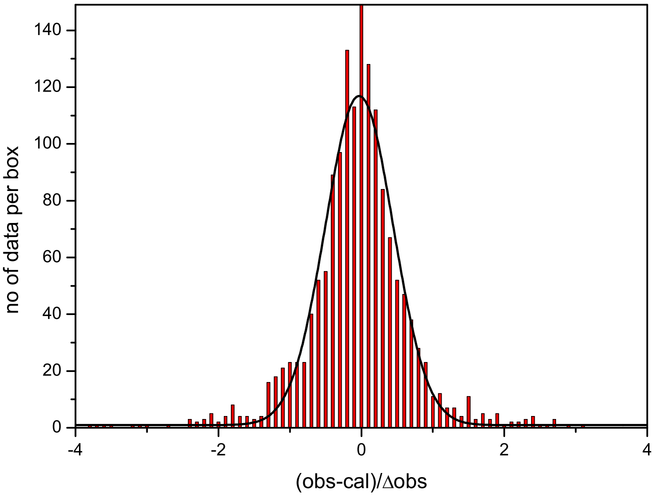

Figure 11.4 – *Histogram of the relative residuals of the fit. The curve represents a Gaussian distribution with a width of 0.431(7) and position -0.029(7).*

distance, but it has smaller absolute values than the old one when going to the lower or upper data range limit. We emphasize that the functions are still effective functions, on the one hand, because we were not able to separate the contributions of the upper and the lower state due to the correlations between the BOC parameters and, on the other hand, because the nonadiabatic contribution from the kinetic energy operator is still absorbed in them.

To the best of our knowledge no other investigations of BOC function in iodine exist, and moreover, no theoretical estimations or *ab initio* calculations were found in the literature. So with these results we cannot go further by comparing them to theoretical results, or using theoretical results to obtain a distinction between upper state and lower state contributions.

11.6 Conclusion

We present new measurements of very precise rovibronic transition frequencies in the B-X system of the isotopomers $^{129}I_2$ and $^{127}I^{129}I$ of the iodine molecule. The extended data set (now 380 lines, before 5) was used to derive model potentials and Born-Oppenheimer correction functions. The BOC functions are crucial for the accurate modeling of the spectrum, but in spite of the high accuracy of the present

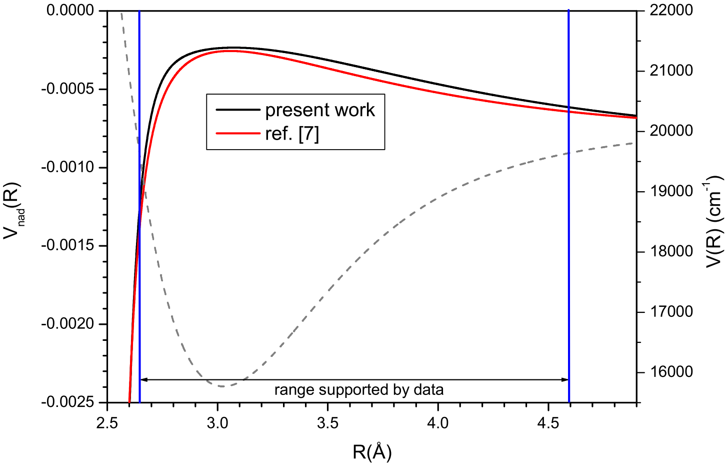

Figure 11.5 – *Comparison of the present nonadiabatic BOC function with that from Ref. 180. The potential of the B state, given as the dashed line, has a similar position of the minimum as $V_{nad}(R)$ for the maximum.*

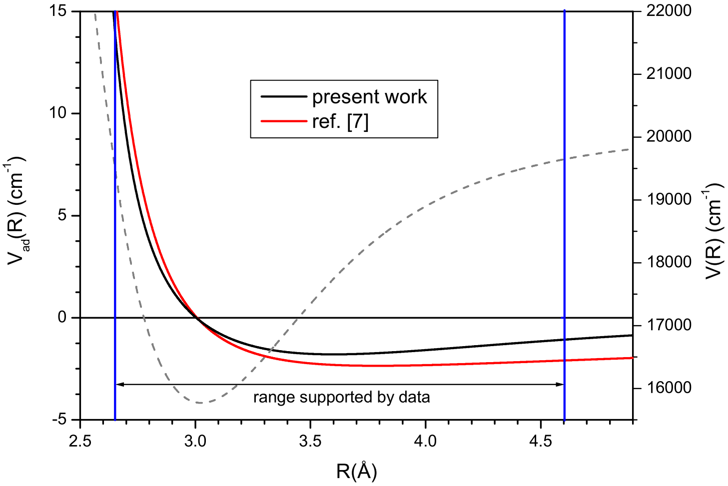

Figure 11.6 – *Comparison of the present adiabatic BOC function with that from Ref. 180. To compare it with the total energy, the potential for the B state is given as dashed line.*

data set, the BOC contributions of the upper and the lower state cannot yet be separated due to correlations. The effective BOC contributions seem to be well determined. The difference energy T_e of the potential minima between B and X state, whose isotopic dependence is determined by the adiabatic BOC contribution, varies by $T_e(^{127}I_2)$ - $T_e(^{129}I_2) = 94(11)$ MHz, when comparing the potentials of $^{127}I_2$ with those of $^{129}I_2$. This value was stable in the various fits described above to within the quoted 1σ standard deviation. R_e is the same for $^{129}I_2$ within the digits given in Table 11.1. Further interpretation is not yet possible due to the lack of theoretical calculations or modeling.

The derived model parameters can be used to calculate the rovibrational spectrum of all three isotopomers of the iodine molecules with a precision of about 1.5 MHz for a prediction to within a $1\ \sigma$ uncertainty margin for the quantum number range of the observations. Perturbations were not observed in the spectral range covered by the data, thus we have good reason that the description for the isotopomers $^{129}I_2$ and $^{127}I^{129}I$ can be extrapolated from the whole range of quantum numbers for the main isotopomer.

Together with the recently published models of the hyperfine structure a model system is available now, which allows to predict iodine lines including the hyperfine structure with essentially the uncertainty stated above.

In several regions of the total range, where the iodine B-X spectrum can be observed, lines with less precise frequencies only are available yet. Here the prediction uncertainty is also reduced. For a more detailed picture of the spectral ranges and the corresponding prediction accuracy, the reader is referred to Figure 11.3 in our previous paper.[180]

As a next step in this project, further precise measurements of iodine lines in the near infrared spectral region are planned, where the frequencies will be determined by use of a frequency comb based on a femtosecond pulsed laser.

Acknowledgement

This study is also supported by the European Community, Integrated Infrastructure Initiative action (RII3-CT-2003-506350) and by the Netherlands Foundation for Fundamental Research of Matter (FOM).

Bibliography

[1] M. J. Duff, L. B. Okun and G. Veneziano, 'Trialogue on the number of fundamental constants'. *Journal of High Energy Physics* **2002**, 023 (2002).

[2] J. D. Barrow, *The Constants of Nature*, Vintage Books (2002).

[3] G. Lewis and E. Adams, 'A Theory of Ultimate Rational Units; Numerical Relations between Elementary Charge, Wirkungsquantum, Constant of Stefan's Law'. *Phys. Rev.* **3**, 92 (1914).

[4] A. Linde, 'The Self-Reproducing Inflationary Universe'. *Sci. Am.* **271**, 48 (1994).

[5] D. N. F. Dunbar, R. E. Pixley, W. A. Wenzel and W. Whaling, 'The 7.68-Mev State in C^{12}'. *Phys. Rev.* **92**, 649–650 (1953).

[6] F. Hoyle, D. N. F. Dunbar, R. E. Pixley, W. A. Wenzel and W. Whaling, 'A state in C-12 predicted from astrophysical evidence'. *Phys. Rev.* **92**, 1095 (1953).

[7] C. W. Cook, W. A. Fowler, C. C. Lauritsen and T. Lauritsen, 'B^{12}, C^{12}, and the Red Giants'. *Phys. Rev.* **107**, 508–515 (1957).

[8] H. Oberhummer, A. Cst and H. Schlattl, 'Stellar Production Rates of Carbon and Its Abundance in the Universe'. *Science* **289**, 88–90 (2000).

[9] A. Sommerfeld, 'Das Plancksche Wirkungsquantum und seine allgemeine Bedeutung für die Molekularphysik'. *Phys. Z.* **12**, 1057–1069 (1911).

[10] F. Paschen, 'Bohrs Heliumlinien'. *Ann. Phys.* **355**, 901–940 (1916).

[11] H. Kragh, 'Magic Number: A Partial History of the Fine-Structure Constant'. *Arch. Hist. Exact Sci.* **57**, 395 (2003).

[12] S. G. Karshenboim, 'Precision physics of simple atoms: QED tests, nuclear structure and fundamental constants'. *Phys. Rep.* **422**, 1 (2005).

[13] J. Ellis, 'Unification and Supersymmetry'. *Philos. T. Roy. Soc. S-A* **310**, 279–292 (1983).

[14] P. Mohr, B. Taylor and D. Newell, 'CODATA recommended values of the fundamental physical constants: 2006'. *Rev. Mod. Phys.* **80**, 633 (2008).

[15] D. Hanneke, S. Fogwell and G. Gabrielse, 'New Measurement of the Electron Magnetic Moment and the Fine Structure Constant'. *Phys. Rev. Lett.* **100**, 120 801 (2008).

[16] P. Cladé, E. de Mirandes, M. Cadoret, S. Guellati-Khélifa, C. Schwob, F. Nez, L. Julien and F. Biraben, 'Precise measurement of h/m_{Rb} using Bloch oscillations in a vertical optical lattice: Determination of the fine-structure constant'. *Phys. Rev. A* **74**, 052 109 (2006).

[17] M. Cadoret, E. de Mirandes, P. Cladé, S. Guellati-Khélifa, C. Schwob, F. Nez, L. Julien and F. Biraben, 'Combination of Bloch Oscillations with a Ramsey-Bordé Interferometer: New Determination of the Fine Structure Constant'. *Phys. Rev. Lett.* **101**, 230 801 (2008).

[18] V. Gerginov, K. Calkins, C. E. Tanner, J. J. McFerran, S. Diddams, A. Bartels and L. Hollberg, 'Optical frequency measurements of $6s^2S_{1/2} - 6p^2P_{1/2}$ (D_1) transitions in ^{133}Cs and their impact on the fine-structure constant'. *Phys. Rev. A* **73**, 032 504 (2006).

[19] M. Born. *Proc. Indian Acad. Sci. A* **2**, 533 (1935).

[20] J. D. Barrow and F. J. Tipler, *The Anthropic Cosmological Principle*, Clarendon Press Oxford (1986).

[21] S. Novaes, 'Standard Model: An Introduction' (2000), arxiv:hep-ph/0001283v1.

[22] T. Dent, 'Fundamental constants and their variability in theories of high energy physics'. *Eur. Phys. J. Spec. Top.* **163**, 297 (2008).

[23] S. Dürr, Z. Fodor, J. Frison, C. Hoelbling, R. Hoffmann, S. D. Katz, S. Krieg, T. Kurth, L. Lellouch, T. Lippert, K. K. Szabo and G. Vulvert, 'Ab Initio Determination of Light Hadron Masses'. *Science* **322**, 1224 (2008).

[24] D. Farnham, R. Van Dyck and P. Schwinberg, 'Determination of the electron's atomic mass and the proton/electron mass ratio via Penning trap mass spectroscopy'. *Phys. Rev. Lett.* **75**, 3598 (1995).

[25] T. Beier, H. Häffner, N. Hermanspahn, S. Karshenboim, H.-J. Kluge, W. Quint, S. Stahl, J. Verdú and G. Werth, 'New Determination of the Electron's Mass'. *Phys. Rev. Lett.* **88**, 011 603 (2002).

[26] R. Van Dyck, D. Farnham, S. Zafonte and P. Schwinberg, 'High precision Penning trap mass spectroscopy and a new measurement of the proton's atomic mass', *in* 'Trapped Charged Particles and Fundamental Physics', (edited by D. H. E. Dubin and D. Schneider), volume 457 of *AIP Conf. Proc.*, 101, AIP, Woodbury (1998).

[27] L. Wolniewicz, 'Nonadiabatic energies of the ground state of the hydrogen molecule'. *J. Chem. Phys.* **103**, 1792 (1995).

[28] H. Li, J. Wu, B.-L. Zhou, J.-M. Zhu and Z.-C. Yan, 'Calculations of energies of the hydrogen molecular ion'. *Phys. Rev. A* **75**, 012 504 (2007).

[29] B. Grémaud, D. Delande and N. Billy, 'Highly accurate calculation of the energy levels of the molecular ion'. *J. Phys. B* **31**, 383–392 (1998).

[30] L. Hilico, N. Billy, B. Grmaud and D. Delande, 'Ab initio calculation of the $J = 0$ and $J = 1$ states of the H_2^+, D_2^+ and HD^+ molecular ions'. *Eur. Phys. J. D* **12**, 449–466 (2000).

[31] V. I. Korobov, 'Relativistic corrections of $m\alpha^6$ order to the rovibrational spectrum of H_2^+ and HD^+ molecular ions'. *Phys. Rev. A* **77**, 022 509 (2008).

[32] V. I. Korobov, 'Leading-order relativistic and radiative corrections to the rovibrational spectrum of H_2^+ and HD^+ molecular ions'. *Phys. Rev. A* **74**, 052 506 (2006).

[33] J. C. J. Koelemeij, B. Roth, A. Wicht, I. Ernsting and S. Schiller, 'Vibrational Spectroscopy of HD^+ with 2-ppb Accuracy'. *Phys. Rev. Lett.* **98**, 173 002 (2007).

[34] S. G. Turyshev, 'Experimental Tests of General Relativity'. *Ann. Rev. Nucl. Part. Sci.* **58**, 207 (2008).

[35] S. Schlamminger, K.-Y. Choi, T. A. Wagner, J. H. Gundlach and E. G. Adelberger, 'Test of the Equivalence Principle Using a Rotating Torsion Balance'. *Phys. Rev. Lett.* **100**, 041 101 (2008).

[36] J. Williams, S. Turyshev and D. Boggs, 'Progress in Lunar Laser Ranging Tests of Relativistic Gravity'. *Phys. Rev. Lett.* **93**, 261 101 (2004).

[37] T. Kaluza, 'The unity problem of physics'. *Sitz. Preuss. Akad. Wiss. Phys. Math.* **K1**, 966–972 (1921).

[38] O. Klein, 'The quantum theory and five-dimensional relativity theory'. Z. *Phys.* **37**, 895–906 (1926).

[39] T. Damour and A. M. Polyakov, 'The string dilation and a least coupling principle'. *Nucl. Phys. B* **423**, 532 (1994).

[40] J.-P. Uzan, 'The fundamental constants and their variation: observational and theoretical status'. *Rev. Mod. Phys.* **75**, 403–455 (2003).

[41] J. Barrow and J. Magueijo, 'Cosmological constraints on a dynamical electron mass'. *Phys. Rev. D* **72**, 043 521 (2005).

[42] D. Shaw and J. Barrow, 'Local effects of cosmological variations in physical "constants" and scalar fields. I. Spherically symmetric spacetimes'. *Phys. Rev. D* **73**, 123 505 (2006).

[43] S. M. Carroll, 'Quintessence and the Rest of the World: Suppressing Long-Range Interactions'. *Phys. Rev. Lett.* **81**, 3067–3070 (1998).

[44] P. P. Avelino, C. J. A. P. Martins, N. J. Nunes and K. A. Olive, 'Reconstructing the dark energy equation of state with varying couplings'. *Phys. Rev. D* **74**, 083 508 (2006).

[45] X. Calmet and H. Fritzsch, 'The cosmological evolution of the nucleon mass and the electroweak coupling constants'. *Eur. J. Phys. C* **24**, 639–642 (2002).

[46] P. Langacker, G. Segr and M. Strassler, 'Implications of gauge unification for time variation of the fine structure constant'. *Phys. Lett. B* **528**, 121 (2002).

[47] V. V. Flambaum, D. B. Leinweber, A. W. Thomas and R. D. Young, 'Limits on variations of the quark masses, QCD scale, and fine structure constant'. *Phys. Rev. D* **69**, 115 006 (2004).

[48] T. Dent and M. Fairbairn, 'Time-varying coupling strengths, nuclear forces and unification'. *Nucl. Phys. B* **653**, 256 (2003).

[49] M. Dine, Y. Nir, G. Raz and T. Volansky, 'Time variations in the scale of grand unification'. *Phys. Rev. D* **67**, 015 009 (2003).

[50] P. A. M. Dirac, 'The cosmological constants'. *Nature (London)* **139**, 323 (1937).

[51] E. A. Milne, 'Cosmological Theories'. *Astrophys. J.* **91**, 129 (1940).

[52] E. Teller, 'On the Change of Physical Constants'. *Phys. Rev.* **73**, 801–802 (1948).

[53] G. Gamow, 'Electricity, Gravity, and Cosmology'. *Phys. Rev. Lett.* **19**, 759–761 (1967).

[54] R. Gold, 'Time Invariance of the Elementary Charge'. *Phys. Rev. Lett.* **20**, 219–220 (1968).

[55] C. Copi, A. Davis and L. Krauss, 'New nucleosynthesis constraint on the variation of *G*'. *Phys. Rev. Lett.* **92**, 171 301 (2004).

[56] R. H. Dicke, 'Gravitation without a Principle of Equivalence'. *Rev. Mod. Phys.* **29**, 363–376 (1957).

[57] A. Shlyakhter, 'Direct test of the constancy of fundamental nuclear constants'. *Nature* **264**, 340 (1976).

[58] Y. Fujii, A. Iwamoto, T. Fukahori, T. Ohnuki, M. Nakagawa, H. Hidaka, Y. Oura and P. Möller, 'The nuclear interaction at Oklo 2 billion years ago'. *Nucl. Phys. B* **573**, 377 (2000).

[59] C. R. Gould, E. I. Sharapov and S. K. Lamoreaux, 'Time variability of alpha from realistic models of Oklo reactors'. *Phys. Rev. C* **74**, 024 607 (2006).

[60] T. Damour and F. Dyson, 'The Oklo bound on the time variation of the fine-structure constant revisited'. *Nucl. Phys. B* **480**, 37 (1996).

[61] K. Olive, M. Pospelov, Y.-Z. Qian, A. Coc, M. Cassé and E. Vangioni-Flam, 'Constraints on the variations of the fundamental couplings'. *Phys. Rev. D* **66**, 045 022 (2002).

[62] P. Stefanescu, 'Constraints on time variation of fine structure constant from WMAP-3yr data'. *New Astronomy* **12**, 635 – 640 (2007).

[63] R. H. Cyburt, B. D. Fields, K. A. Olive and E. Skillman, 'New BBN limits on physics beyond the standard model from ^{4}He'. *Astroparticle Physics* **23**, 313 – 323 (2005).

[64] S. Landau, M. Mosquera, C. Scóccola and H. Vucetich, 'Early universe constraints on time variation of fundamental constants'. *Phys. Rev. D* **78**, 083 527 (2008).

[65] J. Chengalur and N. Kanekar, 'Constraining the variation of fundamental constants using 18 cm OH lines'. *Phys. Rev. Lett.* **91**, 241 302 (2003).

[66] N. Kanekar, J. N. Chengalur and T. Ghosh, 'Conjugate 18 cm OH Satellite Lines at a Cosmological Distance'. *Phys. Rev. Lett.* **93**, 051 302 (2004).

[67] J. Darling, 'Methods for constraining fine structure constant evolution with OH microwave transitions'. *Phys. Rev. Lett.* **91**, 011 301 (2003).

[68] E. R. Hudson, H. J. Lewandowski, B. C. Sawyer and J. Ye, 'Cold Molecule Spectroscopy for Constraining the Evolution of the Fine Structure Constant'. *Phys. Rev. Lett.* **96**, 143 004 (2006).

[69] P. Tzanavaris, J. Webb, M. Murphy, V. Flambaum and S. Curran, 'Limits on Variations in Fundamental Constants from 21-cm and Ultraviolet Quasar Absorption Lines'. *Phys. Rev. Lett.* **95**, 041 301 (2005).

[70] P. Tzanavaris, M. T. Murphy, J. K. Webb, V. V. Flambaum and S. J. Curran, 'Probing variations in fundamental constants with radio and optical quasar absorption-line observations'. *Mon. Not. R. Astron. Soc.* **374**, 634–646 (2007).

[71] S. G. Karshenboim and E. Peik, 'Astrophysics, Clocks and Fundamental Constants'. *Lect. Notes Phys.* **648** (2004).

[72] J. K. Webb, V. V. Flambaum, C. W. Churchill, M. J. Drinkwater and J. D. Barrow, 'Search for Time Variation of the Fine Structure Constant'. *Phys. Rev. Lett.* **82**, 884–887 (1999).

[73] J. K. Webb, M. T. Murphy, V. V. Flambaum, V. A. Dzuba, J. D. Barrow, C. W. Churchill, J. X. Prochaska and A. M. Wolfe, 'Further Evidence for Cosmological Evolution of the Fine Structure Constant'. *Phys. Rev. Lett.* **87**, 091 301 (2001).

[74] M. Murphy, J. Webb, V. Flambaum, V. Dzuba, C. Churchill, J. Prochaska, J. Barrow and A. Wolfe, 'Possible evidence for a variable fine-structure constant from QSO absorption lines: motivations, analysis and results'. *Mon. Not. R. Astron. Soc.* **327**, 1208–1222 (2001).

[75] M. Murphy, J. Webb, V. Flambaum, C. Churchill and J. Prochaska, 'Possible evidence for a variable fine-structure constant from QSO absorption lines: systematic errors'. *Mon. Not. R. Astron. Soc.* **327**, 1223–1236 (2001).

[76] M. T. Murphy, J. K. Webb and V. V. Flambaum, 'Further evidence for a variable fine-structure constant from Keck/HIRES QSO absorption spectra'. *Mon. Not. R. Astron. Soc.* **345**, 609–638 (2003).

[77] M. Murphy, V. Flambaum, J. Webb, V. Dzuba, J. Prochaska and A. Wolfe, 'Constraining variations in the fine-structure constant, quark masses and the strong interaction', *in* 'Astrophysics, Clocks and Fundamental Constants', volume 648 of *Lect. Notes Phys.*, 131–150, EDP Sciences, Springer Verlag (2004).

[78] V. Dzuba, V. Flambaum and J. Webb, 'Space-time variation of physical constants and relativistic corrections in atoms'. *Phys. Rev. Lett.* **82**, 888 (1999).

[79] V. Dzuba, V. V. Flambaum and J. K. Webb, 'Calculations of the relativistic effects in many-electron atoms and space-time variation of fundamental constants'. *Phys. Rev. A* **59**, 230 (1999).

[80] J. C. Berengut, V. A. Dzuba, V. V. Flambaum, M. G. Kozlov, M. V. Marchenko, M. T. Murphy and J. K. Webb, 'Laboratory spectroscopy and the search for space-time variation of the fine structure constant using QSO spectra' (2004), arxiv:physics/0408017.

[81] I. Labazan, E. Reinhold, W. Ubachs and V. V. Flambaum, 'Wavelength calibration of the C I line at 94.5 nm for comparison with quasar data'. *Phys. Rev. A* **71**, 040 501 (2005).

[82] 'Calibration of Ca 423-nm line', Unpublished.

[83] A. L. Wolf, S. A. van den Berg, C. Gohle, E. J. Salumbides, W. Ubachs and K. S. E. Eikema, 'Frequency metrology on the 4s $^2S_{1/2}$ – 4p $^2P_{1/2}$ transition in $^{40}Ca^+$ for a comparison with quasar data'. *Phys. Rev. A* **78**, 032 511 (2008).

[84] A. L. Wolf, S. A. van den Berg, W. Ubachs and K. S. E. Eikema, 'Direct frequency comb spectroscopy of trapped ions' (2008), arXiv:0812.4212v1.

[85] R. Srianand, H. Chand, P. Petitjean and B. Aracil, 'Limits on the Time Variation of the Electromagnetic Fine-Structure Constant in the Low Energy Limit from Absorption Lines in the Spectra of Distant Quasars'. *Phys. Rev. Lett.* **92**, 121 302 (2004).

[86] R. Quast, D. Reimers and S. Levshakov, 'Probing the variability of the fine-structure constant with the VLT/UVES'. *Astron. Astrophys.* **415**, L7–L11 (2004).

[87] H. Chand, R. Srianand, P. Petitjean and B. Aracil, 'Probing the cosmological variation of the fine-structure constant: Results based on VLT-UVES sample'. *Astron. Astrophys.* **417**, 853–871 (2004).

[88] S. A. Levshakov, M. Centurión, P. Molaro, S. D'Odorico, D. Reimers, R. Quast and M. Pollmann, 'Most precise single redshift bound to $\Delta\alpha/\alpha$'. *Astron. Astrophys.* **449**, 879 (2006).

[89] M. T. Murphy, J. K. Webb and V. V. Flambaum, 'Revision of VLT/UVES constraints on a varying fine-structure constant'. *Mon. Not. R. Astron. Soc.* **384**, 1053–1062 (2008).

[90] H. Chand, P. Petitjean, R. Srianand and B. Aracil, 'Probing the time-variation of the fine-structure constant: Results based on Si IV doublets from a UVES sample'. *Astron. Astrophys.* **430**, 47–58 (2005).

[91] M. Savedoff, 'Physical Constants in Extra-Galactic Nebulae'. *Nature* **178**, 688–689 (1956).

[92] J. N. Bahcall, W. L. W. Sargent and M. Schmidt, 'An analysis of the absorption spectrum of 3C 191'. *Astrophys. J.* **149**, L11 (1967).

[93] M. Murphy, J. Webb, V. Flambaum, J. Prochaska and A. Wolfe, 'Further constraints on variation of the fine-structure constant from alkali-doublet QSO absorption lines'. *Mon. Not. R. Astron. Soc.* **327**, 1237–1243 (2001).

[94] R. Thompson, 'The determination of the electron to proton inertial mass ratio via molecular transitions'. *Astroph. Lett.* **16**, 3 (1975).

[95] B. E. J. Pagel, 'Limits to past variability of proton-electron mass ratio set by quasar absorption-line redshifts'. *Mon. Not. R. Astron. Soc.* **179**, 81P (1977).

[96] T. Wiklind and F. Combes, 'Molecular absorption lines at high redshift: PKS 1413+135 (z=0.247)'. *Astron. Astrophys.* **328**, 48 (1997).

[97] V. V. Flambaum and M. G. Kozlov, 'Limit on the Cosmological Variation of m_p/m_e from the Inversion Spectrum of Ammonia'. *Phys. Rev. Lett.* **98**, 240 801 (2007).

[98] M. T. Murphy, V. V. Flambaum, S. Muller and C. Henkel, 'Strong Limit on a Variable Proton-to-Electron Mass Ratio from Molecules in the Distant Universe'. *Science* **320**, 1611–1613 (2008).

[99] C. Willott, P. Delorme, A. Omont, J. Bergeron, X. Delfosse, T. Forveille, L. Albert, C. Reylé, G. Hill, M. Gully-Santiago, P. Vinten, D. Crampton, J. Hutchings, D. Schade, L. Simard, M. Sawicki, A. Beelen, and P. Cox, 'Four Quasars above Redshift 6 Discovered by the Canada-France High-z Quasar Survey'. *Astron. J.* **134**, 2435 (2007).

[100] E. Reinhold, R. Buning, U. Hollenstein, A. Ivanchik, P. Petitjean and W. Ubachs, 'Indication of a cosmological variation of the proton-electron mass ratio based on laboratory measurements and reanalysis of H_2 spectra'. *Phys. Rev. Lett.* **96**, 151 101 (2006).

[101] W. Ubachs, R. Buning, K. Eikema and E. Reinhold, 'On a possible variation of the proton-to-electron mass ratio: H_2 spectra in the line of sight of high-redshift quasars and in the laboratory'. *J. Mol. Spectrosc.* **241**, 155 (2007).

[102] A. Ivanchik, P. Petitjean, D. Varshalovich, B. Aracil, R. Srianand, H. Chand, C. Ledoux and P. Boissé, 'A new constraint on the time dependence of the proton-to-electron mass ratio'. *Astron. Astrophys.* **440**, 45 (2005).

[103] M. T. Murphy, P. Tzanavaris, J. K. Webb and C. Lovis, 'Selection of ThAr lines for wavelength calibration of echelle spectra and implications for variations in the fine-structure constant'. *Mon. Not. R. Astron. Soc.* **378**, 221–230 (2007).

[104] T. Steinmetz, T. Wilken, C. Araujo-Hauck, R. Holzwarth, T. Hänsch, L. Pasquini, A. Manescau, S. D'Odorico, M. Murphy, T. Kentischer, W. Schmidt and T. Udem, 'Laser Frequency Combs for Astronomical Observations'. *Science* **321**, 1335 (2008).

[105] V. V. Meshkov, A. V. Stolyarov, A. Ivanchik and D. A. Varshalovich, 'Ab Initio Nonadiabatic Calculation of the Sensitivity Coefficients for the $X\ ^1\Sigma_g^+ \rightarrow B\ ^1\Sigma_u^+;\ C\ ^1\Pi_u$ Lines of H_2 to the Proton-to-Electron Mass Ratio'. *JETP Lett.* **83**, 303–307 (2006).

[106] D. A. Varshalovich and S. A. Levshakov, ‘On a time-dependence of physical constants’. *JETP Lett.* **58**, 237 (1993).

[107] D. Varshalovich and A. Potekhin, ‘Cosmological variability of fundamental physical constants’. *Space Sci. Rev.* **74**, 259 (1995).

[108] A. V. Ivanchik, E. Rodriguez, P. Petitjean and D. A. Varshalovich, ‘Do the fundamental constants vary in the course of cosmological evolution?’ *Astron. Lett.* **28**, 423 (2002).

[109] H. L. Bethlem, M. Kajita, B. Sartakov, G. Meijer and W. Ubachs, ‘Prospects for precision measurements on ammonia molecules in a fountain’. *Eur. Phys. J. Spec. Top.* **163**, 55 (2008).

[110] J. King, J. Webb, M. Murphy and R. Carswell, ‘Stringent Null Constraint on Cosmological Evolution of the Proton-to-Electron Mass Ratio’. *Phys. Rev. Lett.* **101**, 251 304 (2008).

[111] A. D. Ludlow, T. Zelevinsky, G. K. Campbell, S. Blatt, M. M. Boyd, M. H. G. de Miranda, M. J. Martin, J. W. Thomsen, S. M. Foreman, J. Ye, T. M. Fortier, J. E. Stalnaker, S. A. Diddams, Y. L. Coq, Z. W. Barber, N. Poli, N. D. Lemke, K. M. Beck and C. W. Oates, ‘Sr Lattice Clock at 1×10^{16} Fractional Uncertainty by Remote Optical Evaluation with a Ca Clock’. *Science* **319**, 1805 (2008).

[112] T. Rosenband, D. B. Hume, P. O. Schmidt, C. W. Chou, A. Brusch, L. Lorini, W. H. Oskay, R. E. Drullinger, T. M. Fortier, J. E. Stalnaker, S. A. Diddams, W. C. Swann, N. R. Newbury, W. M. Itano, D. J. Wineland and J. C. Bergquist, ‘Frequency Ratio of Al^+ and Hg^+ Single-Ion Optical Clocks; Metrology at the 17th Decimal Place’. *Science* **319**, 1808 (2008).

[113] S. N. Lea, ‘Limits to time variation of fundamental constants from comparisons of atomic frequency standards’. *Rep. Prog. Phys.* **70**, 1473 (2007).

[114] R. Holzwarth, T. Udem, T. W. Hänsch, J. C. Knight, W. J. Wadsworth and P. S. J. Russell, ‘Optical Frequency Synthesizer for Precision Spectroscopy’. *Phys. Rev. Lett.* **85**, 2264–2267 (2000).

[115] D. Jones, S. Diddams, J. Ranka, A. Stentz, R. Windeler, J. Hall and S. Cundiff, ‘Carrier-Envelope Phase Control of Femtosecond Mode-Locked Lasers and Direct Optical Frequency Synthesis’. *Science* **288**, 635 (2000).

[116] H. Schnatz, B. Lipphardt, J. Helmcke, F. Riehle and G. Zinner, 'First Phase-Coherent Frequency Measurement of Visible Radiation'. *Phys. Rev. Lett.* **76**, 18–21 (1996).

[117] S. Cundiff and J. Ye, 'Colloquium: Femtosecond optical frequency combs'. *Rev. Mod. Phys.* **75**, 325 (2003).

[118] J. Barrow and D. Shaw, 'Varying alpha: New constraints from seasonal variations'. *Phys. Rev. D* **78**, 067 304 (2008).

[119] A. Shelkovnikov, R. Butcher, C. Chardonnet and A. Amy-Klein, 'Stability of the Proton-to-Electron Mass Ratio'. *Phys. Rev. Lett.* **100**, 150 801 (2008).

[120] T. Zelevinsky, S. Kotochigova and J. Ye, 'Precision Test of Mass-Ratio Variations with Lattice-Confined Ultracold Molecules'. *Phys. Rev. Lett.* **100**, 043 201 (2008).

[121] A. Cingöz, A., A.-T. Nguyen, N. Leefer, D. Budker, S. K. Lamoreaux and J. R. Torgerson, 'Limit on the Temporal Variation of the Fine-Structure Constant Using Atomic Dysprosium'. *Phys. Rev. Lett.* **98**, 040 801 (2007).

[122] H. L. Bethlem and W. Ubachs, 'Testing the time-invariance of fundamental constants using microwave spectroscopy on cold diatomic radicals'. *To be published* (2008).

[123] H. Sandvik, J. Barrow and J. Magueijo, 'A Simple Cosmology with a Varying Fine Structure Constant'. *Phys. Rev. Lett.* **88**, 031 302 (2002).

[124] J. D. Bekenstein, 'Fine-structure constant: Is it really a constant?' *Phys. Rev. D* **25**, 1527 (1982).

[125] Y. Fujii, 'Possible time-variability of the fine-structure constant expected from the accelerating universe'. *Phys. Lett. B* **660**, 87 (2008).

[126] Y. Fujii, 'Revised fits to $\Delta\alpha/\alpha$ in consistency with the accelerating universe'. *Phys. Lett. B* **671**, 207 (2009).

[127] E. E. Eyler, 'Tets of basic molecular physics using high-resolution laser spectroscopy of H_2'. *Comments At. Mol. Phys.* **24**, 299 (1990).

[128] B. Stoicheff, 'On the dissociation energy of molecular hydrogen'. *Can. J. Phys.* **79**, 165–172 (2001).

[129] W. Kołos, 'Extrapolated Born-Oppenheimer energy for the ground state of the hydrogen molecule'. *J. Chem. Phys.* **101**, 1330 (1994).

[130] A. Balakrishnan, V. Smith and B. P. Stoicheff, 'Dissociation energy of the hydrogen molecule'. *Phys. Rev. Lett.* **68**, 2149–2152 (1992).

[131] E. McCormack and E. Eyler, 'Perturbed structure of molecular hydrogen near the second dissociation limit'. *Phys. Rev. Lett.* **66**, 1042–1045 (1991).

[132] Y. P. Zhang, C. H. Cheng, J. T. Kim, J. Stanojevic and E. E. Eyler, 'Dissociation Energies of Molecular Hydrogen and the Hydrogen Molecular Ion'. *Phys. Rev. Lett.* **92**, 203 003 (2004).

[133] G. Greetham, U. Hollenstein, R. Seiler, W. Ubachs and F. Merkt, 'High-resolution VUV photoionization spectroscopy of HD between the $X\ ^2\Sigma_g^+\ v^+ = 0$ and $v^+ = 1$ thresholds'. *Phys. Chem. Chem. Phys.* **5**, 2528–2534 (2003).

[134] A. de Lange, E. Reinhold and W. Ubachs, 'Precision spectroscopy on some g symmetry states in H_2 and determination of the ionization potential'. *Phys. Rev. A* **65**, 064 501(R) (2002).

[135] C. Jungen, I. Dabrowski, G. Herzberg and M. Vervloet, 'High orbital angular momentum states in H_2 and D_2. III. Singlet–triplet splittings, energy levels, and ionization potentials'. *J. Chem. Phys.* **93**, 2289 (1990).

[136] D. W. Chandler and L. R. Thorne, 'Measured radiative lifetimes for H_2 and HD in the E,F $^1\Sigma_g^+$ electronic state'. *J. Chem. Phys.* **85**, 1733 (1986).

[137] W. Glab and J. Hessler, 'Multiphoton excitation of high singlet np Rydberg states of molecular hydrogen: Spectroscopy and dynamics'. *Phys. Rev. A* **35**, 2102 (1987).

[138] E. E. Eyler, J. Gilligan, E. McCormack, A. Nussenzweig and E. Pollack, 'Precise two-photon spectroscopy of $E \leftarrow X^*$ intervals in H_2'. *Phys. Rev. A* **36**, 3486 (1987).

[139] E. F. McCormack, J. M. Gilligan, C. Cornaggia and E. E. Eyler, 'Measurement of high Rydberg states and the ionization potential of H_2'. *Phys. Rev. A* **39**, 2260 (1989).

[140] J. Gilligan and E. Eyler, 'Precise determinations of ionization potentials and EF-state energy levels of H_2, HD, and D_2'. *Phys. Rev. A* **46**, 3676 (1992).

[141] D. Shiner, J. Gilligan, B. Cook and W. Lichten, 'H_2, D_2, and HD ionization potentials by accurate calibration of several iodine lines'. *Phys. Rev. A* **47**, 4042 (1993).

[142] M. Vervloet and D. Bailly, private communication.

[143] A. Osterwalder, A. Wuest, F. Merkt and C. Jungen, 'High-resolution millimeter wave spectroscopy and multichannel quantum defect theory of the hyperfine structure in high Rydberg states of molecular hydrogen H_2'. *J. Chem. Phys.* **121**, 11 810 – 11 838 (2004).

[144] A. Yiannopoulou, N. Melikechi, S. Gangopadhyay, J. C. Meiners, C. H. Cheng and E. E. Eyler, 'Determinations of $EF^1\ \Sigma_g^+ \leftarrow X^1\ \Sigma_g^+$ transition frequencies in H_2, D_2, and HD'. *Phys. Rev. A* **73**, 022 506 (2006).

[145] M. Sneep, S. Hannemann, E.-J. van Duijn and W. Ubachs, 'Deep-ultraviolet cavity ringdown spectroscopy'. *Opt. Lett.* **29**, 1378–1380 (2004).

[146] R. Zinkstok, S. Witte, W. Ubachs, W. Hogervorst and K. Eikema, 'Frequency comb laser spectroscopy in the vacuum-ultraviolet region'. *Phys. Rev. A* **73**, 061 801(R) (2006).

[147] S. Witte, R. T. Zinkstok, W. Ubachs, W. Hogervorst and K. S. E. Eikema, 'Deep-Ultraviolet Quantum Interference Metrology with Ultrashort Laser Pulses'. *Science* **307**, 400 (2005).

[148] M. Fee, K. Danzmann and S. Chu, 'Optical heterodyne measurement of pulsed lasers: Toward high-precision pulsed spectroscopy'. *Phys. Rev. A* **45**, 4911 (1992).

[149] N. Melikechi, S. Gangopadhyay and E. Eyler, 'Phase dynamics in nanosecond pulsed dye laser amplification'. *J. Opt. Soc. Am. B* **11**, 2402 (1994).

[150] K. Eikema, W. Ubachs, W. Vassen and W. Hogervorst, 'Lamb shift measurement in the 1^1S ground state of helium'. *Phys. Rev. A* **55**, 1866 (1997).

[151] R. White, Y. He, B. Orr, M. Kono and K. Baldwin, 'Control of frequency chirp in nanosecond-pulsed laser spectroscopy. 1. Optical-heterodyne chirp analysis techniques'. *J. Opt. Soc. Am. B* **21**, 1577 (2004).

[152] R. White, Y. He, B. Orr, M. Kono and K. Baldwin, 'Pulsed injection-seeded optical parametric oscillator with low frequency chirp for high-resolution spectroscopy'. *Opt. Lett.* **28**, 1248 (2003).

[153] S. Hannemann, E. J. Salumbides, S. Witte, R. Zinkstok, E.-J. van Duijn, K. Eikema and W. Ubachs, 'Frequency metrology on the Mg $3s^2\ {}^1S \rightarrow 3s4p\ {}^1P$ line for comparison with quasar data'. *Phys. Rev. A* **74**, 012 505 (2006).

[154] T. Hänsch and B. Couillaud, 'Laser frequency stabilization by polarization spectroscopy of a reflecting reference cavity'. *Opt. Commun.* **35**, 441 (1980).

[155] 'Database and program for calculating absolute frequencies of hyperfine components in the I_2 saturation spectrum kindly provided by Dr. Knöckel, the University of Hannover; see also: H. Knöckel, B. Bodermann, and E. Tiemann, Eur. Phys. J. D **28**, 199 (2004).'

[156] M. Vrakking, A. Bracker, T. Suzuki and Y. Lee, 'Ultrasensitive detection of hydrogen molecules by (2+1) resonance-enhanced multiphoton ionization'. *Rev. Sci. Instr.* **64**, 645 (1993).

[157] S. Gangopadhyay, N. Melikechi and E. E. Eyler, 'Optical phase perturbations in nanosecond pulsed amplification and second-harmonic generation'. *J. Opt. Soc. Am. B* **11**, 231 (1994).

[158] R. W. Boyd, *Nonlinear Optics*, Academic, Boston, Mass. (1992).

[159] H. Li, F. Zhou, X. Zhang and W. Ji, 'Bound electronic Kerr effect and self-focusing induced damage in second-harmonic-generation crystals'. *Opt. Commun.* **144**, 75 (1997).

[160] R. DeSalvo, D. J. Hagan, M. Sheik-Bahae, G. Stegeman, E. W. V. Stryland and H. Vanherzeele, 'Self-focusing and self-defocusing by cascaded second-order effects in KTP'. *Opt. Lett.* **17**, 28 (1992).

[161] E. Jones, T. Olifant and P. Peterson, *SciPy: Open source scientific tools for Python* (2000).

[162] P. Noterdaeme, C. Ledoux, P. Petitjean, F. L. Petit, R. Srianand and A. Smette, 'Excitation mechanisms in newly discovered H_2-bearing damped Lyman-α clouds: systems with low molecular fractions'. *Astron. Astrophys.* **474**, 393 (2007).

[163] S. Hannemann, E. J. Salumbides, S. Witte, R. Zinkstok, E.-J. van Duijn, K. Eikema and W. Ubachs, 'Frequency metrology on the $EF\ {}^1\Sigma_g^+ \leftarrow X\ {}^1\Sigma_g^+$ (0,0) transition in H_2, HD, and D_2'. *Phys. Rev. A* **74**, 062 514 (2006).

[164] S. Hannemann, E.-J. van Duijn and W. Ubachs, 'A narrow-band injection-seeded pulsed titanium:sapphire oscillator-amplifier system with on-line chirp analysis for high-resolution spectroscopy'. *Rev. Sci. Instrum.* **78**, 103 102 (2007).

[165] S. Hannemann, E. Salumbides and W. Ubachs, 'Reducing the first-order Doppler shift in a Sagnac interferometer'. *Opt. Lett.* **32**, 1381 (2007).

[166] D. Bailly and M. Vervloet, 'Rotational analysis of the molecular hydrogen triplet 3*s*,***d*** complex revisited'. *Mol. Phys.* **105**, 1559 (2007).

[167] A. Maki, J. Wells and D. Jennings, 'Heterodyne frequency measurements of CO and OCS beyond 2100 cm^{-1}'. *J. Mol. Spectrosc.* **144**, 224 (1990).

[168] G. Norlén, 'Wavelengths and Energy Levels of Ar I and Ar II based on New Interferometric Measurements in the Region 3400 – 9800 Å'. *Phys. Scripta* **8**, 249 (1973).

[169] D. Jennings, S. Bragg and J. W. Brault, 'The $v = 0 - 0$ spectrum of H_2'. *Astrophys. J.* **282**, L85 (1984).

[170] 'Reference to EPAPS system for full line list.'

[171] W. Ubachs and E. Reinhold, 'Highly Accurate H_2 Lyman and Werner Band Laboratory Measurements and an Improved Constraint on a Cosmological Variation of the Proton-to-Electron Mass Ratio'. *Phys. Rev. Lett.* **92**, 101 302 (2004).

[172] J. Philip, J. P. Sprengers, T. Pielage, C. A. de Lange, W. Ubachs and E. Reinhold, 'Highly accurate transition frequencies in the H_2 Lyman and Werner absorption bands'. *Can. J. Chem.* **82**, 713 (2004).

[173] T. Ivanov, M. Vieitez, C. de Lange and W. Ubachs, 'Frequency calibration of B $^1\Sigma_u^+$ - X $^1\Sigma_g^+$ (6,0) Lyman transitions in H_2 for comparison with quasar data'. *J. Phys. B* **41**, 035 702 (2008).

[174] H. Primas and U. Müller-Herold, *Elementare Quantenchemie*, Teubner Studienbücher, Stuttgart (1984), Section 5.3 (*Fakten und Zahlen: Die Geschichte des Wasserstoff-Moleküls*) gives a complete account of the early efforts invested in the quantitative comparison of the experimental and theoretical values of the dissociation energy of H_2 and explains in detail how studies of molecular hydrogen contributed to establish the validity of molecular quantum mechanics and to understand chemical bonds physically.

[175] G. W. Erickson, 'Energy levels of one-electron atoms'. *J. Phys. Chem. Ref. Data* **6**, 831 (1977).

[176] V. I. Korobov, 'Bethe logarithm for the hydrogen molecular ion H_2^+'. *Phys. Rev. A* **73**, 024 502 (2006).

[177] R. Seiler, T. Paul, M. Andrist and F. Merkt, 'Generation of programmable near-Fourier-transform-limited pulses of narrow-band laser radiation from the near infrared to the vacuum ultraviolet'. *Rev. Sci. Instr.* **76**, 103 103 (2005).

[178] T. Paul and F. Merkt, 'High-resolution spectroscopy of xenon using a tunable Fourier-transform-limited all-solid-state vacuum-ultraviolet laser system'. *J. Phys. B* **38**, 4145–4154 (2005).

[179] T. A. Paul, H. A. Cruse, H. J. Wrner and F. Merkt, 'Structure and dynamics of the high gerade Rydberg states of D_2 in the vicinity of the adiabatic ionization threshold'. *Mol. Phys.* **105**, 871–883 (2007).

[180] H. Knöckel, B. Bodermann and E. Tiemann, 'High precision description of the rovibronic structure of the I_2 B-X spectrum'. *Eur. Phys. J. D* **28**, 199–209 (2004).

[181] I. Reinhard, M. Gabrysch, B. F. von Weikersthal, K. Jungmann and G. zu Putlitz, 'Measurement and compensation of frequency chirping in pulsed dye laser amplifiers'. *Appl. Phys. B* **63**, 467–472 (1996).

[182] K. F. Wall, R. L. Aggarwal, M. D. Sciacca, H. J. Zeiger, R. E. Fahey and A. J. Strauss, 'Optically induced nonresonant changes in the refractive index of $Ti:Al_2O_3$'. *Opt. Lett.* **14**, 180–182 (1989).

[183] T. A. Planchon, W. Amir, C. Childress, J. A. Squier and C. G. Durfee, 'Measurement of pump-induced transient lensing in a cryogenically-cooled high average power Ti:sapphire amplifier'. *Opt. Express* **16**, 18 557 (2008).

[184] A. Smith and M. Bowers, 'Phase distortions in sum- and difference-frequency mixing in crystals'. *J. Opt. Soc. Am. B* **12**, 49–57 (1995).

[185] M. Schäfer and F. Merkt, 'Millimeter-wave spectroscopy and multichannel quantum-defect-theory analysis of high Rydberg states of krypton: The hyperfine structure of $^{83}Kr^+$'. *Phys. Rev. A* **74**, 062 506 (2006).

[186] A. Osterwalder and F. Merkt, 'Using High Rydberg States as Electric Field Sensors'. *Phys. Rev. Lett.* **82**, 1831–1834 (1999).

[187] G. Herzberg and C. Jungen, ‘Rydberg series and ionization potential of the H_2 molecule’. *J. Mol. Spectrosc.* **41**, 425 (1972).

[188] J.-P. Karr, F. Bielsa, A. Douillet, J. Gutierrez, V. Korobov and L. Hilico, ‘Vibrational spectroscopy of H_2^+: Hyperfine structure of two-photon transitions’. *Phys. Rev. A* **77**, 063 410 (2008).

[189] N. F. Ramsey, ‘Theory of Molecular Hydrogen and Deuterium in Magnetic Fields’. *Phys. Rev.* **85**, 60–65 (1952).

[190] G. Gabrielse, D. Hanneke, T. Kinoshita, M. Nio and B. Odom, ‘Erratum: New Determination of the Fine Structure Constant from the Electron g Value and QED [Phys. Rev. Lett. **97**, 030802 (2006)]’. *Phys. Rev. Lett.* **99**, 039 902 (2007).

[191] G. Gabrielse, D. Hanneke, T. Kinoshita, M. Nio and B. Odom, ‘New Determination of the Fine Structure Constant from the Electron g Value and QED’. *Phys. Rev. Lett.* **97**, 030 802 (2006).

[192] F. Biraben, ‘Spectroscopy of atomic hydrogen. How is the Rydberg constant determined?’ (2008), arXiv/0809.2985.

[193] R. E. Moss, ‘Calculations for the vibration-rotation levels of H_2 in its ground and first excited electronic states’. *Mol. Phys.* **80**, 1541 (1993).

[194] G. Herzberg, ‘Dissociation Energy and Ionization Potential of Molecular Hydrogen’. *Phys. Rev. Lett.* **23**, 1081–1083 (1969).

[195] E. E. Eyler, R. C. Short and F. M. Pipkin, ‘Precision Spectroscopy of the nf Triplet Rydberg States of H_2 and Determination of the Triplet Ionization Potential’. *Phys. Rev. Lett.* **56**, 2602–2605 (1986).

[196] W. Kołos and J. Rychlewski, ‘Improved theoretical dissociation energy and ionization potential for the ground state of the hydrogen molecule’. *J. Chem. Phys.* **98**, 3960–3967 (1993).

[197] L. Wolniewicz, ‘Relativistic energies of the ground state of the hydrogen molecule’. *J. Chem. Phys.* **99**, 1851 (1993).

[198] J.-C. D. Meiners, Master’s thesis, University of Delaware, Newark (1994).

[199] T. Ashenfelter, G. Mathews and K. Olive, ‘Chemical evolution of Mg isotopes versus the time variation of the fine structure constant’. *Phys. Rev. Lett.* **92**, 041 102 (2004).

[200] M. Kozlov, V. Korol, J. Berengut, V. Dzuba and V. Flambaum, 'Space-time variation of the fine-structure constant and the evolution of isotope abundances'. *Phys. Rev. A* **70**, 062 108 (2004).

[201] Y. Fenner, M. Murphy and B. Gibson, 'On variations in the fine-structure constant and stellar pollution of quasar absorption systems'. *Mon. Not. R. Astron. Soc.* **358**, 468 (2005).

[202] J. C. Berengut, V. A. Dzuba, V. V. Flambaum and M. G. Kozlov, 'Configuration-interaction calculation for the isotope shift in Mg I'. *Phys. Rev. A* **69**, 044 102 (2004).

[203] J. Berengut, V. Flambaum and M. Kozlov, 'Calculation of relativistic and isotope shifts in Mg I'. *Phys. Rev. A* **72**, 044 501 (2005).

[204] G. Risberg, 'The spectrum of atomic magnesium, Mg I'. *Ark. Fys.* **28**, 381 (1965).

[205] N. Beverini, E. Maccioni, D. Pereira, F. Strumia, G. Vissani and Y.-Z. Wang, 'Wavelength, isotopic shift, and transition rate of the Mg I resonance line'. *Opt. Commun.* **77**, 299 (1990).

[206] J. Pickering, A. P. Thorne and W. J.K., 'Precise laboratory wavelengths of the Mg I and Mg II resonance transitions at 2853, 2803, and 2796 Å'. *Mon. Not. R. Astron. Soc.* **300**, 131 (1998).

[207] L. Hallstadius, 'Extended measurements of isotope shifts in Mg I'. *Z. Phys. A* **291**, 203 (1979).

[208] S. Le Boiteux, A. Klein, J. Rios Leite and M. Ducloy, 'Doppler-free spectroscopy and isotopic shift of the Mg I resonance line at 285 nm'. *J. Phys. France* **49**, 885 (1988).

[209] A. Amy-Klein, O. Gorceix, S. Le Boiteux, J. R. Rios Leite and M. Ducloy, 'Doppler-free spectroscopy of Mg using uv-visible saturated absorption'. *Opt. Commun.* **90**, 265 (1992).

[210] H.-J. Kluge and H. Sauter, 'Level crossing experiments in the first excited $^1P_1$ states of the alkaline earths'. *Z. Phys.* **270**, 295 (1974).

[211] S. Witte, R. T. Zinkstok, W. Hogervorst and K. Eikema, 'Control and precise measurement of carrier-envelope phase dynamics'. *Appl. Phys. B* **78**, 5 (2004).

[212] T. N. Chang, 'Radiative lifetimes of the bound excited states of magnesium and beryllium'. *Phys. Rev. A* **41**, 4922 (1990).

[213] J. Steiner and L. Curtis, 'Branching fractions for the Mg-like $3s3p - 3s3d$ and $3s3p - 3p^2$ transition arrays'. *J. Phys. B* **37**, 3771–3776 (2004).

[214] 'These calculations were performed by L. Veseth (University of Oslo) and kindly made available to us'.

[215] K. Rosman and P. Taylor, 'Isotopic Compositions of the Elements 1997'. *Pure & Appl. Chem.* **70**, 217–235 (1998).

[216] M. Aldenius, S. Johansson and M. T. Murphy, 'Accurate laboratory ultraviolet wavelengths for quasar absorption-line constraints on varying fundamental constants'. *Mon. Not. R. Astron. Soc.* **370**, 444–452 (2006).

[217] M. Fischer, N. Kolachevsky, M. Zimmermann, R. Holzwarth, T. Udem, T. Hänsch, M. Abgrall, J. Grünert, I. Maksimovic, S. Bize, H. Marion, F. Pereira Dos Santos, P. Lemonde, G. Santarelli, M. Haas, U. Jentschura and C. Keitel, 'New limits on the drift of fundamental constants from laboratory measurements'. *Phys. Rev. Lett.* **92**, 230 802 (2004).

[218] J. Webb, M. Murphy, V. Flambaum and S. Curran, 'Does the fine structure constant vary? A third quasar absorption sample consistent with varying alpha'. *Astrophys. Space Sci.* **283**, 565–575 (2003).

[219] M. Murphy, J. Webb, V. Flambaum and S. Curran, 'Does the fine-structure constant vary? A detailed investigation into systematic effects'. *Astrophys. Space Sci.* **283**, 577–582 (2003).

[220] A. Lurio, 'Lifetime of the First Excited $^1P_1$ State of Mg and Ba; hfs of Ba^{137}'. *Phys. Rev.* **136**, A376–A379 (1964).

[221] T. I. Ivanov, M. Roudjane, M. O. Vieitez, C. A. de Lange, W.-U. L. Tchang-Brillet and W. Ubachs, 'HD as a Probe for Detecting Mass Variation on a Cosmological Time Scale'. *Phys. Rev. Lett.* **100**, 093 007 (2008).

[222] E. Salumbides, J. Sprengers, E. Reinhold and W. Ubachs, 'High precision frequency calibration of N I lines in the XUV domain'. *J. Phys. B* **38**, L383–L387 (2005).

[223] R. Huffman, J. Larrabee and T. Y., 'New Absorption Spectra of Atomic and Molecular Oxygen in the Vacuum Ultraviolet. I. Rydberg Series from O I Ground State and New Excited O_2 Bands'. *J. Chem. Phys.* **46**, 2213–2233 (1967).

[224] R. Huffman, J. Larrabee and Y. Tanaka, 'New Absorption Spectra of Atomic and Molecular Oxygen in the Vacuum Ultraviolet. II. Rydberg Series from O I($^1D_2$) and O I($^1S_0$) Metastable States'. *J. Chem. Phys.* **47**, 4462–4471 (1967).

[225] D. C. Morton, 'Atomic Data for resonance absorption lines. I Wavelengths longward of the Lyman limit'. *Astroph. J. Suppl. Ser.* **77**, 119–202 (1991).

[226] C. Moore, 'Selected Tables of Atomic Spectra: A. Atomic Energy Levels - Second Edition; B. Multiplet Tables; O I'. *NSRDS-NBS 3, Section 7* (1976).

[227] K. Eriksson and H. Isberg, 'O-I quintet and triplet terms below the ionization limit'. *Ark. Fys.* **24**, 549 (1963).

[228] K. Eriksson and H. Isberg, 'New measurements in spectrum of atomic oxygen OI'. *Ark. Fys.* **37**, 221 (1968).

[229] L. Zink, K. Evenson, F. Matsushima, T. Nelis and L. Robinson, 'Atomic oxygen fine-structure splittings with tunable far-infrared spectroscopy'. *Astroph. J. Lett.* **371**, L85–L86 (1991).

[230] P. De Natale, M. Bellini, W. Goetz, M. Prevedelli and M. Inguscio, 'Hyperfine structure and isotope shift in the far-infrared ground-state transitions of atomic oxygen'. *Phys. Rev. A* **48**, 3757 (1993).

[231] W. Ubachs, K. Eikema, W. Hogervorst and P. Cacciani, 'Narrow-band tunable extreme-ultraviolet laser source for lifetime measurements and precision spectroscopy'. *J. Opt. Soc. Am. B* **14**, 2469–2476 (1997).

[232] S. C. Xu, R. van Dierendonck, W. Hogervorst and W. Ubachs, 'A Dense Grid of Reference Iodine Lines for Optical Frequency Calibration in the Range 595655 nm'. *J. Mol. Spectrosc.* **201**, 256–266 (2000).

[233] M. Godefroid and C. Fischer, 'Isotope shift in the oxygen electron affinity'. *Phys. Rev. A* **60**, R2637 (1999).

[234] M. Pettini, S. L. Ellison, J. Bergeron and P. Petitjean, 'The abundances of nitrogen and oxygen in damped Lyman α systems'. *Astron. and Astroph.* **391**, 21–34 (2002).

[235] K. T. Compton and J. C. Boyce, 'Arc Spectrum of Nitrogen in the Extreme Ultra-Violet'. *Phys. Rev.* **33**, 145–153 (1929).

[236] K. B. S. Eriksson, 'Revised energy levels for the neutral nitrogen atom'. *Ark. Fys.* **13**, 429 (1958).

[237] K. B. S. Eriksson and I. Johansson, 'The spectrum of the neutral nitrogen atom in the lead-sulfide region'. *Ark. Fys.* **19**, 235 (1961).

[238] V. Kaufman and J. Ward, 'Newly Measured and Calculated Wavelengths in the Vacuum Ultraviolet Spectrum of Neutral Nitrogen'. *Appl. Opt.* **6**, 43 (1967).

[239] M. van Beek and J. ter Meulen, 'An intense pulsed electrical discharge source for OH molecular beams'. *Chem. Phys. Lett.* **337**, 237 – 242 (2001).

[240] G. Herzberg, 'Ionization Potentials and Lamb Shifts of the Ground States of ^{4}He and ^{3}He'. *Proc. Roy. Soc. London B* **248**, 309 (1958).

[241] A. Hibbert, P. L. Dufton and F. P. Keenan, 'Oscillator strengths for transitions in N I and the interstellar abundance of nitrogen'. *Mon. Not. R. Astron. Soc.* **213**, 721–734 (1985).

[242] W. W. Holloway, E. Lüscher and R. Novick, 'Hyperfine Structure of Atomic Nitrogen'. *Phys. Rev.* **126**, 2109–2115 (1962).

[243] P. Cangiano, M. de Angelis, L. Gianfrani, G. Pesce and A. Sasso, 'Hyperfine structure and isotope-shift investigations of atomic nitrogen by saturation spectroscopy'. *Phys. Rev. A* **50**, 1082–1087 (1994).

[244] P. K. Carroll and C. P. Collins, 'High resolution absorption studies of the $b^1\Pi_u \leftarrow X^1\Sigma_g^+$ system of nitrogen'. *Can. J. Phys.* **47**, 563 – 589 (1969).

[245] J. M. Ajello, G. K. James, B. O. Franklin and D. E. Shemansky, 'Medium-resolution studies of extreme ultraviolet emission from N_2 by electron impact: Vibrational perturbations and cross sections of the c_4' $^1\Sigma_u^+$ and b' $^1\Sigma_u^+$ states'. *Phys. Rev. A* **40**, 3524 – 3556 (1989).

[246] G. Stark, K. P. Huber, K. Yoshino, P. L. Smith and K. Ito, 'Oscillator strength and linewidth measurements of dipole-allowed transitions in $^{14}N_2$ between 93.5 and 99.5 nm'. *J. Chem. Phys.* **123**, 214 303 (2005).

[247] W. Ubachs, L. Tashiro and R. N. Zare, 'Study of the N_2 $b\,^1\Pi_u$ state via 1+1 multiphoton ionization'. *Chem. Phys.* **130**, 1 – 13 (1989).

[248] C. W. Walter, P. C. Cosby and H. Helm, '$N(^4S^0)$, $N(^2D^0)$, and $N(^2P^0)$ yields in predissociation of excited singlet states of N_2'. *J. Chem. Phys.* **99**, 3553 – 3561 (1993).

[249] A. van der Kamp, P. Cosby and W. van der Zande, 'Charge-transfer production of predissociated N_2 states. I. The $n = 3$ Rydberg state region (12.8-14 eV)'. *Chem. Phys.* **184**, 319 (1994).

[250] D. Stahel, M. Leoni and K. Dressler, 'Nonadiabatic representations of the $^1\Sigma_u^+$ and $^1\Pi_u$ states of the N_2 molecule'. *J. Chem. Phys.* **79**, 2541 – 2558 (1983).

[251] B. R. Lewis, S. T. Gibson, W. Zhang, H. Lefebvre-Brion and J.-M. Robbe, 'Predissociation mechanism for the lowest $^1\Pi_u$ states of N_2'. *J. Chem. Phys.* **122**, 144 302 (2005).

[252] M. O. Vieitez, T. I. Ivanov, W. Ubachs, B. R. Lewis and C. A. de Lange, 'On the complexity of the absorption spectrum of molecular nitrogen'. *J. Mol. Liq.* **141**, 110–117 (2008).

[253] J. T. Vanderslice, S. G. Tilford and P. G. Wilkinson, 'The High-Resolution Absorption Spectrum of Nitrogen from 1060 TO 1520 Å IV. The $a\,^1\Pi_g \leftarrow X\,^1\Sigma_g^+$ System of $N^{14}N^{15}$.' *Astrophys. J.* **142**, 84 (1965).

[254] K. Dressler and B. L. Lutz, 'Optical Identification of the 12.28-eV Quadrupole Transition in Molecular Nitrogen'. *Phys. Rev. Lett.* **19**, 1219–1221 (1967).

[255] J. W. Ledbetter, 'New Rydberg bands in the visible region and identification of the lowest Rydberg state of the N_2 molecule'. *J. Mol. Spectrosc.* **42**, 100 (1972).

[256] A. Kam and F. Pipkin, 'Measurement of the lifetime of the metastable a'' $^1\Sigma_g^+$ state of N_2'. *Phys. Rev. A* **43**, 3279 (1991).

[257] K. Lykke and B. Kay, 'Rotationally inelastic scattering of N_2 from clean and hydrogen covered Pd(111)'. *J. Chem. Phys.* **90**, 7602–7603 (1989).

[258] T. Hanisco and A. Kummel, 'Resonantly enhanced multiphoton ionization of nitrogen a" $^1\Sigma_g^+(v' = v'') \leftarrow X\,^1\Sigma_g^+(v'' = 0 - -2)$. 1. Determination of rotational populations and virtual state character'. *J. Phys. Chem.* **95**, 8565 (1991).

[259] A. Rijs, E. Backus, C. de Lange, M. Janssen, K. Wang and V. McKoy, 'Rotationally resolved photoelectron spectroscopy of hot N_2 formed in the photofragmentation of N_2O'. *J. Chem. Phys.* **114**, 9413–9420 (2001).

[260] J. Kaplan. *Phys. Rev.* **47**, 259 (1935).

[261] A. de Lange, R. Lang, W. van der Zande and W. Ubachs, 'Highly excited states of gerade symmetry in molecular nitrogen'. *J. Chem. Phys.* **116**, 7893 (2002).

[262] W. C. Ermler, J. P. Clark and R. S. Mulliken, 'Ab initio calculations of potential energy curves and transition moments of $^1\Sigma_g^+$ and $^1\Sigma_u^+$ states of N_2'. *J. Chem. Phys.* **86**, 370–375 (1987).

[263] J. Bominaar, C. Schoemaecker, N. Dam, J. J. T. Meulen and G. C. Groenenboom, '(2+1) REMPI on molecular nitrogen through the $^1\Sigma_g^+$ (II)-state'. *Chem. Phys. Lett.* **435**, 242–246 (2007).

[264] T. Trickl, D. Proch and K. L. Kompa, 'The Lyman-Birge-Hopfield System of Nitrogen: Revised Calculation of the Energy Levels'. *J. Mol. Spectrosc.* **171**, 374 – 384 (1995).

[265] K. Eikema, W. Hogervorst and W. Ubachs, 'On the determination of a heterogeneous vs a homogeneous perturbation in the spectrum of a diatomic molecule: The $K^1\Sigma^+$, $v = 0$ state of $^{13}C^{18}O$'. *J. Mol. Spectrosc.* **163**, 19 – 26 (1994).

[266] G. C. Groenenboom, private communication (2008).

[267] S. Gerstenkorn and P. Luc, *Atlas du Spectre D'Absorption de la Molecule D'Iode: 14 000 cm^{-1} - 15 600 cm^{-1}*, Laboratoire Aimé Cotton, CNRS II, 91405 Orsay, France (1978).

[268] S. Gerstenkorn and P. Luc, *Atlas du Spectre D'Absorption de la Molecule D'Iode: 15 600 cm^{-1} - 17 600 cm^{-1}*, Laboratoire Aimé Cotton, CNRS II, 91405 Orsay, France (1977).

[269] S. Gerstenkorn and P. Luc, *Atlas du Spectre D'Absorption de la Molecule D'Iode: 17 500 cm^{-1} - 20 000 cm^{-1}*, Laboratoire Aimé Cotton, CNRS II, 91405 Orsay, France (1977).

[270] S. Gerstenkorn, J. Verges and J. Chevillard, *Atlas du Spectre D'Absorption de la Molecule D'Iode: 11 000 cm^{-1} – 14 000 cm^{-1}*, Laboratoire Aimé Cotton, CNRS II, 91405 Orsay, France (1982).

[271] H. Katô, M. Baba, S. Kasahara, K. Ishikawa, M. Misono, Y. Kimura, J. O'Reilly, H. Kuwano, T. Shimamoto, T. Shinano, C. Fujiwara, M. Ikeuchi, N. Fujita, M. H. Kabir, M. Ushino, R. Takahashi and Y. Matsunobu, *Doppler-Free High Resolution Spectral Atlas of Iodine Molecule*, Japan Society for the Promotion of Science (2000).

[272] B. Bodermann, H. Knöckel and E. Tiemann, 'Widely usable interpolation formulae for hyperfine splittings in the $^{127}I_2$ spectrum'. *Eur. Phys. J. D* **19**, 31–44 (2002).

[273] Such program is available under the name "IodineSpec" from TOPTICA Corp., (www.toptica.com).

[274] L. Chen, W.-Y. Cheng and J. Ye, 'Hyperfine interactions and perturbation effects in the $B0_u^+(^3\Pi_u)$ state of $^{127}I_2$'. *J. Opt. Soc. Am. B* **21**, 820–832 (2004).

[275] L. Chen, W. A. de Jong and J. Ye, 'Characterization of the molecular iodine electronic wave functions and potential energy curves through hyperfine interactions in the $B0_u^+(^3\Pi_u)$ state'. *J. Opt. Soc. Am. B* **22**, 951 (2005).

[276] D. Cerny, R. Bacis and J. Verges, 'Laser-induced-fluorescence Fourier transform spectrometry of the XO_g^+ state of I_2: Extensive analysis of the $BO_u^+ \rightarrow XO_g^+$ fluorescence spectrum of $^{127}I^{129}I$ and $^{129}I_2$'. *J. Mol. Spectrosc.* **116**, 458–498 (1986).

[277] G. W. King, I. M. Littlewood, J. R. Robins and N. T. Wijeratne, 'Energy levels of iodine-129 near the B state dissociation limit from two-photon spectroscopy'. *Chem. Phys.* **50**, 291 (1980).

[278] M. Tesic and Y.-H. Pao, 'Theoretical assignment of the observed hyperfine structure in the saturated absorption spectra of I_2^{129} and $I^{127}I^{129}$ vapors in the 633 nm wavelength region'. *J. Mol. Spectrosc.* **57**, 75 (1975).

[279] T. Quinn, 'Practical realization of the definition of the metre, including recommended radiations of other optical frequency standards (2001)'. *Metrologia* **40**, 103 (2003).

[280] M. Klug, K. Schulze, U. Hinze, A. Apolonskii, E. Tiemann and B. Wellegehausen, 'Frequency stable I_2 Raman laser excited by a cw frequency doubled monolithic Nd:YAG laser'. *Opt. Commun.* **184**, 215 (2000).

[281] I. Velchev, R. van Dierendonck, W. Hogervorst and W. Ubachs, 'A Dense Grid of Reference Iodine Lines for Optical Frequency Calibration in the Range 571-596 nm'. *J. Mol. Spectrosc.* **187**, 21–27 (1998).

[282] R. Raj, D. Bloch, J. Snyder, G. Camy and M. Ducloy, 'High-Frequency Optically Heterodyned Saturation Spectroscopy Via Resonant Degenerate Four-Wave Mixing'. *Phys. Rev. Lett.* **44**, 1251–1254 (1980).

[283] J. Snyder, R. Raj, D. Bloch and M. Ducloy, 'High-sensitivity nonlinear spectroscopy using a frequency-offset pump'. *Opt. Lett.* **5**, 163 (1980).

[284] M. Broyer, J. Vigué and J. C. Lehmann, 'Effective hyperfine Hamiltonian in homonuclear diatomic molecules. Application to the B state of molecular iodine'. *J. de Physique* **39**, 591–609 (1978).

[285] H. Knöckel, S. Kremser, B. Bodermann and E. Tiemann, 'High precision measurement of hyperfine structures near 790 nm of I_2'. *Z. Phys. D* **37**, 43–48 (1996).

[286] K. F. Freed, 'On the Hyperfine Structure of InH and the Theory of the Hyperfine Structure of Molecules in Hund's Case (C)'. *J. Chem. Phys.* **45**, 1714–1722 (1966).

[287] V. Spirko and J. Blabla, 'Nuclear quadrupole coupling functions of the $^1\Sigma_g^+$ and $^3\Pi_{0u}^+$ states of molecular iodine'. *J. Mol. Spectrosc.* **129**, 59 – 71 (1988).

[288] J. Tellinghuisen, 'Spontaneous Predissociation in I_2'. *J. Chem. Phys.* **57**, 2397–2402 (1972).

[289] J. Vigué, M. Broyer and J. Lehmann, 'Natural hyperfine and magnetic predissociation of the I_2 B state I. Theory'. *J. Physique* **42**, 937–947 (1981).

[290] S. Gerstenkorn and P. Luc, 'Description of the absorption spectrum of iodine recorded by means of Fourier Transform Spectroscopy : the (B-X) system'. *J. Physique* **46**, 867 (1985).

[291] H. Walchli, R. Livingston and G. Hebert, 'The nuclear magnetic moment of I^{129}'. *Phys. Rev.* **82**, 97 (1951).

[292] R. Livingston and H. Zeldes, 'The Quadrupole Moment Ratio of $I^{1}29$ and $I^{1}27$ from Pure Quadrupole Spectra'. *Phys. Rev.* **90**, 609–610 (1953).

[293] F. James and M. Roos, 'D506 Minuit', Cern library PACKLIB (1989).

[294] 'Supplementary data files deposited in the archive of Mol. Phys.'

[295] F.-L. Hong, J. Ishikawa, A. Onae and H. Matsumoto, 'Rotation dependence of the excited-state electric quadrupole hyperfine interaction by high-resolution laser spectroscopy of $^{1}27I_2$'. *J. Opt. Soc. Am. B* **18**, 1416–1422 (2001).

[296] F.-L. Hong, Y. Zhang, J. Ishikawa, A. Onae and H. Matsumoto, 'Hyperfine structure and absolute frequency determination of the R(121)35-0 and P(142)37-0 transitions of $^{127}I_2$ near 532 nm'. *Opt. Commun.* **212**, 89 – 95 (2002).

[297] F.-L. Hong, Y. Zhang, J. Ishikawa, A. Onae and H. Matsumoto, 'Vibration dependence of the tensor spin–spin and scalar spin–spin hyperfine interactions by precision measurement of hyperfine structures of $^{127}I_2$ near 532 nm'. *J. Opt. Soc. Am. B* **19**, 946–953 (2002).

[298] F.-L. Hong, S. Diddams, R. Guo, Z.-Y. Bi, A. Onae, H. Inaba, J. Ishikawa, K. Okumura, D. Katsuragi, J. Hirata, T. Shimizu, T. Kurosu, Y. Koga and H. Matsumoto, 'Frequency measurements and hyperfine structure of the R(85)33-0 transition of molecular iodine with a femtosecond optical comb'. *J. Opt. Soc. Am. B* **21**, 88–95 (2004).

[299] P. Dubé and M. Trinczek, 'Hyperfine-structure splittings and absorption strengths of molecular-iodine transitions near the trapping frequencies of francium'. *J. Opt. Soc. Am. B* **21**, 1113–1126 (2004).

[300] C. J. Sansonetti, 'Precise measurements of hyperfine components in the spectrum of molecular iodine'. *J. Opt. Soc. Am. B* **14**, 1913–1920 (1997).

[301] J. Watson, 'The isotope dependence of diatomic Dunham coefficients'. *J. Mol. Spectrosc.* **80**, 411 (1980).

[302] E. Salumbides, K. Eikema, W. Ubachs, U. Hollenstein, H. Knöckel and E. Tiemann, 'The hyperfine structure of $^{129}I_2$ and $^{127}I^{129}I$ in the $B^3\Pi_{0_u}^+$ - $X^1\Sigma_g^+$ band system'. *Mol. Phys.* **104**, 2641–2652 (2006).

[303] Landolt-Börnstein, Springer, Berlin (1960).

[304] J. Pique, F. Hartmann, S. Churassy and R. Bacis, 'Hyperfine interactions in homonuclear diatomic molecules and u-g perturbations. I. Theory'. *J. Physique* **47**, 1909–1916 (1986).

[305] J. Pique, F. Hartmann, S. Churassy and R. Bacis, 'Hyperfine interactions in homonuclear diatomic molecules and u-g perturbations. II. Experiments on I_2'. *J. Physique* **47**, 1917–1929 (1986).

[306] J. Vigué, M. Broyer and J. Lehmann, 'Natural hyperfine and magnetic predissociation of the I_2 B state II. Experiments on natural and hyperfine predissociation'. *J. Physique* **42**, 949–959 (1981).

[307] J. Vigué, M. Broyer and J. Lehmann, 'Natural hyperfine and magnetic predissociation of the I_2 B state III. Experiments on magnetic predissociation'. *J. Physique* **42**, 961–978 (1981).

[308] J. Seto, Z. Morbi, F. Charron, S. Lee, P. Bernath and R. J. Le Roy, 'Vibration-rotation emission spectra and combined isotopomer analyses for the coinage metal hydrides: CuH & CuD, AgH & AgD, and AuH & AuD'. *J. Chem. Phys.* **110**, 11 756 (1999).

[309] J. Seto, R. J. Le Roy, J. Vergès and C. Amiot, 'Direct potential fit analysis of the $X\,^1\Sigma_g^+$ state of Rb_2: Nothing else will do!' *J. Chem. Phys.* **113**, 3067 (2000).

[310] R. J. Le Roy, Y. Huang and C. Jary, 'An accurate analytic potential function for ground-state N_2 from a direct-potential-fit analysis of spectroscopic data'. *J. Chem. Phys.* **125**, 164 310 (2006).

[311] A. Pashov, W. Jastrzebski and P. Kowalczyk, 'Construction of potential curves for diatomic molecular states by the IPA method'. *Comp. Phys. Comm.* **128**, 622–634 (2000).

[312] R. Bacis, D. Cerny and F. Martin, 'Laser-induced-fluorescence Fourier transform spectrometry of the XO_g^+ state of I_2: Tests of the long-range behavior for three isotopes of iodine'. *J. Mol. Spectrosc.* **118**, 434 – 447 (1986).

[313] S. Gerstenkorn, P. Luc and R. J. Le Roy, 'Molecular constants describing the $B(^3\Pi^+_{0u})$ - $X(^1\Sigma^+_g)$ transitions of $^{127,129}I_2$ and $^{129,129}I_2$'. *Can. J. Phys* **69**, 1299 (1991).

[314] S. Gerstenkorn, P. Luc and C. Amiot, 'Analysis of the long range potential of iodine in the B 3 state'. *J. Physique* **46**, 355 (1985).

[315] J. Watson, 'On the question of determining molecular electric dipole moments from field-free frequency data'. *J. Mol. Spectrosc.* **217**, 157 (2003).

[316] M. Rey, V. Tyuterev, J. Coxon and R. J. Le Roy, 'Resolution of a convergence problem in direct-potential-fit data analyses: Applications to GaH($X^1\Sigma^+$) and ArH$^+$($X^1\Sigma^+$)'. *J. Mol. Spectrosc.* **238**, 260 (2006).

[317] R. J. Le Roy and Y. Huang, 'Representing Born-Oppenheimer breakdown radial correction functions for diatomic molecules'. *THEOCHEM* **591**, 175 (2002).

[318] J. Blatt, 'Practical points concerning the solution of the Schrödinger equation'. *J. Comput. Phys.* **1**, 382 – 396 (1967).

[319] T. Badr, J.-P. Wallerand, P. Juncar, M. Himbert, D. Knight and M. Plimmer, Poster on the ETTF05, European Forum on Time and Frequency (2005).

[320] S. Reinhardt, G. Saathoff, S. Karpuk, C. Novotny, G. Huber, M. Zimmermann, R. Holzwarth, T. Udem, T. Hänsch and G. Gwinner, 'Iodine hyperfine structure and absolute frequency measurements at 565, 576, and 585nm'. *Opt. Commun.* **261**, 282 (2006).

[321] S. Reinhardt, B. Bernhardt, C. Geppert, R. Holzwarth, G. Huber, S. Karpuk, N. Miski-Oglu, W. Nörtershäuser, C. Novotny and T. Udem, 'Absolute frequency measurements and comparisons in iodine at 735nm and 772nm'. *Opt. Commun.* **274**, 354 (2007).

List of publications

The following publications are reproduced as chapters in this thesis:

Chapter 2: S. Hannemann, E. J. Salumbides, S. Witte, R. Th. Zinkstok, K. S. E. Eikema, and W. Ubachs, 'Frequency metrology on the EF $^1\Sigma_g^+ \leftarrow X\,^1\Sigma_g^-$ transition in H_2, HD, and D_2'. *Phys. Rev. A* **74**, 062 514 (2006).

Chapter 3: E. J. Salumbides, D. Bailly, A. Khramov, A. L. Wolf, K. S. E. Eikema, M. Vervloet, and W. Ubachs, 'Improved laboratory values of the H_2 Lyman and Werner lines for constraining time variation of the proton-to-electron mass ratio'. *Phys. Rev. Lett.* **101**, 223 001 (2008).

Chapter 4: J. Liu, E. J. Salumbides, U. Hollenstein, J. C. J. Koelemeij, K. S. E. Eikema, W. Ubachs, F. Merkt, 'Determination of the ionization and dissociation energies of hydrogen molecule'. *J. Chem. Phys.*, accepted (2009).

Chapter 5: S. Hannemann, E. J. Salumbides, S. Witte, R. Th. Zinkstok, K. S. E. Eikema, and W. Ubachs, 'Frequency metrology on the Mg $3s^2 - 3s4p$ line for comparison with quasar data'. *Phys. Rev. A* **74**, 012 505 (2006).

Chapter 6: E. J. Salumbides, S. Hannemann, K. S. E. Eikema, and W. Ubachs, 'Isotopically resolved calibration of the 285 nm Mg I resonance line for comparison with quasar absorption'. *Mon. Not. R. Astron. Soc.* **373**, L41 (2006).

Chapter 7: T. I. Ivanov, E. J. Salumbides, M. O. Vieitez, P. C. Cacciani, C. A. de Lange, and W. Ubachs, 'Extreme-ultraviolet laser metrology of O I transitions'. *Mon. Not. R. Astron. Soc.* **389**, L4 (2008).

Chapter 8: E. J. Salumbides, J. P. Sprengers, E. Reinhold, and W. Ubachs, 'High precision frequency calibration of N I lines in the XUV domain'. *J. Phys. B* **38**, L383 (2005).

Chapter 9: E. J. Salumbides, A. Khramov, and W. Ubachs, 'High-resolution 2+1 REMPI study of the $a''\,{}^1\Sigma_g^+$ state in N_2'. *J. Phys. Chem. A* **113**, 2383 (2009).

Chapter 10: E. J. Salumbides, K. S. E. Eikema, W. Ubachs, U Hollenstein, H. Knöckel, and E. Tiemann, 'The hyperfine structure of ${}^{129}I_2$ and ${}^{127}I^{129}I$ in the $B^3\Pi_{0_u^+} - X^1\Sigma_g^+$ band system'. *Mol. Phys.* **104**, 2641 (2006).

Chapter 11: E. J. Salumbides, K. S. E. Eikema, W. Ubachs, U Hollenstein, H. Knöckel, and E. Tiemann, 'Improved potentials and Born-Oppenheimer corrections by new measurements of transitions of ${}^{129}I_2$ and ${}^{127}I^{129}I$ in the $B^3\Pi_{0_u^+} - X^1\Sigma_g^+$ band system'. *Eur. Phys. J. D* **47**, 171 (2008).

The author also contributed to the following publications:

i) A.L. Wolf, S.A. van den Berg, Ch. Gohle, E.J. Salumbides, W. Ubachs, K.S.E. Eikema, 'Frequency metrology on the $4s\,{}^2S_{1/2} - 4p\,{}^2P_{1/2}$ transition in ${}^{40}Ca^+$ for comparison with quasar data'. *Phys. Rev. A* **78**, 032 511 (2008).

ii) S. Hannemann, E. J. Salumbides, and W. Ubachs, 'Reducing first order Doppler shifts in a Sagnac interferometer'. *Opt. Lett.* **32**, 1381 (2007).

Summary

The 19th-century philosopher Auguste Comte once declared that it is impossible to determine the chemical composition of stars by virtue of their enormous distance from the earth. A few decades after this pessimistic assessment, Robert Bunsen and Gustav Kirchoff were pioneering *spectrum analysis*, the study of the spectrum of light emitted or absorbed by a material, as a tool to analyse and classify substances. Since then, spectrum analysis or spectroscopy has been extensively used to probe the structure of matter. Today, astronomers collect and study light emanating from the farthest objects in the visible universe. The chemical composition of astronomical objects are being routinely deduced from their spectra, fortunately in spectacular contradiction to Comte's declaration.

The widespread application of spectroscopy is due to the ubiquity of the electromagnetic interaction, which is responsible for almost all familiar physical phenomena (except for gravitational processes). The attempt to explain this fundamental interaction, specifically in the interpretation of atomic spectra, has led to the development of quantum mechanics, which has since revolutionized our understanding of the structure of matter. It is now established that in atoms, the constituents of matter, the bound electrons can only have discrete energies corresponding to distinct atomic states. The absorption of a photon (quantum of radiation) with a definite energy that is equal to the energy difference between states results in the *excitation* of the atom, where an electron makes a transition from a lower-energy state to a higher-energy one. Since the energy of the electromagnetic radiation or a photon is proportional to the frequency, it is evident that the spectral components of radiation contain information about the energy level structure of the material that it has interacted with.

The absorption or emission spectra of atoms are relatively simple, consisting of sharp features (spectral lines). Molecular spectra increase in complexity as the number of constituent atoms (of the molecule) increases due to the additional interatomic interactions. In high-resolution atomic and molecular spectroscopy, it is important to minimize as many unwanted (external) interactions or perturbations, e.g. due to stray electric and magnetic fields, or collisions between the particles. These interactions might cause a shift in the position of the spectral line or the broadening of the spectral linewidth. An important problem in high-resolution spectroscopy is to address the Doppler effect due to the relative motion of the atoms or molecules with respect to the probing radiation. The Doppler effect often limits the spectroscopic resolution since it shifts and broadens the spectral lines, so that Doppler-free techniques are employed whenever possible. The laser is mostly used in high-resolution spectroscopy, since it has high intensity and can have high spectral purity, making it possible to resolve sharp spectral lines.

Atomic and molecular electronic transitions from the ground state mostly occur in the ultraviolet (UV), deep-UV (DUV), and extreme-UV (XUV) spectral range, corresponding to wavelengths from 400 nm to 100 nm. We produce radiation in this range by exploiting nonlinear optical effects induced by short and intense laser pulses (ns duration) in crystals and gases. For instance, the narrowband and tunable DUV laser source used in most of the experiments described in this dissertation is based on a Titanium:Sapphire (Ti:Sa) pulsed laser. The Ti:Sa output at ∼800 nm is first amplified and subsequently frequency-upconverted in crystals to obtain the 4th harmonic at ∼200 nm. The resulting DUV radiation is used for spectroscopy and has a spectral linewidth in the order of 50 MHz with pulse energies of $\sim 200\mu$J.

An important aspect of high-resolution spectroscopy is the precise and accurate calibration of the excitation laser frequency. One approach is to use a frequency standard, e.g. molecular iodine I_2, where a great number of spectral lines have been calibrated to high accuracy (at $\sim 10^{-9}$ of the transition frequency). The recent development of frequency comb lasers has revolutionized the field of frequency measurements. A frequency comb can be used as a ruler for optical frequencies by providing a precisely known set of equidistant reference frequencies (*comb teeth*). Using a frequency comb, optical frequencies with hundreds of THz can be counted directly with the same accuracy as the RF frequency standard that controls the comb laser.

The main molecule investigated in this thesis is the simplest of all neutral molecules, H_2. Doppler-free spectroscopy of the two-photon EF←X transition in H_2 is discussed in Chapter 2. Using the DUV laser source and frequency comb calibration, the transition frequencies were determined with relative accuracies on the order of 10^{-9}. In Chapter 3, the H_2 EF←X results are combined with high-resolution Fourier Transform (FT) data of H_2 transitions connecting the EF, B, and C electronic states. This combination of the DUV and FT results leads to the determination of the Lyman (B–X) and Werner (C–X) transition wavelengths with improved accuracy in comparison to direct XUV excitation.

The accurate results obtained can be used in investigations that attempt to address the possibility of variation of fundamental physical constants. Since a possible variation is expected to be very subtle, extremely sensitive (accurate) techniques are required. The method most relevant to this dissertation is based on the comparison of quasar absorption spectra with high-resolution spectra measured in the laboratory. Since quasar light was emitted in the distant past, there is a time separation of billions of years between the astronomical and lab spectra. During this time interval, physical constants could have changed, leading to very subtle differences in atomic and molecular spectra. The possible variation of the proton-to-electron mass ratio μ can be probed by comparing molecular rovibronic transitions. The H_2 Lyman and Werner transitions (Chapter 3) have been used in such μ-variation studies. The possible variation of the fine structure constant α on the other hand, can be probed by comparing the spectral lines of atoms and ions, where the transition frequencies are α-dependent. Among the many atomic and ionic transitions used in the α-variation analysis are those transitions in Mg, N, and O that are described in Chapters 5, 6, 7, and 8 of this thesis.

The determination of the H_2 ionization energy $E_\mathrm{i}(H_2)$ is described Chapter 4. The ionization energy of H_2, representing the binding energy of the electron to the molecule, is a quantity that can be calculated with *ab initio* molecular quantum theory. A comparison of the experimental and theoretical values is essential in testing the validity of fundamental molecular theory. Our obtained value for $E_\mathrm{i}(H_2)$ improves upon previous experimental results by ~ 30 times, and is more accurate than the current theoretical result.

Another example of the advantage of accurate spectroscopic investigations is demonstrated in the high-resolution study of N_2 (Chapter 9), where a perturbation in the molecular spectroscopic structure has been followed in great detail. Our highly-accurate frequency calibrations of I_2 and its isotopologues are described in Chapter 10. These measurements have enabled us to improve the predictions of I_2 molecular transitions accounting for effects beyond the Born-Oppenheimer approximation as discussed in Chapter 11.

The results reported in this dissertation demonstrate the importance of high-resolution atomic and molecular spectroscopy, as a powerful tool to further deepen our understanding of Nature.

Samenvatting

Volgens de 19e eeuwse filosoof Auguste Comte zou het onmogelijk zijn de chemische samenstelling van sterren te achterhalen vanwege hun enorm grote afstand van de aarde. Enkele decennia na dit pessimistische oordeel zetten Robert Bunsen en Gustav Kirchhoff de eerste stappen in de richting van spectrale analyse, de studie van de spectrale verdeling van het licht uitgezonden of geabsorbeerd door materialen. Sindsdien is de spectrale analyse, of de spectroscopie, intensief toegepast om de structuur van de materie te bestuderen. Tegenwoordig onderzoeken sterrenkundigen licht afkomstig van de meest veraf gelegen objecten in het zichtbare universum. De scheikundige samenstelling van astronomische objecten wordt nu veelvuldig afgeleid uit de waargenomen spectra, waarmee de uitspraken van Comte gelukkig zijn weerlegd.

De veelvuldige toepassing van spectroscopische methoden hangt samen met de alomtegenwoordigheid van de elektromagnetische wisselwerking, die verantwoordelijk is voor alle bekende alledaagse natuurkundige fenomenen, met uitzondering van de gravitatieverschijnselen. Pogingen om deze fundamentele wisselwerking te verklaren, in het bijzonder de interpretatie van gemeten atoomspectra, hebben geleid tot de ontwikkeling van quantummechanica, hetgeen sindsdien voor een revolutie in ons begrip van de structuur der materie heeft gezorgd. Het is nu bekend dat in atomen, de bouwstenen van de materie, de gebonden elektronen alleen discrete hoeveelheden energie in zich kunnen dragen, en zich als gevolg daarvan in quantumtoestanden bevinden. De absorptie van een foton met een bepaalde hoeveelheid energie, passend bij het energieverschil tussen dergelijke toestanden, leidt tot excitatie van het atoom, waarbij een electron een overgang maakt van een lage energietoestand naar een hogere energietoestand. Aangezien de energie van de elektromagnetische straling, of een foton, evenredig is met de frequentie, bevatten de spectrale componenten van de straling informatie over de energieniveaustructuur van het materiaal waarmee de straling wisselwerkte.

Absorptie- en emissiespectra van atomen zijn relatief eenvoudig, en bevatten scherpe structuren (spectrale lijnen). Moleculaire spectra worden ingewikkelder naarmate het aantal atomen in het molecuul toeneemt, als gevolg van de wisselwerking tussen de atomen onderling. In atomaire en moleculaire spectroscopie met hoge resolutie is het van belang ongewenste invloeden zoveel mogelijk te onderdrukken, zoals bijvoorbeeld de aanwezigheid van elektrische en magnetische strooivelden en botsingen tussen de deeltjes, welke interacties kunnen leiden tot verschuivingen of verbredingen van de spectrale lijnen. Zo kan het Dopplereffect, als gevolg van de relatieve beweging van de atomen of moleculen ten opzichte van de straling waarmee zij wisselwerken, de resolutie in spectropisch onderzoek limiteren. Daarom worden waar mogelijk Doppler-vrije technieken toegepast. Daarnaast worden in hoge-resolutie spectroscopie veelal lasers gebruikt, aangezien deze tegelijkertijd hoge intensiteit en hoge spectrale zuiverheid bezitten, waardoor scherpe lijnen waargenomen kunnen worden en een hoog oplossend vermogen wordt verkregen.

Elektronische overgangen in atomen en moleculen vinden plaats in het ultraviolette (UV), het diep-ultraviolette (DUV) en extreem ultraviolette (XUV) spectrale domein, overeenkomend met golflengtes tussen 400 en 100 nanometer (nm). We produceren straling in dit gebied door gebruik te maken van niet-lineaire optische effecten in kristallen en gassen, geïnduceerd door korte en intense laserpulsen (van nanoseconde tijdsduur). Zo is bijvoorbeeld de smalbandige en verstembare DUV-stralingsbron, gebruikt in de meeste van de in dit proefschrift beschreven experimenten, gebaseerd op een titaan-saffier (Ti:Sa) gepulste laser. Het licht van de Ti:Sa laser bij 800 nm wordt eerst versterkt en daarna in frequentie geconverteerd naar 200 nm in een serie van drie kristallen. De resulterende DUV-straling, die gebruikt wordt in spectroscopische experimenten, heeft een spectrale bandbreedte van 50 MHz en een pulsenergie van 200 μJ.

Een belangrijk aspect van hoge-resolutie spectroscopie is de nauwkeurige ijking van de frequentie van de laserstraling. Een mogelijkheid is het gebruik van een frequentiestandaard, bijvoorbeeld moleculair jodium (I_2), waarvan een groot aantal spectrale lijnen met hoge nauwkeurigheid (op 10^{-9} van de overgangsfrequentie) zijn gecalibreerd. De recente ontwikkeling van zogeheten frequentiekamlasers heeft een revolutie ontketend op het gebied van frequentie-ijkingen. Een frequentiekam kan gebruikt worden als een meetlat voor optische frequenties, doordat een dergelijk instrument een verzameling van referentiefrequenties op onderling gelijke afstand levert (kamtanden). Met behulp van een frequentiekam kunnen optische frequenties in het Terahertz gebied direct geteld worden met eenzelfde nauwkeurigheid als de radiofrequentie standaard, waaraan de kamlaser gestabiliseerd is.

Het belangrijkste molecuul dat in dit proefschrift onderzocht is, is het meest eenvoudige van alle neutrale moleculen: H_2. In Hoofdstuk 2 wordt Dopplervrije spectroscopie van de EF–X tweefotonovergang in H_2 beschreven. Met behulp van de DUV-laser en de frequentiekamijking zijn de overgangsfrequenties bepaald met een relative nauwkeurigheid in de orde van 10^{-9}. In Hoofdstuk 3 worden de resultaten voor het EF–X systeem gecombineerd met hoge-resolutie "Fourier-Transform"-metingen (FT) aan H_2 overgangen, die een verbinding leggen met de EF, B and C elektronische toestanden. Uit de combinatie van de resultaten die bereikt zijn met de DUV en FT technieken kunnen overgangsfrequenties in het Lyman (B–X) en het Werner (C–X) systeem worden afgeleid met een nauwkeurigheid die hoger ligt dan bij directe XUV-excitatie.

De zo verkregen nauwkeurige resultaten kunnen worden gebruikt om een mogelijke variatie van fundamentele natuurkundige constanten te onderzoeken. Omdat zo'n mogelijke variatie uiterst miniem zal zijn, zijn uiterst gevoelige (nauwkeurige) technieken vereist. De voor dit proefschrift meest relevante methode is gebaseerd op de vergelijking van quasar absorptie spectra met de hoge-resolutie spectra die in het laboratorium worden gemeten. Aangezien het quasar licht in een ver verleden is uitgezonden, ligt er een tijdsinterval van miljarden jaren tussen de waargenomen quasarspectra en de gemeten laboratoriumspectra. In de tussenliggende tijd zouden natuurkundige constanten veranderd kunnen zijn, wat leidt tot hele kleine veranderingen in atomaire en moleculaire spectra. De mogelijke variatie van de massaverhouding tussen het proton en het electron μ kan onderzocht worden door moleculaire rotatie-, vibratie- en translatieovergangen te vergelijken. De Lyman en Werner overgangen in H_2 (Hoofdstuk 3) zijn gebruikt in dergelijke studies naar veranderingen van μ. De mogelijke variatie van de fijnstructuurconstante α anderzijds, kan onderzocht worden door spectraallijnen van atomen en ionen te vergelijken, waarbij de overgangen α-afhankelijk zijn. Onder de vele overgangen in atomen en ionen die gebruikt worden in de analyse van α-variatie bevinden zich ook de overgangen in Mg, N, en O die beschreven worden in de Hoofdstukken 5, 6, 7, en 8 van dit proefschrift.

De bepaling van de H_2- ionisatie-energie $E_\mathrm{i}(H_2)$ wordt beschreven in Hoofdstuk 4. De ionisatie-energie van H_2, die de bindingsenergie van het elektron aan het molecuul vertegenwoordigt, is een getal dat met *ab initio* moleculaire quantumtheorie kan worden berekend. Een vergelijking van de experimentele en theoretische waardes is noodzakelijk om de geldigheid van fundamentele moleculaire theorie te testen. De door ons verkregen waarde voor E_i (H_2) is een verbetering van voorgaande experimentele resultaten van 30 maal, en is nauwkeuriger dan het huidige theoretische resultaat.

Een ander voorbeeld van het voordeel van nauwkeurige spectroscopie wordt gedemonstreerd in het hoge-resolutie onderzoek van N_2 (Hoofdstuk 9), waarin de verstoring van de moleculaire spectroscopische structuur in detail is gevolgd. Onze zeer accurate frequentiecalibratie van I_2 en zijn isotopen wordt beschreven in Hoofdstuk 10. Deze metingen hebben geleid tot een verbeterde voorspelling van moleculaire overgangen in I_2 waarvoor de Born-Oppenheimer benadering niet opgaat, zoals besproken wordt in Hoofdstuk 11.

De in dit proefschrift vermelde resultaten demonstreren het belang van hoge-resolutie-spectroscopie van atomen en moleculen als een krachtig instrument om ons begrip van de natuurwetten te verbeteren.

Acknowledgements

This enormous undertaking would have been impossible to complete if not for the important contributions of others. I will seize this opportunity to express my boundless gratitude to them.

I count myself most fortunate to be taken under the wing of Wim Ubachs, my thesis adviser or *promotor*. I admire your predisposition towards the fundamental and even the philosophical questions. In combination with your pragmatic attitude towards the experiments, this proves to be a successful approach. I am very grateful for the opportunity to have worked in your group. Thank you for the guidance and support that extends even beyond my stay at the VU. Your continuing support towards my future plans in Cebu is greatly appreciated and immensely motivating. Finally, your relaxed and engaging attitude towards science and life in general is worthy of emulation, and attempt I will.

I also feel privileged to have Kjeld Eikema as my second thesis adviser or *co-promotor*. Since starting as a MS student in your lab and throughout the duration of my PhD study, I have only benefited from your wealth of knowledge and experience. More than five years on, I am still rather impressed by what you have built-up and continue to develop in your lab. It was really convenient for me to be able to borrow a few things from your well-stocked cupboards, which of course, I always return afterwards (*wink*). Thank you for all the help and support, for your great tips, for the constructive criticisms and encouraging remarks, and lastly, for the great humor.

Sandro Hannemann is my predecessor who built the Ti:Sa laser, the *workhorse* of the experiments described in this thesis. He also programmed the python-based ScanUtil (a slightly more dignified choice of name than *Harry Plotter*), that may then be considered the *carriage driver* of the experiments. Dude, those graveyard shifts (all-nighters) in the lab were an exhaustingly enjoyable experience. Sandro, a.k.a. *El Duderino*, many, many thanks for all the help and support. I have thoroughly enjoyed our phase-coherent and long time-overlap in the Laser Centre; your company in the lab was dearly missed when you left.

My thanks to Jacques Bouma for his indispensable technical assistance. Your quick and elegant solutions, made adaptations to the setup really convenient. I still remember your remark that you are willing to help in setting up some sort of lab infrastructure in Cebu, I will remind you of this in the future. Thanks is also due to Eric-Jan van Duijn for lending equipment and optics and general support in the Ti:Sa laser alignment. I enjoyed our good-natured interactions and I'm thankful for your encouragements.

Of course, my colleagues in the Atomic, Molecular and Laser Physics (alf) group, have made research even more enjoyable. **Dr.** Arjan Sprengers, thanks for the fun times and your crazy jokes that thankfully were less than 10 in total. To Maria Ofelia Vieitez, thanks for those very interesting conversations about anything, everything and nothing. It is amazing that we still recognize some shared Spanish colonial influences, despite the enormous distance between the Philippines and Uruguay. Toncho Ivanov, the other dude, who share some common interests and not just in science. It was fun to launch campaigns of virtual slaughter in our virtual lands of Imperia Online. The inimitable Lineke van der Sneppen, whose good spirit and idiosyncratic way of expressing herself never fail to amuse. Alex Khramov, whom I worked with for 6 months on H_2 and N_2 spectroscopy. I hope that despite the busy times in the lab, you managed to enjoy your stay in Europe.

I am grateful to the first-generation, ultrafast duo of Stefan Witte and Roel Zinkstok. I really appreciate both your assistance with the frequency comb laser, your input in scientific discussions, and your general eagerness to help, not to mention the LOTR movie nights. Anne Lisa Wolf, one of the second-generation ultrafast crew, who built the second frequency comb laser. Thank you for the invaluable help and willingness to compromise with the measurement schedules.

The alf group members and other Laser Centre colleagues are a delightful bunch to work with. Over the years, these people are responsible for producing a truly *gezillig* atmosphere in the group: Itan Barmes, Martynas Barkauskas, Joost van Barneveld, Rick Bethlem, Fernando Brandi, Ruth Buning, Oliver Cochet, Gareth Dickenson, Thomas van Dijk, Petra de Gijssel, Christoph Gohle, Martijn Heck, Marja Herronen, Norbert Herschbach, Wim Hogervorst, Dmitry Ityaksov, Paul Jansen, Tom Jeltes, Arno de Lange, Kees de Lange, Harold Linnartz, Dominik Kandula, Rantej Kler, Jeroen Koelemeij, Valdas Maslinskas, John McNamara, Joop Mes, Daniel Noom, Stefan Petra, Josselin Philipp, Tjeerd Pinkert, Ruud van Putten, Elmar Reinhold, Amandine Renault, Rob van Rooij, Mourad Roudjane, Roel Rozendaal, Maarten Sneep, Roland Stas, Karin Stenback, Paul Tol, Andrej Tychkov, Wim Vassen, Guorong Wu, Dimitar Dobrikov, Wim Roeterdink, Arno Vredenborg. Thank you very much, for the superlatively "damn-hell-of-a-good" time I had in the group.

The number of people that appears as co-authors of the publications reproduced in this thesis, shows my extensive cooperation with almost the whole group. This is a clear demonstration of the major contribution made by these people, and I can only hope that they are not too disappointed with the end result. I feel very privileged to work with all of you.

We have been collaborating with Horst Knöckel already since I was still doing my MS project. The times that you visited us in Amsterdam were pleasant and productive. The Hannover iodine cell setup, which you brought to the Laser Centre VU, has proved to be pretty reliable. Thank you for all your help and for the wonderful collaboration.

Urs Hollenstein, whom I worked with on my MS project in Amsterdam, but also later when I visited ETH Zurich. Urs is always fun to have in the lab, and could always be depended upon the croissants in the morning, not to mention the legendary cup-cleaning exercise when he visits Amsterdam. Thank you for your kindness and hospitality in Zurich.

I worked with Jinjun Liu at the ETH Zurich on the investigation described in Chapter 4. I really appreciate your strong drive to push through with our experiment and writing the paper. Many thanks for the hard work, Jinjun.

Prof. Frederic Merkt heads the ETH Zurich XUV Spectroscopy group, where Jinjun and Urs are members of. Thank you for accommodating me when I visited your group. I have found it an enriching experience to interact with another group in the scientific sense, and very pleasant in the personal sense. And for that I thank the members of the Merkt group, for making me feel most welcome and comfortable in my short stay.

Thanks also goes to our French collaborators Denise Bailly and Michel Vervloet for the pleasant cooperation with the investigations described in Chapter 3.

The life of an exile is always a strange experience. Fortunately, the Netherlands is not too bad a country to get stuck in, actually it is quiet pleasant, and would have been perfect if it had been more sunny. Most certainly the comfort of the familiar is very welcome and perhaps necessary, and I am grateful to our Filipino friends for this. Thanks to our friends Renante Violanda and Marites Labora. We often stay-over at their place and chat the weekend away. I wish both of you the best of luck with the PhD studies. Raymund Sarmiento for the pleasant times in Nijmegen or Amsterdam, it would have been great if you stayed longer in the Netherlands. Our *honorary Cebuano* compatriots Jonathan Palero and Yoli Villanueva for the great parties and the good times. Thanks to Rommel Bacabac, for the scientific discussions, and also for facilitating our Halo-experience on Xbox. To Arni and Eloise Sicam, and their girls Beryl and Chrys, thanks for being my adopted family specially at the time before my wife came. Thanks also to Ed and Daday van den Berg, and May Ann Kuik for organizing Filipino gathering events. Finally, to the Filipino community in the Netherlands who never forgets the challenges back home, your efforts are truly inspirational.

I will be always grateful to the people who carried out the work on the Physics Development Project (PDP) in the University of San Carlos (USC) in Cebu. My gratitude to Ben Zuidberg and Kees Karremanns, for their scientific guidance in my formative years as a researcher. I am appreciative of their support and confidence in sending me to the VU for MS studies. To Gerrit Kuik, who was the manager at the start of PDP, who is again helping us at present. Thank you very much for your enthusiastic efforts in spearheading the search for future research funds for the USC Physics Department.

I am thankful to our USC Physics Department Head, Roland Otadoy, for keeping things rolling despite the limited funds and difficult circumstances. I am excited to go back and work with my former and new colleagues at USC.

I truly missed my family in the many years spent away from them. I thank my mother Cely, my brothers Bongbong and Bobet, and my little sister Celestine, for their love and support. It was during the early part of my stay in Holland when sadly, my dear grandma and my father passed away. But then, such is life that upon my return I will meet my first nephew (kudos to Chat and Bongbong).

In the end, I am deeply thankful to my wife Marian, for her unwavering support and her great patience to endure the times that I (and also she) had to spend working on my thesis. It is to Her that this thesis is dedicated to.